Atmospheric pollutant dispersion on industrial sites : concentration fluctuations in complex geometry terrains

Claudia Schiavini

To cite this version:

Claudia Schiavini. Atmospheric pollutant dispersion on industrial sites : concentration fluctuations in complex geometry terrains. Other [cond-mat.other]. Ecole Centrale de Lyon; Politecnico di Torino, 2026. English. ⟨NNT : 2026ECDL0001⟩. ⟨tel-05567193⟩

HAL Id: tel-05567193
https://theses.hal.science/tel-05567193v1

Submitted on 25 Mar 2026

N° d’ordre NNT : 2026ECDL0001

THESE DE DOCTORAT DE L’ECOLE CENTRALE DE LYON membre de l’Université de Lyon

En cotutelle internationale avec
Politecnico di Torino

Ecole Doctorale N°162
MEGA - Mécanique, Énergétique, Génie Civil, Acoustique

Spécialité de doctorat : Mécanique des fluides

Soutenue publiquement le 20 janvier 2026, par :

Claudia SCHIAVINI

Dispersion atmosphérique de polluants en zones industrielles : fluctuations de concentration dans les terrains à géométrie complexe

---

Devant le jury composé de :

Riccardo BUCCOLIERI, Full professor, University of Salento - Dipartimento di Scienze e Tecnologie Biologiche ed Ambientali - Laboratory of Micrometeorology	Président
Mélanie ROCHOUX, Directrice de recherche, CECI, Cerfacs / CNRS / IRD	Rapporteure
Sergio TEGGI, Full professor, Università degli studi di Modena e Reggio Emilia, Department of Engineering	Rapporteur
Giulia COSTA, Associate professor, Università di TorVergata	Examinatrice
Pietro SALIZZONI, Professeur, Ecole Centrale de Lyon	Directeur de thèse
Lionel SOULHAC, Professeur, INSA Lyon	Co-directeur de thèse
Deborah PANEPINTO, Associate professor, Politecnico di Torino	Co-directrice de thèse
Mariachiara ZANETTI, Full professor, Politecnico di Torino	Co-directrice de thèse

Unité de recherche : LMFA - Laboratoire de Mécanique des Fluides et Acoustique

Abstract

Accidental releases of airborne pollutants at industrial sites pose serious risks to human health and the environment. Toxic, reactive, or explosive compounds emitted during such events endanger onsite workers, emergency responders, and nearby populations. The severity of these incidents depends on whether pollutant concentrations exceed toxicity, flammability, or explosivity thresholds. Accurate estimation of concentration fields is therefore essential for emergency management and impact assessment. However, the complex geometry of industrial sites—comprising buildings, tanks, and pipes —enhances turbulence and flow irregularities, making reliable predictions of mean and peak concentrations difficult. Instantaneous peaks may exceed average levels by several orders of magnitude, representing an additional hazard.

This work experimentally investigates concentration fluctuations from a gaseous pollutant released over an idealised industrial site representative of refineries, chemical plants, and steelworks. The site includes a porous structure mimicking pipe and tank assemblies, whose effects on flow and turbulence are analysed. The experiments reveal complex recirculating and channelling patterns, with wake dynamics strongly influenced by the porous density.

Several analytical models for the one-point concentration probability density function (PDF) are evaluated. The gamma distribution best represents the midfield, while the lognormal performs better near the source; neither fully reproduces the complete experimental PDF, though both capture the high-concentration tails (95th–99th percentiles). An analytical model for threshold exceedance times offers a rapid, though approximate, tool for operational estimates.

Finally, two Lagrangian dispersion models are compared and validated against experiments. The semi-empirical PMSS model computes flow fields from adjusted meteorological profiles accounting for obstacle-induced recirculation, while SLAM (Safety Lagrangian Atmospheric Model) employs precomputed RANS simulations with a k-ε turbulence closure. Their respective advantages and limitations are discussed across varying source locations, wind directions, and site configurations.

Résumé

Les rejets accidentels de polluants atmosphériques sur les sites industriels représentent un risque majeur pour la santé humaine et pour l'environnement. Les composés toxiques, réactifs ou explosifs émis lors de tels événements mettent en danger les travailleurs du site, les équipes d'intervention d'urgence ainsi que les populations environnantes. La gravité de ces incidents dépend du dépassement éventuel des seuils de toxicité, d'inflammabilité ou d'explosivité des polluants. L'estimation précise des champs de concentration est donc essentielle pour la gestion de crise et l'évaluation des impacts. Cependant, la géométrie complexe des sites industriels — comprenant bâtiments, réservoirs et canalisations — accentue la turbulence et les irrégularités de l'écoulement, rendant difficile la prévision fiable des concentrations moyennes et des valeurs extrêmes. Les pics instantanés peuvent dépasser les valeurs moyennes de plusieurs ordres de grandeur, constituant ainsi un risque supplémentaire.

Ce travail étudie expérimentalement les fluctuations de concentration d'un polluant gazeux émis au-dessus d'un site industriel idéalisé, représentatif des raffineries, usines chimiques et aciéries. Le site comporte une structure poreuse reproduisant les assemblages de canalisations et de réservoirs, dont les effets sur l'écoulement et la turbulence sont analysés. Les expériences mettent en évidence des régimes complexes de recirculation et de canalisation, avec des dynamiques de sillage fortement influencées par la densité de porosité.

Plusieurs modèles analytiques de la fonction de densité de probabilité (PDF) des concentrations ponctuelles sont évalués. La distribution gamma décrit le mieux la zone intermédiaire, tandis que la loi log-normale reproduit plus fidèlement les concentrations proches de la source ; aucune ne restitue toutefois entièrement la PDF expérimentale, bien que les deux capturent correctement la queue de la distribution, associée aux fortes concentrations (95e et 99e percentiles). Un modèle analytique des temps de dépassement de seuil est également proposé, fournissant un outil rapide, quoique approximatif, pour des estimations opérationnelles.

Enfin, deux modèles de dispersion lagrangiens sont comparés et validés à partir des données expérimentales. Le modèle semi-empirique PMSS calcule les champs d'écoulement à partir de profils météorologiques ajustés pour tenir compte des recirculations induites par les obstacles, tandis que SLAM (Safety Lagrangian Atmospheric Model) s'appuie sur des simulations RANS préalablement calculées avec une fermeture de turbulence k–ε. Leurs avantages et limites respectifs sont discutés selon les positions de la source, les directions de vent et les configurations du site.

Sintesi

Le emissioni accidentali di inquinanti atmosferici nei siti industriali rappresentano un grave rischio per la salute umana e per l'ambiente. I composti tossici, reattivi o esplosivi emessi durante tali eventi mettono in pericolo i lavoratori presenti sul sito, i soccorritori e le popolazioni circostanti. La gravità di questi incidenti dipende dal superamento delle soglie di tossicità, infiammabilità o esplosività degli inquinanti. Una stima accurata dei campi di concentrazione è pertanto essenziale per la gestione delle emergenze e la valutazione degli impatti. Tuttavia, la geometria complessa dei siti industriali — comprendente edifici, serbatoi e tubazioni — amplifica la turbolenza e le irregolarità del flusso, rendendo difficile la previsione affidabile delle concentrazioni medie e di picco. I picchi istantanei possono superare i valori medi di diversi ordini di grandezza, costituendo un ulteriore pericolo.

Il presente lavoro analizza sperimentalmente le fluttuazioni di concentrazione di un inquinante gassoso rilasciato sopra un sito industriale idealizzato, rappresentativo di raffinerie, impianti chimici e acciaierie. Il sito include una struttura porosa che riproduce gli assemblaggi di tubazioni e serbatoi, i cui effetti sul flusso e sulla turbolenza sono analizzati. Gli esperimenti evidenziano schemi complessi di ricircolazione e canalizzazione, con dinamiche di scia fortemente influenzate dalla densità di porosità.

Sono valutati diversi modelli analitici della funzione di densità di probabilità (PDF) delle concentrazioni puntuali. La distribuzione gamma rappresenta meglio la zona intermedia, mentre la distribuzione lognormale si adatta meglio alle concentrazioni prossime alla sorgente; nessuna delle due riproduce completamente la PDF sperimentale, sebbene entrambe descrivano correttamente le code di alta concentrazione (95° e 99° percentili). Un modello analitico dei tempi di superamento delle soglie fornisce inoltre uno strumento rapido, seppur approssimato, per valutazioni operative.

Infine, due modelli di dispersione lagrangiani sono confrontati e validati rispetto ai risultati sperimentali. Il modello semi-empirico PMSS calcola i campi di flusso a partire da profili meteorologici corretti per tener conto delle ricircolazioni indotte dagli ostacoli, mentre SLAM (Safety Lagrangian Atmospheric Model) utilizza simulazioni RANS precomputate con una chiusura di turbolenza k–ε. I rispettivi vantaggi e limiti vengono discussi in funzione della posizione della sorgente, della direzione del vento e della configurazione del sito.

Acknowledgements

I would like to thank all the persons who made this project possible, especially my supervisors, whose guidance and support throughout my PhD were invaluable. Their insightful scientific advice was an immense source of help and encouragement. At the Politecnico di Torino, Deborah Panepinto, Marco Ravina and Marichiara Zanetti provided me with unwavering support and a precious help with the numerical part of this work, in addition to the scholarship which made this project possible. I am extremely grateful to Pietro Salizzoni, Massimo Marro and Lionel Soulhac, at Ecole Centrale de Lyon, for their guidance in the experimental and numerical parts of this work, their valuable scientific insight and for accompanying my development as a researcher with care and kindness.

I also want to express my gratitude to Horacio Correia, who provided me with precious help during the experimental campaign, from the construction of the reduced-scale model of the industrial site to the technical management of the measurement tools. I would like to extent my sincere thanks to Guillevic Lamaison and Perrine Charvolin-Volta, who supervised my discovery of SLAM and performed the RANS simulations forming the underlying database.

The PMSS simulations would not have been possible without the help of the developers at ARIANET, Daniela Barbero and Umberto Giuriato, who patiently helped me during this project, neither without the computational resources that were provided by HPC@POLITO, a project of Academic Computing within the Department of Control and Computer Engineering at the Politecnico di Torino (http://www.hpc.polito.it).

My sincere thanks go to Mariam Mannaa and Antoine Duclaux, who worked alongside me and shared the challenges of the experimental campaign and numerical modelling during their internships. As my PhD project was a co-tutelle, I want to acknowledge the two institutions that welcomed me: the Politecnico di Torino and the Ecole Centrale de Lyon. I am grateful to all the members of both laboratories, as they provided an ideal environment and a warm atmosphere that brightened my everyday life. I particularly appreciated the nice atmosphere in the DIATI department at Politecnico di Torino, as well as the warm friendship that I enjoyed at LMFA in Lyon.

Finally, I am deeply thankful to my family and my friends, who encouraged me and helped me during this adventure. My lifelong friends were very precious to me during this adventure, and I will also keep especially good memories with the singers of PoliEtcnico and the musicians of the AMOSUD orchestra, as well as with the capoeiristas which I had the chance to meet in Turin and in Lyon. Last but not least, special thanks go to my brother and my parents, as they were always encouraging me with endless love and lots of laughs!

Table of contents

List of Figures

List of Tables

List of symbols and acronyms

ABL	Atmospheric Boundary Layer
AFB	absolute fractional bias
$\overline{C}$	average of concentration
CFD	Computational Fluid Dynamics
C_p	p percentile of the concentration distribution
δ_{BL}	boundary layer height
δ_{ij}	Kronecker delta
DNS	Direct Numerical Simulation
$FAC2$	fraction of prediction within a factor of 2 of the observations
FID	Flame Ionisation Detector
$i_C = \sigma_C/\overline{C}$	concentration fluctuation intensity
κ	von Kármán constant
KL	Kullback-Leibler divergence
Ku	kurtosis
LDA	Laser Doppler Anemometer
L_{MO}	Monin-Obukov length
μ	dynamic viscosity
LES	Large Eddy Simulation
MG	geometric mean bias
N_ϕ^+	average frequency of exceeding the concentration threshold ϕ
$NMSE$	normalised mean square error
ν	kinematic viscosity
ν_T	turbulent viscosity
PDF	Probability Density Function
PMSS	Parallelised Micro Swift Spray
R	correlation coefficient
RANS	Reynolds-Averaged Navier-Stokes
Re	Reynolds number
σ_C	standard deviation of the one-point concentration distribution
σ_x, σ_y, σ_z	standard deviation of the spatial concentration distribution
ppm	part per million
Sk	skewness
SLAM	Safety Lagrangian Atmospheric Model
τ_C	integral time scale
T_ϕ^+	average time of exceeding the concentration threshold ϕ
TKE	Turbulent Kinetic Energy
u^*	friction velocity
U_∞	wind velocity at the top of the boundary layer
VG	geometric variance
z_0	aerodynamic roughness length

Chapter 1

General introduction

1.1 Introduction: impacts of air pollution and industrial accidents

Air pollution is a major societal challenge that poses serious threats to both public health and the environment. According to the World Health Organization, 99% of the global population breathes air containing pollutant concentrations that exceed recommended guideline limits. Populations in low- and middle-income countries are particularly vulnerable to air pollution exposure (World Health Organisation, 2025). Although air quality has improved in many developed nations over the past decades (such as France, see CITEPA, 2024), increasing urbanisation leads to a greater proportion of people being exposed to pollutants emitted within densely populated areas. Health problems associated with degraded air quality include cardiovascular and respiratory diseases (Duan et al., 2020), various forms of cancer (Loomis et al., 2013), and systemic inflammation (World Health Organisation, 2025). Once released into the atmosphere, airborne pollutants can contaminate soil, water, and living organisms, ultimately accumulating in groundwater and the biomass. Major emission sources include transportation, energy production, residential energy use (such as heating and cooking), industrial activities, waste management, and agriculture. The pollutants of greatest concern for human health include particulate matter, carbon monoxide, ozone, nitrogen oxides, sulphur oxides, and volatile organic compounds (VOCs). Beyond these traditionally monitored substances, newly recognized contaminants have emerged as subjects of increasing scientific attention, as studies investigate their toxicity and environmental persistence. Recent concern has focused particularly on per- and polyfluoroalkyl substances (PFAS), microplastics, and pesticide residues.

In contrast to daily emissions that cause chronic exposures, accidental releases occur over short time periods, typically involving large pollutant quantities that can pose immediate risks to human health and the environment. Uncontrolled releases over industrial sites may involve hazardous chemicals, radioactive materials, dense gases, ashes, or toxic combustion products generated during fires or explosions. Such events can result from accidents or deliberate actions, including terrorism, and pose significant risks not only to onsite workers and emergency responders but also to surrounding populations — sometimes affecting areas located thousands of kilometres from the source. A tragic example occurred in 1984, when the release of pesticide compounds over the city of Bhopal, India, caused thousands of deaths and became known as the world's worst industrial accident. Similarly, the 1986 Chernobyl disaster highlighted the severe dangers of radiation, as the radioactive plume spread across Europe in the days following the explosion.

Figure 1.1: Smoke plume in very low wind conditions. Fluctus clouds typical of Kelvin-Helmholtz instability are visible in the background. Image credits: M. von Allmen.

To mitigate the consequences of industrial accidents and protect exposed populations, it is essential to rapidly provide accurate information on pollutant concentration fields, despite often relying on incomplete emission and meteorological data. Such information is critical for firefighters and onsite personnel to stop or limit the release and to identify the affected areas afterward in order to implement appropriate decontamination measures. Estimating pollutant concentrations within industrial sites during accidental releases is particularly challenging due to their complex layouts and dense infrastructure dedicated to the production or storage of hazardous materials. Facilities such as chemical plants, steelworks, incinerators, and refineries feature intricate geometries that generate highly turbulent and difficult-to-predict airflow patterns. Typical site characteristics include storage areas filled with tanks, buildings of varying sizes and shapes, aligned structures forming enclosed courtyards, and dense networks of pipes and vessels. Human-scale objects are generally much smaller than the surrounding structures, and their influence on the flow field is therefore negligible in comparison.

A direct approach to assess pollutant concentrations over a site is through field measurements. However, this method is limited by the high cost of sensors and the potential risks to operators. Consequently, numerical modelling of dispersion is essential to estimate concentration fields across the entire domain with high spatial resolution. The main challenge of this approach lies in balancing computational cost —both in terms of simulation time and infrastructure requirements —with the accuracy of the results. Various numerical modelling techniques have been developed, each achieving a different compromise between these factors depending on their intended application, such as emergency response, routine monitoring, chronic exposure assessment, or development studies. Most of these methodologies provide only the mean concentration field, neglecting concentration fluctuations. However, concentration fluctuations are crucial for assessing short-term exposure to hazardous pollutants and for estimating peak concentration values. They are particularly important for evaluating the potential health effects of acute exposures and for estimating the probability of (potentially explosive) chemical reactions. Accordingly, this work focuses on airborne pollutant dispersion over industrial sites during accidental releases. The first major objective is to investigate the effect of complex site geometry —including building shapes and arrangements —on the wind velocity field. The geometry is idealised, capturing the main geometrical characteristics of typical production plants while avoiding site-specific details. Realistic features, such as tanks and intricate piping networks, are reproduced in a simplified form.

The second objective is to assess the impact of the built environment on the dispersion of pollutants released from a point source within the site, with particular emphasis on concentration fluctuations, which are strongly influenced by turbulence induced by obstacles. Finally, two operational modelling methodologies for wind and concentration fields are compared. They both rely on the Lagrangian formulation of pollutant dispersion, however they differ by the modelling methodology simulating the wind velocity field. The goal of this work is to provide an evaluation of how the choice of flow modelling approach affects the resulting concentration simulations.

1.2 Pollutant dispersion in the Atmospheric Boundary Layer

The atmospheric boundary layer (ABL) constitutes the lowest part of the troposphere (see Fig.1.2) that is directly influenced by its interaction with the Earth's surface. Its depth typically extends up to about 1km, although it can vary substantially depending on atmospheric stability, surface heating, and meteorological conditions (Stull, 1988). Within the ABL, air motion is dominated by turbulence generated by surface friction and buoyancy effects arising from temperature gradients. These turbulent processes govern the transport and dispersion of heat, momentum, moisture, and pollutants near the surface. In contrast to the free atmosphere above —where large-scale circulations and pressure gradients prevail —the dynamics of the ABL are primarily driven by small-scale, surface-induced phenomena that respond rapidly to diurnal variations in solar radiation. Since most human activities and pollutant emissions occur within this layer, understanding the structure and dynamics of the ABL is essential for accurately modelling dispersion and air quality processes.

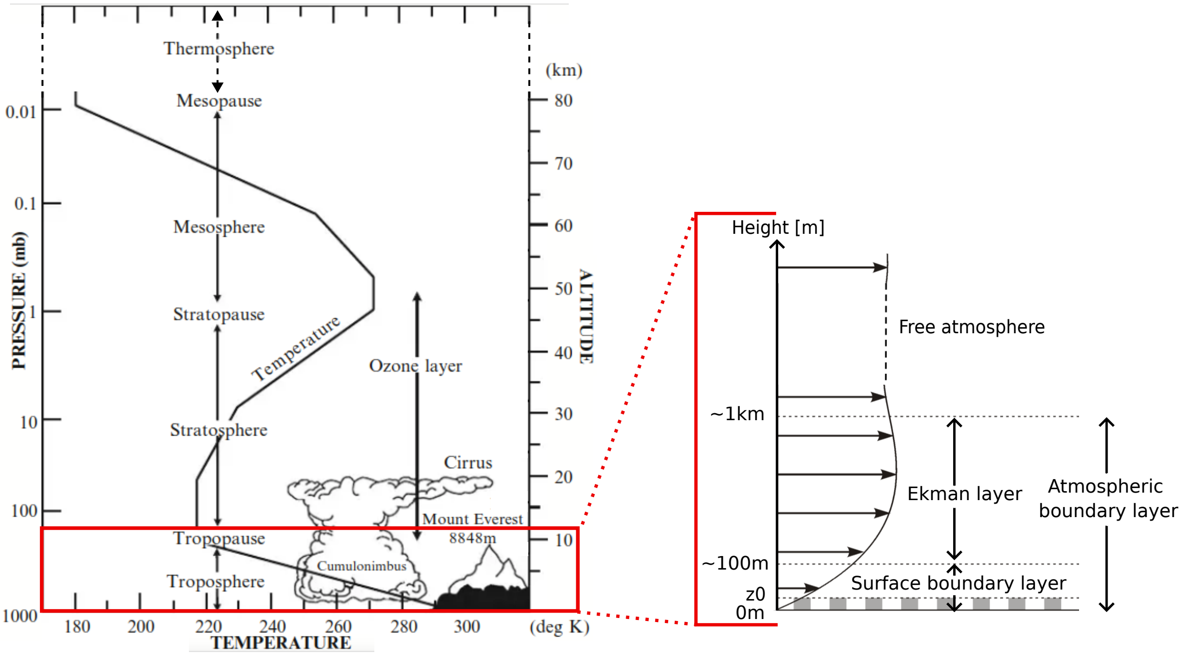

Figure 1.2: Structure of the Earth's atmosphere and its lowest layer, the troposphere. Image adapted from Lazaridis (2011) and Soulhac (2000).

As the air motion within the ABL is turbulent, a statistical approach is required to model both the flow and the dispersion of pollutants. This can be achieved either by numerically solving the averaged form of the momentum equations (eq.(6.3) and eq.(6.4), detailed in chapter 6) or by employing analytical models based on simplified descriptions of the velocity field. These approaches will be described in section 6.2.

In neutral conditions, when the surface sensible heat flux is null, and horizontal flow variations are low compared to the vertical variation, the simplest model commonly adopted for the mean wind variations along the vertical coordinate is the well known logarithmic profile. Assuming that the flow is incompressible, stationary, and horizontally homogeneous, the wind shear does not vary with height. The shear stress, defined as:

$$\tau(z) = \mu \frac{\partial u}{\partial z}$$

is thus constant and equals its ground value τ_0. The wind velocity inside the surface boundary layer scales with a characteristic surface velocity, called the friction velocity, that is obtained as:

$$u_* = \sqrt{\frac{\tau_0}{\rho}}$$

The corresponding mean wind velocity profile is given by the well-known logarithmic law of the wall (Tennekes and Lumley, 1972):

$$\frac{u(z)}{u_*} = \frac{1}{\kappa} \ln \left(\frac{z}{z_0} \right) \tag{1.1}$$

where z_0 is the aerodynamic roughness length of the surface and $\kappa \simeq 0.4$ is the von Kármán constant. The aerodynamic roughness length z_0 characterizes the surface rugosity and depends on the type of terrain, as summarized in Table 1.1 (Wieringa, 1993).

Surface type	Roughness length [m]
Sea, loose sand and snow	$\simeq$ 0.0002 (depending on the wind)
Short grass and moss	0.008 - 0.03
High mature crops (like grain)	0.12 -0.18
Mature pine forest	0.8 - 1.6
Dense low buildings (like suburbs)	0.4 - 0.7
Regularly-built large town	0.7 - 1.5

Table 1.1: Roughness length of various types of ground surfaces. Extract of the table presented by Wieringa (1993).

The flow description becomes more complex under non-neutral dynamical conditions, that is, when turbulence production from buoyancy and shear do not equilibrate. The balance between the two mechanisms, buoyancy and shear turbulence generation, is commonly characterized by the Monin–Obukhov length (Obukhov, 1971), defined as:

$$L_{MO} = \frac{-\rho\, C_p\, \overline{\theta}\, u_*^3}{\kappa\, g\, H_0},$$

where g is the gravitational acceleration, ρ the air density, C_p the specific heat capacity of air at constant pressure, $\overline{\theta}$ the mean temperature, κ the von Kármán constant, and H_0 the surface sensible heat flux. The value and sign of the parameter L_{MO} provides a straightforward indication of the dynamical state of the ABL. Specifically, unstable, neutral, and stable atmospheric conditions correspond respectively to negative, zero, and positive values of $1/L_{MO}$. The absolute magnitude of L_{MO} can be interpreted as the height at which buoyancy and wind shear contribute equally to the production of turbulent kinetic energy in unstable atmospheric conditions.

Variations of eq.(1.1) have been developed to account for the effects of atmospheric stability (Garratt, 1994), as:

$$\frac{u(z)}{u_*} = \frac{1}{\kappa}\left[\ln\left(\frac{z-d+z_0}{z_0}\right) - \psi_m\Big(\frac{z_0}{L_{MO}}\Big)\right]$$

where the zero-plane displacement, d, accounts for the height over the ground at which zero velocity is reached, due to the presence of obstacles. The stability function $\psi_m(\frac{z_0}{L_{MO}})$ provides the empirical correction of the log profile for all stability cases and writes (Garratt, 1994):

$$\Psi_m\Big(\frac{z_0}{L_{MO}}\Big) = \begin{cases} 2\ln\left(\frac{1+x}{2}\right) + \ln\left(\frac{1+x^2}{2}\right) - 2\arctan(x) + \frac{\pi}{2} & \text{if } L_{MO} < 0 \\ 0 & \text{if } L_{MO} = 0 \\ -5\frac{z_0}{L_{MO}} & \text{if } L_{MO} > 0 \end{cases}$$

where $x = (1 - 16\frac{z_0}{L_{MO}})^{1/4}$

Similar considerations apply to the mathematical modelling of the concentration field resulting from a localized pollutant release. A fully detailed representation of the concentration field would require solving the Eulerian or Lagrangian transport equations for the pollutant (chapter 6). However, simplified analytical solutions are often used as screening tools, relying on idealised descriptions of the dispersion process. A common example is provided by the Gaussian plume model. Assuming that molecular diffusion is negligible compared to turbulent dispersion, and that the latter can be described by constant turbulent diffusivity coefficients K_i, the Gaussian solution for a continuous release is given by:

$$C(x,y,z,t) = \frac{Q}{2\pi\,\sigma_y\sigma_z}\exp\left[-\frac{1}{2}\Big(\frac{(y-y_0)^2}{\sigma_y^2} + \frac{(z-z_0)^2}{\sigma_z^2}\Big)\right]$$

where x_0, y_0, z_0 are the coordinates of the point release, Q is the mass flow rate of the pollutant release, and σ_y and σ_z are the standard deviation of the spatial concentration distribution obtained as:

$$\sigma_i = \sqrt{2K_i(t-t_0)}$$

The plume standard deviation σ_y and σ_z depend on the atmospheric stability and can be described according to the Pasquill-Guifford classification of atmospheric stability (Pasquill, 1961). The latter contains 6 classes, which quantify the instability level of the atmosphere, and are defined depending on wind velocity, sun radiative flux and cloud cover.

A	extremely unstable
B	moderately unstable
C	slightly unstable
D	neutral
E	slightly stable
F	moderately stable

Table 1.2: Pasquill-Gifford stability classes

As the plume standard deviation depends on atmospheric stability, Briggs (1973) proposed empirical relations describing them for each of the Pasquill-Guifford stability class as:

$$\sigma_y = \alpha\, x\, (1 + \beta\, x)^{-0.5}$$

and

$$\sigma_z = \gamma\, x\, (1 + \delta\, x)^{-n}$$

where $n \in \{-0.5, 0, 0.5\}$ and values of α, β, γ, and δ depend on the stability class and the type of environment (urban or rural).

The Gaussian formulation is a simple analytical model that provides an estimate of the spatial distribution of mean concentration values, which reproduces the observations far from the source in simple geometries. However, it does not capture the near field plume behaviour, and it reaches its limits in the presence of obstacles, as they produce complex turbulent flow motion, such as the one pictured in Fig.1.3. Numerical models, which take the simulated flow field as input, are thus necessary to provide accurate simulations in complex geometry terrains (see chapter 6).

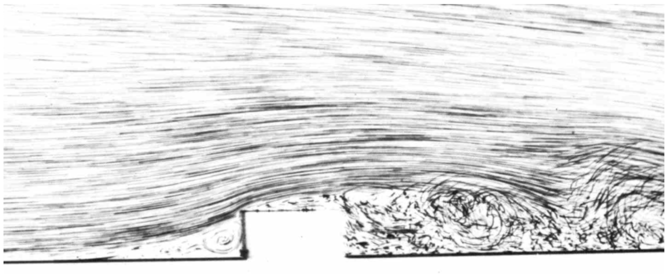

Figure 1.3: Turbulence produced by a cubic obstacle inside a two dimensional flow. Image adapted from Van Dyke (1982).

Nowadays, a major challenge in the development of pollutant dispersion models for operational applications is to provide estimates that extend beyond the mean concentration at a given receptor, by also accounting for the concentration fluctuations around the mean. A complete statistical description of these fluctuations would require reconstructing the entire one-point concentration probability density function (PDF). However, for operational purposes, the PDF can often be approximated using only the *fluctuation intensity*:

$$i_C = \frac{\sigma_C}{\overline{C}},$$

where σ_C is the standard deviation of the concentration and $\overline{C}$ is the mean concentration, together with general assumptions about the *functional form* of the one-point PDF (e.g., assuming a gamma, lognormal, or beta distribution). Figure 1.4 illustrates the evolution of the concentration time series (middle line) and the corresponding probability density function (PDF) of concentration values (bottom line), resulting from a localized pollutant release within the atmospheric boundary layer (ABL). Close to the source ($i_C > 1$), sharp concentration peaks regularly occur in the time series, and the concentration signal is very intermittent due to eddies alternatively bringing pollutant puffs and pure air at the measurement point. The corresponding PDF presents an exponential shape, which is the consequence of a large number of near-zero concentration values, while few very large concentrations are measured sporadically. Further from the source, peaks become wider and the concentration signal smooths. At some point, $i_C \simeq 1$ marks a transitional state, after which

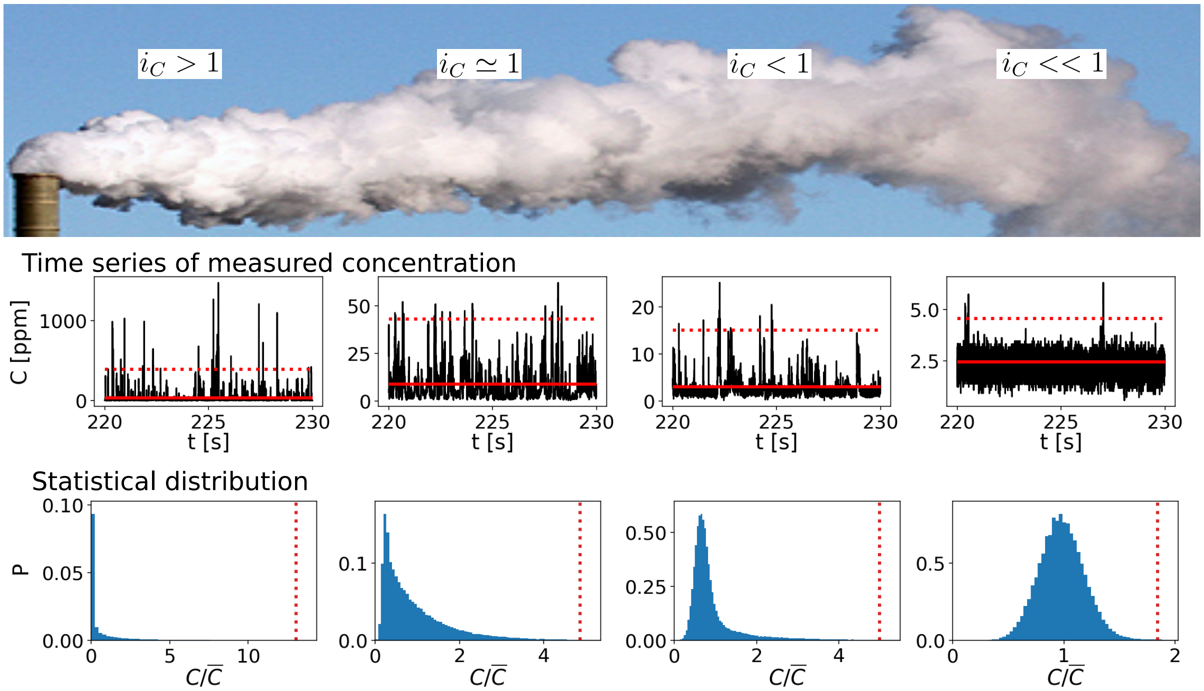

Figure 1.4: Concentration fluctuation evolution inside a pollutant plume as a function of the intensity of concentration fluctuations $i_C = \sigma_C/\overline{C}$. Red lines indicate the mean concentration value, while dotted lines correspond to the $90th$ percentile. The corresponding evolution of the statistical distribution of one-point concentration is shown on the bottom line, with the 90th percentiles as dotted lines. Plume photo ©Walter Baxter (cc-by-sa/2.0)

the concentration PDF transitions towards a Gaussian distribution. In the far field, peaks widen ($i_C < 1$) until the time series reaches a more homogeneous state ($i_C << 1$), in which peaks are more rare and closer to the mean concentration value. The 90th percentile, which is indicated by red dotted lines on Fig.1.4, corresponds to the threshold over which 10% of concentration values are lying. It thus provides information on the peaks that were recorded over the whole time series. More advanced analysing tools for the concentration fluctuations will be presented in part I.

1.3 Thesis Outline

The research carried out during this PhD focuses on the impact of built-area geometry on wind fields and pollutant dispersion. The work is structured into an experimental part, which includes the analysis of concentration fluctuations, and a numerical part.

In the first step, typical geometrical features of real industrial sites were analysed to identify the most common elements influencing pollutant spread. This phase also involved designing an idealised industrial site incorporating realistic characteristics typical of existing production plants, such as steelworks, refineries, and chemical facilities.

In the second step, numerical simulations were performed to obtain an initial representation of the wind field, considering a comprehensive set of incoming wind directions at 20° increments. Pollutant dispersion was simulated for various source positions and types (point and area sources), leading to the identification of five configurations of interest. These configurations were selected to allow a systematic analysis of the effects of different wind directions, source positions, and building porosity on dispersion patterns.

The third step involved wind tunnel experiments for the five configurations, including measurements of both velocity and concentration fields. Particular attention was given to concentration fluctuations and the influence of industrial building geometry on airflow and pollutant dispersion. This analysis is critical for risk assessment, as short-term and localized exceedances of concentration thresholds can pose health hazards or trigger chemical reactions, including potentially explosive events. Existing mathematical models for threshold exceedances were evaluated against experimental data to assess their feasibility for integration into numerical dispersion models as a tool for risk estimation.

To facilitate the presentation of this work, the experimental part is described first in Part I, detailing the site design and the five studied configurations. The numerical part is presented in Part II, including detailed comparisons of wind and concentration fields across the configurations. A particular emphasis is placed on the impact of built areas and the ability of the tested dispersion models to reproduce these effects. Finally, the thesis concludes with a dedicated section (General conclusion and perspectives) summarizing the main findings and perspectives.

Part I

Wind tunnel experiments

This first part focuses on the measurements performed in the wind tunnel at the Ecole Centrale de Lyon, to assess the effect of the geometry of an idealised industrial site on the velocity and concentration fields. Pointwise velocity measurements were performed on the small scale model of the site for two wind directions and several building porosities in order to determine the impact of the combined elements of the site on the velocity field. In a second time, several gas source positions were considered and point measurements of the concentration field lasting 5 minutes were performed in order to compute the mean and the statistics of tracer concentration.

For each measurement point we collected the time series of concentration values (one-point concentration temporal signal) and we analysed the statistical distribution of concentration values in the signal. We compared the experimental distributions with probability density functions (PDF) previously proposed for scalar dispersion modelling in the literature. The goal of these studies is to obtain probability density functions that model the experimental distribution of concentration with a reduced number of parameters. The latter are mainly the mean and the variance of the one-point concentration, which can be obtained by operational dispersion models, meaning simple dispersion models coupled to an appropriate analytical PDF model could provide the entire statistical distribution of concentration with a reasonable cost. However, probability density functions were validated mostly for academical configurations, and their validity in complex geometry contexts was insufficiently proven. Our goal was thus to determine which model distribution best reproduces the experimental PDF of concentration in complex geometry contexts.

Finally, we tested a model for the mean time of exceeding of concentration thresholds, which has strong applicative interests, hypothesising a gamma distribution.

Part of the work presented in this first part of the manuscript lead to the submission of a journal article and was presented at the EGU (European Geosciences Union) General Assembly 2025 (Schiavini et al., 2025a). Consequently, chapters 2, 3, 4 and 5 reproduce text sequences and/or figures from the article and the conference abstract.

Chapter 2

State of the art and methods

This chapter is dedicated to the presentation of the state of the art of atmospheric pollutant dispersion with a focus on fluctuations of concentration and wind tunnel experiments (see section 2.1). We then detail the experimental methods employed to model pollutant dispersion over an idealised industrial site in wind tunnel (see section 2.2).

2.1 State of the art

Accidental events at industrial sites, such as fires and chemical leaks, frequently lead to the release of hazardous airborne pollutants. Once emitted, these pollutants are dispersed by atmospheric turbulence, forming highly fluctuating plumes. At a fixed location downwind of the source, the concentration exhibits strong variability across a wide range of time scales, with intermittent peaks reaching up to 50 times the mean value (Lim and Vanderwel, 2023). Such extreme fluctuations can cause local concentrations to exceed critical thresholds for toxicity or flammability, even when the time-averaged mean remains safely below those limits. As a result, relying solely on mean concentration values is inadequate for assessing the true risk of hazardous exposure. Accurate modelling of concentration fluctuations, across both temporal and spatial scales, is therefore essential for effective risk assessment and mitigation.

To address this problem, numerous field and laboratory experiments have been conducted, primarily focusing on pollutant releases from localized sources, such as point and line releases, in boundary layer flows over flat terrain, as reviewed by Cassiani et al. (2020). To model the one-point concentration probability density function (PDF) observed experimentally (meaning the distribution of concentration values obtained at a single point for a continuous measurement lasting several minutes), several analytical relations were tested. Most of them are two-parameter distributions, having the advantage that the whole PDF can be obtained from only the mean $\overline{C}$ and the variance σ_C^2 of the pollutant concentration (Hanna, 1984). As discussed by Cassiani et al. (2020), among all models, mainly the gamma, lognormal and Weibull distributions reproduce most accurately the experimental results. However, identifying the statistical distribution that best represents the concentration probability density function (PDF) is not straightforward and depends on experimental conditions, particularly the Schmidt number as well as the position and geometry of the source (point, line, or area).

The case of a steady release from a point source over a flat terrain was investigated in the seminal wind tunnel experiments of Fackrell and Robins (1982a) and Fackrell and Robins (1982b). These experiments provided a detailed characterization of the influence of source characteristics on concentration fluctuations and have since served as a reference case for validating numerical models (Xie et al., 2007; Cassiani et al., 2024). In particular, Fackrell and Robins (1982a) and Fackrell and Robins (1982b) examined the impact of source height and diameter, with a focus on two key metrics: the intermittency of the single-point concentration signal (defined as the probability of non-zero concentrations) and the intensity of the concentration fluctuations $i_C = \sigma_C/\overline{C}$. A decade ago, Nironi et al. (2015) replicated the wind tunnel study of Fackrell and Robins (1982b) and extended the analysis to higher-order statistical moments and the shape of the one-point concentration PDF. The concentration fluctuations due to a point source have also been replicated numerically, most notably using Large Eddy Simulations (LES), by Xie et al. (2007), who focused on extreme concentration values for both elevated and ground-level sources, by Ardeshiri et al. (2020), who investigated the mechanisms generating concentration fluctuations, and by Cassiani et al. (2024), who analysed the production, transport, and dissipation of concentration fluctuations, as well as the modelling of one-point PDFs. This combined body of experimental and numerical works on scalar dispersion over a flat terrain consistently indicates that the gamma distribution provides the most suitable model for the concentration PDF across a wide range of distances from the source, for both elevated and ground-level releases. However, the accuracy of the gamma distribution declines both near the source (Yee et al., 1993a) and at the plume edges (Lim and Vanderwel, 2023), where the lognormal distribution has been found to provide a better fit to experimental concentration PDFs. Moreover, its ability to capture the upper tail of the concentration PDF has been questioned by several authors (Efthimiou et al., 2016). In such cases, alternative distributions, such as the exponential-tail (exponential) function, have shown improved performance (Talluru et al., 2017), particularly in the near-field region (Yee et al., 1994). As an alternative to the gamma distribution, some studies have explored the use of the Weibull distribution (Lung et al., 2002; Oettl and Ferrero, 2017), which offers the notable advantage of providing an analytical formulation for the PDF percentiles. This feature has practical relevance, particularly for predicting peak-to-mean concentration ratios, an important consideration in applications such as odour impact assessment (Oettl and Ferrero, 2017). While the Weibull distribution captures key features of concentration statistics, it generally reproduces the full PDF with slightly less accuracy than the gamma distribution. A notable exception is the water channel study by Yee et al. (1993b), which found the Weibull distribution to outperform the gamma distribution. This discrepancy may be attributed to the fundamentally different flow regime in that experiment, which involved a passive scalar with a Schmidt number of approximately 830, around three orders of magnitude higher than values typical of atmospheric pollutant dispersion.

Apart from the many studies focusing on flat terrains, fewer experimental works aimed at determining the effects of the built environment on the statistics of concentration fluctuations. Most of them were dedicated to urban environments (Ono and Nozu, 2024; Gailis and Hill, 2006; Gailis et al., 2007), at the scale of a neighbourhood or a street canyon (Andronopoulos et al., 2001). Gailis and Hill (2006) and Gailis et al. (2007) reproduced the MUST (Mock Urban Setting Test, Yee and Biltoft, 2004) field experiment in a wind tunnel and a water channel, and validated the gamma distribution in these conditions. They also observed the broadening of the plume close to the source due to the wakes of obstacles. In such regularly spaced obstacles configurations, thermal stratification of the boundary layer impacts both plume shape and maximum concentration levels (Marucci and Carpentieri, 2020). Simpler cases containing only one single element proved the effect of both obstacle shape and height on the velocity field and, hence, on the concentration field (Mavroidis et al., 2015). Notably, Salizzoni et al. (2025) characterized the dispersion from a line source downwind of a single obstacle, and tested the accuracy of the lognormal and the gamma distributions respectively inside and outside the recirculating region. However, the relevance of modelling the concentration PDF with a gamma distribution was questioned in more complex geometries, particularly in street canyons (Papp et al., 2024; Del Ponte et al., 2024). Notably, Del Ponte et al. (2024) showed the lognormal model to be more adapted to model the PDF of a scalar released by a line source. The gamma distribution is however an accurate predictor of high percentiles of concentration within urban geometries (Efthimiou et al., 2016; Oettl and Ferrero, 2017), similarly to the Weibull model, which can be considered as an analytically convenient variation of the former.

In operational contexts, meaningful information on concentration fluctuations encompass mainly the concentration levels reached over shorter periods than the duration over which concentration average is computed. Regulatory problems often require either to determine short term mean concentration values while only the long term average is accessible, or to estimate the peak to mean variation of concentration and the statistics of threshold exceeding. Typical situations involve the simulation of dispersion by models providing only hourly averages, while health and regulatory limits for the considered pollutants are based on average exposures over 15 minutes. To provide an answer to this kind of problems, a simple power law relation was developed by Smith (1968) and validated against experimental data (Hinds, 1969). Despite adaptations of the model by several authors to capture more accurately such short-time averages (Bartzis et al., 2008; Venkatram, 2002; Naden and Leeds, 1972), this method is now a frequent tool for short time concentration estimation (Ravina et al., 2025; Bartzis et al., 2008; Schauberger et al., 2012).

The evaluation of very short term exposures, which are necessary for odour assessment and the management of toxic and reactive pollutant spread, led to the development of analytical models to determine peak values (Schauberger et al., 2012). Peak concentrations are generally estimated by the 90th percentile of concentration, which corresponds to the concentration value that is exceeded 10% of the time (Brancher et al., 2020). The most common relation linking the 90th percentile to the mean of concentration considers a factor 4, based on Janicke and Janicke (2004). Other approaches include empirical procedures such as the model developed by Piringer et al. (2015) based on the relation of Smith (1968) and the computation of concentration variance (Oettl and Ferrero, 2017).

In other contexts, a comprehensive assessment of the risks induced by accidental releases may require evaluating the duration during which toxic or flammable substances exceed critical thresholds for a given receptor. For this purpose, the aforementioned empirical simplifications of the PDF are insufficient, as they do not account for the temporal variation of the concentration signal.

Peak-to-mean ratios, whether computed using the factor-4 method or derived directly from the PDF, provide only statistical information on peak intensities, without capturing their frequency or duration. This information is essential in scenarios where health impacts depend not only on the total exposure to concentrations above a hazard threshold but also on the number and duration of short-term exposure events. To date, few authors considered the modelling of the average exceeding time of a given threshold. To our knowledge, only Yee (2001) and Bertagni et al. (2020) developed such models, based on the assumption of a lognormal and a gamma PDF, respectively. Both models were tested against wind tunnel measurements including no obstacle, which let the question of their validity in real configurations unanswered.

As previously pointed out, wind-tunnel experiments investigating the effects of the built environment on higher-order concentration statistics are rare (Ono and Nozu, 2024; Arnold et al., 2004; Carpentieri et al., 2012), and there is therefore a lack of knowledge about which model best represents the one-point concentration probability density function (PDF) in these particular geometries. To fill this gap, in this work we therefore focus on the atmospheric dispersion of a passive scalar on a realistic industrial site. Details of the site design, the measurement methods and the mathematical tools necessary to describe concentration fluctuations will be provided in section 2.2. In chapter 3, we first characterize the velocity field induced by the numerous obstacles (section 3.1), while varying the incoming wind direction and the porosity of the tallest building. The concentration field is analysed in section 3.2. We assess the impact of the site geometry on the mean and standard deviation of the concentration field. In chapter 4, we first focus on the shape of the one-point probability density function of concentration in section 4.2, to then analyse some relevant statistical parameters (section 4.3). We compare the experimental distribution of concentration to the gamma, 2-parameters Weibull and lognormal distributions, which are the most validated models in the literature. We conclude the analysis in chapter 5 by testing a model for the statistics of exceeding concentration thresholds.

2.2 Experimental protocol

2.2.1 Wind tunnel for atmospheric dispersion experiments

The experiments took place in the atmospheric wind tunnel at the Ecole Centrale de Lyon, France (see Fig.2.1). This is a recirculating wind tunnel of dimensions 14 m x 3.7 m x 2 m apt to simulate flows reproducing the dynamics of a neutral atmospheric boundary layer. This is achieved by combining the effects of a turbulence grid and Irwin spires (Irwin, 1981), placed at the entrance of the test section, and roughness elements distributed over the entire wind tunnel floor.

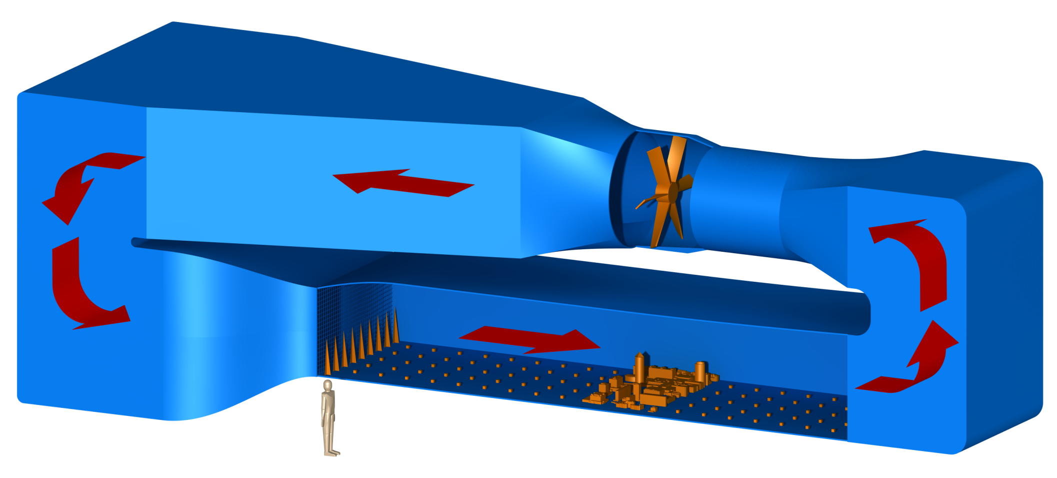

Figure 2.1: View of the wind tunnel at the Ecole Centrale de Lyon in the Laboratoire de Mécanique des Fluides et d'Acoustique (LMFA). Image courtesy of Horacio Correia. Orange elements represent the fan, Irwin spires, roughness elements and an urban reduced-scale model. Red arrows indicate the wind recirculation. The human shape is at scale.

In this study, we chose to adopt the wind tunnel set up generating the boundary layer flow presented and analysed by Nironi et al. (2015). This implied the use of Irwin spires of 0.5m high and the placement of staggered rows of cubes of dimension 0.02m × 0.02m as roughness elements over the whole wind tunnel floor. The boundary layer is fully developed starting 7m from the entrance of the wind tunnel, which determines the zone where the reduced-scale model is placed.

2.2.2 Reduced-scale model of the industrial site

The upwind part of the site is formed by a group of obstacles designed to replicate the key geometric features of a real industrial site. The site presents a simplified geometry, building shapes being approximated by parallelepipeds and cylinders, in order to avoid site specificities. The spatial arrangements of the obstacles however reproduce those commonly observed over real industrial sites such as chemical production plants, refineries and steelworks. The site is thus realistic, despite the removal of small-scale details such as pipes, wall roughness and elements lower than the human size. The characteristic height of the blocks representing the site is an order of magnitude smaller than the depth of the boundary layer δ_{BL}. This scale allows the wind tunnel experiment to capture the characteristic scale separation between the larger atmospheric eddies, whose size scales with δ_{BL}, and the smaller vortices shed in the wake of the reduced-scale buildings. The turbulent boundary layer produced at the inlet of the wind tunnel develops over the test section to resemble atmospheric boundary layers before reaching the site that perturbs the flow field.

Two incoming wind directions were investigated, namely 130° and 40° with respect to a reference direction, as shown on Fig.2.2. For the 40° wind configuration, the approaching flow first encounters a group of columns representing storage tanks, followed by a tall building, and two long parallelepipeds. The remainder of the site consists of smaller obstacles arranged to form an inner open space resembling a courtyard that contains additional tanks. The 130° wind direction generates a flow encountering first the small obstacles and one of the long parallelepipeds. Although the buildings have simplified geometries compared to those in real industrial sites, the model effectively captures the diversity of scales and spatial layouts typical of facilities such as refineries, chemical plants, and steelworks.

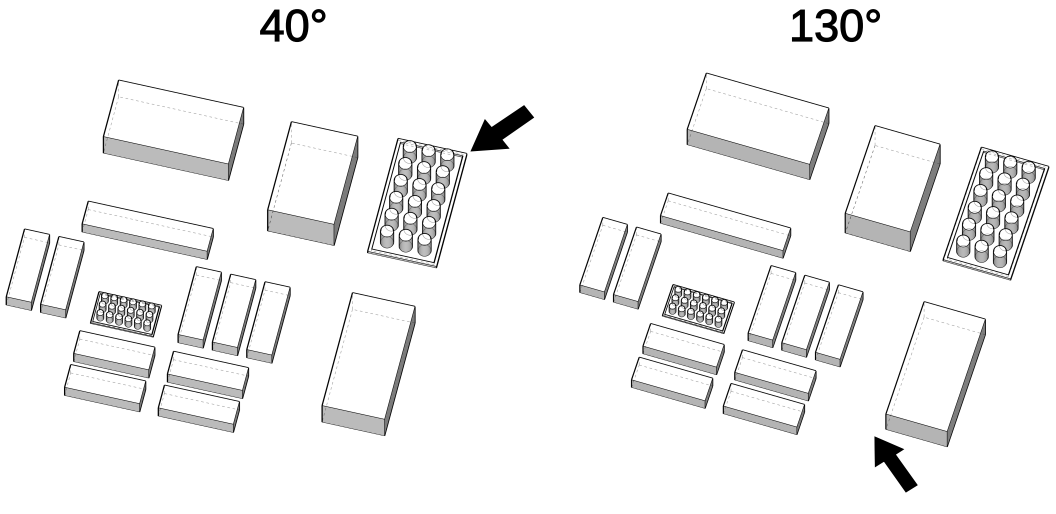

Figure 2.2: Idealised industrial site with the two wind directions investigated in this work. Images generated on SketchUp.

In addition to analysing the effect of the incoming wind direction on the wind field over the site, we assess the impact of complex structures commonly found on industrial sites, such as intertwined pipes and tanks. Such piping structures can form large conglomerations that act on the flow as a porous obstacle. In cases of accidental spread of pollutants, they impact the structure of the flow field and modify dispersion. Investigating the effect of building porosity on scalar dispersion is thus particularly relevant for operational approaches applied to industrial sites. We represent the assembly of small elements collectively as a single porous obstacle that captures the overall aerodynamic influence of such scaffolding. To evaluate how obstacle porosity affects flow and dispersion across the site, the building placed upwind in the 40° wind direction case is modelled in three different configurations (see Fig.2.3):

1. a solid parallelepiped, referred to as ‘solid’;
2. a densely packed array of columns, referred to as ‘dense’;
3. a sparse array of rectangular columns, referred to as ‘spaced’.

The ‘dense’ and ‘spaced’ configurations have solid volume fractions (ratio of filled volume over the total building volume) of 0.24 and 0.1, respectively, and are used as alternatives to the ‘solid’ configuration in the wind tunnel experiments (see Fig.2.3a). This obstacle is the tallest of the site and its height is not changed in the ‘dense’ and ‘spaced’ cases. For the 130° wind direction, it is replaced exclusively by its ‘solid’ version, as it is not located upwind and its impact on scalar dispersion is expected to be low.

The densities of columns forming the porous versions of the building were decided based on the experimental study of a flow crossing cylindrical patches made by Taddei et al. (2016). This wind tunnel experiment investigated the wake generated by a solid cylinder and by circular patches made of thinner cylinders, all patches having the same dimensions as the solid cylinder. Interestingly, Taddei et al. (2016) reported a higher drag coefficient and a wider wake for the densest patch compared to the solid cylinder. In the present work, we selected obstacle densities similar to two configurations examined by Taddei et al. (2016) to analyse their influence on the flow. However, since the wake and drag characteristics of square-section columns differ from those of circular cylinders, the increased wake extent observed in their study may not occur over the idealised industrial site. Nevertheless, we expect the chosen densities to produce differences in wake shapes and intensities downwind of the porous building.

A source of ethane of diameter 8 mm is placed at various positions of the site, as shown by the green crosses on Fig.2.4. Ethane has a density very close to that of air and can therefore be considered a passive scalar, i.e., it does not affect the flow dynamics.

We selected in total 2 wind directions, 3 source positions and 3 configurations of the tallest building of the site, in order to investigate the effects of the built elements on pollutant dispersion. For the 130° wind direction we investigated the concentration field due to 2 different source locations. Conversely, for the 40° wind direction we investigated three different geometries of the upwind building, while maintaining the source position fixed.

The configurations, which are detailed on Fig.2.4, can be summarised as follows:

- S4: wind 130°, ‘solid’ tallest building, source in between the smallest buildings
- S5: wind 130°, ‘solid’ tallest building, source in a corridor between the smallest buildings
- S25 solid: wind 40°, ‘solid’ tallest (upwind) building, source at its corner
- S25 dense: wind 40°, ‘dense’ tallest (upwind) building, source at its corner
- S25 spaced: wind 40°, ‘spaced’ tallest (upwind) building, source at its corner

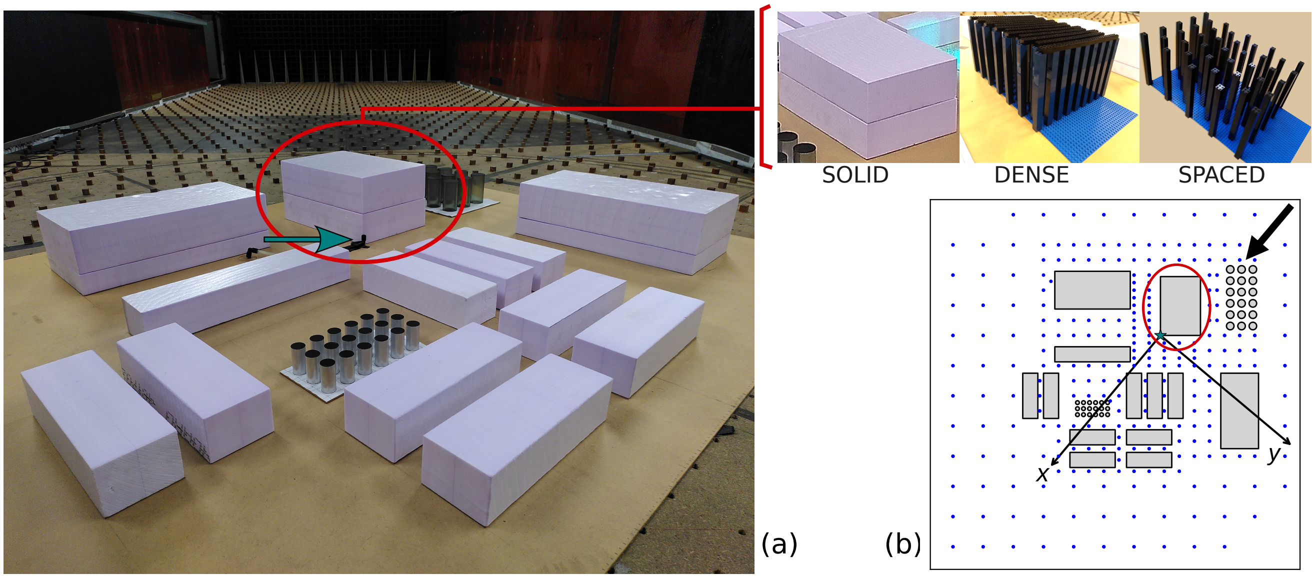

Figure 2.3: Industrial site in wind tunnel : ‘solid’, ‘dense’ and ‘spaced’ configurations in the 40° incoming wind direction case. **a** Reduced-scale model of the idealized industrial site in the wind tunnel where velocity and concentration measurements were performed. The source (identified by the green arrow), is placed at the corner of the highest building of the site. The entrance of the wind tunnel, with the grid, Irwin spires and roughness elements are visible in the background. The highest building (of height δ, circled in red) is replaced by the porous elements on the top right corner. **b** x and y axes (shown with a length of 6δ) and velocity measurement points. The incoming wind direction is indicated by the black arrow.

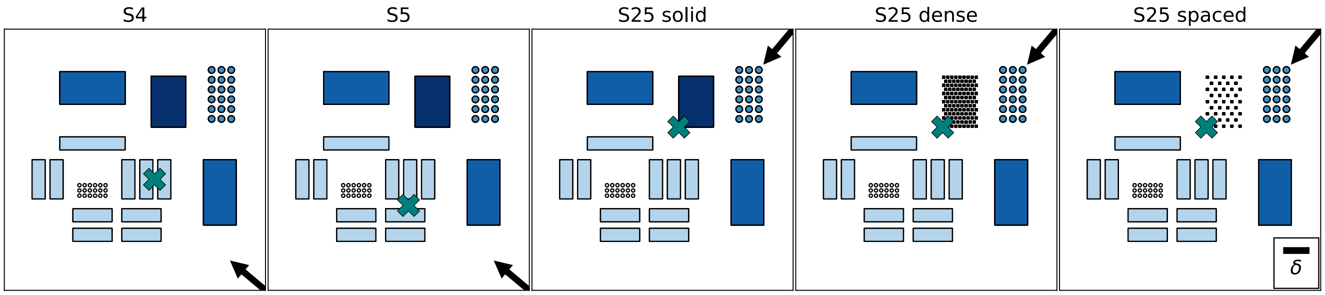

Figure 2.4: The five configurations that are studied. Arrows indicate the wind direction and crosses show the source position. Colour levels correspond to the heights of the buildings, from light to dark: $0.26\,\delta$ (small tanks), $0.39\,\delta$ (group of small buildings) , $0.52\,\delta$ (big tanks), $0.78\,\delta$ (two big parallelepipeds) and $1\,\delta$ (filled/column building). The reference scale, δ, is shown at the bottom right corner and corresponds to the height of the tallest element of the site (filled/column building). Reference axes are defined for each configuration and have their origin at the source position.

For all 5 configurations we analyse the velocity and concentration fields measured in the wind tunnel. For each configuration, we set the reference framework (Fig.2.3), with the axis x directed along the incoming mean wind direction, and y and z along the transversal and vertical directions, respectively. The velocity components along x, y and z are referred to as u, v and w respectively. In the following, positions on the site indicated by ‘left’ and ‘right’ will refer to the left hand side and right hand side of the considered image, for simplicity.

2.2.3 Measurement techniques

Velocity measurements were performed with a Laser Doppler anemometer (LDA). Two 5 W power lasers of respective wavelengths 488 nm and 514.5 nm were used to measure simultaneously two components of velocity. Each laser generated two beams of diameter 0.1 mm crossing at the measurement point and forming a measurement volume of dimensions about 0.1 mm x 0.1 mm x 2 mm. A mirror was used to redirect the beams for measurements on the vertical plane. Seeding particles of diameters from 1 to 2 micrometers were used and the average acquisition frequency was around 1550 Hz. Acquisition lasted until at least 200000 particles were detected, in order to obtain reliable statistics, notably the mean and variance of velocity. Measurement quality was controlled to limit potential biases due to the number of detected seeding particles, uncertainties in the estimation of the position of the measurement volume and potential reflections of the laser beams on reflective surfaces (Wang, 1988; Marro et al., 2020).

Ethane concentration was measured with a fast flame ionization detector (FFID) (Fackrell, 1980). The apparatus collects the air at the measurement point through a 0.3 m long sampling tube and driven towards the instrument which response frequency reached approximately 800 Hz (Nironi et al., 2015). The instrument voltage ranged from 0 to 10 V corresponding to concentrations between 0 and 5000 ppm by a linear relation. The instrument was calibrated twice a day using air-ethane mixtures of known concentrations, respectively of 0, 500, 1000 and 5000 ppm. Since the wind tunnel is closed, the concentration increased during the measurement period and background concentration had to be measured before and after measuring each point and removed from the signal. Measurements lasted for 300 s, ensuring the convergence of the first four order moments of concentration statistics. As shown by Nironi (2013), this measurement duration is sufficient to obtain reliable statistics with uncertainties that are below 3% for the mean and standard deviation of concentration and below 4.5% for the third- and fourth-order moments. This estimate includes the effects of the main sources of error, namely the presence of atmospheric aerosols in the sampled air, variations of the source mass flow rate and uncertainties linked to the calibration of the FFID.

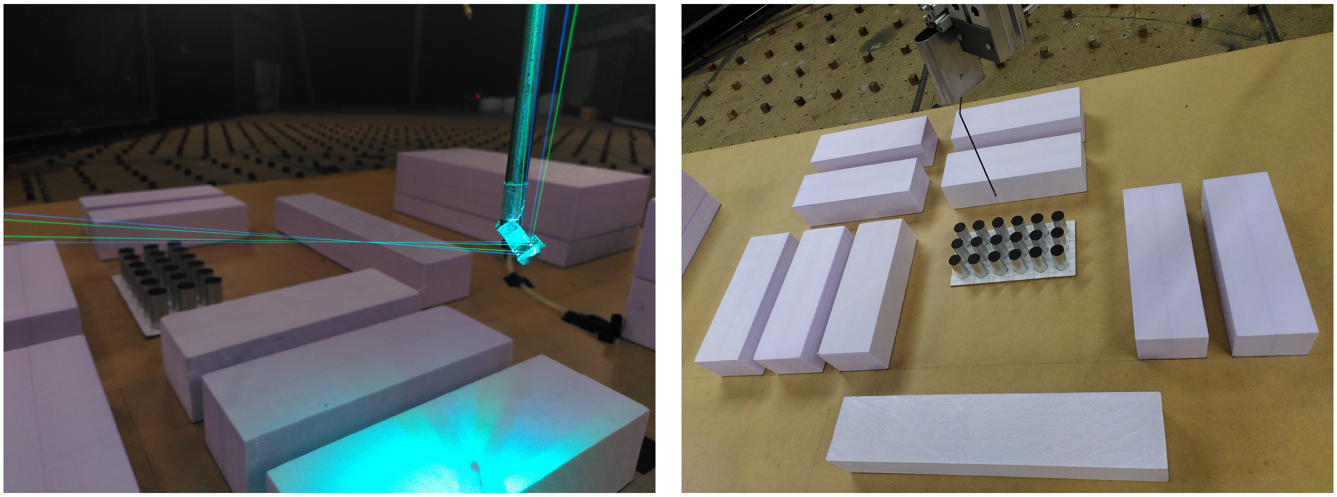

Figure 2.5: Wind tunnel measurement methods. **a**: Laser beams crossing at the measurement point after reflection on a mirror during LDA velocity measurements. **b**: Sampling tube of the FID leading to the measurement head over the reduced-scale model of the site.

To avoid saturation of the FFID during measurements close to the source, ethane was diluted with air, maintaining a global mass flow rate at the source of $0.5\,\mathrm{L\,min^{-1}}$.

Dimensionless concentrations are calculated as $C^* = C/\Delta C$ (Nironi et al., 2015), with $\Delta C = Q/(U_\infty \delta_{BL}^2)$, where Q is the mass flow rate of ethane at the source.

Chapter 3

Velocity and concentration fields

This chapter focuses on the evaluation of the velocity (section 3.1) and concentration (section 3.2) fields, with the aim of assessing the influence of the site geometry on the mean flow and scalar dispersion. Both the mean concentration (section 3.2.1) and its variance (section 3.2.2) are analysed for the five configurations introduced in chapter 2.

3.1 Mean velocity field

LDA measurements of the longitudinal (u) and transversal (v) components of wind velocity were performed at two heights of the site for all configurations, following regularly spaced grid points in order to provide a general description of the wind velocity field over the site. We focus in particular on the shape of the recirculation zones generated by the obstacles and their combined effects on the wind field. Some measurement points were added to the regular grid in order to increase the space resolution and the accuracy. Measurements of the vertical (w) velocity component were conducted at a limited number of key locations across the site. Section 3.1.1 presents the analysis of the flow field for a 130° incoming wind, without accounting for any site modifications. Section 3.1.2 focuses on the velocity field induced by a 40° wind, emphasizing the influence of the B2 building's structure (porosity). Distances are normalized by the height of the tallest building in the site ($\delta = 0.192\,\mathrm{m}$), while velocities are scaled by the reference velocity at the top of the boundary layer, U_∞. Dimensionless quantities are denoted by the superscript *.

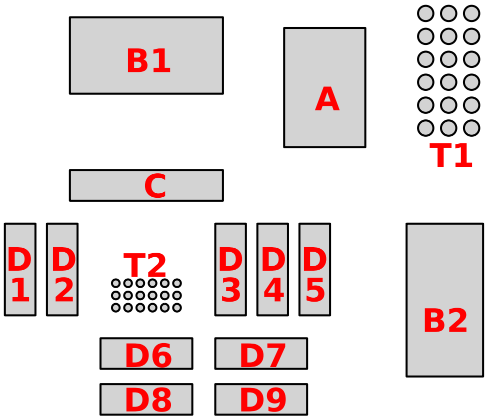

Figure 3.1: Identification of buildings forming the site.

For convenience, we denominate the buildings from the tallest to the smallest, as indicated in Fig.3.1: building A is alternatively replaced by its porous versions, B1 and B2 are the big parallelepipeds, C is the long rectangular obstacle and D1 to D9 form the group of smaller buildings (from left to right). Finally, T1 and T2 correspond to the bigger and the smaller tanks, respectively.

The experimental setup, described in section 2.2.1, produces a turbulent boundary layer previously characterized by Nironi et al. (2015). A free-stream velocity of $U_\infty = 5.0\,\mathrm{m\,s^{-1}}$ yields a boundary-layer height $\delta_{BL} = 0.8\,\mathrm{m}$ and a Reynolds number $Re = U_\infty \delta/\nu = 2.65 \times 10^5$, with $\nu = 1.51 \times 10^{-5}\,\mathrm{m^2\,s^{-1}}$ corresponding to air at $T = 20$°C. The friction velocity is $u_f = 0.185\,\mathrm{m\,s^{-1}}$.

3.1.1 Configuration with a 130° incoming wind direction

In this configuration, building B2 is the first obstacle encountered by the incoming flow. The x-axis divides the site into two distinct areas: larger site elements are located in the upper-right corner of the domain, while the lower-left corner is mainly composed of lower obstacles.

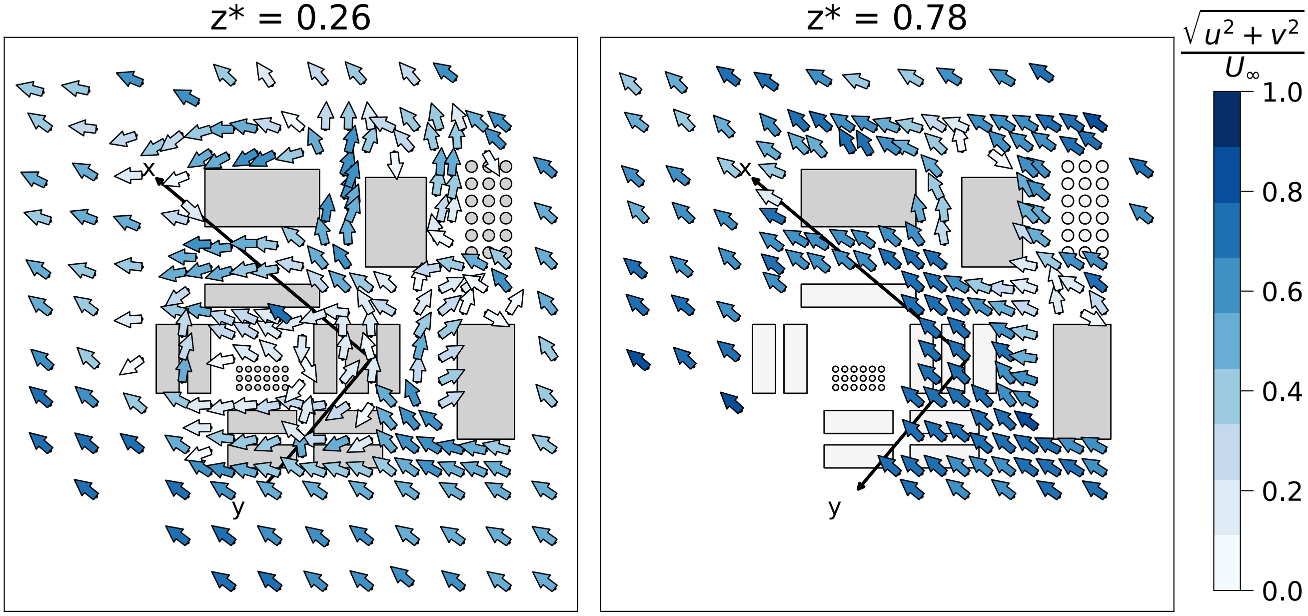

Figure 3.2: Longitudinal (u) and transversal (v) velocity components measured with LDA on two horizontal slices of the site with an incoming wind direction of 130° (used in the 'S4' and 'S5' configurations). Buildings appearing with the lightest grey shade are situated below the considered height.

Figure 3.2 presents the longitudinal (along x) and transversal (along y) wind components measured with LDA at two heights of the site. At $z^* = 0.26$, flow canalisation produced by the obstacles is visible notably between buildings A and B1, B1 and C, D5 and B2, as well as inside the corridors formed by the D buildings. In these regions, the wind direction follows the axis of the corridor instead of the incident wind direction, which is not the case at $z^* = 0.78$. Recirculation zones are observed at $z^* = 0.26$, evidenced by a local decrease in the wind velocity magnitude. Notably, building B2 generates a broad wake that strongly affects both wind speed and direction. This obstacle deflects the flow, which subsequently impinges on buildings D5, D7, and D9 at ground level. At the highest measurement level, this effect becomes less pronounced, as both the magnitude and direction of the velocity above the group of D buildings closely resemble those of the approaching flow. At this height, only the tallest obstacles (A, B1, and B2) significantly perturb the flow field. Conversely, in the downwind region of the site, the global influence of the entire building array remains evident at both measurement heights, extending up to the upper-left edge of the domain, even beyond the smaller buildings. This indicates a combined effect of interacting recirculation zones that is stronger than the simple superposition of wakes from individual buildings, as expected (Taddei et al., 2016; Yee and Biltoft, 2004).

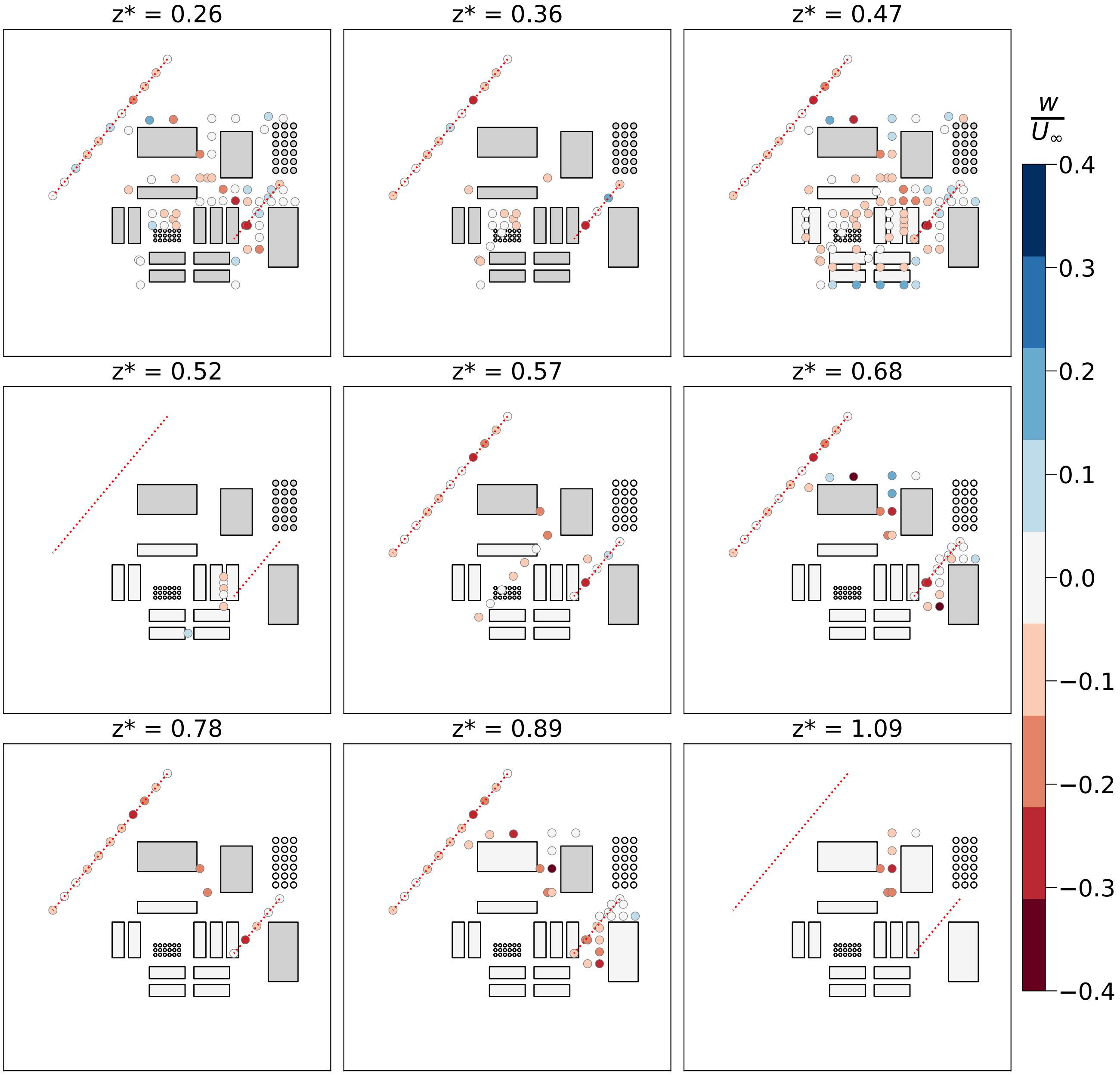

Figure 3.3: Vertical (w) wind velocity component at several heights. Red lines locate profiles of Fig.3.4 and Fig.3.5.

Measurements of the vertical (w) wind component were performed over two transversal slices and at key locations of the site to describe the upward and downward fluxes inside the recirculation zones, as shown in Fig. 3.3. We focus in particular on the wake of the B2 building, and potential upward wind velocities above the groups of D buildings. Within the recirculation zones generated by buildings A, B1, and B2, vertical velocities were measured from the ground level up to $z = \delta$. The strongest downward motion reached $w = -0.4\,U_\infty$ in these regions, although the vertical velocity component remains negligible compared to the streamwise velocity (u) over most of the site. The wake generated by building B2 and the overall recirculation induced by the entire site are clearly identifiable and are shown in Fig. 3.4 and Fig. 3.5, where the values of $\sqrt{u^2 + w^2}/U_\infty$ are reported on the vertical sections y-z. Figure 3.4 shows a region of reduced velocity downstream

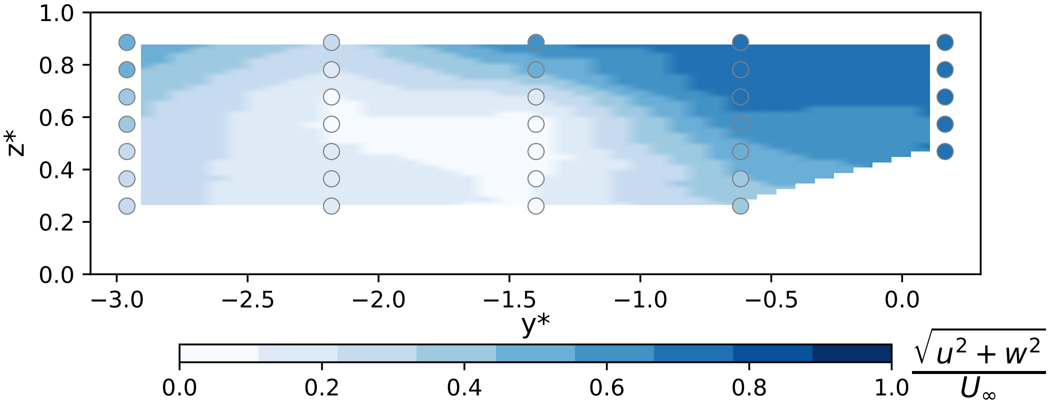

Figure 3.4: Vertical slice of the norm of u and w components inside the wake of the furthest upstream building of the site. This corresponds to the view of an observer facing the wind. Background colours are qualitative (smoothed interpolation of point data).

of the B2 building, located at the corner, extending across the entire vertical direction. The wake reaches the group of D buildings ($-3 < y^* < -2$).

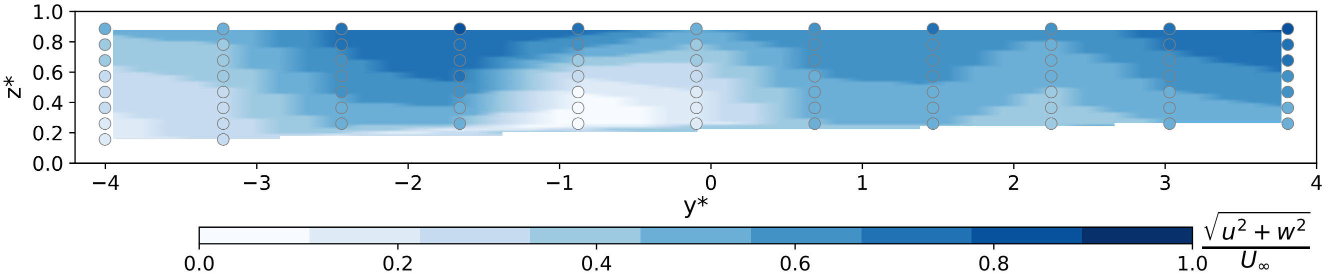

Figure 3.5: Vertical slice of the norm of u and w components downwind of the site. View of an observer facing the wind (as in Fig.3.4). Background colours are qualitative.

Figure 3.5 highlights the width of the global recirculation measured downwind of the site, which is much larger than the closest obstacle (B1). Indeed, a decrease of the norm of velocity is visible from $y^* = -4$ to $y^* = 4$, mainly due to the contribution of the u component of velocity.

3.1.2 Configurations with a 40° wind direction

In this configuration, the wind approaches at a 40° angle relative to the reference direction and first encounters the large tanks (T1) and the tallest obstacle (A building), which is also used in its 'dense' and 'spaced' versions to assess the impact of porosity on the velocity field. Note that in this case the larger obstacles are positioned upwind of the smaller buildings, and the recirculation zones they generate affect the flow across the entire site.

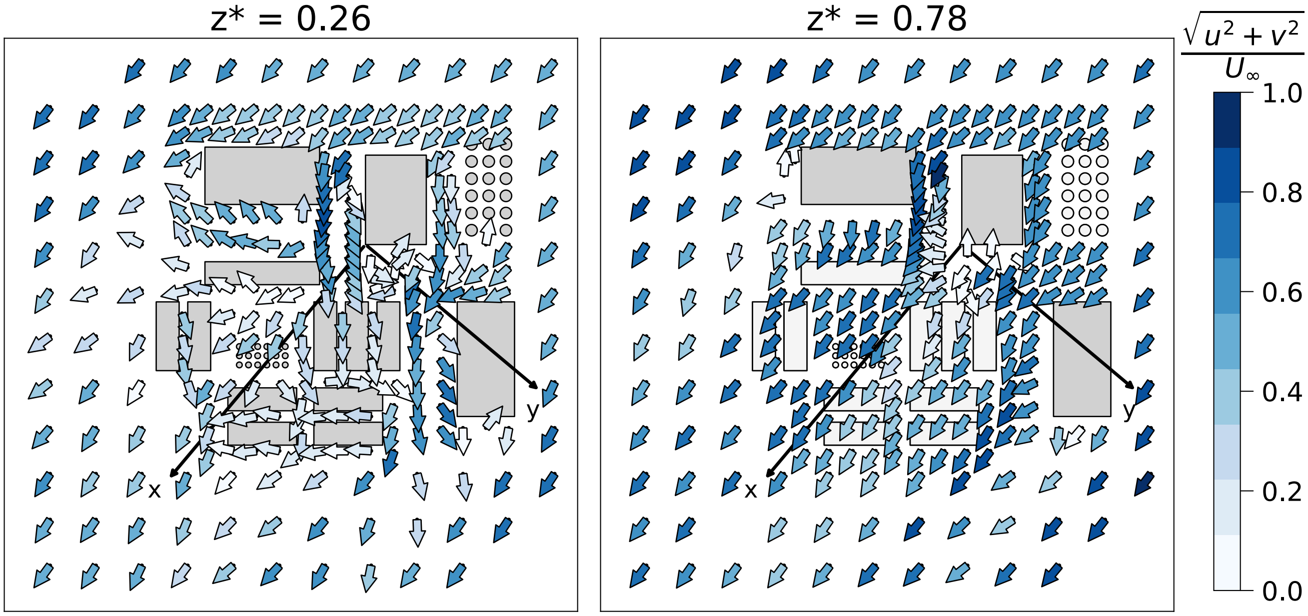

Figure 3.6: u and v velocity components measured with LDA on two horizontal slices of the site with an incoming wind direction of 40° in the 'solid' configuration.

Figure 3.6 illustrates the interactions of recirculation zones produced by the combined influence of the large upwind obstacles and the smaller downwind buildings. Although the wind direction over the group of D buildings is not really modified and it remains largely aligned with the x axis, the velocity magnitude decreases in this region due to the strong perturbing effect of the upwind obstacle (A) on the flow.

In the solid configuration, the u and w velocity components were measured on a regularly spaced grid for several values of z^*. Additionally, a vertical slice was taken downwind of the A building, as shown in Fig. 3.7. The data reveal changes in the sign of the vertical velocity, indicating the presence of upward and downward flows within the wakes of buildings A, B1, and B2. Figure 3.8 shows a reduction in velocity magnitude across the entire profile width, indicating that the recirculation zone generated by the upwind obstacle affects the downwind flow at all heights.

We now compare the velocity field measured for the three configurations of the upwind building: 'solid', 'dense' and 'spaced', with a focus on the recirculation zone generated by this element of the site. For both the 'dense' and 'spaced' configurations of the A building, measurements were conducted exclusively within the recirculation zone generated by the porous obstacle, and only the u and v velocity components were recorded due to limited measurement time.

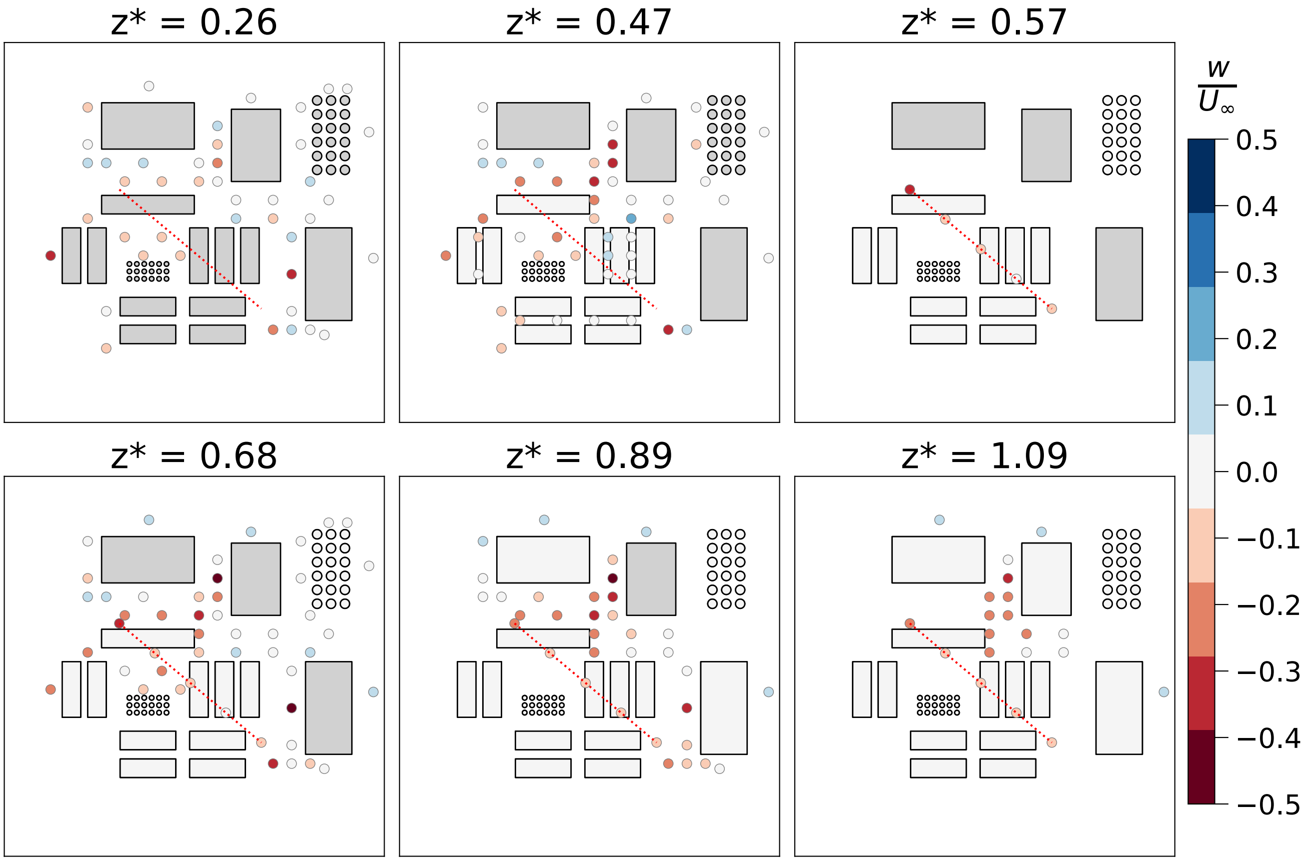

Figure 3.7: Vertical (w) wind velocity component at several heights. Red lines locate profiles of Fig. 3.8.

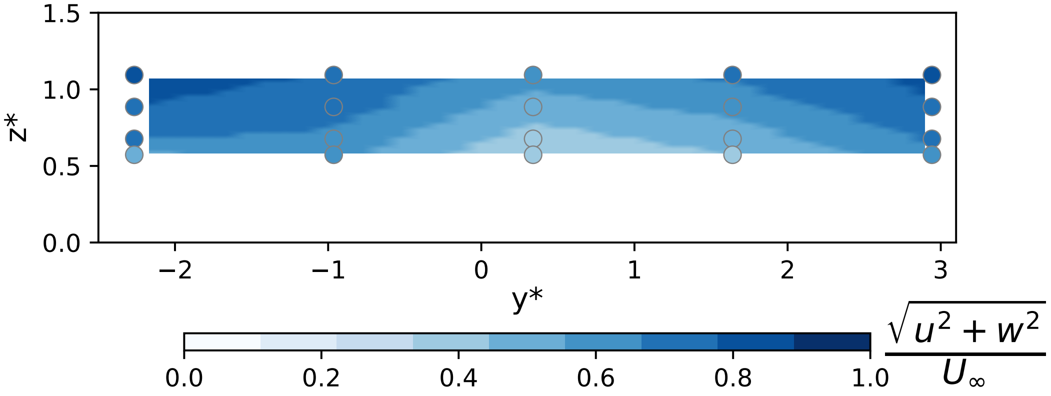

Figure 3.8: Vertical slice of the norm of u and w components, over the group of small buildings of the site. Background colours are qualitative.

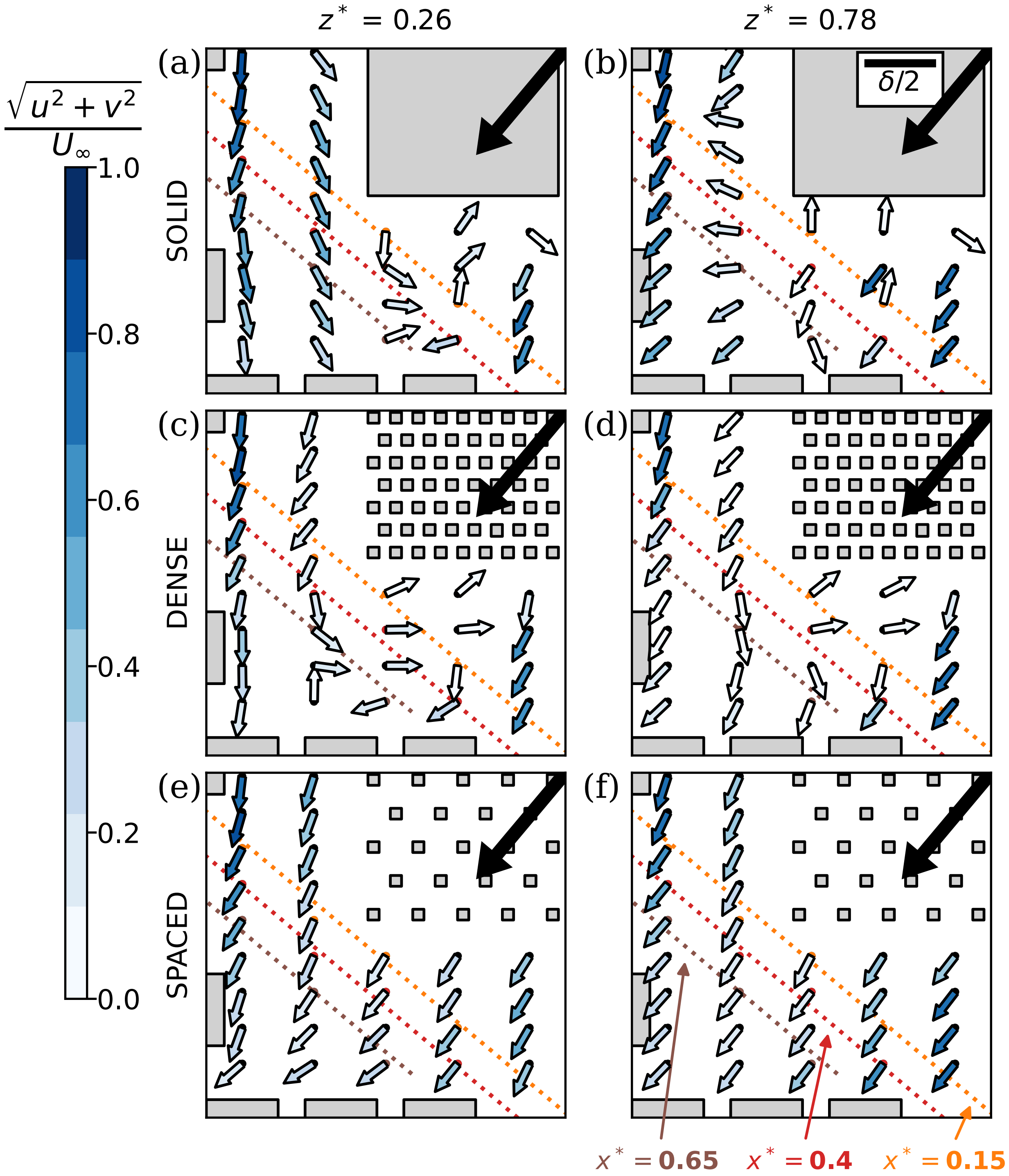

Figure 3.9: Maps of dimensionless mean velocity, considering components along x^* (u) and y^* (v) for two horizontal slices for the three configurations. **a-b**: 'solid', **c-d**: 'dense', **e-f**: 'spaced'. Black arrows show the forcing wind direction, the scale is shown on the top right corner. Recirculation is clearly visible in the 'solid' and 'dense' configurations, but the forcing wind direction stays predominant in the 'spaced' configuration. Diagonal lines with their corresponding distances to the source indicate positions of horizontal profiles reported in Fig. 3.10.

Figure 3.9 shows that the upwind building generates a recirculation region, and that its porosity influences both the location and the velocity distribution within the wake. In the ‘solid’ configuration (Fig. 3.9a), a high, channelled flow develops along the left edge of the building (negative y values) at $z^* = 0.26$, displacing the recirculation zone toward positive y values. At the upper layer $z^* = 0.78$ (Fig. 3.9b), a weaker counter-current appears from right to left within the same corridor, but the flow remains mainly aligned with the forcing wind direction. This enlightens that, as expected, the ‘solid’ configuration has a strong blocking effect which highly perturbs the flow. Conversely, the ‘dense’ configuration (Fig. 3.9c and d) generates a wider recirculating region that extends more towards negative y values, showing smaller velocities compared to the ‘solid’ case. Finally the ‘spaced’ configuration has the weakest impact on the velocity field. It does not generate a recirculation zone, as visible in Fig. 3.9e and f, the norm of velocity attains values very close to those of the upwind flow, and the wind direction is slightly impacted by the presence of the spaced columns.

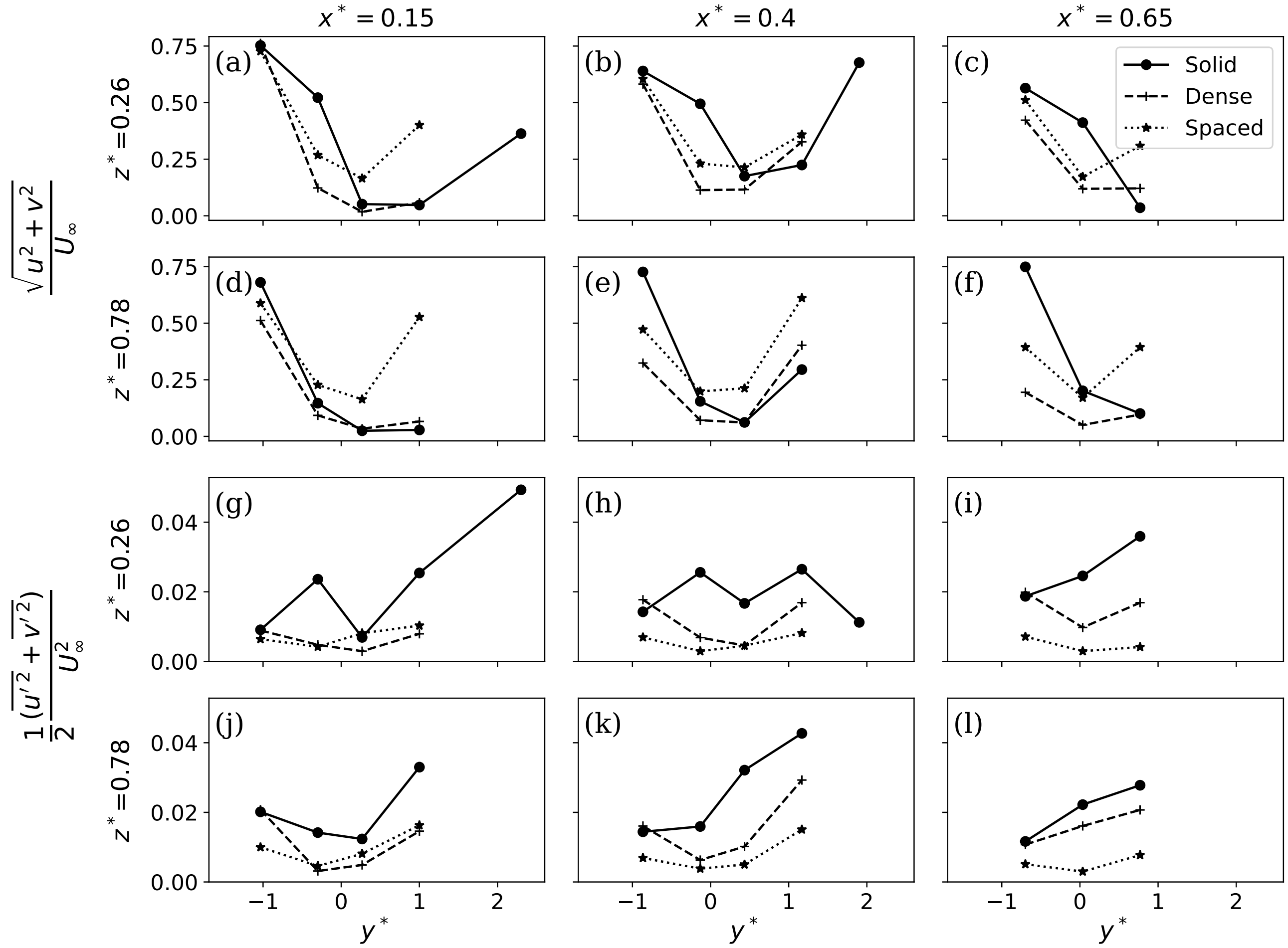

Figure 3.10: Norm of mean velocity (panels **a** to **f**) and turbulent kinetic energy (panels **g** to **l**) along the diagonals downwind of the porous building shown in Fig.3.9, computed from the two horizontal velocity components u and v only. Both shape and intensity of the wind field are affected by the upwind elements.

Figure 3.10a-f presents horizontal profiles of the norm of the mean velocity components u and v along the downwind sections shown in Fig.3.9. Similarly, Fig.3.10g-l reports the profiles of the velocity variance $1/2(\overline{u'^2} + \overline{v'^2})$. In the following we refer to this quantity as turbulent kinetic energy (TKE), acknowledging that a complete computation would also require the contribution of the vertical component $\overline{w'^2}$. Since measurement points follow a square grid in this region, their positions do not overlap perfectly with the lines shown in Fig. 3.9. However, their distance to the line is negligible and does not introduce additional uncertainty. The shift to the right-hand side of the recirculating region in the 'solid' case corresponds to a strong reduction of mean velocity (Fig. 3.10a to f), which reaches its minimum at higher y^* values than in the other configurations. The 'dense' case exhibits the lowest velocity levels in most of the building wake, due to the effect of densely packed columns, but the 'solid' configuration reaches locally comparable velocity levels at the minimum of the depletion. Turbulent kinetic energy levels (shown in Fig.3.10g to l) have stronger variability in the 'solid' configuration than in other cases, and it is globally highest and lowest in the 'solid' and 'spaced' cases, respectively.

3.2 Concentration field: mean and variance

In this section, we first characterize the concentration field over the whole site for all cases. In the 40° configurations ('S25 solid', 'dense' and 'spaced'), we analyse the effect of the upwind building porosity on the statistics of the scalar concentration. Mean dimensionless concentration ($\overline{C^*}$) and fluctuation intensity ($i_C = \sigma_C/\overline{C}$) are showed on horizontal slices at several heights ($z^* = 0.16$ and $z^* = 0.47$) and on vertical profiles (which horizontal positions are shown with special marker shapes) for the three configurations.

3.2.1 Mean concentration field

Figure 3.11 presents the measured mean concentration field for the 'S4' (top) and 'S5' (bottom) configurations, in which the source is placed inside corridors formed by neighbouring buildings of the D group. Source 'S4' is located inside the corridor formed by buildings D4 and D5, while source 'S5' is situated close by, along the edge of the D7 building. In the 'S4' case (see Fig. 3.11a), the tracer is transported towards the top of the image, consistent with the velocity field analysed in Fig. 3.2. The plume then splits around obstacle C, and again around building B1. In the far field, the majority of the tracer is recorded at the exit of the corridor separating buildings C and B1, while a second contribution appears at the top of the image, coming from the part of the plume that crossed the area between the A and B1 obstacles. The flow driven by the geometry of the grouped buildings thus generates a narrow and highly concentrated plume which behaviour is strongly impacted by the downstream obstacles.

In configuration S5, the source is located between buildings D4 and D7. The plume initially fills the corridor and subsequently spreads into the open area containing the small tanks (T2). It adopts a narrow shape with high concentrations, consistent with the geometry of the small-building group, which the plume locally bypasses—particularly around buildings D3 and D2. In the far field, the plume exhibits a nearly uniform horizontal concentration profile, resulting from the combined contributions of the main plume, which passes between buildings C and D2, and a secondary portion circumventing D1. Values of concentration collected at $z^* = 0.62$ are higher than in the 'S4' configuration, which could be explained by the combination of three effects: the flow deviation produced by the B2 building, the wake of D7, and the blocking effect of the small tanks, which all together generate a local upward flow that we did not capture with the velocity measurements (see Fig. 3.3).

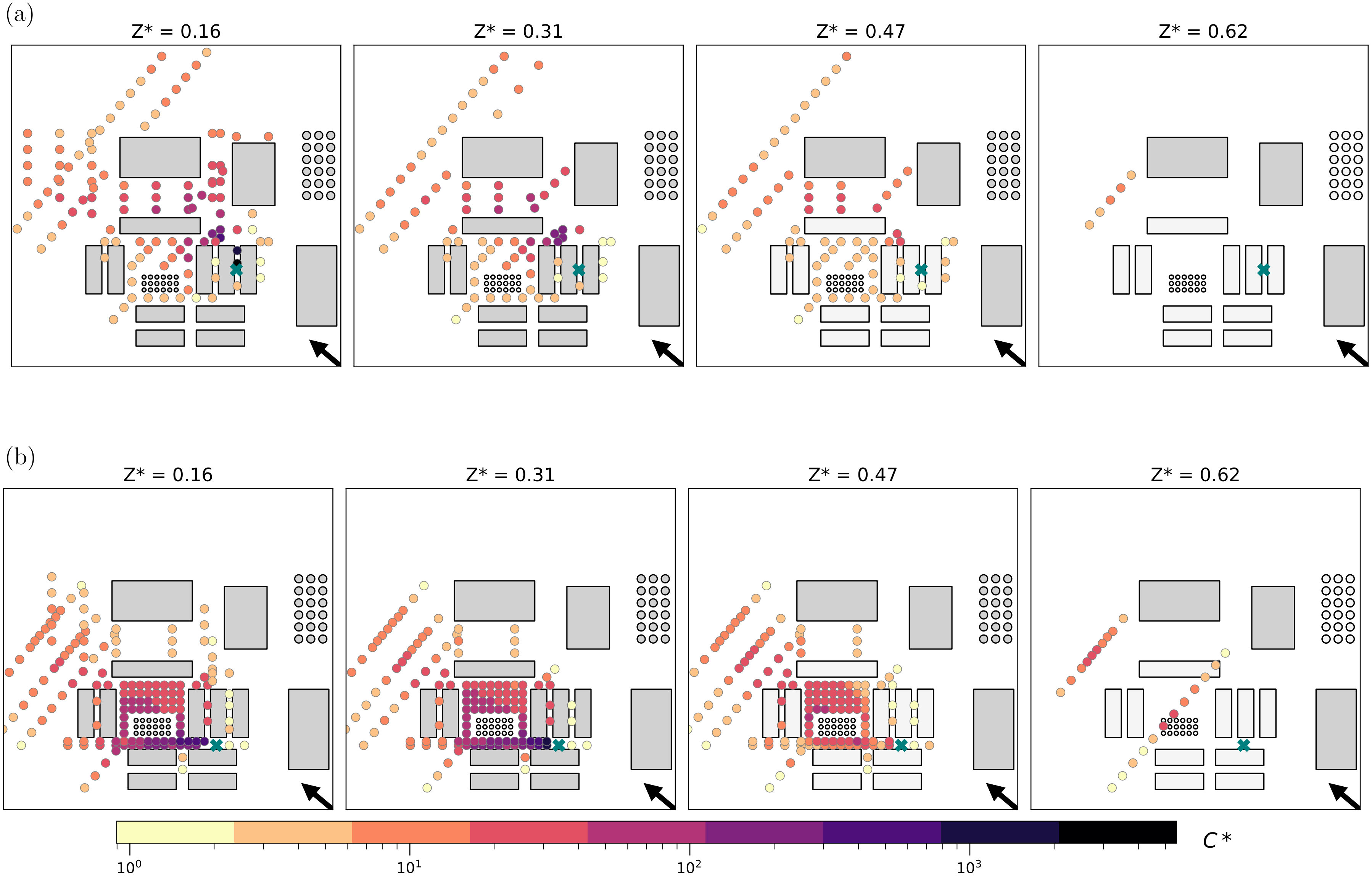

Figure 3.11: Mean concentration over several horizontal planes for the ‘S4’ (top) and ‘S5’ (bottom) configurations.

Figure 3.12 shows the locations of the concentration measurement points at ground level (panels a, d, g) and mid-height (panels b, e, h) for configurations ‘S25 solid’, ‘S25 dense’ and ‘S25 spaced’. The incident wind direction and the source direction are common to these three configurations, but the geometry of the upwind building differs. In the ‘solid’ configuration, the A building is a filled cuboid, while it is formed of closely and widely spaced columns in the ‘dense’ and the ‘spaced’ configurations, respectively. The points are arranged in a spatial grid, which enables a clear identification of the pollutant plume. Locations of the vertical profiles shown on Fig. 3.12c, f and i are chosen in order to capture the plume behaviour at increasing distance from the source (the exact location of the points vary therefore from a case to another). Three main distances are targeted, a first one close to the source inside the solid/dense/spaced building wake, a second one further in the mid-field inside the group of small buildings, and a last one in the far field downwind of the whole site.

The impact of the site configuration on the mean concentration field is visible mainly in the shape of the plume spread, as shown on the maps of Fig. 3.12a-b, d-e and g-h. In the ‘solid’ configuration (Fig. 3.12a-b) the plume is shifted to the right-hand side of the wake. This is a consequence of the velocity field shown in Fig. 3.9. Downwind, the plume spreads throughout the whole group of buildings. In the ‘dense’ configuration (Fig. 3.12d-e), the plume assumes high concentration values much closer to the corner of the porous building, due to the shape of the recirculation. This feature is still visible in the midfield, since the plume is located towards more negative y^* values compared to the ‘solid’ case. Finally, in the ‘spaced’ configuration (Fig. 3.12g-h), the plume is narrower (see Fig. 3.12g versus Fig.3.12d, particularly the points between buildings A and D4-D5), it is elongated along the forcing wind direction, and exhibits higher mean concentration values.

The vertical profiles in Fig. 3.12c, f, and i indicate that the porosity of the upwind building has a significant impact on the mean concentration field. In the ‘solid’ case, profiles near the source reach a maximum at approximately $z^* = 0.6$ (Fig. 3.12c). Concentration values above and below this height decrease almost symmetrically, reaching levels at the top of the building comparable to those near the ground. This indicates that the tracer is advected by the recirculation and undergoes stronger dilution around the mid-height of the building wake.

On the contrary, close to the source, the vertical profiles of mean concentration in the ‘dense’ case are much more uniform (Fig. 3.12f). The tracer is diluted throughout nearly the entire wake volume, resulting in lower concentrations at mid-height compared with the ‘solid’ case. However, concentrations near the ground are higher in the ‘dense’ configuration, as the vertical profile close to the source remains nearly constant below $z^* = 0.8$ (Fig. 3.12f).

The ‘spaced’ configuration shows an opposite behaviour (Fig. 3.12i). The plume is narrower and the maximum mean concentration is reached below $z^* = 0.6$, i.e. below the height of maximum mean concentration in the ‘solid’ case. This is a consequence of the low impact of columns on the velocity field. As a result, the plume exhibits a dispersion pattern similar to that observed in the absence of an upwind obstacle.

Differences in the shapes of vertical concentration profiles reflect in the values of maximum concentration and their positions on the first circle (evidenced in light blue on Fig.3.12a-b, d-e and g-h), flatter profiles being linked to lower concentration maxima. On the first circle, these are $\overline{C^*} = 367.9$ in the ‘spaced’ case (at plume centre), $\overline{C^*} = 135.6$ in the ‘solid’ case (close to the bottom right corner of the upwind building), and $\overline{C^*} = 111.5$ in the ‘dense’ case (at the entrance of the corridor separating D4 and D5). This is due to strong wakes generated in the ‘solid’ and ‘dense’ configurations that dilute the plume and displace its centre of mass.

These differences, that are highly visible in the short range, tend to fade at larger distances from the source. The main differences in the mid range are the higher values of mean concentration

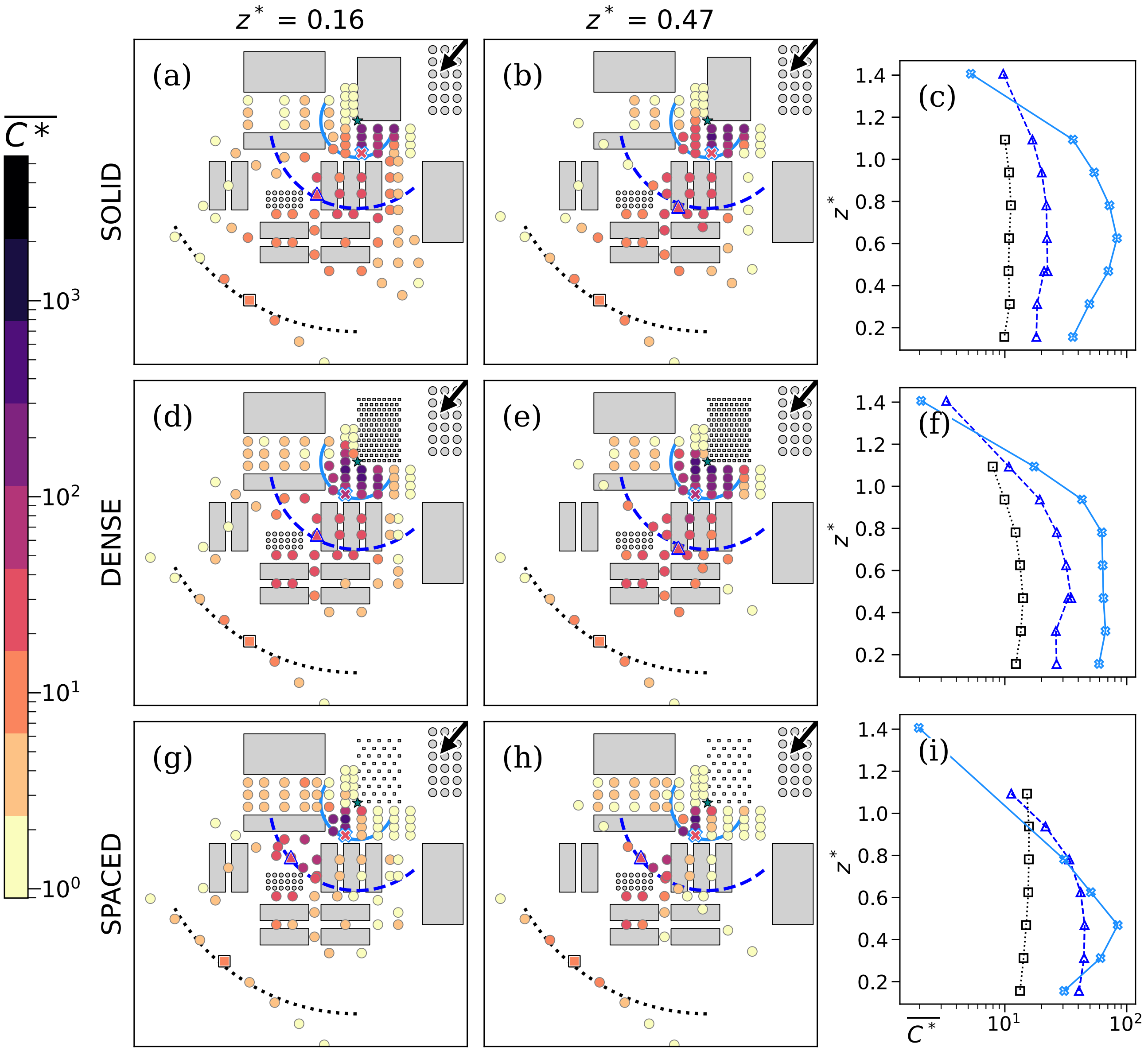

Figure 3.12: Average dimensionless concentration ($\overline{C^*}$) on 2 horizontal slices (panels **a-b**, **d-e** and **g-h**) and 3 vertical profiles (panels **c**, **f** and **i**) for the 3 configurations. Positions of vertical profiles (shown as cross, triangle and diamond markers on the maps) were chosen according to their distances to the source (circles of corresponding colours). For the middle range, vertical profiles were split into a lower and an upper layer where the presence of buildings rendered it necessary. The source is placed at the corner of the upwind building (green star) and the black arrows indicate the forcing wind direction. Both plume shape and extent are impacted by building porosity.

reached in the profile of the 'spaced' case (Fig. 3.12i), compared to the other site configurations (Fig. 3.12c and f). The maximum mean concentration attained in the 'spaced' configuration on the second circle still is 3 times higher than the maximum of 'dense' and 'solid' configurations, and it is reached at the plume centreline close to the tanks.

In the far field, the main noticeable difference between the three configurations is the position of plume maximum, which is still shifted towards positive values of y^* in the 'solid' and 'dense' cases (see Fig. 3.12a-b, d-e and g-h). The maximum mean concentration values measured in this region are similar between all three configurations, considering the spatial resolution available in the data. We observe in the far field the shift of the plume centreline in the ‘solid’ and ‘dense’ cases with respect to the ‘spaced’ configuration. The influence of the building porosity on the plume is thus not confined to the region near the source where it directly affects the velocity field and wake, but it also produces observable effects extending into the far field.

3.2.2 Intensity of the concentration fluctuations

We evaluated the fluctuation intensity $i_C = \sigma_C/\overline{C}$ and investigated how it is impacted by the geometry of the site.

Figure 3.13 presents measured values of i_C for the ‘S4’ configuration (top) and the ‘S5’ configuration (bottom). Concentration fluctuation intensity is higher close to the source and at plume borders in both cases. This behaviour is typical of a plume dispersing over a flat terrain, since the highly concentrated puffs emitted at the source meander and slowly dilute with pure air. Close to the source, point measurements alternatively detect the highly concentrated puffs and pure air, meaning the variance of the concentration signal is high compared to the mean concentration ($i_C > 1$). Further from the source, inside the plume, the tracer dilutes with the air, generating a more homogeneous signal on the sensor ($i_C < 1$). At plume borders, however, the instantaneous (and mean) concentration is low and both pure air from the surroundings and puffs escaping from the plume are alternatively detected, resulting in a strong intermittency of the concentration signal, associated to high i_C values (Cassiani et al., 2020).

In complex geometrical terrains, obstacles can locally amplify or suppress tracer fluctuations due to their perturbative effects on the flow field. Enhanced mixing within recirculation zones is associated with lower values of i_C, whereas alternating wind regimes, which transport portions of the plume that have experienced different degrees of dilution, can increase the local concentration fluctuations. In Fig. 3.13, obstacles are locally associated to higher values of i_C, notably between buildings C and D3 in the ‘S4’ configuration, and along the bottom side of building C in configuration ‘S5’. These are recirculating regions in which several wind regimes collapse: notably, the flows directed by the D3-D4 and D4-D5 corridors reach the region between the A and C buildings, while complex recirculating behaviours take place inside the open area surrounding the small tanks (see Fig. 3.2). The high scalar fluctuation levels associated with the complex velocity field can be explained by considering that the concentration signal is composed of puffs following different trajectories, each experiencing a variable degree of dilution depending on the flight time. Their statistics would reflect these differences in the history of the puffs, leading to a global statistical distribution at the measurement point that would be a convolution of different PDF. The complex PDF shapes observed in chapter 4 tend to support this hypothesis, although it remains very difficult to verify experimentally. Thus, the geometry of the site strongly affects the spatial distribution of both the mean concentration and the fluctuation intensity in the S4 and S5 configurations.

We now focus on the 40° wind direction cases with a varying geometry. Vertical profiles with the same structure as Fig. 3.12 are presented in Fig. 3.14. The highest values of i_c are reached on the first circle in the ‘solid’ and ‘spaced’ configurations, contrary to the ‘dense’ configuration, in which i_C is up to two times smaller. Profile shapes are also impacted, as shown on Fig.3.14c, f and i where the minimum of i_C is reached around $z^* = 0.6$ in the ‘dense’ case (Fig.3.14f). The particularly low values of i_C visible for the first circle in Fig.3.14f correspond to an almost flat mean concentration profile for the first circle in Fig.3.12f, which indicates a more efficient mixing in the dense configuration close to the source compared to the other configurations.

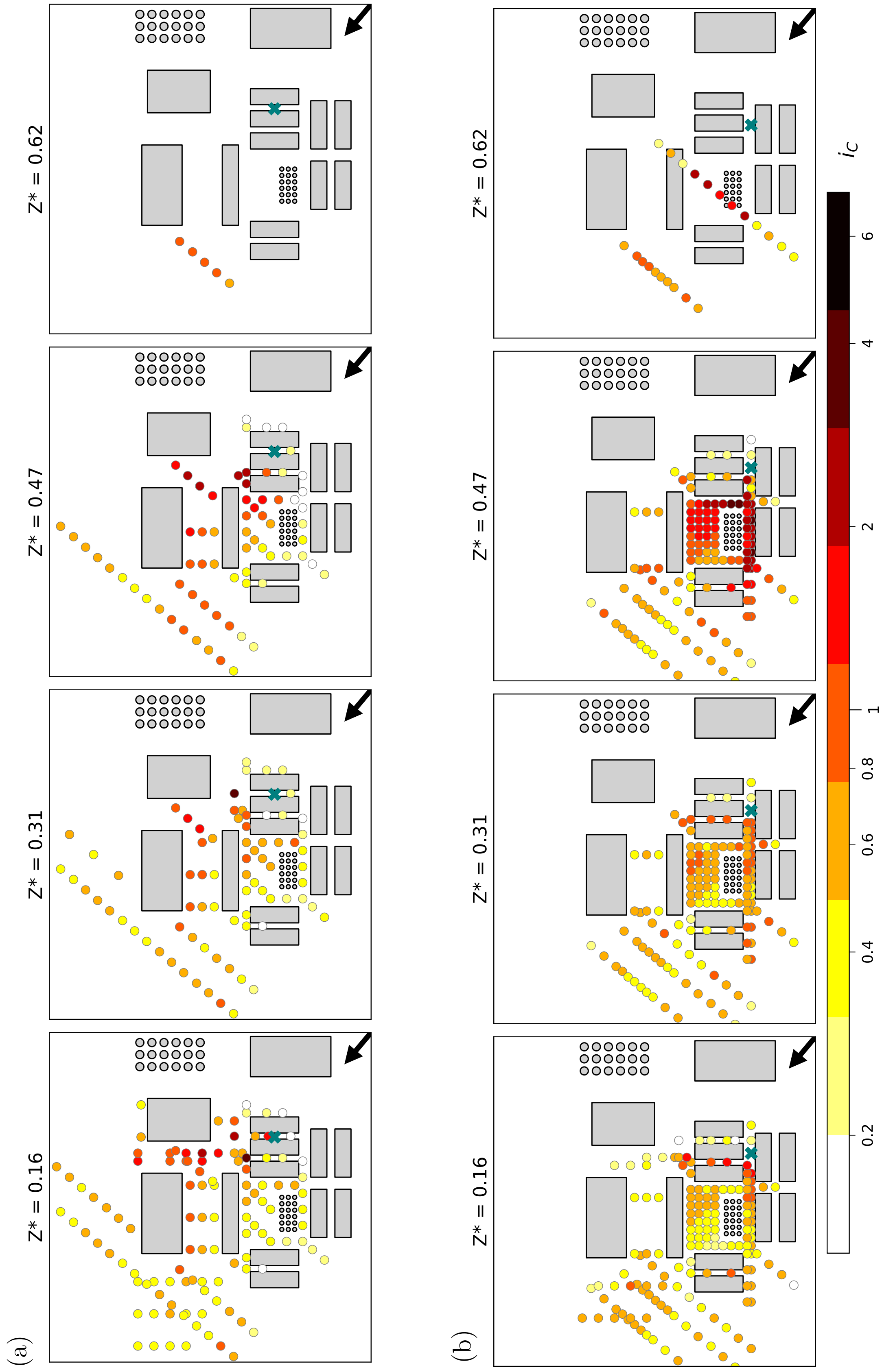

Figure 3.13: Fluctuation intensity for the 'S4' (top) and 'S5' (bottom) configurations. Same structure as Fig.3.11.

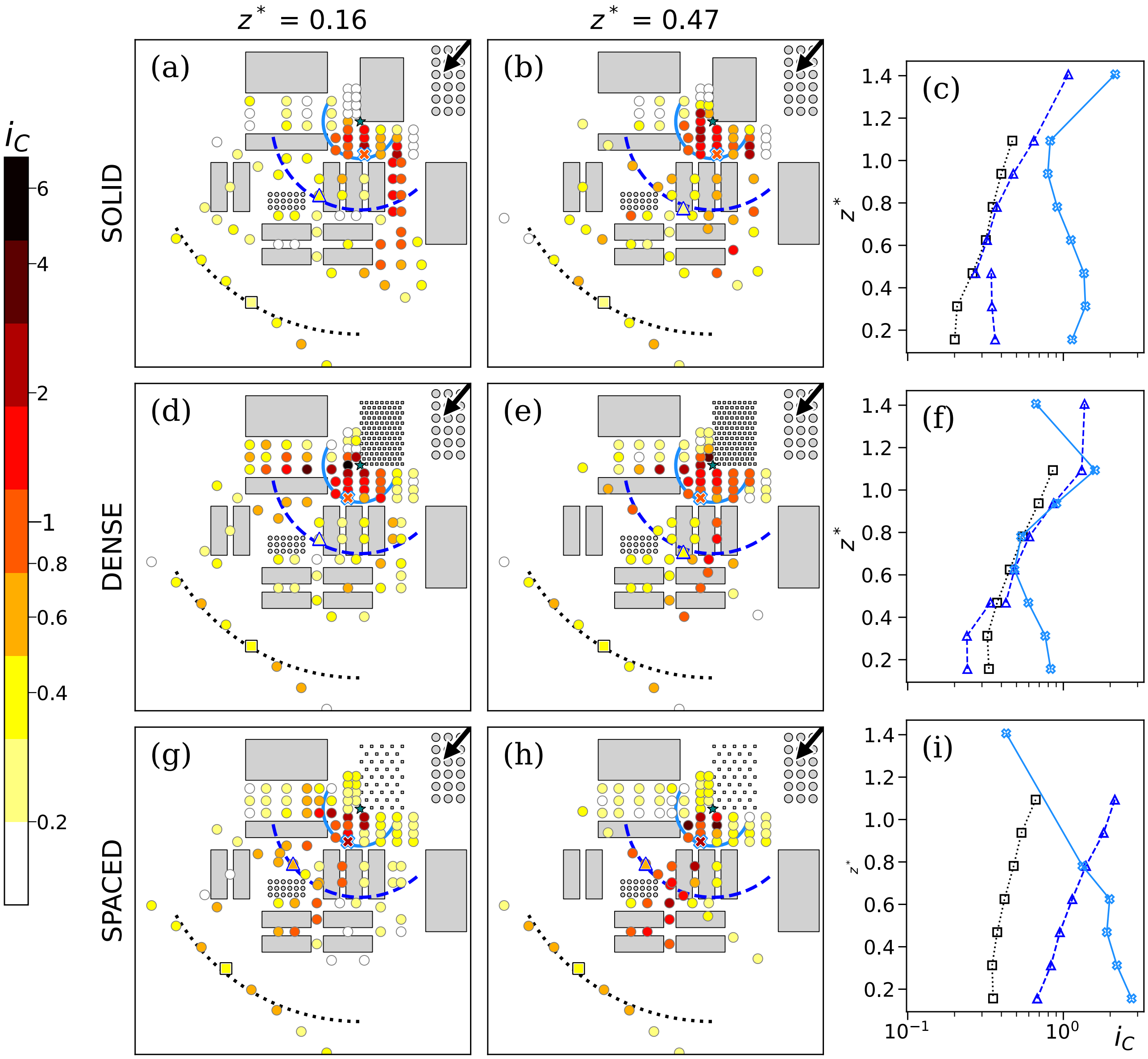

Figure 3.14: Intensity of the concentration fluctuations. Panels **a-b**, **d-e** and **g-h**: horizontal slices at two heights, panels **c**, **f** and **i**: vertical profiles, for the 3 configurations. Same structure as Fig.3.12.

As shown on Fig.3.14i, fluctuation intensity also reaches a slight minimum in the 'spaced' case, at the altitude of the maximum of the corresponding mean concentration profile. This is closer to the typical behaviour of a passive scalar plume over flat terrains (Nironi et al., 2015). On the contrary, in the 'solid' configuration, close to the source, i_C exhibits higher values close to the ground, as shown in Fig. 3.14c. The fluctuation intensity close to the source is clearly smaller at the top of the building than below $z^* = 0.6$ (Fig. 3.14c, light blue curve). Near the source, the 'dense' configuration exhibits lower fluctuation intensities than the 'solid' one (Fig. 3.14f). This behaviour is consistent with the flat mean concentration profile shown in Fig. 3.12f, indicating that, compared with the 'solid' configuration, the recirculation zone of building A promotes more efficient mixing of the tracer gas. In the maps (see Fig. 3.14a-b, d-e and g-h), values of i_C are major inside the wake of the A building in all configurations and at plume border. We can identify the plume edges mainly in the area between buildings D5 and B2 in the ‘solid’ configuration (see Fig. 3.14a and b), and over the group of D buildings in the ‘dense’ configuration (see Fig. 3.14d and e). The least efficient mixing is observed in the ‘spaced’ configuration (Fig. 3.14i), for which vertical profiles of fluctuation intensity show higher values than other configurations at all distances from the source.

Nevertheless, scalar dispersion is influenced not only by the upwind obstacle but also significantly by the smaller elements located downwind. Within the group of downwind buildings in both the ‘solid’ and ‘dense’ cases (see Fig. 3.14a, b, d and e), the mean concentration is spatially homogeneous. However, i_C is impacted by the local geometry, and reaches high values on the right side (positive y^* values) of the group of D buildings in the ‘solid’ configuration (Fig. 3.14a). In contrast, inside most of the corridors between buildings, fluctuation intensity remains below 0.5 in both ‘solid’ and ‘dense’ configurations (see Fig. 3.14a and d). In the ‘dense’ case at $z^* = 0.47$ (Fig. 3.14e), a line of larger values of i_C is visible, which corresponds to the plume border, where values of σ_C exceed those of $\overline{C}$. A similar pattern is observed in the ‘spaced’ configuration (see Fig. 3.14g and h), where the fluctuation intensity locally exceeds 1 at the plume boundary within the group of D buildings. Thus, in both the solid and dense configurations, the local geometry of the mid-field building cluster affects i_C more strongly than it affects $\overline{C^*}$. These obstacles, that are smaller than the upwind building, tend to homogenize and widen the plume, but their effect on concentration fluctuations is more local.

3.3 Conclusion

This chapter aims at analysing the experimental mean velocity and concentration fields in the 5 configurations of the idealised industrial site that were investigated. We assess the effect of the site geometry on both the flow and the tracer concentration fields while varying the wind direction, the site geometry and the source position. The results evidence the strong effect of the site geometry on both the flow field and the tracer mean concentration. Complex effects such as flow canalisation and interactions between the recirculation zones of individual obstacles produce an intricate wind velocity field over the site. Plume shapes are thus perturbed by obstacles geometries from the near- to the far-field. In the configurations with the 40° incoming wind direction, the porosity of the upwind building strongly impacts the shape of its recirculation zone as well as the turbulence intensity in this region, therefore impacting the plume characteristics downwind. The solid configuration of this obstacle produces a large plume, showing strong concentration fluctuation intensity, and which centreline is shifted towards positive y^* values due to the very turbulent recirculation zone near the source. The configuration with a densely packed group of columns replacing the upwind building generates a less turbulent wake, which produces a more homogeneous plume in which mixing is more efficient than in the ‘solid’ configuration. Finally, the patch of spaced columns produces no recirculating behaviour, which in turns generates a narrower plume with high concentration fluctuation intensities. Building shapes and arrangement thus strongly impact pollutant dispersion, not only close to the source but also in the far-field, which motivates the further analysis of the concentration field that we perform in chapter 4, focusing on concentration fluctuations.

Chapter 4

One-point concentration probability density function

The effects of the site geometry on the first two moments of the scalar field were evidenced in the previous chapters. However, the mean and variance of concentration alone are not sufficient to provide information on the temporal evolution of the concentration signal and the duration, frequency and intensity of peaks. To estimate these quantities, it is necessary to describe with more details the statistical properties of the concentration signal. Notably, the key element to capture concentration fluctuations is to determine an appropriate model for the statistical distribution of the one-point concentration, from which quantities such as high order percentiles can be retrieved to estimate concentration peaks.

This chapter is dedicated to the comparison of the experimental distribution of concentration to three statistical model distributions that are presented in section 4.1. Only the 'S25' configurations are considered (incident wind at 40°) with a focus on the effect of varying the porosity of the building A on the concentration statistics (see section 4.2). The analysis is completed by the comparison between modelled and measured statistical quantities (section 4.3).

4.1 Mathematical models for the concentration probability distribution

In the following, we present some of the models of probability distributions that we compared to the experimental distributions of measured concentrations. It is important to note that we do not consider the spatial distribution of concentration, but the statistical distribution of concentration values at a specific point, called one-point concentration probability density function.

Probability density functions (PDF) are mathematical functions that describe the probability of a statistical event (measuring a specific concentration value) among a defined set of possibilities (the whole range of possible values for concentration between 0 and the source concentration).

The spatial variability of concentration fluctuation intensity results from the turbulent flow interacting with the plume. The tracer released at the source and advected by the mean wind forms a plume that is highly concentrated in the near-source region. Most eddies in this region have a characteristic size that is larger than the plume width, meaning that their main effect is to displace the entire plume (or its center of mass), generating what is called 'meandering' (Gifford, 1959). Close to the source, a sensor placed at a fixed position would thus measure alternatively rare high concentration values from puffs originating almost directly from the source, followed by much more frequent low concentration values corresponding to clean air. The PDF in this region therefore approaches an exponential form, characterized by a high probability of very low concentration values and a small probability of high concentration events. This behaviour is associated to $i_C > 1$ since the variation of the concentration signal is large compared to the mean.

Further from the source, the plume widens due to mixing with the ambient air and fluctuations of concentration decrease to reach a transition point at which $i_C = 1$. This is associated to a change of the shape of the PDF.

In the far field, the plume becomes wider than most eddies, which thus mainly mix the tracer inside the plume without any strong displacement of the plume centre line. This region is characterised by a higher homogeneity of concentration values associated to $i_C < 1$ and to a PDF approaching a Gaussian distribution.

The mathematical models that we compare to the measurements were proposed in the literature because they have the ability to reproduce this specific behaviour. All of them are 2-parameter distributions, meaning they provide the distribution of concentration values based on two parameters, which can be linked to the mean and the variance of concentration. The shape of the distribution is thus able to evolve with the distance from the source and the position within the plume.

4.1.1 Gamma distribution

The most validated model in the literature for the PDF of concentration is the gamma distribution (Cassiani et al., 2020), which has a PDF of the form:

$$PDF_\Gamma(c) = \frac{c^{k-1}\exp\left(-c/\theta\right)}{\Gamma(k)\theta^k}$$

where $k = \frac{1}{i_C^2}$ and $\theta = \frac{\overline{C}}{k}$ are the shape and scale parameters, respectively.

The mean, standard deviation, fluctuation intensity, skewness and kurtosis are respectively computed by the following relations:

$$\begin{aligned} \overline{C} &= k\theta \\ \sigma_C &= \overline{C}/k \\ i_C &= 1/\sqrt{k} \\ Sk &= 2/\sqrt{k} \\ Ku &= (6/k) + 3 \end{aligned}$$

Which lead to the following properties of the high order statistical moments :

$$\begin{aligned} Sk &= 2i_c \\ Ku &= \frac{3}{2}Sk^2 + 3 \end{aligned}$$

The percentiles are not given analytically. We compute them from the gamma distribution obtained from the experimental mean and standard deviation of concentration.

4.1.2 2p-Weibull distribution

The 2-parameter Weibull PDF is:

$$PDF_W(c) = \beta\alpha(\beta c)^{\alpha-1}\exp\left(-(\beta c)^{\alpha}\right)$$

where α is defined from $i_C^2 = \frac{\Gamma(1+\frac{2}{\alpha})}{[\Gamma(1+\frac{1}{\alpha})]^2} - 1$, but can be approximated by $\alpha \simeq (1/i_C)^{1.086}$ and is called the shape parameter. The scale parameter is $\beta = \Gamma(1+\frac{1}{k})/\overline{C}$ (Yee et al., 1993b; Oettl and Ferrero, 2017)

Statistical moments (mean, skewness and kurtosis) are computed as:

$$\begin{aligned}
\overline{C} &= \frac{1}{\beta}\,\Gamma(1+\frac{1}{\alpha}) \\
Sk &= \frac{\Gamma(1+3/\alpha) - 3\,\Gamma(1+1/\alpha)\,\Gamma(1+2/\alpha) + 2\,\Gamma^3(1+1/\alpha)}{[\Gamma(1+2/\alpha) - \Gamma^2(1+1/\alpha)]^{3/2}} \\
Ku &= \frac{\Gamma(1+4/\alpha) - 4\,\Gamma(1+1/\alpha)\,\Gamma(1+3/\alpha) + 6\,\Gamma^2(1+1/\alpha)\,\Gamma(1+2/\alpha) - 3\,\Gamma^4(1+1/\alpha)}{[\Gamma(1+2/\alpha) - \Gamma^2(1+1/\alpha)]^2}
\end{aligned}$$

Peak to mean ratios computed from the p percentile are obtained analytically as:

$$R_p = \frac{[-\log(1-p)]^{1/\alpha}}{\beta\,\overline{C}}$$

the p percentile being the value of concentration below which p percent of concentration values are situated inside the statistical distribution of concentration values. For risk assessment, mainly the 90th, 95th, 98th and 99th percentiles are considered.

4.1.3 Lognormal distribution

The PDF of the lognormal distribution expands as:

$$PDF_L(c) = \frac{1}{c\lambda\sqrt{2\pi}}\exp\left(-\frac{(\ln(c)-\mu)^2}{2\lambda^2}\right)$$

where $\lambda = \ln(i_C^2+1)^{1/2}$ and $\mu = \ln(\overline{C}) - \frac{\lambda^2}{2}$ correspond to the standard deviation and average of the logarithm of concentration.

Statistical moments (mean, fluctuation intensity, skewness and kurtosis) are thus (Yee et al., 1993b):

$$\begin{aligned}
\overline{C} &= \exp\left(\mu + \frac{\lambda^2}{2}\right) \\
i_C^2 &= \exp(\lambda^2) - 1 \\
Sk &= \frac{[\exp(\lambda^2)]^3 - 3\exp(\lambda^2) + 2}{[\exp(\lambda^2) - 1]^{3/2}} \\
Ku &= \frac{[\exp(\lambda^2)]^6 - 4[\exp(\lambda^2)]^3 + 6\exp(\lambda^2) - 3}{[\exp(\lambda^2) - 1]^2}
\end{aligned}$$

Percentiles are not provided analytically and are thus computed from the lognormal distribution with parameters λ and μ obtained from the experimental data for each point.

4.1.4 Computation of the experimental concentration distribution

Since the experiments were performed in a recirculating wind tunnel, the background concentration in the flow progressively increased over time. To accurately determine the concentration signal, this background contribution had to be removed from the measurements. For each measurement point, background concentration values were collected at the beginning and at the end of the acquisition, and then linearly interpolated and subtracted from the time series. In some cases, this procedure resulted in negative concentration values. To address this issue, two correction strategies were applied depending on the shape of the concentration distribution. For points with $i_C > 1$ (exponential-like distributions), negative concentration values were replaced by zero to preserve the exponential character of the PDF. For points with $i_C < 1$ (more Gaussian-like distributions), the entire signal was shifted so that the minimum concentration value corresponded to zero. Although this procedure may introduce a small uncertainty in the estimation of the PDF, it ensures the preservation of its overall shape. The impact on the statistical quantities computed from the data remains negligible.

4.1.5 Kullback-Leibler divergence

A quantitative assessment of the fit between experimental concentration distribution and model distributions is obtained by applying a statistical distance, the Kullback-Leibler divergence (Kullback and Leibler, 1951). It is defined as:

$$D_{KL}(P||Q) = \sum_{x \in X} P(x) \log(P(x)/Q(x))$$

where $P(x)$ is the probability of the value x, lying in the ensemble X, given by the observed distribution and $Q(x)$ the probability of x given by the model distribution.

Lower values of the Kullback-Leibler divergence thus correspond to a better agreement between the model and observed distributions.

A more statistically robust approach would have consisted into a hypothesis test, namely assessing the probability that the experimental data having a given Kullback-Leibler value follows the specific considered PDF.

4.2 Analysis of the statistical distribution of the one-point concentration signal

We present a comparison between experimentally measured concentration distributions and several theoretical models for the one-point concentration PDF. Our objective is to identify the model that most accurately captures the statistics of concentration fluctuations within our complex site. All results are shown principally for the 'solid' configuration, which generates the most turbulent wake. In this configuration, the group of small buildings downwind the source is entirely covered by the plume. We eliminated points with a low signal to noise ratio. Practically, this implied that we removed only measurement points with an average concentration below 10 ppm, as in Andronopoulos et al. (2001). We test the gamma, 2 parameter Weibull (2p-Weibull) and lognormal distributions, which are the most validated models in the literature (Cassiani et al., 2020). Mathematical details about these distributions are provided in section 4.1.

As a measure of the agreement between the model and the experimental distributions of concentration values in the time series, we consider the Kullback-Leibler (KL) divergence. Smaller

KL values correspond to a better model-data agreement. Figure 4.1a shows a map of KL values at the lowest measurement layer ($z^* = 0.16$) with some examples of experimental concentration distributions compared to model PDFs (Fig. 4.1b-f). The horizontal layer shown in Fig. 4.1a lies below the height at which the plume reaches its maximum mean concentration. Nevertheless, it remains highly relevant, as the majority of risks associated with pollutant dispersion concern human exposure near ground level.

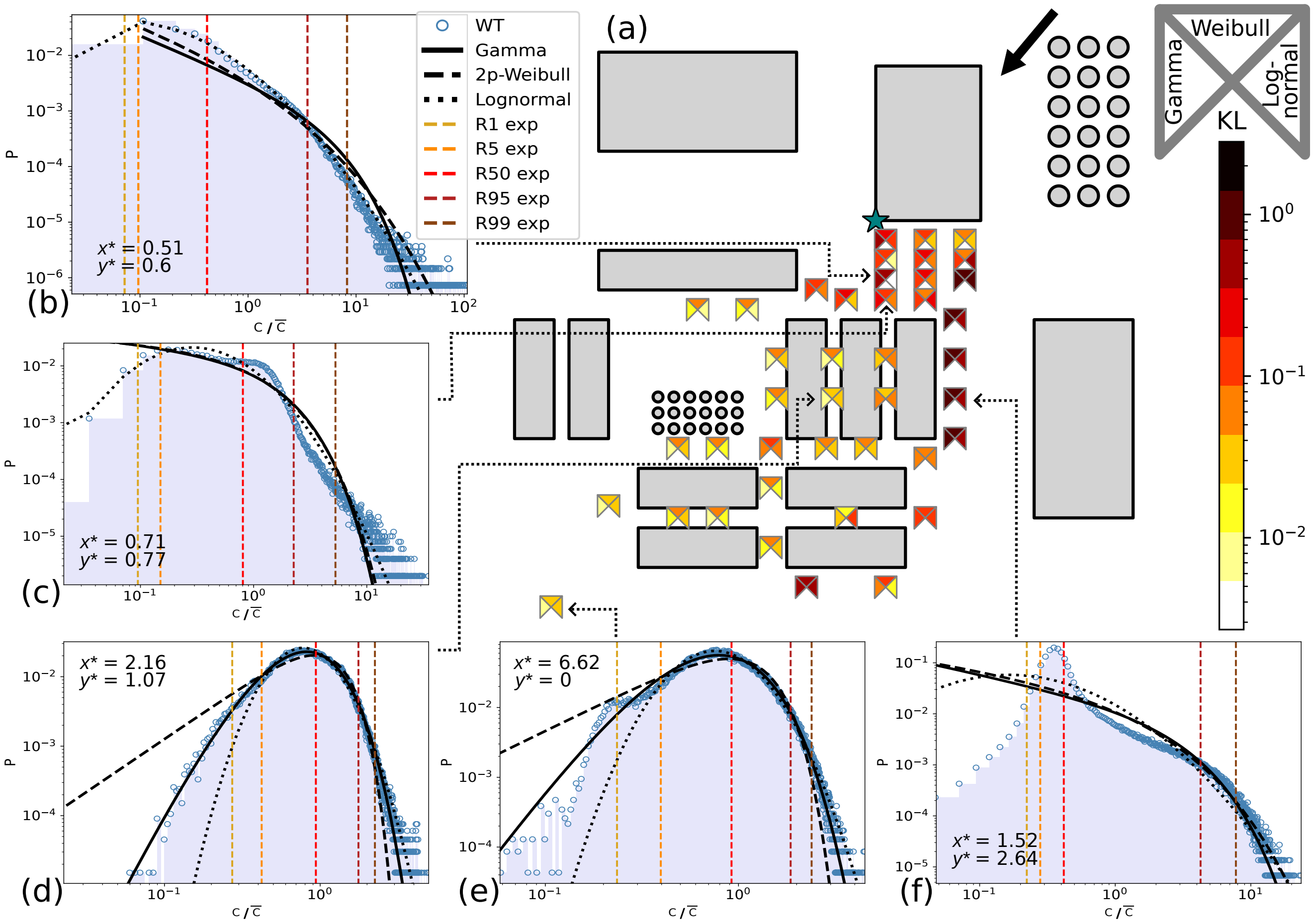

Figure 4.1: Kullback-Leibler divergence (KL) at ground level (panel **a**) and distributions of concentration values for the wind tunnel data (WT) and the model distributions at particular points (panels **b-f**). Ratios of first, 5th, 50th, 95th and 99th percentiles to the mean value (R1 to R99) are shown on the PDF. On the map (panel **a**), the KL values of the gamma, 2p-Weibull and lognormal distributions are shown as triangles respectively on the left, top and right of the point location.

In Fig.4.1, examples of one-point experimental and modelled distributions of concentration are shown at key places on the site. All distributions perform better in the group of small buildings, rather than on the right side of the group of buildings (Fig. 4.1a), i.e. at the plume border, characterized by high i_C values. We observe complex statistical distributions that do not resemble any classical PDF. We hypothesise that the concentration signal results from tracer puffs following different trajectories and, consequently, experiencing different flight times. The observed distributions could therefore arise from the convolution of PDFs with distinct parameters, leading to the complex shapes shown in Fig. 4.1.

As a support to this hypothesis, Klippel (2025) observed a link between tracer concentration fluctuations and flow features such as intermittent wind direction and street-scale flow structures, from Direct Numerical Simulations (DNS) in street network configurations. Different wind flow regimes could thus produce different puff histories leading to the complex PDF shapes observed in Fig. 4.1. Determining the convoluted distributions is however a difficult task that we did not perform as part of this study.

We observe that KL values are higher in the wake of the tallest building, except on the left (negative y^* values) side of the wake for the lognormal model. In this zone the lognormal distribution suits better to experimental data than the gamma and 2p-Weibull models, at all heights (not shown on Fig. 4.1). Nevertheless, over the group of small buildings, better KL values are obtained by the gamma model. These results are in accordance with those of Salizzoni et al. (2025), who modelled the PDF of a scalar emitted by a line source with a lognormal distribution in the wake of a single obstacle, and with a gamma distribution further from the source. Below and over the height of small buildings, respectively, the lognormal and the 2p-Weibull distributions are almost as accurate as the gamma model. In the far field, KL values of the 2p-Weibull model are slightly lower (meaning better) than other distributions.

The best model distribution hence varies with the distance to the source and the local impact of geometry. The lognormal distribution is more appropriate in the wake of the tallest building, while the gamma distribution is more accurate in the mid range, even in the presence of grouped obstacles perturbing the flow. This extends the validity of the gamma model, previously tested over flat terrains (Cassiani et al., 2020), to built environments. Finally, the 2p-Weibull model performs better in the far field. Regions where the geometry has a strong impact, particularly at plume border, present high KL values for all distributions. However, it is important to note that the KL values computed over the entire concentration PDF reflect an overall agreement across both low and high concentration levels relative to the mean. For example, Fig. 4.1f shows that, on the side of the group of small buildings, the experimental concentration distribution exhibits a highly complex shape that is not accurately captured by the models below the 50th percentile, even though high concentration values are reasonably well reproduced, particularly around the 95th percentile. To our knowledge, no previous studies have reported such complex shapes in the experimental PDFs of concentration measured over complex terrain (e.g. Del Ponte et al., 2024). A possible explanation is that experimental PDFs result from the convolution of two or more simpler distributions, leading to a very complex shape that cannot be accurately captured by the models that are tested.

In order to identify reliable predictors of the quality of agreement between model and experimental distributions, we plot the KL values depending on the distance from the source d^*, and the intensity of the concentration fluctuations i_C in Fig. 4.2 for the ‘solid’ configuration, in Fig.4.3 for the ’dense’ configuration and in Fig.4.4 for the ‘spaced’ configuration.

Figures 4.2, 4.3, and 4.4 show no dependence of KL values on the distance to the source (see panels a, c and e), but they evidence a strong link with i_C for the gamma and 2p-Weibull models (see panels b and d). The relation is much less evident for the lognormal distribution (see panel f) since lower values of KL are reached even at $i_C > 1$, particularly for the ‘solid’ and ‘dense’ configurations (Fig. 4.2 and Fig. 4.3). These points are mainly located inside the building wake, where, as shown previously in Fig. 4.1, the lognormal distribution performs better than other models. This effect is less visible on Fig. 4.4 due to the lower impact of the site geometry on the tracer plume. The intensity of fluctuations of concentration can therefore be considered a good indicator of the prediction of the PDF by the gamma and 2p-Weibull models. A high value of i_C corresponds to more intermittent signals, typically at plume border and close to the source, which is in agreement with the spatial distribution of KL values observed in Fig. 4.1. Therefore, both the

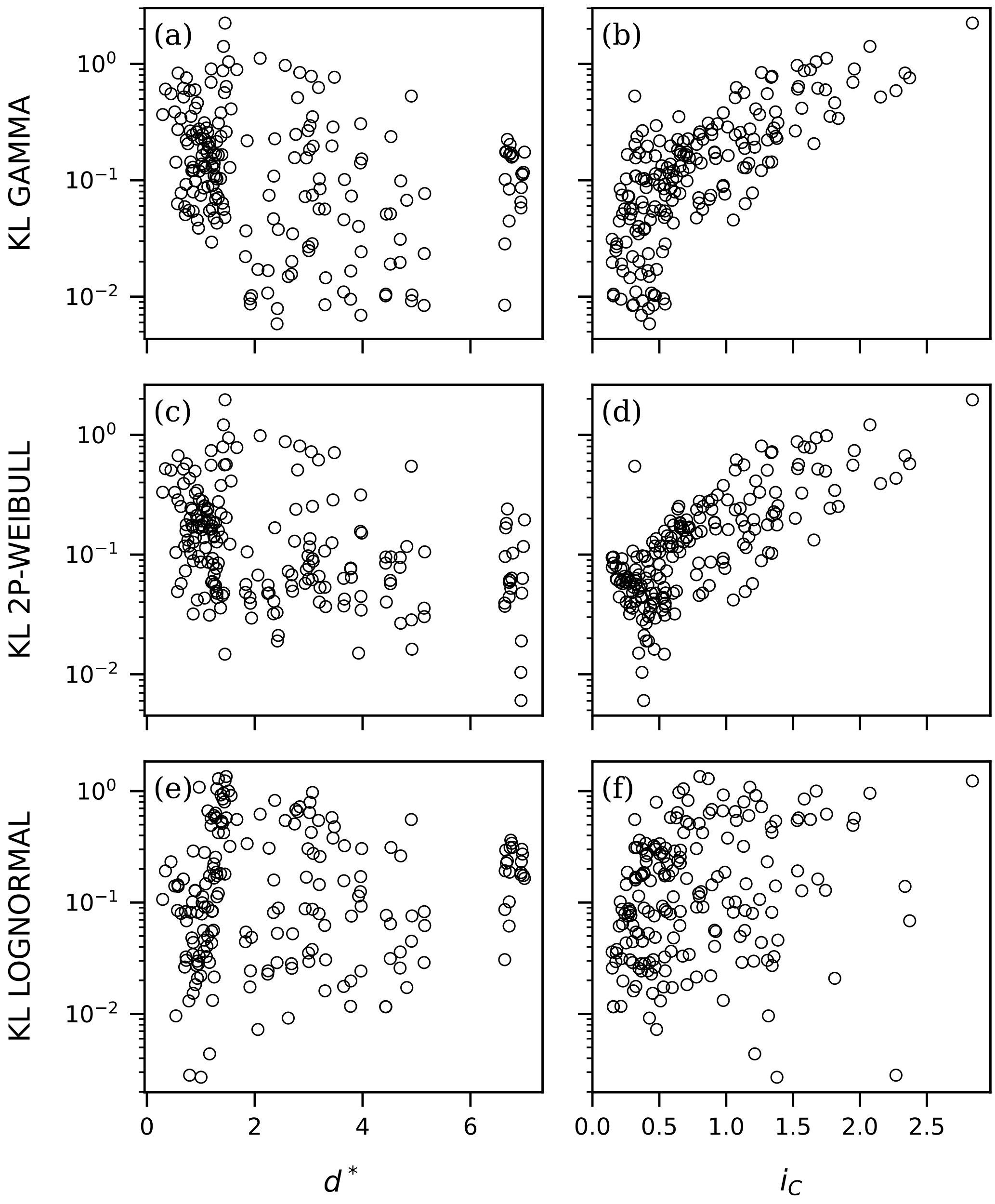

Figure 4.2: Evolution of the Kullback-Leibler divergence in the ‘S25 solid’ configuration, panels **a**, **c** and **e**: with the dimensionless distance from the source d^*, and panels **b**, **d** and **f**: with the concentration fluctuation intensity i_C for the gamma, 2p-Weibull and lognormal distributions. There is no clear dependence to the distance from the source but an evident link with the intensity of concentration fluctuations for the gamma and 2p-Weibull distributions. This link is not as patent for the lognormal distribution.

accurate prediction of high concentration levels and a reliable estimate of the overall PDF shape can be achieved based solely on the mean and variance of the concentration.

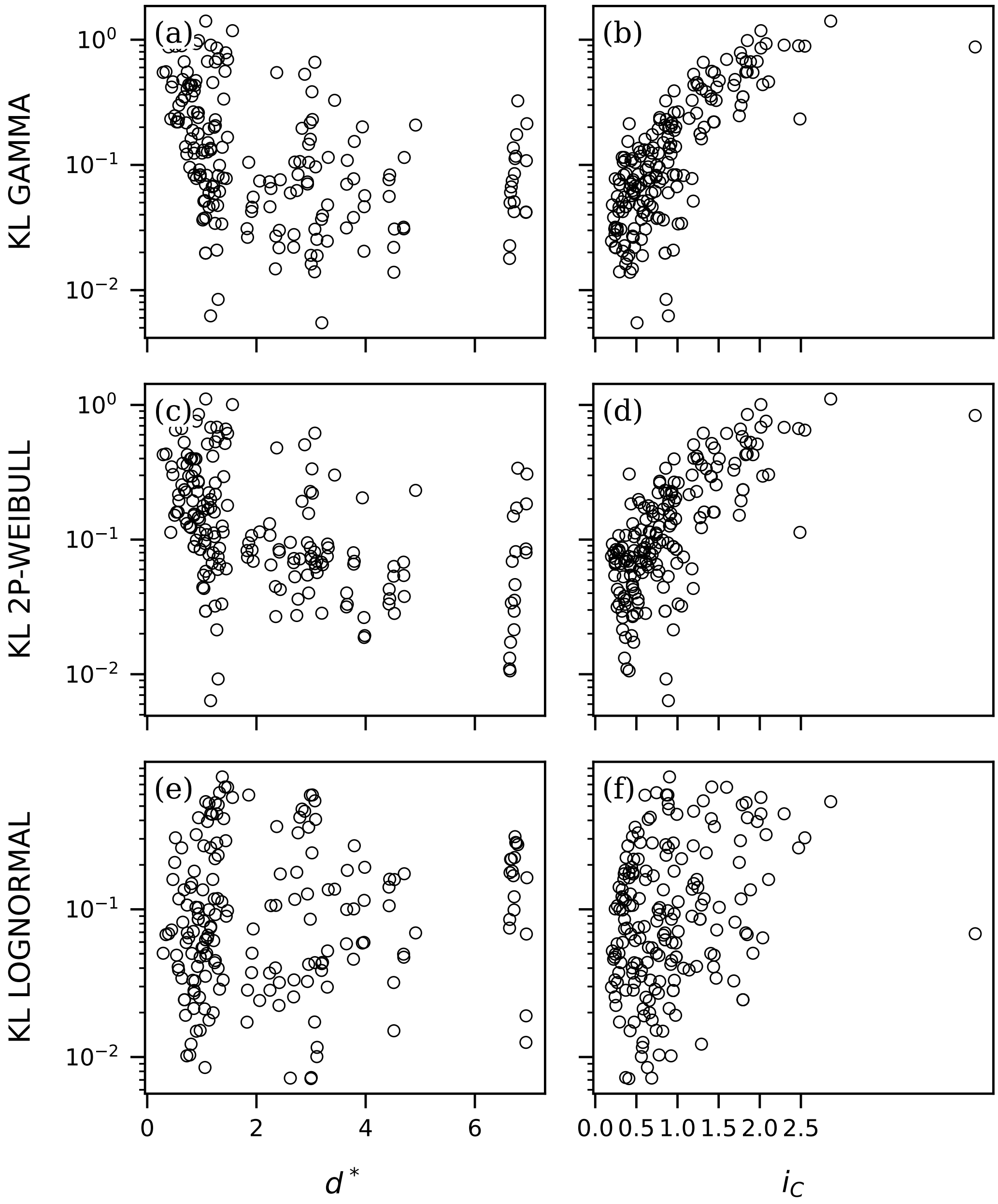

Figure 4.3: Same as Fig.4.2 for the ‘S25 dense’ configuration.

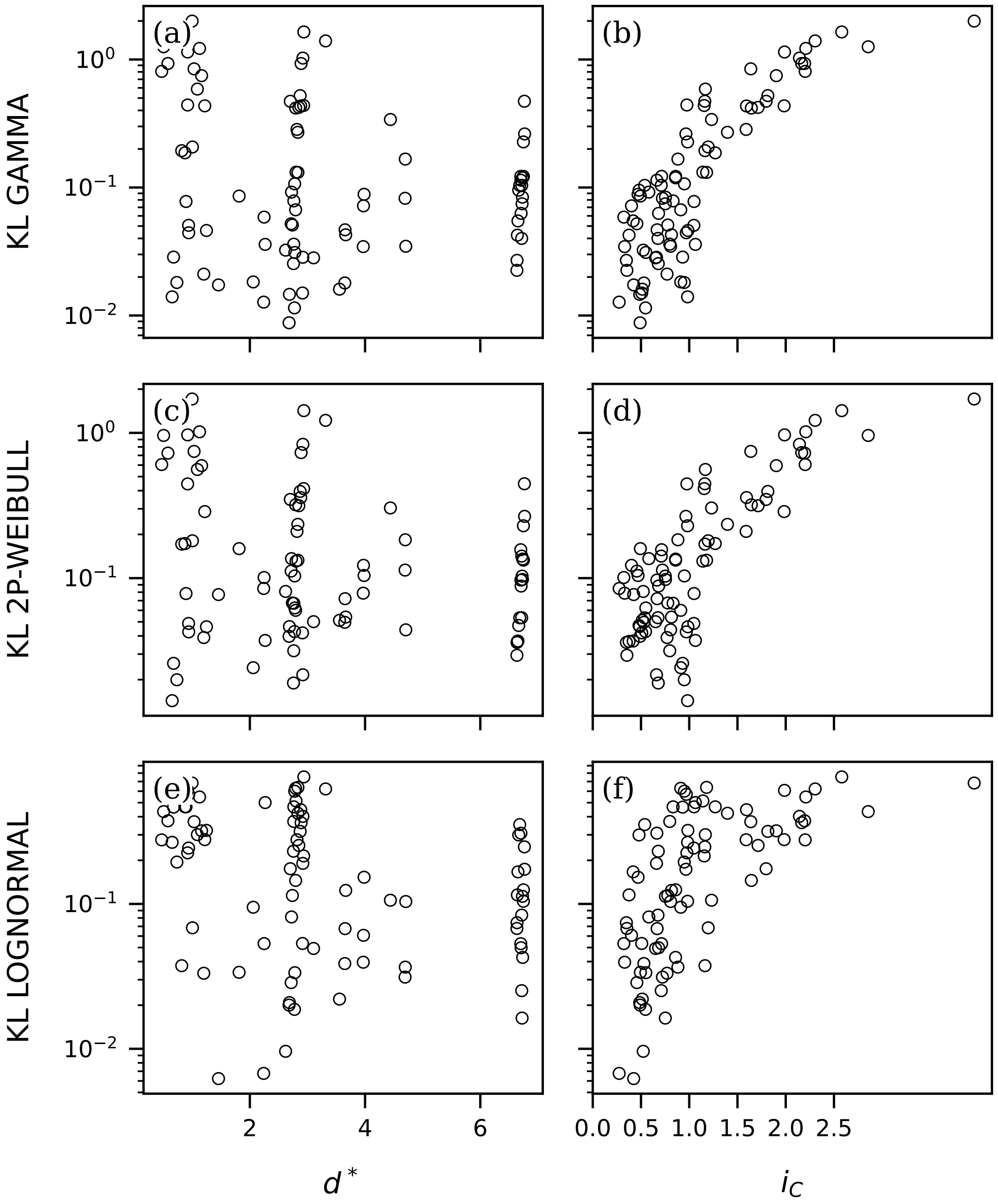

Figure 4.4: Same as Fig.4.2 for the 'S25 spaced' configuration.

4.3 Statistical parameters to determine the fit with the model distributions

We focus on the concentration higher-order moments, peaks and percentiles. Higher order statistical moments, namely skewness and kurtosis, are computed from the three distributions and compared to the experimental quantities (see Fig. 4.5, Fig. 4.6, and Fig.4.7), imposing the concentration mean and variance from experimental data (which were analysed in section 3.2).

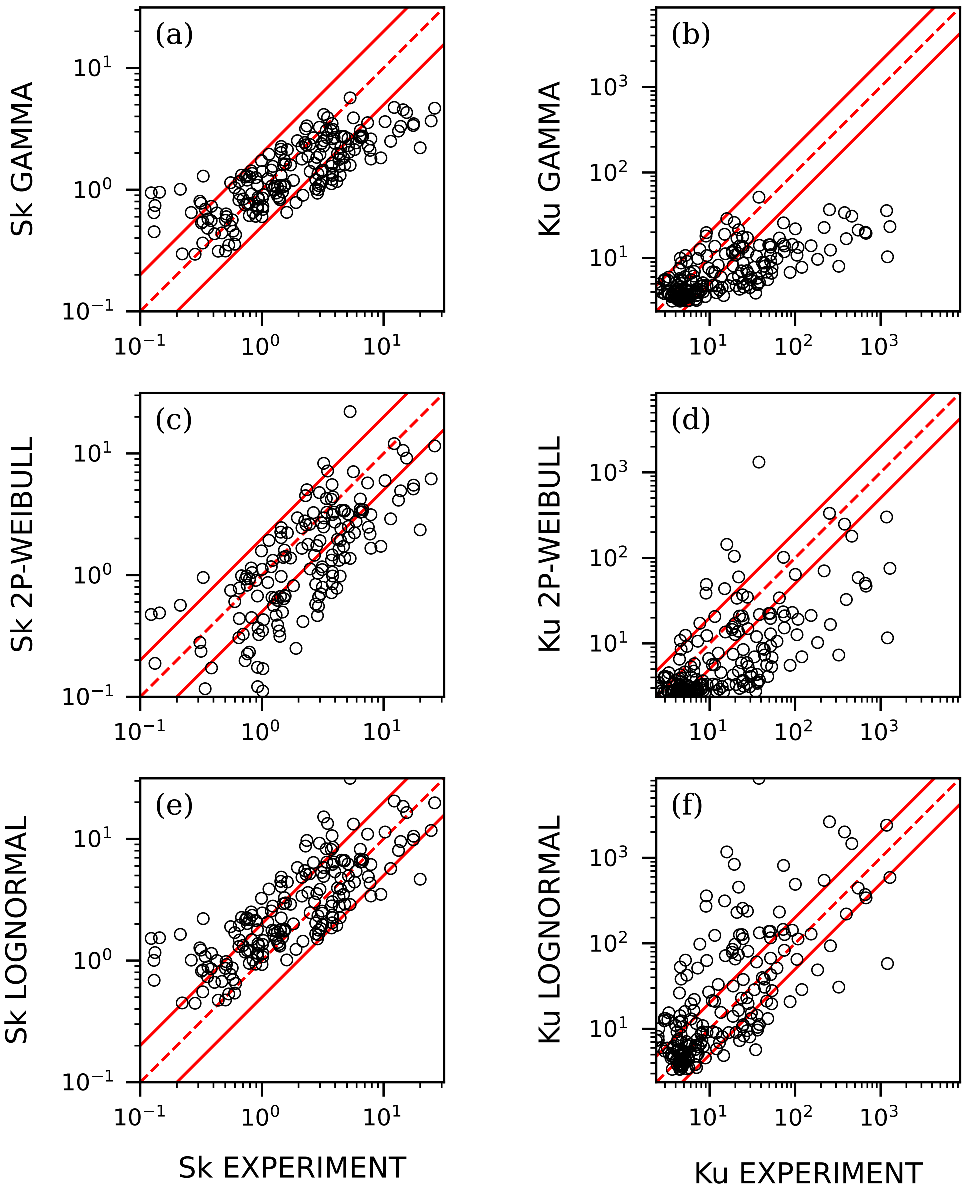

Figure 4.5: Experimental **a**, **c** and **e**: skewness and **b**, **d** and **f**: kurtosis with respect to their modelled versions in the 'S25 solid' configuration. Red lines correspond to a factor of 2 and 0.5 of the observations. Points with skewness values below 0.1 are not shown on the graphs (10 points for the gamma and lognormal cases, 40 points for the Weibull model over a total of 200 points).

In the 'solid' configuration, shown in Fig.4.5, the gamma and lognormal models predict more accurately the skewness, compared to the 2p-Weibull model (see Fig. 4.5a, c, and e). The fractions of predictions within a factor of 2 of the observations are $FAC2_G = 0.60$, $FAC2_W = 0.38$, $FAC2_L = 0.61$ for the gamma, 2p-Weibull and lognormal models respectively. Even though the lognormal and gamma distributions have a similar ratio of more accurate predictions, the positions of the points where these predictions perform better are different. Skewness values inside a factor of 2 are mainly located inside the group of small buildings for the gamma model, whereas they are inside the wake of the upwind building for the lognormal model. Prediction of skewness by the 2p-Weibull model is worse than the gamma model within the group of small buildings but comparable elsewhere. Hence, the gamma distribution is a better predictor of skewness in the mid field, while the lognormal distribution is more adapted in the recirculation zone in the near field, even though none of the three tested distributions provides satisfactory results in general.

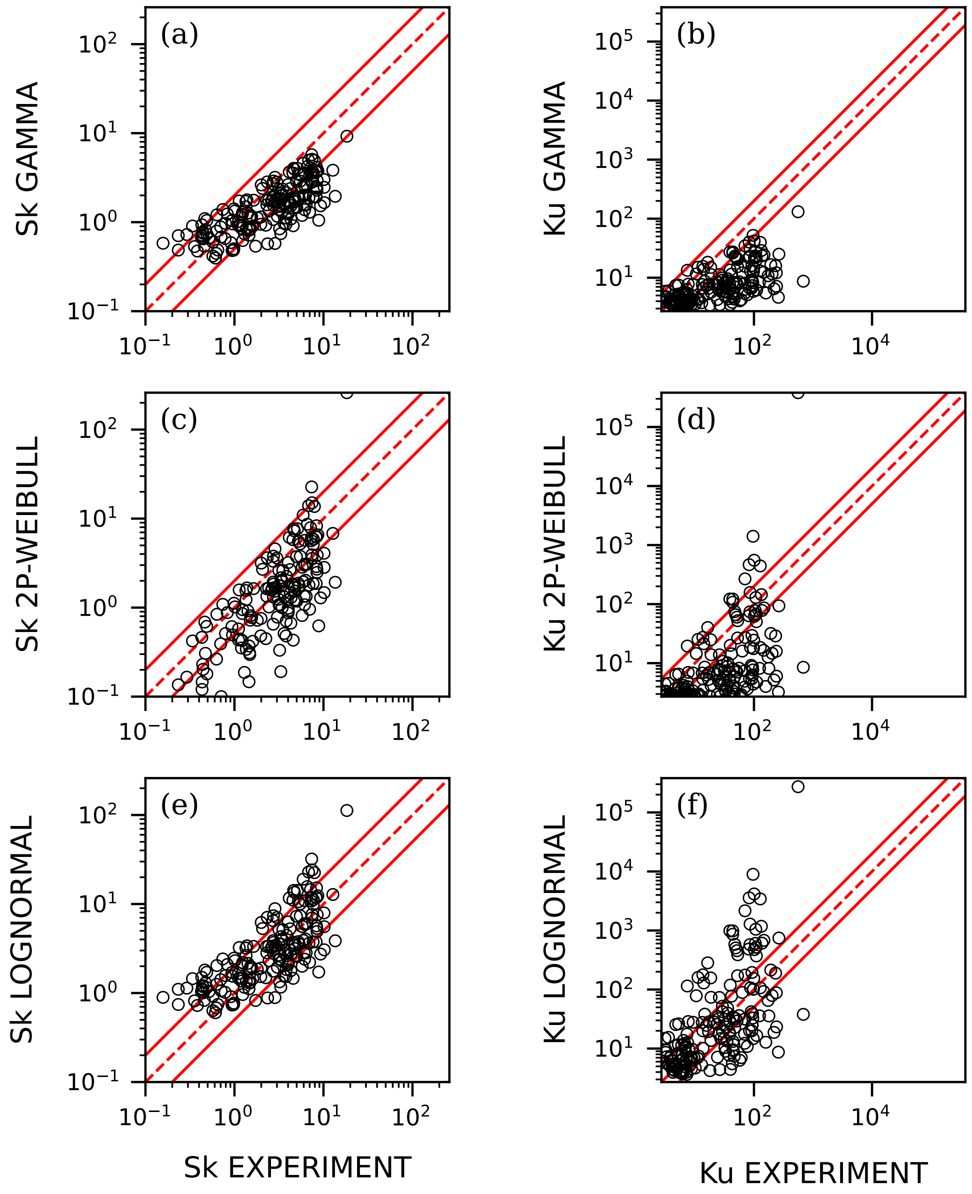

Figure 4.6: Same as Fig.4.5 for the ‘S25 dense’ configuration.

Kurtosis is even more poorly estimated by the models (see Fig. 4.5b, d and f) since fractions of prediction within a factor of 2 of the observations reach only $FAC2_G = 0.60$, $FAC2_W = 0.50$, $FAC2_L = 0.53$. Again, the gamma and lognormal models perform slightly better in the mid and near field, respectively. The low quality of prediction of the high order statistical moments is mainly due to low concentration levels that are highly impacted by the local effects of the site geometry.

Similar behaviours of both skewness and kurtosis are observed in the 'dense' (see Fig. 4.6) and the 'spaced' (see Fig. 4.7) configurations. Although the tested model distributions may not perfectly reproduce the whole PDF of the experimental data (see Fig. 4.5), they capture the overall shape and, notably, peaks and percentiles (see Fig. 4.8).

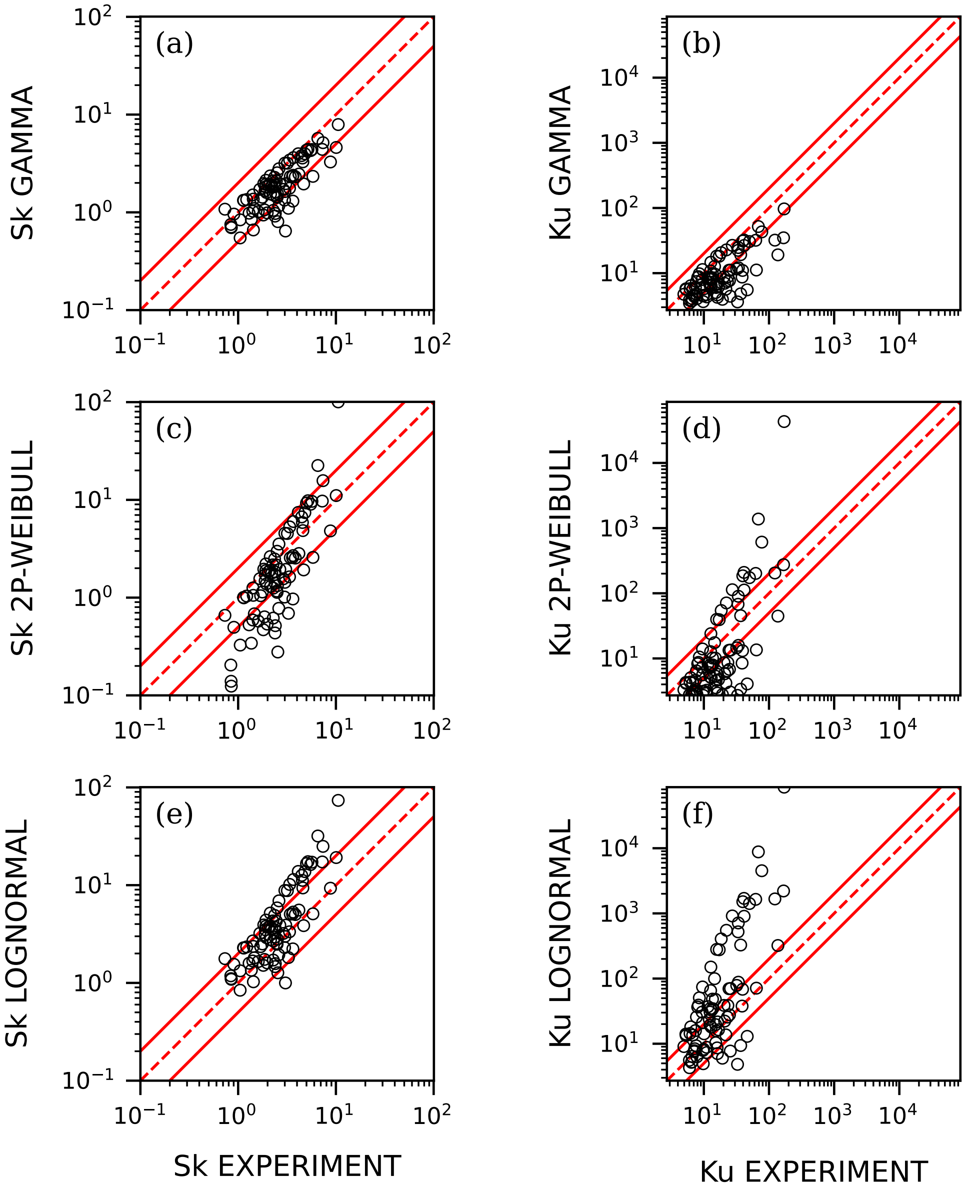

Figure 4.7: Same as Fig.4.5 for the 'S25 spaced' configuration.

Peak to mean ratios, estimated as the 95th, i.e. $R_{95} = C_{95}/\overline{C}$, and 99th percentiles, are presented in Fig. 4.8 for the 'solid' configuration, Fig. 4.9 for the 'dense' case and Fig. 4.10 for the ‘spaced’ configuration. The 95th (panels a, c, and e) and 99th (panels b, d, and f) percentiles are derived from the model distributions computed using the method of moments, based on the experimental mean and variance of concentration. They are then compared to the experimental percentiles.

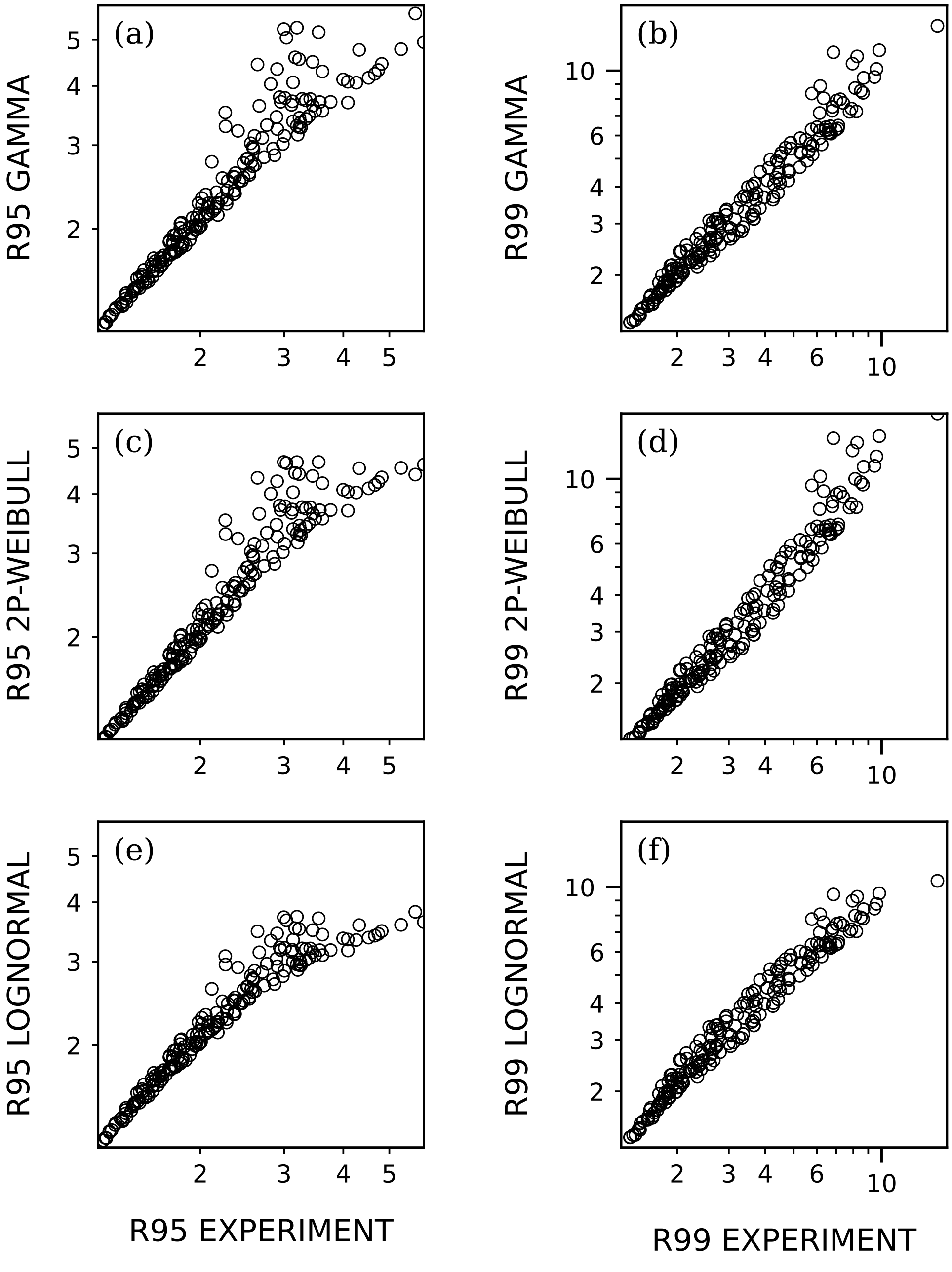

Figure 4.8: Peak-to-mean ratios from **a**, **c**, **e**: the 95th and **b**, **d** and **f**: the 99th percentiles in the ‘S25 solid’ configuration. Experimental values and predicted ratios from the 3 distributions are compared.

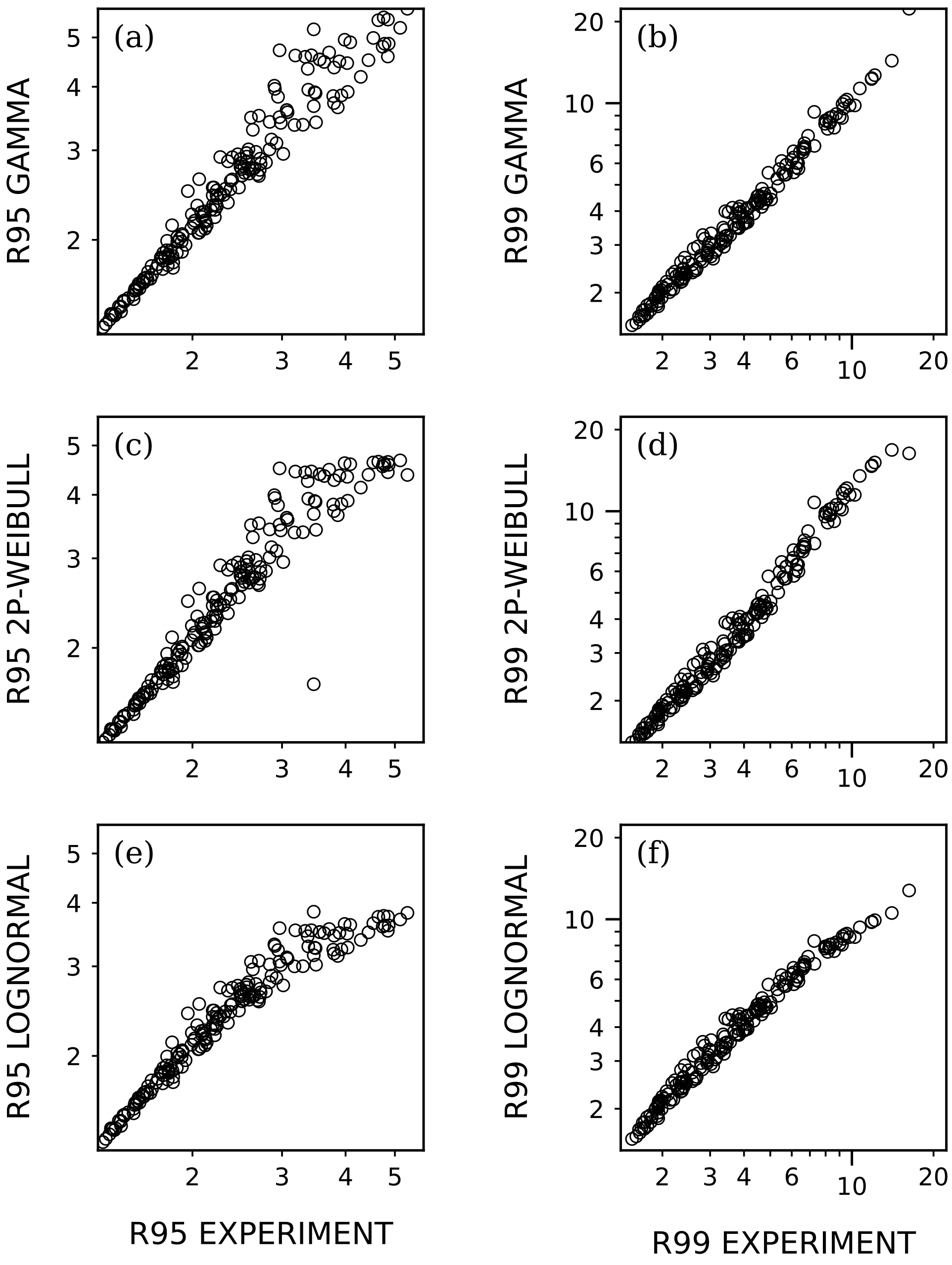

Figure 4.9: Same as Fig.4.8 for the ‘S25 dense’ configuration.

All models are accurate into reproducing peak to mean ratios in all configurations, since all points lie within a factor of two, except one point in the ‘dense’ configuration for the Weibull 95th percentile which is visible on Fig. 4.9c. This point is located to the left of the source, with $i_C \simeq 5$, with an exponential shape of the PDF that is not reproduced accurately by the Weibull distribution below the 99th percentile.

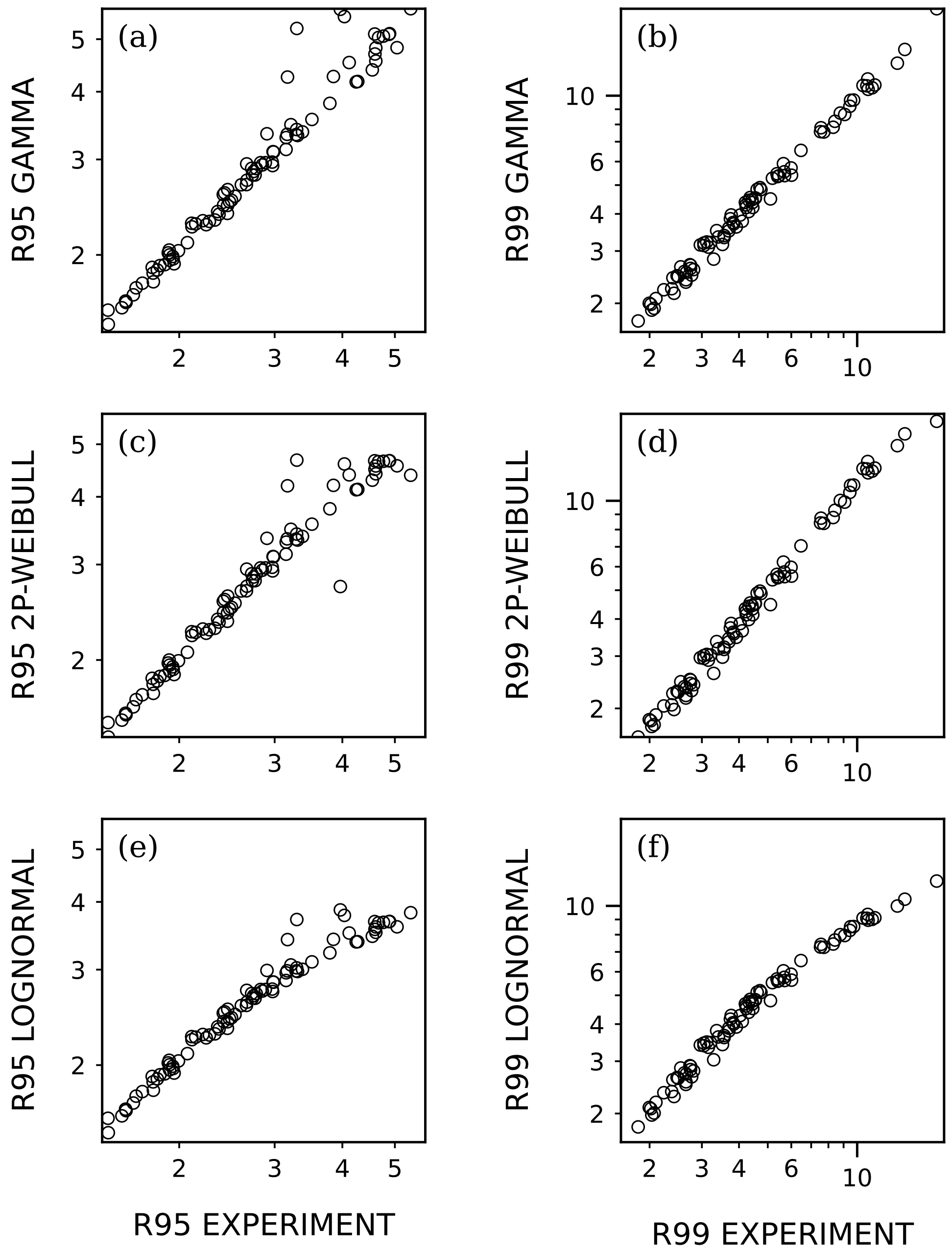

Figure 4.10: Same as Fig.4.8 for the 'S25 dense' configuration.

This demonstrates the capacity of all tested distributions to reproduce very high, and hence hazardous, concentration values. Contrary to Oettl and Ferrero (2017), we observe that the performance of the gamma and the Weibull distributions are similar. Peak to mean ratios can hence be computed from high percentiles of the three models with a similar accuracy, and the analytical definition provided only by the 2p-Weibull model enables much faster computations (Oettl and Ferrero, 2017). It is much easier to obtain an accurate value of higher percentiles than the 3rd and 4th order moments of the distribution, which confirms the previous conclusions detailed over section 4.2. Similar results were obtained by Papp et al. (2024) on completely different geometrical configurations, namely street canyons. The complex PDF shapes that we observe could explain the difficulties encountered by Papp et al. (2024) into reproducing the kurtosis of concentration, while high percentiles were accurately predicted by the gamma distribution.

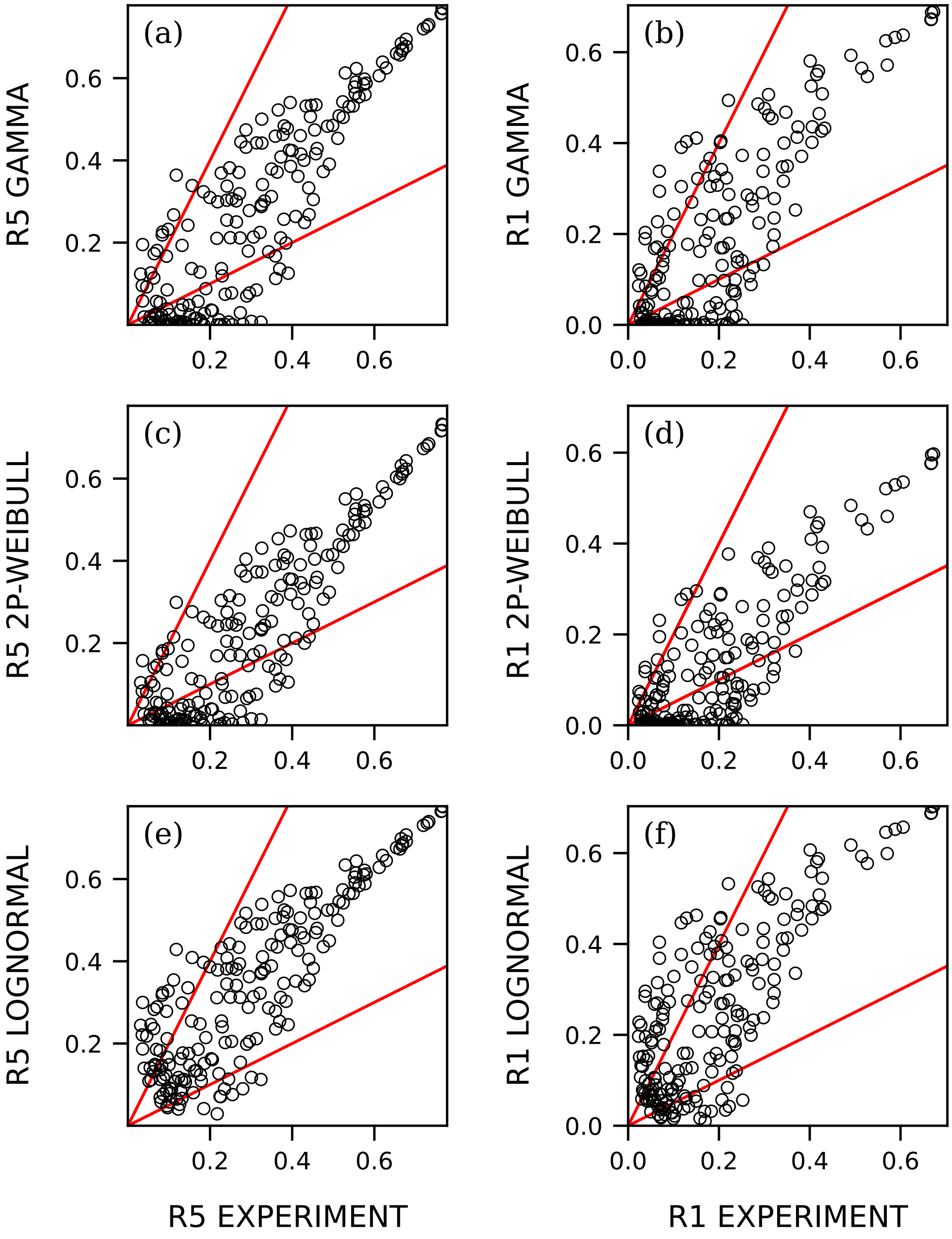

Figure 4.11: Percentile-to-mean ratios using **a**, **c**, **e**: the 1tst and **b**, **d** and **f**: the 5th percentiles in the 'S25 solid' configuration. Red lines correspond to a factor of 2 and 0.5 of the experiment.

Figure 4.11 shows the ratios of low percentiles to the mean value of concentration, for each measurement point of the 'solid' configuration. The scatter is much higher than in Fig. 4.8, which enlightens the better ability of all tested distributions to reproduce the concentration peaks than concentration values below the mean.

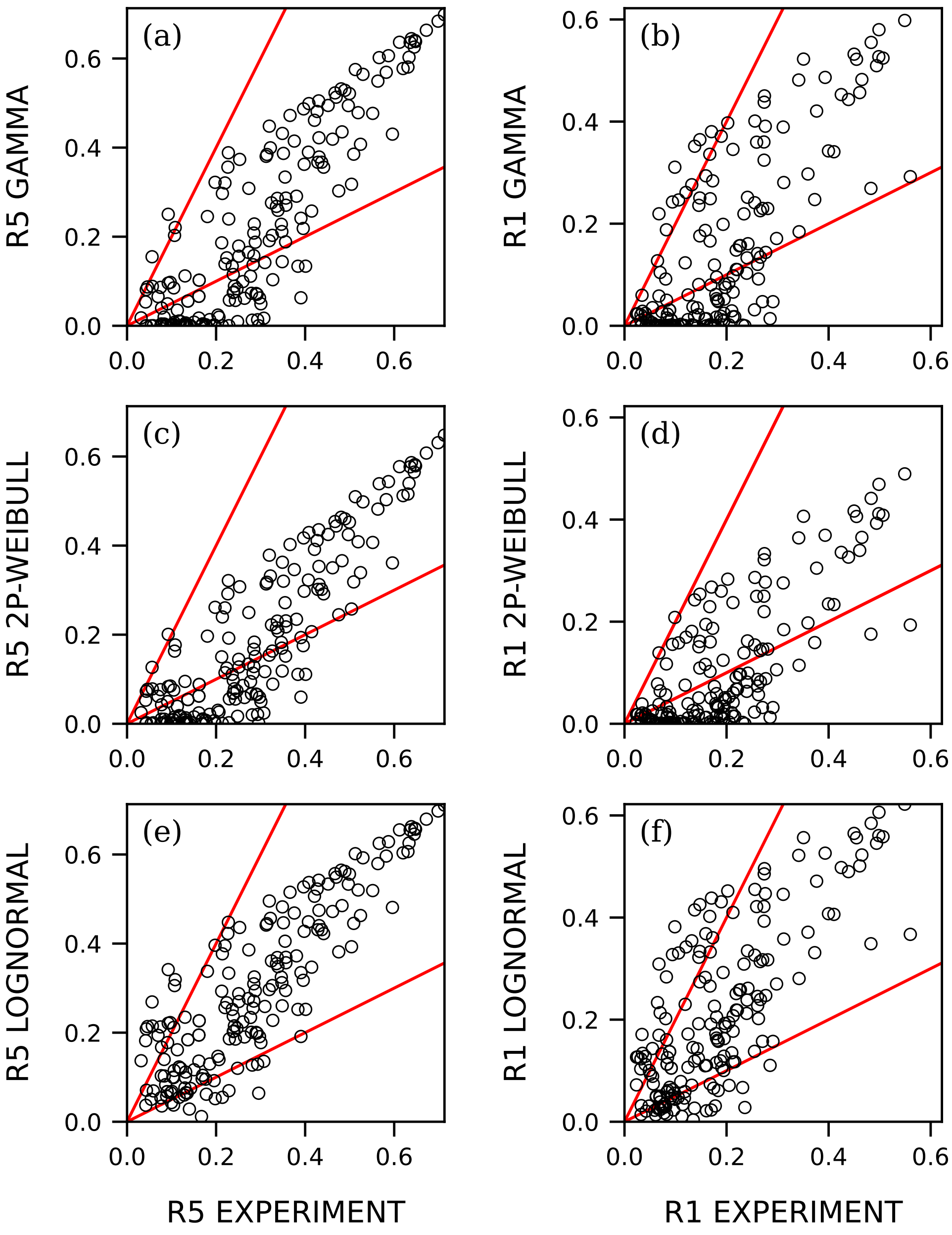

Figure 4.12: Same as Fig.4.11 for the ‘S25 dense’ configuration.

Similar behaviours are visible in Fig. 4.12 and Fig.4.13 that correspond to the ‘dense’ and ‘spaced’ configurations, respectively, which indicates that there is almost no impact of the type of geometry of the site on the difficulties of model distributions to capture the lower half of the concentration range. Notably, there seem to be a limit, $R5 < 0.5$ and $R1 < 0.4$ below which none of the three tested distributions is able to capture the experimental first and fifth percentiles. Points within these ranges correspond to highly variable signals, with minimum concentration values much lower than the mean.

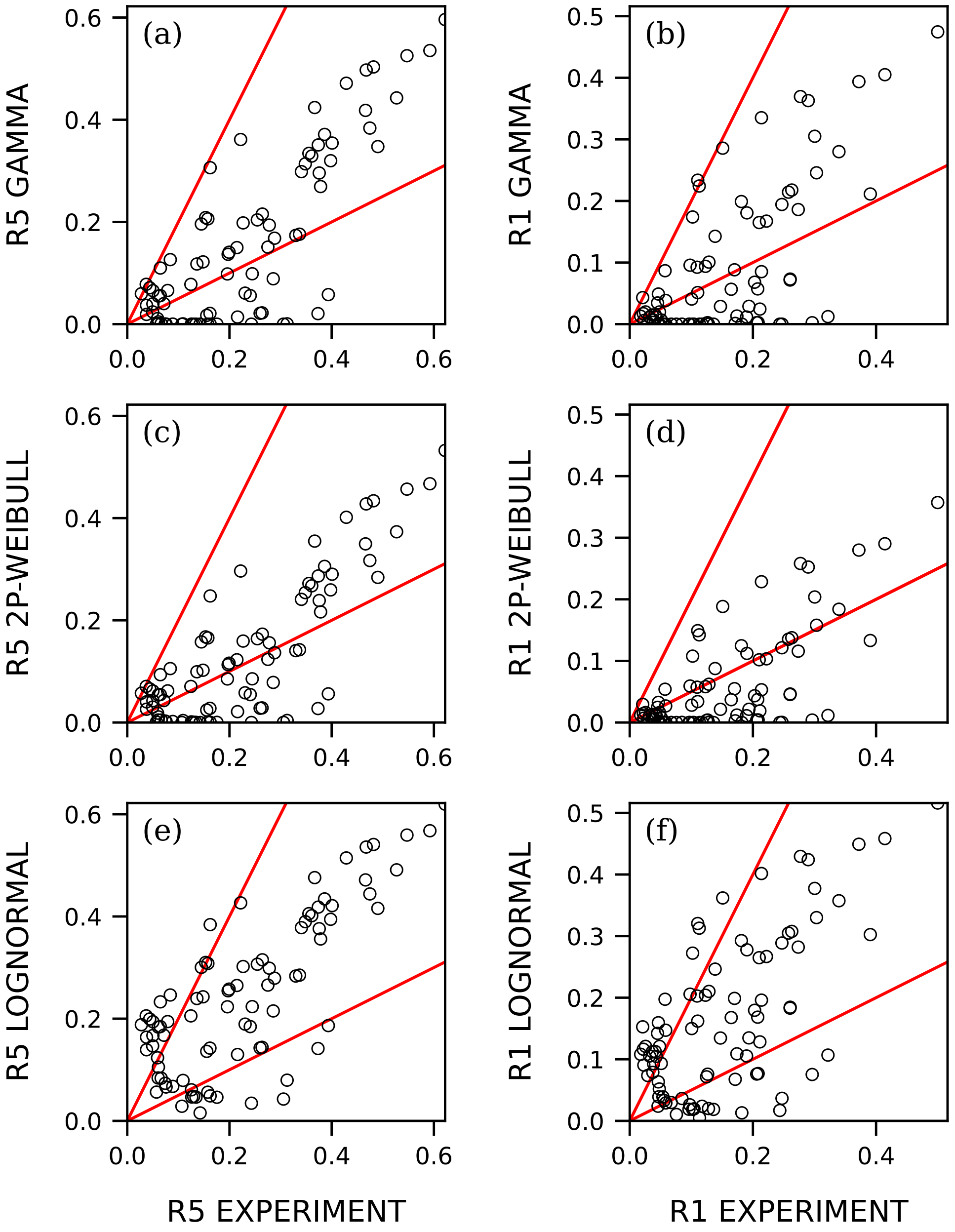

Figure 4.13: Same as Fig.4.11 for the ‘S25 spaced’ configuration.

4.4 Conclusion

In this chapter, we analyse the statistical distribution of the measured one-point concentration, in order to identify appropriate statistical models for concentration fluctuations in key regions of the site, namely the near-, mid- and far-fields. Three statistical models —the lognormal, gamma and 2-parameter Weibull distributions —are evaluated against the experimental data. The most significant outcome of this analysis is the pronounced influence of the site geometry on one-point concentration statistics, as well as the inability of all tested models to reproduce the complex shapes of the experimental probability density functions (PDFs) across the entire site.

Nevertheless, the accuracy of the model distributions depends strongly on the distance from the source. The lognormal distribution provides the best fit in the near-field, while the gamma distribution performs better in the mid-field. In the far-field, the Weibull distribution slightly outperforms the gamma model. Despite these trends, none of the three distributions is able to reproduce the lower half of the experimental PDFs, as the observed distribution shapes are too intricate to be adequately represented by two-parameter models. In contrast, the upper tails of the PDFs, corresponding to the highest concentration values, are captured with substantially greater accuracy by all three distributions.

In particular, the 95th and 99th percentiles of the concentration distribution —associated with extreme concentration events —are well reproduced once the model distributions are scaled using the experimentally measured mean and variance. This result suggests promising practical applications, notably for estimating peak concentrations using only the mean and variance of concentration fields obtained from numerical simulations.

Chapter 5

Risk estimate: statistics of threshold exceedance

In this chapter, we extend our analysis beyond the statistical results presented in chapter 4 to focus on the temporal characteristics of the one-point concentration signals. In particular, we aim to analyse the average duration of exceedance of hazard thresholds, which has important implications for the risk assessment of hazardous airborne substances released during accidental emissions. To this end, we evaluate the reliability of the model proposed by Bertagni et al. (2020) by comparing its predictions with our experimental data. For simplicity, we focus only on a single case, namely the ‘S25solid’ configuration.

5.1 Risks associated to threshold exceeding

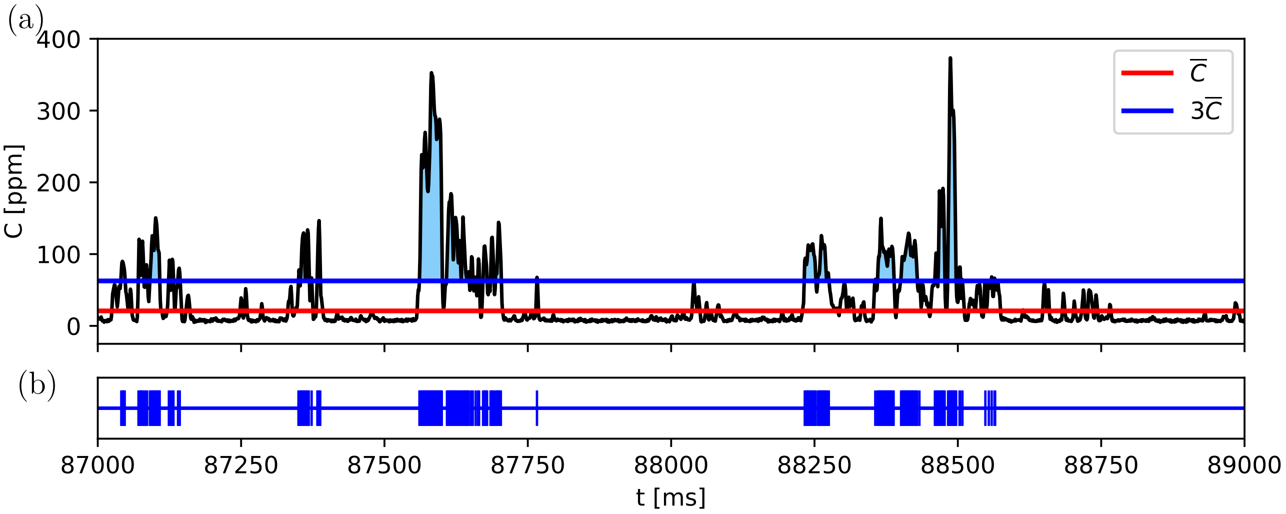

Figure 5.1: Extract of a time series of concentration measurements. **a**: concentration signal in which the mean (in red) and an arbitrary threshold (three times the mean, in blue) are indicated. Periods in which the signal exceeds the threshold are highlighted in blue. **b**: time periods in which the concentration signal exceeds the threshold.

The concentration time series shown in Fig. 5.1 illustrates the variability of the signal measured downwind of the source in one of our experiments. Sharp peaks, resulting from puffs with concentrations significantly higher than average, alternate with longer periods of lower concentrations. Notably, the time-averaged concentration over the 300-second series (shown in red) is roughly one order of magnitude lower than the peak values. This demonstrates that, in the case of toxic or explosive releases, where hazards arise when specific concentration thresholds are exceeded, the mean concentration is not a meaningful measure for risk assessment.

The duration and frequency of peaks vary widely, and even when average concentrations remain below toxicity limits, short-lived exceedances may still pose hazards. Analysing the temporal behaviour of the signal is particularly important when local exceedances can trigger chemical reactions that are explosive or produce harmful species. Similar considerations apply to odour assessment, as human olfaction responds to instantaneous concentrations, with discomfort driven more by rapid fluctuations than by the mean level (Piringer and Schauberger, 2012).

To quantify these effects, it is necessary to estimate statistics related to the average duration of threshold exceedances. For illustration, an arbitrary threshold set at three times the mean concentration is shown in blue in Fig. 5.1. The light blue areas highlight peaks exceeding this threshold, while Fig. 5.1b shows the corresponding time intervals.

The duration of exceedances spans a wide range: the shortest peaks exceed the threshold for about 1ms, approaching the temporal resolution limit of the FID, while longer peaks may persist for tens to hundreds of milliseconds depending on the measurement location. This variability motivates the analysis of averaged statistical properties in the following sections.

Developing methods to estimate the mean frequency and duration of threshold-exceeding peaks is therefore essential for risk assessment in operational contexts. However, few analytical models exist, and to our knowledge, none have been validated in complex terrain geometries. We compare one such model, which assumes a one-point gamma distribution of concentration, to our wind tunnel measurements, allowing evaluation of its validity over terrains with built elements typical of industrial sites. Although the gamma distribution hypothesis was verified only in the mid-field, it remains the most appropriate among the three distributions tested for the majority of the site (see chapter 4). Consequently, the use of a model based on a gamma distribution is justified over a large portion of the site, particularly in the mid-field near the plume centreline, where concentration levels are higher.

5.2 Analytical modelling of threshold exceeding mean times

The aim of our analysis is to assess the reliability of the model developed by Bertagni et al. (2020), which has so far been evaluated only for localized releases in flat terrains. The model is based on a synthetic reconstruction of concentration signals, assuming sudden rises in concentration followed by an exponential decay (see Fig.5.2). The decay rate is determined by a characteristic integral time scale, τ_C, which corresponds to the memory of the one-point concentration dynamics (Ridolfi et al., 2011), and is derived from the autocorrelation function of the concentration:

$$\tau_C = \int_0^\infty \frac{\left(C(t+\tau) - \overline{C}\right)\left(C(t) - \overline{C}\right)}{\sigma_C} d\tau$$

where the integration variable τ is the time lag at which the correlation of the concentration signal is computed.

The mean time of exceeding a concentration threshold ϕ, written T_ϕ^+ and called upcrossing

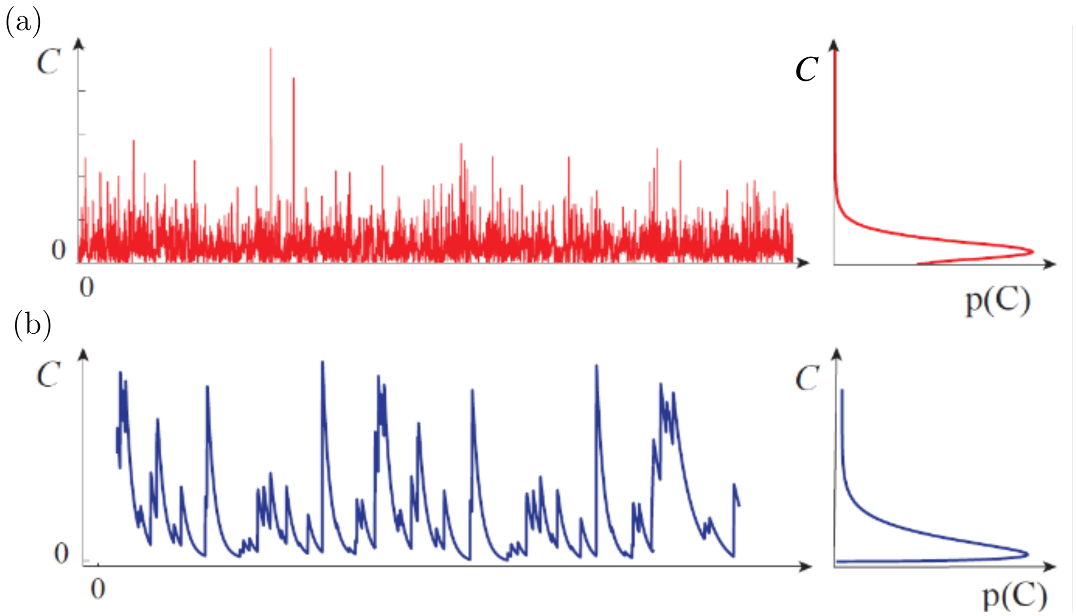

Figure 5.2: Concentration time series and PDF from **a**: the experiment and **b**: the synthetic reconstruction of peaks. This image is adapted from Bertagni et al. (2019a).

time, is obtained by Bertagni et al. (2020) as:

$$T_\phi^+ = \tau_C \exp\left(\phi k/\overline{C}\right) \int_1^\infty \exp\left(-\frac{k\phi}{\overline{C}} \cdot s\right) / s^{1-k} ds \tag{5.1}$$

with $k = (\overline{C}/\sigma_C)^2$ the shape parameter of the gamma distribution as defined in sec.4.1, and the integral term represents the exponential integral function (Abramowitz and Stegun, 1965), in which s is the integration variable. Once defined P_ϕ^+ the probability of $C > \phi$, the mean upcrossing frequency is given by:

$$N_\phi^+ = \frac{P_\phi^+}{T_\phi^+} = \frac{\frac{k\phi}{\overline{C}} \cdot \exp\left(\frac{-k\phi}{\overline{C}}\right)}{\tau_C \cdot \Gamma(k)} \tag{5.2}$$

In his study, Bertagni et al. (2020) verified the agreement between theoretical and experimental estimates of both T_ϕ^+ and N_ϕ^+, using analytical models for all three parameters ($\overline{C}$, σ_C, and τ_C). In contrast, in our work we use the experimentally measured mean, variance, and integral time scale of the concentration and compare the measured mean upcrossing times with the modelled times across a wide range of threshold values. First, we focus on the experimental data. For each threshold value, we compute the mean duration in which the concentration exceeds the threshold, as well as the mean upcrossing frequency. The autocorrelation function of the concentration is then computed as $R_{cc} = \overline{c'(t+\tau) \cdot c'(t)} = \frac{1}{N} \sum_{i=0}^{N=300000} c'_{i+j} \cdot c'_i$, where $c' = C - \overline{C}$, for a measurement lasting 300 s with a 1000 Hz measurement rate. Once the autocorrelation function is obtained for a wide range of values of τ, we approximate its integral as the value of τ at which $R_{cc} \simeq \frac{1}{e}$, to avoid the high uncertainty generated by fluctuations of R_{cc} close to zero at large τ. We then compute the mean upcrossing time and frequency as defined by eq.(5.1) and eq.(5.2), respectively.

Subsequently, we model the integral time scale and compute the threshold exceeding statistics according to the model by Bertagni et al. (2020) using the experimental mean and variance of concentration, together with the modelled integral time scale. We chose to model τ_C as an attempt to test the model for operational applications relying on numerical simulation outputs. Since the latter would provide at best only the mean and variance of concentration, it is necessary to assess the model sensitivity to the accuracy of the modelling of τ_C.

Finally, we compute the mean upcrossing time and frequency obtained with the modelled integral time scale and compare the results to the experimental data.

5.3 Comparison of the model of Bertagni et al. (2020) to the experiment

We present a comparison between the experimental data and the model developed by Bertagni et al. (2020), focusing exclusively on the 'S25 solid' configuration. The comparison concerns the modelled and experimental upcrossing times and frequencies at several representative positions across the site. As a first step, in Sect. 5.3.1, we compute the values of T_ϕ^+ and N_ϕ^+ using equations 5.1 and 5.2, respectively. The input parameters, $\overline{C}$, σ_C, and τ_c, are estimated from the experimental data. Subsequently, in Sect. 5.3.2, we evaluate the performance of the model for T_ϕ^+ and N_ϕ^+ using, as input parameters, the experimental values of $\overline{C}$ and σ_C (as before), while adopting an analytical expression for τ_c obtained by fitting the experimental data.

Since the model, that is, equations 5.1 and 5.2, assumes that the one-point concentration probability density function (PDF) follows a Gamma distribution, we also report the corresponding Kullback–Leibler divergence. This provides insight into whether a key assumption of the model, namely that the concentration PDF is Gamma-distributed, is actually satisfied by the experimental data, before assessing the model's predictive accuracy. As chapter 4 evidenced the better suitability of the gamma distribution in the mid-field than in the region close to the source, we do not expect the modelled exceeding statistics to perfectly fit the experimental data over the whole site. Instead, we focus on the order of magnitude of the results, for concentration threshold values up to 10 times the mean. This upper limit of concentration threshold was chosen to maintain the reliable computation of exceeding statistics on experimental data. Meaningful threshold values depend on the properties of the considered pollutant, and could thus vary over the whole range of concentration thresholds investigated in this chapter.

5.3.1 Mean time and frequency of threshold exceedance

Figure 5.3 presents the spatial arrangement of the Kullback-Leibler divergence of the gamma distribution over the site at ground level (see Fig.5.3a), as well as the mean upcrossing time measured and modelled at several representative points of the site. Close to the source, concentration values reach several tens of times the average. As shown in Fig. 5.3b, upcrossing times close to the source decrease with increasing threshold values. In this region, modelled T_ϕ^+ fit to experimental data up to 3 to 4 times the mean, but average upcrossing times are underestimated for thresholds over $\phi/\overline{C} = 4$. This mismatch is stronger at points located closer to the upwind building, as in Fig.5.3i, which is representative of all the neighbouring points. Due to the high KL values of the gamma distribution in this region (see Fig.5.3a), no better accuracy of the model is to be expected. The model for threshold exceeding statistics proposed by Yee (2001), who hypothesises a lognormal distribution, could be more suitable in this region.

Conversely, the accuracy of the Bertagni et al. (2020) model is higher in the mid-field, where the Kullback-Leibler divergence of the gamma distribution is below 10^{-1}. As presented in Fig.5.3c, modelled T_ϕ^+ reproduce the experimental values up to $\phi/\overline{C} = 5$ with a good accuracy. However,

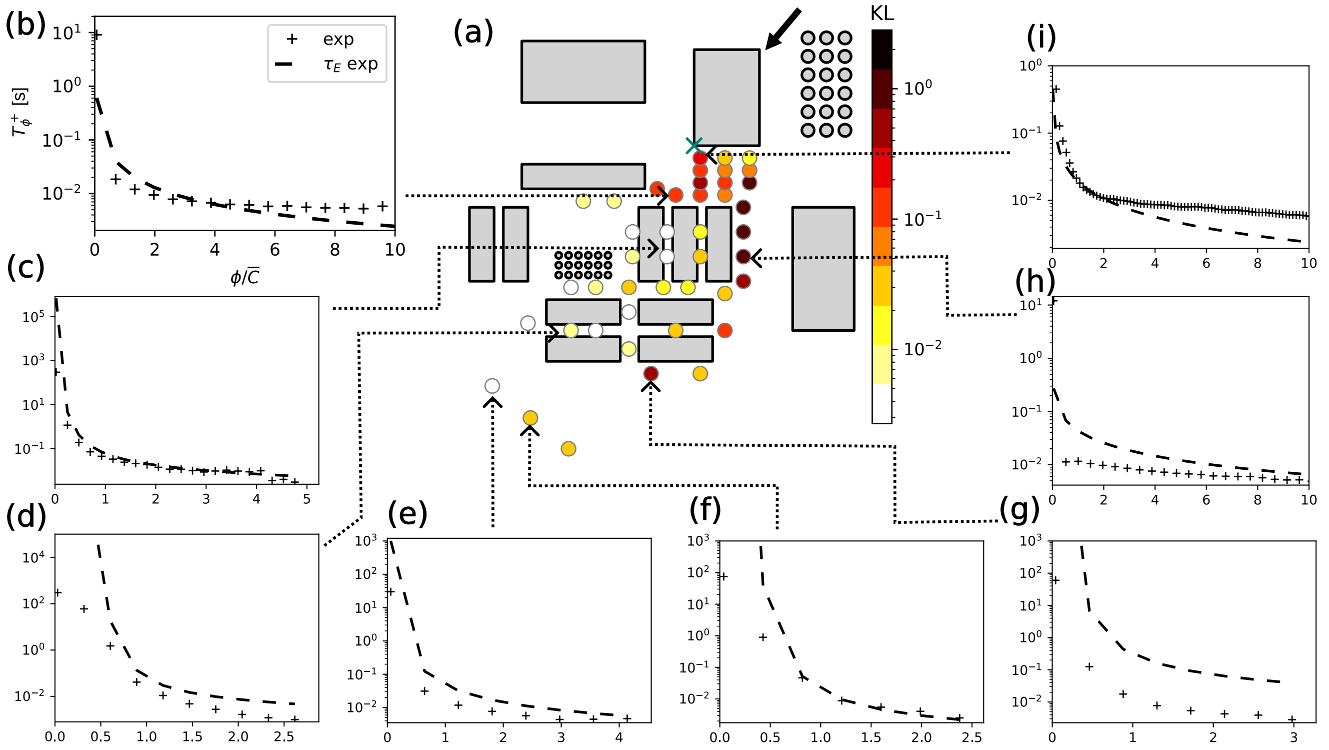

Figure 5.3: Upcrossing times (in seconds) as a function of the threshold at several representative positions of the site. Coloured dots represent the Kullback-Leibler divergence values for the gamma distribution.

this is the only region of the site where the model produce a satisfactory estimate of upcrossing times. Further from the source, T_ϕ^+ tends to be overestimated, even at points for which the gamma Kullback-Leibler divergence is low (see Fig.5.3d, e and f). Points with high KL values, such as in Fig.5.3g and h, show overestimations of the mean upcrossing time reaching up to 2 orders of magnitude. As a consequence, this model should be used with caution, since we observed its validity to be limited to a narrow zone in the mid-field, where the PDF of concentration actually follows a gamma distribution. The general tendency of the model to overestimate upcrossing times in the mid- and the far-field at ground level is compatible with worst-case scenario risk assessment. However, the model underestimates upcrossing times at higher vertical levels (not shown). Additionally, mean upcrossing times in the near field are underestimated, particularly for threshold values over 4 times the mean, which represents an obstacle to the correct estimation of the risk posed by high concentrations in this area.

One of the limits of this analysis is the duration of concentration measurements. More precision on the statistics associated to higher threshold values could be obtained from measurements three times longer than ours, particularly in the mid- and the far-field.

Frequencies of threshold exceeding are presented in Fig.5.4, whose structure is the same as that of Fig.5.3. Modelled values of N_ϕ^+ are globally slightly less accurate than those of T_ϕ^+. Close to the source, we observe a satisfying model-experiment agreement only for threshold values around the mean (see Fig.5.4i). Notably, the slope at which N_ϕ^+ decreases with increasing ϕ is not captured by the model, which alternatively over- and under-estimates upcrossing frequencies as the threshold increases. A mismatch in this region is however expected, since the lognormal distribution is more adapted than the gamma distribution close to the source (as we observed in chapter 4). In the mid-

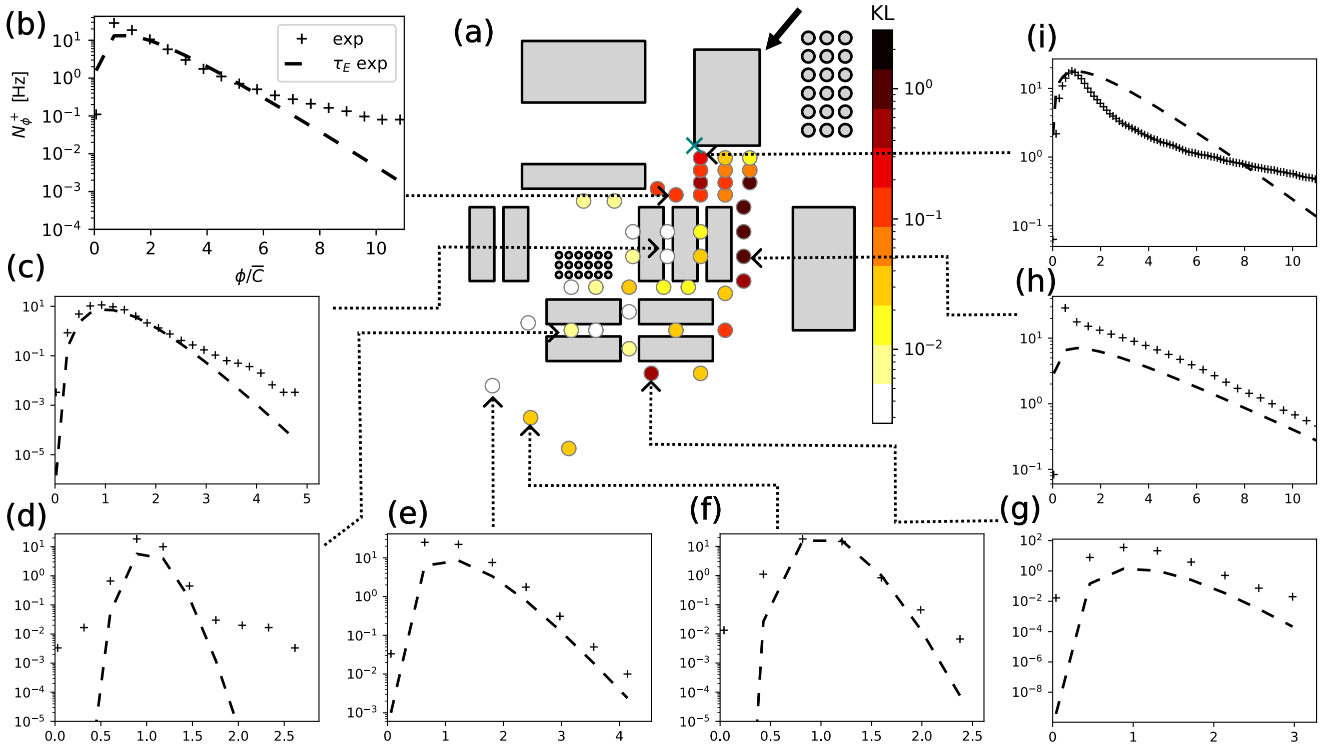

Figure 5.4: Upcrossing frequency (in hertz) as a function of the threshold at several representative positions of the site. Coloured dots represent the Kullback Leibler divergence values for the gamma distribution.

and the far-field, mean upcrossing frequencies tend to be under-estimated, as a consequence of the over-estimation of mean upcrossing times. A reasonable accuracy is reached in the mid-field (see Fig.5.4c) below 3 to 4 times the mean, and in the far field around the mean value (see Fig.5.4d, e and f). As for upcrossing times, points in which KL values are above 10^{-1} are associated to less accurate modelling of N_ϕ^+.

5.3.2 Modelling the integral time scale

The evolution of the integral time scale with respect to the dimensionless distance from the source is shown in Fig.5.5. A considerable scatter of data points can be observed in Fig.5.5, as the integral time scales of points lying along the same transverse profile may differ by up to one order of magnitude. Experimental τ values generally show an overall increase with the distance from the source, following a slope on the semi-log representation of Fig.5.5, which value was determined by an exponential fit. We could not identify underlying processes that would explain this exponential relation or the amount of scatter of points, such as the flying time of fluid particles emitted from the source, the intensity of fluctuations or the shape of the experimental concentration PDF. Additionally, preliminary analyses of the ‘S25 dense’ and ‘S25 spaced’ configurations did not evidence any similar exponential relation between the integral time scale and the distance from the source, τ being closer to a constant in these configurations. More precise and adapted estimations of the integral time scale are thus necessary and may depend on the geometrical configuration of the site. Here, the exponential fit presented in Fig.5.5 was used as a simple model for the integral timescale, as an attempt to estimate the sensitivity of the model presented in eq.(5.1) and eq.(5.2)

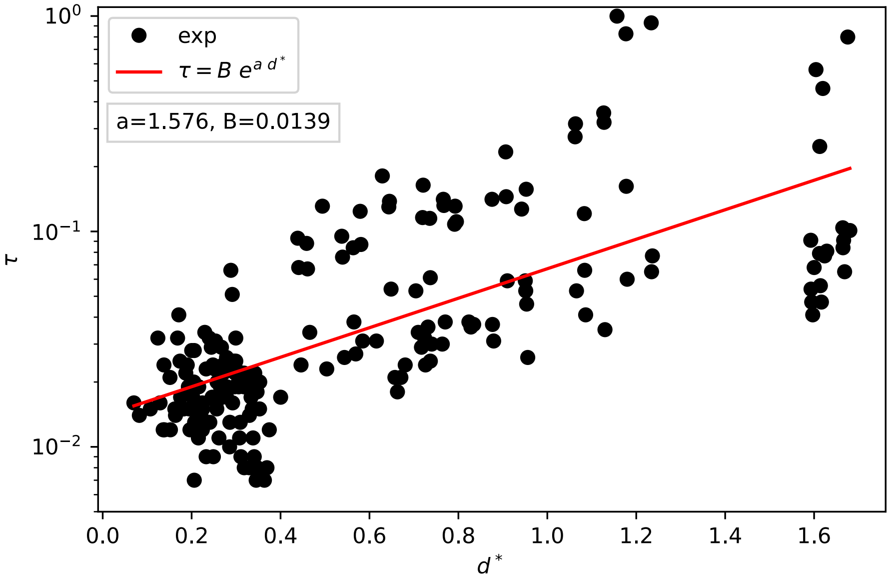

Figure 5.5: Experimental integral timescale as a function of the dimensionless distance from the source. The red line presents the exponential law that was used to model this parameter.

to a rough estimate of this parameter.

Mean upcrossing times obtained using both the experimental and modelled integral time scales are presented in Fig. 5.6. The accuracy of the modelling of T_ϕ^+ varies strongly from one point to another. Mean upcrossing times computed from the modelled integral time scale can be higher (as in Fig. 5.6f) or lower (as in Fig. 5.6g) than those computed from the experimental τ. Overall, the estimates of mean upcrossing times are closer to the experimental values when the experimental integral time scale is used. However, for the majority of locations within the site, T_ϕ^+ values derived from the modelled τ exhibit a closer agreement with those obtained using the experimental τ than with the values directly computed from the experimental data T_ϕ^+. Higher mismatches between the two models could not be explained as due to the location within the site.

The mean exceedances frequencies shown in Fig. 5.7 indicate that the estimates provided by the two model formulations, whether using τ_c derived from experimental data or obtained from an empirical analytical model, differ only slightly. This difference is of the same order as the discrepancy between the model predictions and the experimental values of N_ϕ^+. Estimates of the mean threshold exceeding time and frequency could thus be provided by eq.(5.1) and eq.(5.2), respectively, in which the integral time scale is estimated by a simple power law. Adequate caution is however required since modelled T_ϕ^+ can over- or under-estimate the experiment by an order of magnitude.

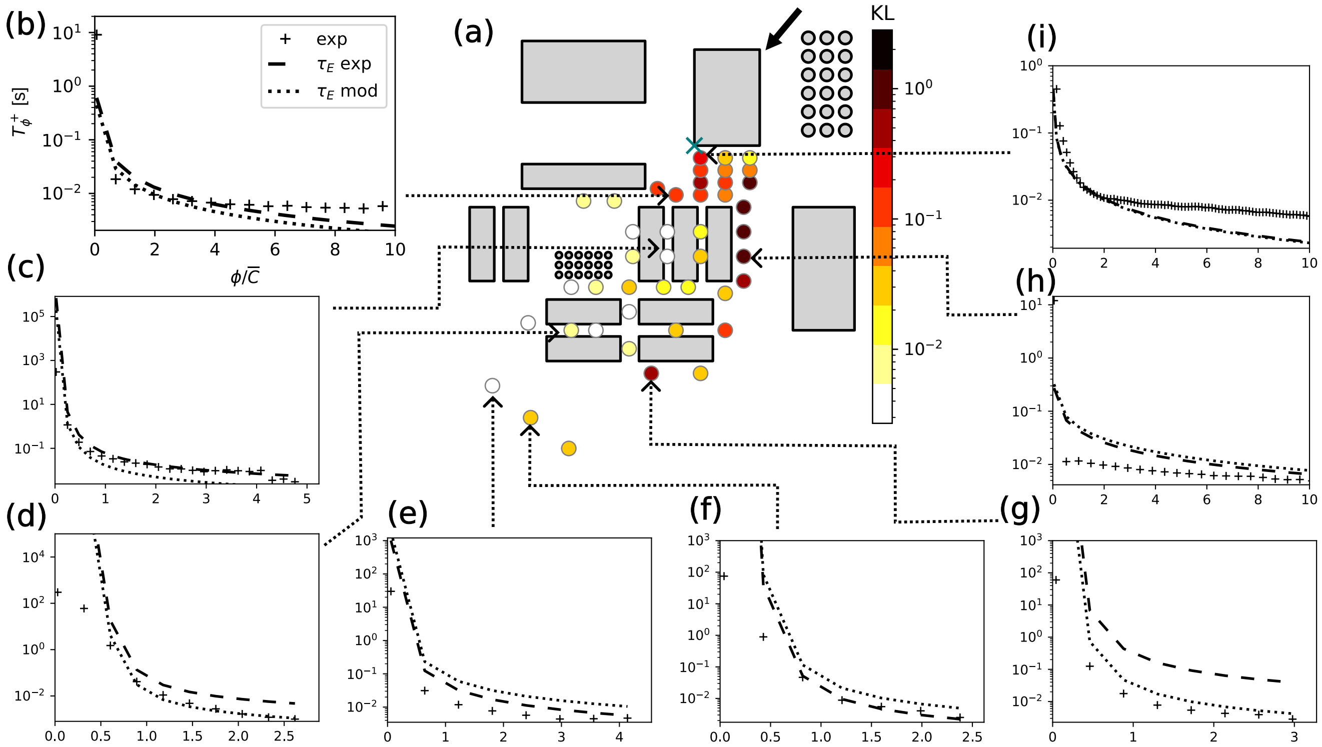

Figure 5.6: Same as Fig.5.3 including modelled exceeding mean times computed from the modelled integral time scale.

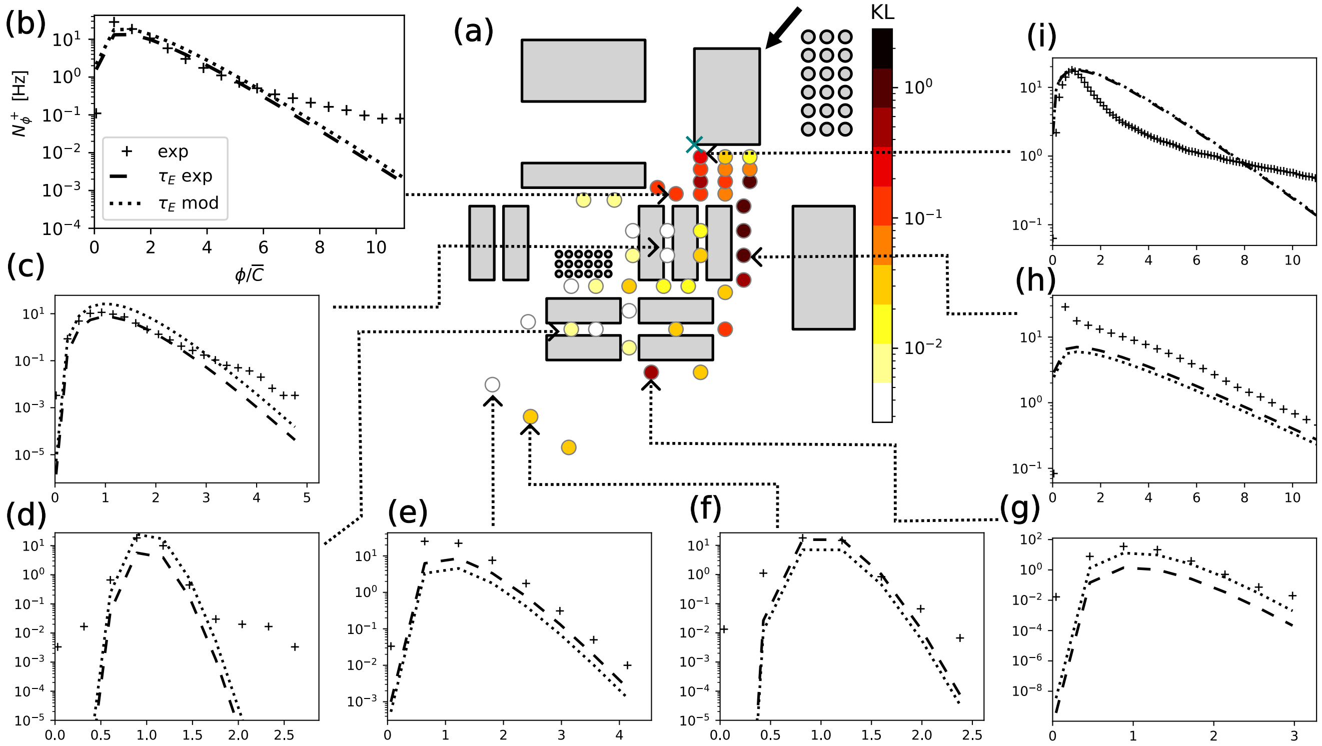

Figure 5.7: Same as Fig.5.4 including modelled exceeding mean frequencies computed from the modelled integral time scale.

5.4 Conclusion

As chapter 4 evidences the ability of the tested model distributions to capture the peak concentration values, this chapter focuses on the estimate of the intensity, frequency and duration of these peaks, by using a model based on the hypothesis of a gamma distribution. As the gamma distribution is more accurate in the mid- than in the near-field, and as it is not able to reproduce the lower tail of the concentration PDF, we do not expect the modelled statistics to perfectly fit the experimental data. Moreover, the model of Bertagni et al. (2020) relies on the knowledge of the mean and the variance of the concentration signal, in addition to the integral time scale, which is rarely provided by numerical models of dispersion. We thus investigate the effect of modelling this parameter —which increases the model uncertainty —on the resulting statistics. However, obtaining the right order of magnitude of exceeding mean time and frequency would already be sufficient to provide meaningful data for risk assessment, such as toxicity analyses.

We found that the mean exceeding time is more accurately captured by the model than the exceeding frequency. Modelled values globally lie within the right order of magnitude at locations where the gamma distribution is valid, meaning in regions of the mid-field where the local perturbative effect of obstacles on the plume is limited. However, for points where the gamma distribution does not fit the experimental PDF, the mismatch between modelled and experimental mean exceeding times and frequencies reaches up to two orders of magnitude. Modelling the integral time scale can change the modelled threshold exceeding statistics, but the mismatch with experimental data does not exceed the mismatch obtained while using the experimental integral time scale. As a consequence, this model should be used with caution, notably if the information on the validity of the gamma distribution is not accessible, and particularly over complex geometry terrains. Nevertheless, numerical dispersion models providing the mean and the variance of the concentration distribution could be improved by integrating this approach as a rough estimator of peak statistics. Applications notably include the estimate of the cumulative or acute exposure to toxic pollutants, as well as studies linked to odour perception.

Conclusion of Part I

This study investigates the atmospheric dispersion of an airborne pollutant within an industrial site. We analysed the velocity and concentration fields of a scalar released from a steady point source positioned at ground level, immediately downstream of the site upwind building. The experiments were conducted by modifying the site geometry through alterations of the configuration of the tallest upwind building. Specifically, this building was replaced with porous variants designed to reproduce typical arrangements of pipes and tanks commonly found in industrial environments.

The velocity field is strongly affected by the upwind building configuration. The solid version generates a wake with higher turbulence intensities, whereas densely packed porous columns promote mixing and sparsely arranged ones mainly reduce the mean flow without inducing recirculation. As a result, the concentration field is also influenced by the upwind configuration, with porosity-induced plume displacements remaining visible even in the far field. The upwind element most strongly affects plume width and peak concentration in the near and mid fields. Smaller obstacles primarily alter the concentration standard deviation, enhancing fluctuation intensity near the plume edges.

We analysed the statistics of one-point concentration fluctuations, focusing on modelling the concentration probability density function (PDF) at different distances from the release point. Following previous studies (Cassiani et al., 2020), we assessed the ability of the gamma, two-parameter Weibull, and lognormal distributions to reproduce the experimental data. None of these distributions fully captured the complex shapes of the measured PDFs, which were influenced by the presence of obstacles. Notably, the lower tail of the experimental concentration PDF exhibited highly irregular shapes, which are too complex to be captured by any of the tested model distributions, associated with elevated fluctuation intensity. Therefore, i_C serves as an indicator of the fit quality between the lower tail of the modelled and experimental concentration PDFs. Additionally, modelled skewness and kurtosis values showed considerable uncertainty, and no single distribution consistently represented the experimental concentration PDF across all distances from the source.

Despite these limitations, we could identify model distributions that better fit the data, depending on the distance from the source and the site region considered. Our results show that the lognormal distribution provides a more accurate fit in the wake of the upwind obstacle near the source, while the gamma distribution performs better in the mid field, even when grouped obstacles disrupt the flow. This finding extends the previously established validity of the gamma model over flat terrains (Cassiani et al., 2020) to built industrial environments. In the far field, the two-parameter Weibull distribution slightly outperforms the gamma model in describing the concentration PDF. Moreover, the quality of agreement between the model distributions and experimental concentration PDFs is linked to the fluctuation intensity particularly for the gamma and Weibull models.

Unlike lower concentration values, high percentiles are accurately captured by all three distributions across the entire site. This finding is particularly valuable for risk assessment in scenarios involving hazardous peak contaminant exposures, such as evaluating threshold exceedance and peak concentrations. With this objective in mind, we tested the model of Bertagni et al. (2020), that provides analytical estimates of threshold exceeding statistics based on three input parameters only: the concentration integral time scale, the average and the variance of concentration. Mean exceeding times are more accurately modelled than mean exceeding frequencies, and the best accuracy is reached in the mid-field where the validity of the gamma distribution is highest. Modelling the integral time scale by a simple exponential relation to the distance from the source does not significantly worsen the estimate of threshold exceeding statistics. The Bertagni et al. (2020) model can thus provide an estimate of mean threshold exceeding times in complex geometry terrains. However, implementing crossing time estimators into dispersion models depends on the availability of concentration variance values, which are not provided by most operational models. Simulating the concentration variance is thus a crucial feature that should be implemented in dispersion models to enable adequate risk estimation of accidental releases inside real built environments.

Part II

Numerical modelling

In this second part, we are interested in the practical tools that can be used before or during accidental crises, to prevent and to manage them. These tools are numerical dispersion models that are able to provide the three-dimensional field of concentration with a refined spatial resolution from meteorological inputs and source characteristics (position and mass flow rate). On one side, they are necessary to simulate preventively the consequences of potential accidental releases, notably to determine the most adapted emergency measures that should be taken during real accidents. On the other side, they provide crucial information during accidental events, particularly about the most impacted and hazardous areas of the site. Data of equivalently high spatial resolution would hardly be obtained from field measurements alone due to the high cost of sensors and potential health hazard for their handlers.

In the following, we analyse the same configurations as those studied in Part I. We compare two numerical modelling approaches to the experimental measurements. They differ in the formulation of the computation of the velocity field, but they include the Lagrangian formulation of dispersion, and they both are able to capture the effect of built elements on dispersion with a high applicative potential. The objective behind this comparison is to determine how the choice of the modelling approach impacts the simulated pollutant concentration field. Since the models are proprietary, they were applied in compliance with the usage guidelines provided by their developers, representing the most effective use under available conditions. Detailed inspection of the underlying implementations and comprehensive sensitivity analyses were beyond the scope of this work. The simulation tools were used in their standard operational configurations, as made available to stakeholders, without direct access to source code or implementation details.

On one side, we consider PMSS (Parallelised Micro Swift Spray, Oldrini et al., 2017) which is a suite of models based on the SWIFT wind modelling system and the SPRAY Lagrangian particle model. SWIFT is a numerical interpolator that generates a wind field affected by the presence of buildings based on geometrical features that are typical of a flow perturbed by obstacles. The atmospheric dispersion model SPRAY takes the wind field generated by SWIFT as an input to compute dispersion of the fluid particles emitted at the source over the site and to retrieve the mean concentration field. Both SWIFT and SPRAY were designed to perform micro-scale simulations (hence the ‘micro’ denomination), meaning they provide results with a high spatial resolution (below 10m). They both exist in parallelised versions (respectively PSWIFT and PSPRAY) which enable faster simulations on computing servers, hence the name PMSS to talk about the entire suite.

On the other side, we call ‘SLAM’ the approach based on the coupling of a database of Reynolds-Averaged Navier Stokes (RANS) simulations of the wind field produced with the software ANSYS FLUENT to the Lagrangian dispersion model SLAM (in its version simulating statistically stationary flows, Vendel et al., 2011).

The differences in the results for both the velocity field and the concentration field are hence mainly attributable to the different modelling methods of the velocity and turbulence fields, since both models rely on the Lagrangian formulation of atmospheric dispersion. We present each of the modelling methods for the wind field and the main characteristics of Lagrangian models. Then, we compare the wind fields obtained with SWIFT and the RANS simulations to the experimental measurements of velocity in wind tunnel. Finally, we compare the mean concentration fields of both PMSS and SLAM to the experimental concentrations measured in wind tunnel. The work presented in the following was presented at the PhysMOD 2024 conference (International Workshop on Physical Modelling of Flow and Dispersion Phenomena, Schiavini et al., 2024) and the HARMO23 conference (Harmonisation within Atmospheric Dispersion Modelling for Regulatory Purposes, Schiavini et al., 2025b).

Chapter 6

State of the art and methods

In this chapter, we present a state of the art of numerical modelling of atmospheric pollutant dispersion, focusing on the approaches that are adapted to operational applications (see section 6.1). We then detail the modelling methods of the wind velocity and concentration fields chosen for the two methodologies that are analysed in this work (see section 6.2). We focus in particular on the modelling features that have a strong impact on the velocity field, and thus also on the simulated concentration field.

6.1 State of the art

Accidental releases occurring in industrial environments pose significant risks to both human populations and the environment. Incidents such as heavy gas leaks, fires, and the dispersion of toxic substances threaten human health and lead to environmental contamination that must be detected, monitored, and mitigated. To identify the areas of the site and its surroundings that are affected, it is essential to simulate the dispersion of the pollutant plume. However, this process is complicated by the inherently unpredictable nature of turbulence and the influence of built structures on the wind field. Therefore, operational dispersion models used for risk assessment must account for the effects of site geometry on pollutant transport, while maintaining sufficient computational efficiency to deliver results within operationally relevant time frames. These modelling tools estimate flow and concentration fields based on physical input parameters, including meteorological conditions, source characteristics, and terrain complexity. However, the combined effects of turbulence and geometrical obstacles greatly increase the complexity of accurately simulating the flow field.

Isolated obstacles predominantly generate two distinct recirculation zones and one influence zone (Hosker, 1981; Hatcher et al., 1977). The first recirculation zone, known as the *displacement zone*, develops upwind of the obstacle and alters both wind speed and direction. As the airflow encounters the obstacle, it decelerates, which is associated to a pressure increase and the formation of a downward flow along the windward face. This results in a near-ground recirculation pattern, whose extent depends on the building's aspect ratio and the characteristics of the approaching flow. For parallelepiped-shaped obstacles with sharp edges, flow separation occurs predominantly at the roof and lateral edges. A horseshoe vortex typically forms as the frontal eddy extends along the sides of the structure. Downwind of the obstacle, the second recirculation zone, referred to as the *cavity zone*, forms due to the detachment of streamlines from the structure. This region is marked by low-velocity recirculating flow and elevated turbulence levels. Fluid particles trapped within this zone undergo extensive recirculation before mixing with the ambient airflow. Further downstream lies the *wake zone*, which follows the cavity zone and is characterized by reduced velocities and enhanced turbulence compared to the incoming flow. Wake lengths generally extend between 10 and 20 times the obstacle height and are highly sensitive to both the properties of the obstacle and the upstream flow conditions. Two-dimensional obstacles were extensively investigated due to their geometric simplicity (Hunt, 1971; Counihan et al., 1974; Salizzoni et al., 2025). In contrast, three-dimensional obstacles provoke more complex interactions involving the roof and lateral surfaces, as shown in Fig.6.1 (Peterka et al., 1985).

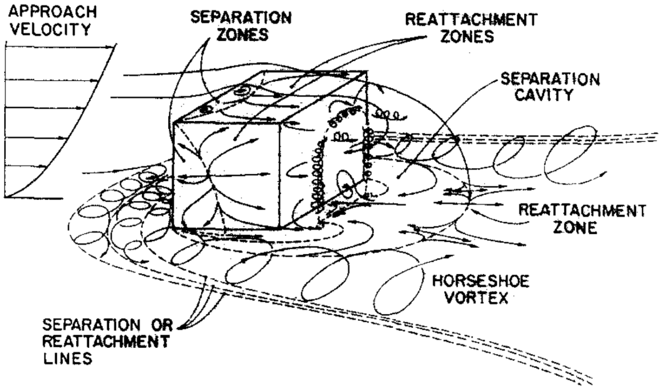

Figure 6.1: Streamlines of the flow encountering a three-dimensional obstacle, from Peterka et al. (1985).

The already complex flow around a three-dimensional obstacle becomes even more complicated when multiple obstacles are clustered, notably in urban geometries. Intricate recirculation zones and channelling effects typical of these configurations were initially elucidated primarily through wind tunnel studies (Gadilhe et al., 1993; Bastigkeit, 2011). The influence of multiple obstacles on the flow field has been addressed through various approaches. These obstacles are often arranged into large arrays of identical, predominantly cubic elements, forming an idealised representation of the urban landscape that have been extensively studied both in field and wind tunnel experiments (Yee et al., 2006; Davidson et al., 1995; Macdonald et al., 1998; Theurer et al., 1996). Research efforts involving such simplified geometries have focused on turbulence at pedestrian level (Hirose et al., 2022; Hang et al., 2012), the influence of overall city geometry on the flow field (Hang et al., 2009) and the aerodynamics of street canyons (Macdonald et al., 2002; Tan et al., 2019). Even simplified configurations can lead to complex flow phenomena, such as the backward flow reported by Hang et al. (2009) within narrow streets, where a backward stream opposes the inflow from the leeward entrance and exits through the open roof. Further complexity arises from lateral channelling effects naturally developing along on the sides of cubic obstacle arrays, characterized by inflow and outflow through streets oriented perpendicularly to the prevailing wind direction, as observed by Princevac et al. (2010). More realistic configurations investigated the influence of obstacle height variations, particularly the presence of individual elements exceeding the height of their surroundings (Hajra et al., 2013; Elshaer et al., 2016; Xu et al., 2017). Princevac et al. (2010) specifically observed that the blocking effect of a tall obstacle embedded within an array of smaller elements deflects individual wakes and alters the lateral channelling behaviour.

Real configurations were investigated in field and wind tunnel experiments at the level of a single street (Arnold et al., 2004), a campus (H'ng et al., 2022), a city district (Ono and Nozu, 2024; Hertwig et al., 2019) and industrial sites (Janour et al., 2010; Quaranta et al., 2001; Hatcher et al., 1977) focusing on the statistics of the wind flow. Notably, Hertwig et al. (2019) demonstrated that the urban landscape provokes structural changes to the wake of tall obstacles, an amplification of vertical velocities and a decrease of turbulence spatial scales.

Therefore, modelling pollutant concentration over complex geometry terrains is complicated by the influence of the wind field on dispersion processes. Factors such as building density (Ku and Tsai, 2020; Jiang et al., 2023), the presence of open spaces (Balczó and Lajos, 2015), buildings shape (Xu et al., 2017) and spatial arrangement (Hajra et al., 2013) exert a significant impact on both the wind field and pollutant dispersion patterns. Arrays of cubic elements tend to enhance turbulent mixing and broaden the pollutant plume, whose extent is closely related to the characteristic dimensions of the obstacles (Macdonald, 2000). Depending on the source position, channelling effects immediately downstream of the source tend to reduce dispersion in the near field, leading to higher concentrations downwind of the site (Janour et al., 2010). Consequently, the capacity of numerical models to capture realistic flow dynamics over complex geometry terrains is essential for accurately reproducing atmospheric dispersion characteristics.

Numerical modelling of the velocity field can be achieved through a range of computational approaches, each establishing a distinct balance between flow accuracy and computational cost. The most accurate methods involve the full or partial numerical solution of the Navier–Stokes equations to determine the velocity field across the domain (Pantusheva et al., 2022; Pope, 2000; Blazek, 2015). In the Direct Numerical Simulation (DNS) framework, all spatial and temporal scales of turbulence are explicitly resolved. However, the computational cost of DNS scales with the cube of the Reynolds number (Pope, 2000), making this approach impractical for operational applications.

Large Eddy Simulation (LES) reduces the computational cost of flow simulations by modelling the effects of the smaller turbulent eddies analytically, as these scales account for the majority of the computational expense. In LES, the Navier-Stokes equations are solved numerically only for the large-scale motions, which contain most of the energy and flow anisotropy, while small-scale turbulent motions are parametrised, as they are assumed to be more universal and less dependent on the specific flow geometry (Pope, 2000). However, for applications in which small-scale effects play a crucial role, such as near-wall flows, the impact of this modelling becomes non-negligible, particularly at high Reynolds numbers (Piomelli and Balaras, 2002; Pope, 2000). Despite these limitations, LES generally achieves good accuracy for atmospheric flow applications. Xie and Castro (2009) demonstrated good agreement between LES results and experimental data for a typical urban site in London (DAPPLE). Furthermore, Xie and Castro (2006) validated LES results against Direct Numerical Simulation (DNS) for an array of cubic obstacles. LES is widely employed in research as a reference method for local-scale atmospheric simulations and has been used to investigate the influence of obstacle height variability (Xie and Castro, 2006; Boppana et al., 2010). It also provides valuable insights into turbulence processes within urban (Kanda, 2006) and forest canopies (Bohrer et al., 2009), as well as into the effects of building details on turbulent flow structures (Bou-Zeid et al., 2009). Nevertheless, LES remains computationally too demanding for routine operational applications.

The Reynolds Averaged Navier–Stokes (RANS) approach optimizes computational efficiency by solving the ensemble averaged Navier-Stokes equations. Consequently, the solution describes only the flow from a statistical point of view. RANS methodologies are widely employed in engineering contexts due to their computational efficiency. In the context of atmospheric boundary layer studies, RANS provides a practical means of estimating mean wind fields within industrial sites (Zhao et al., 2024) and urban geometries (Ramponi et al., 2015; Ku and Tsai, 2020; Crank et al., 2018). However, implementing RANS in operational frameworks remains challenging when simulation runtimes must be limited to only a few minutes. Common computational fluid dynamics

(CFD) software packages capable of performing RANS or LES simulations include ANSYS Fluent, OpenFOAM, Code_Saturne, StarCCM+.

In an effort to reduce computational costs to durations compatible with operational use, semi-empirical models employ a simplified representation of the flow field, seeking a balance between computational efficiency and flow accuracy. The simplest approaches assume horizontally homogeneous conditions, where flow properties vary solely with height above the ground. These one-dimensional models are based on theoretical formulations complemented by empirical and semi-empirical parametrisations derived from observational data. They typically require input observations collected in the vicinity of the area of interest. While they provide rapid results and achieve good accuracy over flat and homogeneous terrains, they are irrelevant in more complex configurations. Such approaches are commonly implemented in meteorological pre-processors, which extrapolate limited local meteorological measurements across the computational domain to supply input data for pollutant dispersion models.

Mass-consistent models reconstruct a three-dimensional flow field from observational data and basic physical principles (Ratto et al., 1994). Rather than solving the full Navier–Stokes equations, these models enforce only the mass conservation equation to ensure physically coherent flows. Although simpler and computationally less demanding than CFD approaches, their inherent simplifications produce less accurate results. The modelling process begins with an initialization step, during which the flow field is interpolated across the entire domain using available observations (e.g., vertical profiles and surface measurements). The resulting field is then adjusted to account for the presence of obstacles. Subsequently, a variational method, similar to that developed by Sasaki (1958), is applied to obtain the flow field that most closely matches the interpolated field while satisfying the mass conservation constraint. Atmospheric thermal stability is represented through a weighting parameter between the horizontal and vertical wind components, allowing the flow to adjust preferentially in one direction depending on stability conditions. These methodologies are commonly used at the microscale, such as within urban districts or industrial sites, as they provide operationally efficient tools capable of incorporating obstacle effects (Kaplan and Dinar, 1996). Notable examples include the PMSS model (Oldrini et al., 2017) and QUIC-URB (Sasaki, 1958).

Zonal models were developed for applications focusing on urban environments. They divide the computational domain into distinct spatial zones, within which simplified flow parametrisations are applied. These approaches are particularly suitable for configurations where the flow structure within each zone can be well characterized. They are mainly employed for the simulation of urban airflow, where the flow above rooftops, which is typically represented using a one-dimensional model adapted for urban environments, is treated separately from the flow within street canyons. The latter are represented as interconnected street segments joined at intersections. Representative implementations of this modelling framework include SIRANE (Soulhac et al., 2011) and MUNICH (Kim et al., 2018).

Pollutant dispersion modelling takes place once the numerical wind velocity field is established, and is generally independent of the flow simulation tool. The wind velocity and turbulence fields serve as input of dispersion models, enabling a wide variety of coupling possibilities with the approaches described above. Simpler dispersion models are based on the assumption of a Gaussian spatial distribution of concentrations, derived from Fick's law for diffusion in an unbounded environment. While Gaussian plume models are adapted to represent point sources inside statistically stationary flows, Gaussian puff models are capable of accounting for non-stationary meteorological and source conditions (Snoun et al., 2023). Examples of the former category include ADMS (Smith et al., 2017) and AERMOD (Pandey et al., 2023), whereas CALPUFF (Dong et al., 2013) and

SCIPUFF (Sykes, 2010) belong to the latter. These approaches can be extended to incorporate ground and wall reflections, thermal stratification, as well as various source characteristics, such as line sources. While these models are frequently used for crisis management and preliminary impact assessment due to their time efficiency, their accuracy diminishes in complex environments where the flow interacts with numerous obstacles, such as in urban or industrial domains.

Eulerian approaches provide a more detailed representation of dispersion by solving the advection–diffusion equation, often in parallel with the underlying flow field (RANS, LES, or DNS). These models are particularly suitable for scenarios involving multiple sources and complex chemical reactions. However, their accuracy can be affected by numerical discretization errors and the choice of closure schemes. Examples of Eulerian dispersion models coupled with LES flow fields include PALM (Maronga et al., 2015) and DALES (Heus et al., 2010). Due to their high computational cost, Eulerian models are resource-intensive, making Lagrangian formulations an attractive compromise in many operational applications.

As an alternative to Eulerian formulations, Lagrangian approaches represent the pollutant release as an ensemble of small fluid volumes, called fluid particles, which are tracked individually following a Lagrangian perspective of the flow field (Thomson, 1987). The total emission is discretized into a large number of particles, each carrying a fraction of the total pollutant mass. The particle motion is governed by an acceleration composed of a deterministic component, which is determined from the local flow velocity, and a stochastic component accounting for turbulent fluctuations. Lagrangian approaches generally provide a more realistic representation of turbulent fluxes than first order closure Eulerian formulations. However, they are less suited to problems involving complex chemical reactions or numerous pollutant sources, as the number of particles increases linearly with the number of emission sources, and as chemical reactions require numerous interactions between particles. Representative Lagrangian dispersion models include SPRAY (Tinarelli et al., 2007), FLEXPART (Pisso et al., 2019), NAME (Ryall and Maryon, 1998), and SLAM (Vendel et al., 2011).

Lagrangian dispersion models represent an effective compromise between physical accuracy and computational efficiency, making them particularly suitable for operational applications. However, their performance strongly depends on the numerical approach used to compute the underlying wind and turbulence fields (Tinarelli and Trini Castelli, 2019). For this reason, the present work focuses on Lagrangian dispersion models, which offer high applicative relevance, and compares two methodologies based on different flow computation strategies: a RANS-based approach (SLAM) and a semi-empirical model (PMSS). The objective of this study is to identify the processes specific to each flow-modelling methodology that influence the performance of Lagrangian dispersion models.

6.2 Numerical modelling tools of the wind velocity and turbulence fields

This section presents the numerical tools used in this study to simulate the wind and concentration fields over the idealised industrial site. The two methodologies that were employed and compared have a similar approach to model the concentration field. However, they differ by the methods they rely on to compute the velocity field. We first present the Reynolds Averaged Navier-Stokes (RANS) simulations, which solve the Navier-Stokes equations in their averaged form, in order to reduce the computation time. We then present the semi-empirical approach by SWIFT, which rely on the geometrical definition of the shape of recirculation zones upwind and downwind of the obstacles. Finally, we present the Lagrangian modelling of dispersion, which is common to the two methodologies employed in this work.

6.2.1 Reynolds Averaged Navier-Stokes simulation framework

In principle, the spatial and temporal evolution of the velocity field ($\mathbf{u}(\mathbf{x}, t)$) can be obtained by numerically solving the Navier–Stokes equations, together with the mass conservation equation. For an incompressible flow, the mass conservation equation is expressed as:

$$\nabla \cdot \mathbf{u} = 0, \tag{6.1}$$

while Newton's second law applied to the fluid yields the momentum equation:

$$\rho \frac{\partial \mathbf{u}}{\partial t} + \rho(\mathbf{u} \cdot \nabla)\mathbf{u} = -\nabla p + \rho \mathbf{g} + \mu \Delta \mathbf{u}. \tag{6.2}$$

where p is the pressure, ρ is the density, g is the Earth gravitational acceleration and μ is the dynamic viscosity.

The Reynolds-Averaged Navier–Stokes (RANS) approach simplifies the Navier–Stokes equations (eq.(6.1) and eq.(6.2)) by adopting a statistical approach, providing only the averaged flow field. To apply the averaging operator to the governing equations, it is first necessary to separate the mean and fluctuating components of each variable involved. This concept was introduced by Reynolds (1895) through the Reynolds decomposition, in which any flow quantity A (such as velocity or pressure) is expressed as the sum of a mean component $\overline{A}$ and a fluctuating component A' such that $A = \overline{A} + A'$. By definition, the fluctuating term has a zero mean, i.e. $\overline{A'} = 0$. However, the mean of the product of fluctuating quantities, $\overline{A'B'}$ is not necessarily zero. Substituting this decomposition into the Navier–Stokes equations allows the identification of contributions from both the mean and fluctuating components to the overall flow. After applying the time-averaging operator to the equations, the single fluctuating terms vanish, but the cross-correlations of fluctuations remain, giving rise to additional terms that represent the effects of turbulence on the mean flow. These additional terms lead to the Reynolds-Averaged Navier–Stokes formulation of the continuity equation:

$$\frac{\partial \overline{u_i}}{\partial x_i} = 0 \tag{6.3}$$

and momentum equation:

$$\rho \frac{\partial \overline{u_i}}{\partial t} + \rho \overline{u_j} \frac{\partial \overline{u_i}}{\partial x_j} = -\frac{\partial \overline{p}}{\partial x_i} + \delta_{ij} \rho g_j + \mu \frac{\partial^2 \overline{u_i}}{\partial x_j \partial x_j} + \rho \left(-\frac{\partial \overline{u_i' u_j'}}{\partial x_j} \right) \tag{6.4}$$

in which x_i and u_i are the position and velocity vectors. The last term of eq.(6.4) corresponds to the momentum transfer induced by turbulence and involves the correlations between the fluctuating velocity components, commonly referred to as Reynolds stresses $\tau_{ij} = -\overline{u_i' u_j'}$. While they are essential for capturing the influence of turbulence on the mean flow, they also introduce new unknowns into the system. As a result, the ten unknowns (p, the three components of velocity and the six components of the Reynolds stress) exceed the four equations (the continuity equation and the three components of the momentum equation), leading to what is known as the closure problem. To resolve this issue, various turbulence models have been developed to relate the Reynolds stresses to the mean flow quantities, thereby closing the system of equations. A widely adopted approach to close the RANS equations is the Boussinesq eddy-viscosity hypothesis (Boussinesq, 1897). This assumption postulates that the turbulent Reynolds stresses can be related to the mean velocity gradients in a manner analogous to the molecular viscous stresses in laminar flow. The turbulent fluctuations are thus modelled as an additional, isotropic viscosity term, the turbulent viscosity, denoted by ν_T. Mathematically, this relationship is expressed as:

$$-\overline{u_i'u_j'} = 2\nu_T\overline{S_{ij}} - \frac{2}{3}k\delta_{ij}$$

where the strain rate tensor $\overline{S_{ij}}$ is defined as $\overline{S_{ij}} = \frac{1}{2}\left(\frac{\partial\overline{u_i}}{\partial x_j} + \frac{\partial\overline{u_j}}{\partial x_i}\right)$. However, the kinetic energy k and the turbulent viscosity ν_T are still unknown, and have to be modelled.

To estimate these quantities, two-equation turbulence models are commonly employed. The approach most extensively applied in engineering and atmospheric flow simulations is the $k-\epsilon$ model, which solves transport equations for the turbulent kinetic energy $k = \frac{1}{2}\overline{u_i'u_i'}$ and its dissipation rate ϵ. The $k-\epsilon$ model has become the most commonly used for atmospheric boundary-layer applications due to its robustness, simplicity, and relatively low computational cost. It performs reasonably well in fully developed turbulent flows and under neutral atmospheric conditions. Despite its wide applicability, the standard $k-\epsilon$ model tends to perform less accurately in flows with strong streamline curvature, high strain rates, or strong buoyancy effects, which are frequently encountered in complex atmospheric and urban environments. The turbulent viscosity is expressed from k and ϵ as:

$$\nu_T = C_\mu\frac{k^2}{\epsilon}$$

where C_μ is a constant. The transport equation for k is obtained from the continuity and momentum equations (eq.(6.3) and eq.(6.4)) as:

$$\frac{\partial k}{\partial t} + \overline{u_k}\frac{\partial k}{\partial x_k} = P_k - \frac{\partial}{\partial x_k}(D_{T_k} + D_{P_k} + D_{\mu_k}) - \epsilon$$

with

$P_k = -\overline{u_i'u_k'}\frac{\partial\overline{u_i}}{\partial x_k}$ the kinetic energy production by shear,

$D_{T_k} = \frac{1}{2}\overline{u_i'u_i'u_k'}$ the turbulent diffusion,

$D_{p_k} = \frac{1}{\rho}\overline{p'u_i'}$ the diffusion due to pressure,

$D_{\mu_k} = -\nu\frac{\partial k}{\partial x_k}$ the molecular diffusion, and

$\epsilon = \nu\overline{\left(\frac{\partial u_i'}{\partial x_k}\right)^2}$ the kinetic energy dissipation rate.

This equation is solved modelling the terms:

$$(D_{T_k} + D_{P_k} + D_{\mu_k}) = \frac{-\nu_T}{\sigma_k}\frac{\partial k}{\partial x_k}$$

The dissipation term ϵ is obtained from an empirical transport equation, analogous to that of k, and involving empirical parameters (Pope, 2000):

$$\frac{\partial\epsilon}{\partial t} + \overline{\mu_j}\frac{\partial\epsilon}{\partial x_j} = \frac{\partial}{\partial x_j}\left[\left(\nu + \frac{\nu_T}{\sigma_\epsilon}\right)\frac{\partial\epsilon}{\partial x_j}\right] + C_{1\epsilon}\frac{\epsilon}{k}P_k - C_{2\epsilon}\frac{\epsilon^2}{k}$$

The values of the constants were adjusted to fit to experimental data. The most widely used form was obtained by Jones and Launder (1972) and are $C_\mu = 0.09$, $C_{1\epsilon} = 1.44$, $C_{2\epsilon} = 1.92$, $\sigma_k = 1$ and $\sigma_\epsilon = 1.3$.

This model for the $k - \epsilon$ closure is called the standard $k - \epsilon$ model since several improved formulations have been developed to address its limitations. Notably, the RNG $k - \epsilon$ model shows enhanced performance in rapidly strained and swirling flows, while the realisable $k - \epsilon$ model features improved stability and accuracy in complex shear flows and near-wall regions (ANSYS, 2021).

6.2.2 SWIFT modelling system

The SWIFT model is a diagnostic meteorological pre-processor designed to compute the three-dimensional wind and turbulence fields from meteorological input profiles. It operates at the microscale, with typical horizontal grid resolutions below 10m, making it particularly suitable for applications over domains of several hundred metres, such as industrial sites or urban districts (Oldrini et al., 2017). Unlike computational fluid dynamics approaches that solve the Navier–Stokes equations, SWIFT reconstructs the flow field through an interpolation of the incoming wind, followed by the application of the mass conservation equation. This diagnostic formulation ensures a realistic flow representation while substantially reducing computational cost. The influence of obstacles on the flow is accounted for through semi-empirical parametrisations, which describe the formation of recirculation and wake zones downstream of buildings.

The computation proceeds in two main stages. First, the meteorological input data, which must be representative of the whole domain, are interpolated to initialize the flow field, during which SWIFT defines the recirculation and influence zones associated with each obstacle. In the second stage, the mass conservation constraint is applied to adjust the flow field, enforcing physically consistent boundary conditions such as zero normal fluxes at the ground and domain top. During this step, both horizontal and vertical velocity components are corrected to ensure flow continuity, and impermeability is imposed at building walls and roofs.

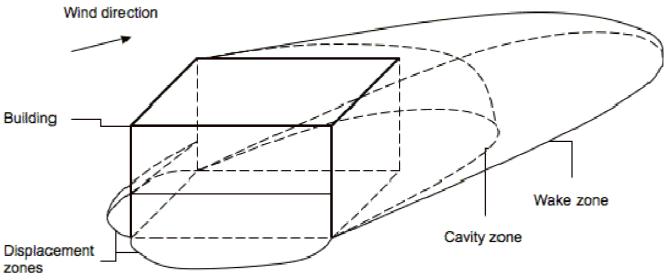

Figure 6.2: Recirculation and influence zones attached to an obstacle. Image extracted from ARIA Technologies (2010).

Recirculation regions surrounding obstacles are defined following (Röckle, 1990; Kaplan and Dinar, 1996) and are classified into three main zones, which are represented on Fig.6.2:

- the displacement zone, upwind of the obstacle, where the wind has no component normal to the building surface;
- the cavity zone, immediately downwind of the obstacle, characterized by a vortex-like recirculating flow;

- the wake zone, where the flow transitions toward the external undisturbed stream

A form of building interaction is implemented when obstacles are closer than a limit distance L_s, therefore producing a skimming zone (Kaplan and Dinar, 1996). In SWIFT, L_s is defined as a function of the height H and the width W of the most upwind of the two buildings as:

$$\begin{aligned} L_s &= 1.25H + 0.15W && \text{if } W < 2H \\ &= 1.55H && \text{otherwise} \end{aligned}$$

In this zone, the flow follows the formulation developed by Hotchkiss and Harlow (1973), which defines the velocity components as a function of the distance to the closest obstacle and the width of the skimming zone.

Several turbulence schemes are available in the SWIFT modelling system. The parametrisations that we used to perform our simulations rely on the interpolation and adjustment of the wind field, the turbulence computation, and the resolution of the equation for momentum conservation. Turbulence has to be parametrised following a framework inspired from RANS equations. The turbulent viscosity is obtained from a closure involving a mixing length, L_m, which is estimated at each position on the site from the distance to the closest surface (the ground or a building wall) L_b. The simplest formulation is $L_m = L_b$, with an arbitrary maximum threshold applied to L_m values, corresponding to the typical maximum eddy size. The turbulent viscosity is then obtained from the mixing length following:

$$\nu_T = L_m^2 \sqrt{2 S_{ij} S_{ij}}$$

with S_{ij} defined as in section 6.2.1. The production rate of turbulent kinetic energy is modelled from the mixing length as:

$$P = 2 \nu_T S_{ij} S_{ij}$$

and dissipation ϵ is obtained by equilibrating the production term $\epsilon = P$. Finally, the turbulent kinetic energy is obtained as in the standard $k - \epsilon$ model as:

$$k \propto \sqrt{\nu_T \epsilon}$$

In this study, we applied the additional equation, ensuring momentum conservation, that is provided by SWIFT in the version 2.2.8 that we used. The Navier-Stokes momentum equation is solved, providing pressure and wind velocity from the turbulence parameters which were estimated from the modelled mixing length.

6.2.3 Lagrangian modelling of dispersion

The Lagrangian stochastic particle modelling approach of dispersion is based on the Lagrangian description of fluid motion, in which individual fluid elements are tracked as they move through the flow field. In this framework, the continuous fluid is discretized into a large number of small fluid volumes, referred to as particles, each representing a fraction of the total mass of the dispersed substance. By following the trajectories of these particles over time, statistical information on their spatial distribution and dispersion characteristics can be derived. The application of the Lagrangian concept to turbulent diffusion was first introduced by Taylor (1921), who established the theoretical foundation for describing the stochastic motion of fluid particles in turbulent flows.

The particle position in the Lagrangian frame is computed from the particle velocity as:

$$dX_i = (\overline{U_i} + U_i')dt$$

where $\overline{U_i}$ is the average flow velocity in the i direction, which is provided by the input flow simulation. The term U_i' corresponds to the particle fluctuating velocity, which is not provided by the input flow field (as it is an ensemble-averaged flow) and has to be modelled from turbulent quantities. It must ensure that the particle motion has the same statistical properties as the background turbulent flow. Specifically, the fluctuations of U_i' are expected to remain correlated over a limited time span, representing the persistence of particle memory before being randomized by the stochastic turbulent noise.

According to Thomson (1987), the variation of the fluctuating velocity, dU_i', can be expressed as:

$$dU_i' = a_i\,dt + b_{ij}dW_j \tag{6.5}$$

where a_i is a deterministic coefficient ensuring consistency with the Eulerian statistics of the turbulent flow (memory term), b_{ij} is a stochastic term (noise), and dW_j is an increment of a Wiener process representing a Gaussian PDF of mean 0 and variance dt (Gardiner, 1985; Revuz and Yor, 1999).

Eq.(6.5) is called the generalised Langevin equation. The terms a_i and b_{ij} have to be determined in order to satisfy the well mixed condition of Thomson (1987), which states that an initially uniform distribution of particles must remain homogeneous at all subsequent times. As a consequence, the term a_i depends on $P(\mathbf{x}, \mathbf{u})$, the joint probability density function of particle position and velocity at time t, which provides the probability of finding a fluid particle in the vicinity of position $\mathbf{x}$ with a velocity near $\mathbf{u}$, at time t. A process following eq.(6.5) can be described from a statistical point of view with the Fokker-Planck equation for $P(\mathbf{x}, \mathbf{u})$ (Kampen, 1992), which reads:

$$\frac{\partial P(\mathbf{x}, \mathbf{u})}{\partial t} = -\frac{\partial}{\partial x_i}(u_i(\mathbf{x}, \mathbf{u})P(\mathbf{x}, \mathbf{u})) - \frac{\partial}{\partial u_i}(a_i(\mathbf{x}, \mathbf{u})P(\mathbf{x}, \mathbf{u})) + \frac{1}{2}\frac{\partial^2}{\partial u_i \partial u_j}(b_{ij}^2 P(\mathbf{x}, \mathbf{u})) \tag{6.6}$$

The term b_{ij} can be derived from the Kolmogorov-Obukov similarity theory as (Thomson and Wilson, 2013):

$$b_{ij} = \sqrt{C_0 \epsilon}\,\delta_{ij}$$

where C_0 is the Kolmogorov constant, which is approximately equal to 4, and δ_{ij} is the Kronecker delta. The well mixed condition imposes that, for a statistically stationary flow, the statistical moments of $P(\mathbf{x}, \mathbf{u})$ correspond to those of the turbulent air motion. Accordingly, $P(\mathbf{x}, \mathbf{u})$ in eq.(6.6) is replaced by the distribution of atmospheric velocities to derive the drift coefficient a_i, thereby ensuring that the stochastic model remains statistically consistent with the underlying Eulerian turbulence field.

Assuming a non-homogeneous Gaussian PDF, and a diagonal steady Reynolds tensor, the drift term a_i of eq.(6.5) can be determined as (Thomson, 1987):

$$a_i = -\frac{C_0 \epsilon}{2}\frac{1}{\sigma_{u_i}^2}U_i' + \frac{1}{2}\frac{\partial \sigma_{u_i}^2}{\partial x_i} + \frac{1}{2}\frac{U_i'}{\sigma_{u_i}^2}\left(\overline{U_j}\frac{\partial \sigma_{u_i}^2}{\partial x_j}\right)$$

It is more common to represent this equation as depending on the Lagrangian timescale $T_L = \int_0^\infty R_{uu}(s)ds$ where $R_{uu}(s) = \frac{\overline{U'(t+s)U'(t)}}{\overline{U'(t)U'(t)}}$ is the Lagrangian auto-correlation function. The latter provides the correlation of Lagrangian velocity fluctuations separated by a time s. As U' perpetuates over a limited time period, strong correlations are expected at short time intervals, while velocity fluctuations should be completely decorrelated at large s. T_L can thus be interpreted as the decorrelation time of the particle fluctuating velocity, meaning the characteristic time of its motion memory.

Assuming R_{uu} follows a decreasing exponential form $R_{uu}(s) = \exp(-s/T_{L_i}) \simeq 1 - s/T_{L_i}$ for $s/T_{L_i} << 1$, the Lagrangian structure function, defined as $D_L(s) = 2\sigma^2_{u_i}(1 - R_{uu}(s))$ (Pope, 2000), can be written as:

$$D_L(s) = \frac{2\sigma^2_{u_i} s}{T_{L_i}}$$

From the Kolmogorov hypothesis (Kolmogorov, 1941), $D_L(s)$ can also be approximated as:

$$D_L(s) \simeq C_0 \epsilon s$$

with $C_0 \simeq 4$ the Kolmogorov constant (Wilson and Sawford, 1996) and ϵ the dissipation rate of turbulent kinetic energy. Therefore, the Lagrangian time scale writes (Tennekes, 1982):

$$T_{L_i} = \frac{2\sigma^2_{ui}}{C_0 \epsilon}$$

In the case of isotropic turbulence, eq.(6.5) becomes the classical Langevin equation (Langevin, 1908):

$$dU'_i = -\frac{1}{T_L} U'_i \, dt + \sigma_u \sqrt{\frac{2}{T_L}} dW_i$$

After advection, particles interact with solid boundaries such as the ground or building walls, where they undergo reflection. In the simplest approximation, this reflection is treated as specular, meaning that particles are reflected with an angle symmetric to the normal of the surface. Situations in which the turbulence tensor is non-diagonal close to the wall require a non-specular turbulence scheme (Soulhac et al., 2025).

The concentration within each grid cell is computed from the number of particles contained inside its volume (Luhar and Rao, 1994). Specifically, the masses of all particles located inside a cell are summed and divided by the cell volume to obtain its concentration. Although this approach is computationally efficient, it is very sensitive to the size of the cells (Haan, 1999). Consequently, a large number of particles is required to reduce uncertainties (Borgas and Sawford, 1994), which in turn increases the computational cost of the simulations. In this work, we performed simulations involving approximately 500000 particles as a compromise between a sufficient accuracy and a reasonable computation time.

6.2.4 Differences between the two approaches

The formulation of the pollutant dispersion is essentially the same in both models, relying on the solution of the Langevin equation and adopting the well-established well-mixing condition (Thomson, 1987) in order to determine the coefficients of the drift and diffusion terms. The differences between the two approaches lie in the simulated flow field.

In the SLAM methodology, a database of RANS simulations is created beforehand with ANSYS Fluent. The incoming flow direction is varied every 20° and seven atmospheric stability conditions are considered: one neutral, three stable and three unstable cases. Dimensionless velocity and turbulence fields are obtained from the reference velocity, in order to allow the rescaling of the flow field for any input velocity. Once the exact meteorological conditions of the applicative case are known, pre-computed simulations from the database are interpolated to conform to the actual wind direction and Monin-Obukov length. In this work, two main wind direction and only one stability condition, namely a neutral case, were investigated. The 40° wind direction simulation is provided inside the database for all site geometrical configurations (which were presented in section 2.2.2). In contrast, the 130° wind direction is not directly simulated by solving the RANS equations. The flow field under neutral stratification for this direction is estimated through interpolation between the simulations performed for the 120° and the 140° wind directions. To optimise the computational cost, all particles involved in the simulation are emitted at the first time step, and their successive contributions to each of the traversed cells is recorded over the whole simulation. This methodology was chosen as it is a good compromise between modelling accuracy and operational efficiency. Contrary to LES and DNS, RANS simulations have a limited computation time, which is further optimised by the beforehand computation of the entire database needed by SLAM. However, this approach relies on the computation of the average field, which does not enable the modelling of the instantaneous flow behaviour, notably intermittent phenomena. The questions which are raised in this work concerning this methodology are therefore: "How accurate are the flow and concentration fields obtained with SLAM when the flow field is provided by a database of RANS simulations?", "Which modelling features most strongly impact the simulation accuracy?" and "Are the effects of the site geometry captured by this modelling methodology?".

PMSS simulations are based on a distinct modelling framework, since the (averaged) flow is computed with the semi-empirical approach detailed in section 6.2.2. The Lagrangian dispersion model SPRAY uses the wind field computed by SWIFT as input and derives the Lagrangian time scales from externally provided turbulence parameters. Particles are released at each time step, and their concentrations are periodically recorded and subsequently averaged over the entire simulation period. This methodology strongly differs from SLAM, as it relies on the semi-empirical formulation of the flow field rather than on solving the Navier-Stokes equations. Although the PMSS approach offers significant advantages in terms of computational cost and turnaround time, it may not fully capture the entire complexity of the flow, particularly in geometrically complex environments. The present study therefore aims to assess whether the principal characteristics of flow and dispersion are accurately reproduced by the PMSS methodology on the fictitious site, with particular emphasis on the influence of site geometry. In addition, the impact of potential modelling inaccuracies in the near field on plume evolution and characteristics up to the far field is analysed.

In both methodologies, the resulting concentration fields are smoothed using similar procedures to mitigate numerical spatial inhomogeneities arising from variations in particle density between neighbouring cells.

Dimensionless quantities representative of the flow field are obtained by considering a reference velocity $U_{\text{ref}} = \|\vec{u}(h_{\text{ref}})\|$ at the reference height $h_{ref} = 0.0625\,\delta_{BL}$, which corresponds to the characteristic size of the buildings forming the site. Concentration was rendered dimensionless by the following procedure:

$$C^* = \frac{C\,U_{\text{ref}}\,h_{\text{ref}}^2}{Q}$$

where Q is the ethane mass flow rate at the source. For all maps presented in chapter 7 and chapter 8, the minimum and maximum of the colour scale were chosen as the minimum and maximum values of the experiment.

6.3 Input boundary layer characteristics

As the input meteorological profiles provided to the models were adapted to each methodology, we present in Fig.6.3 the differences between the input boundary layer flows. While SWIFT takes as input the wind tunnel measurements, the database of RANS simulations was produced considering a logarithmic profile. This choice enables the fast generation of a realistic boundary layer from rare meteorological measurements, which is necessary in operational frameworks. The logarithmic profile is scaled to correspond to the wind tunnel measurements on the lowest part of the profile.

Since the wind tunnel measurements follow a logarithmic law only near the ground, the RANS profile agrees with the experiment only in its lower portion, near the reference height h_{ref}. However, this limitation does not affect the present study, as the focus is on the wind field within the industrial site, below the height where the two profiles begin to diverge.

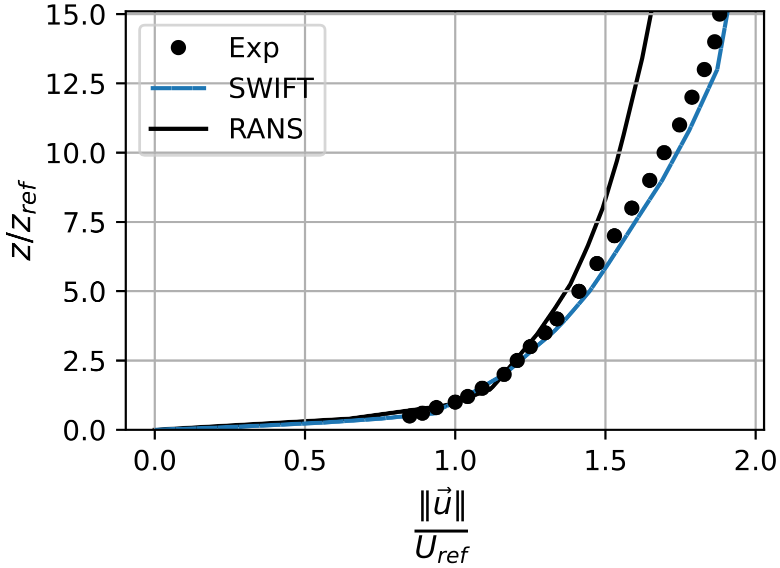

Figure 6.3: Boundary layer profiles in input of the simulations, and wind tunnel profile.

Chapter 7

Inter-comparison of the experimental and simulated velocity fields

This chapter presents the results of numerical simulations of the velocity field of the site. The considered configurations are the same as the configurations that were studied in wind tunnel in Part I. Simulations were performed with the two models, PMSS and SLAM, in order to compare the results of the two modelling approaches to the experiment. While SLAM is based on a database of RANS simulations of the flow field, PMSS relies on the semi-empirical definition of recirculation zones. Each model establishes a different compromise between computational efficiency and flow simulation accuracy. The main points which are analysed here are "How accurate is the velocity field predicted by both approaches?", "Do the models capture the effects of built elements on the wind field inside the site?" and "What are the numerical parameters that affect the most the resulting wind field?".

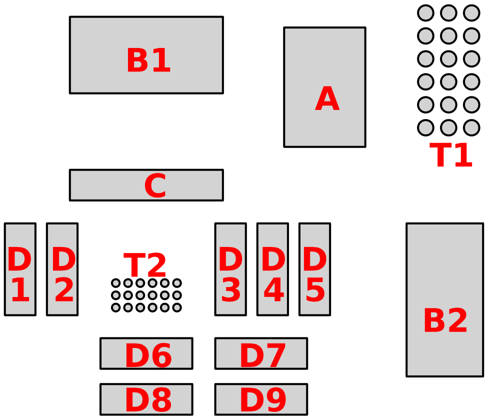

Figure 7.1: Identification of buildings forming the site.

For convenience, we denominate the buildings from the tallest to the smallest, as indicated in Fig.7.1: building A is alternatively replaced by its two porous versions, B1 and B2 are the big parallelepipeds, C is the long rectangular obstacle and D1 to D9 form the group of smaller buildings (from left to right). Finally, T1 and T2 correspond to the biggest and the smallest groups of tanks, respectively.

7.1 'Solid' configuration with a $130°$ incoming wind direction

In Figure 7.2, we present the comparison of the velocity field measured with LDA in the wind tunnel (see Fig.7.2a) to the RANS (see Fig.7.2b) and the SWIFT simulated wind field (see Fig.7.2c). In a second time, we compare transversal horizontal and vertical profiles of velocity which positions are indicated on Fig.7.2a.

Figure 7.2b presents the wind field of the 130° configuration as simulated by the interpolated RANS computations. Note that the 130° incident wind direction case was not directly simulated, thus the wind field is obtained by interpolating the simulations with a 120° and a 140° wind direction. The presence of obstacles substantially decreases the norm of velocity over the whole site, particularly at $z^* = 0.26$. The simulation produced extended recirculation zones identified by the strong decrease of velocity and abrupt changes in wind direction. Notably, the wake of the B2 building is large enough to reach the D5 building in the simulation, which is associated to a greater decrease of the wind velocity norm than in the experiment. Downwind of the site, the strong flow perturbation observed in the experiment is accurately reproduced by the RANS interpolated wind field. Globally, recirculation zones and channelling effects, such as between buildings B1 and C, qualitatively reproduce those observed in the experiment (see Fig.7.2a).

The wind field simulated with SWIFT is presented in Fig.7.2c. In contrast to Fig.7.2b, recirculation zones are narrower and are delimitated by steep spatial variations of the norm of velocity. The model agreement with the experiment (see Fig.7.2a) is not homogeneous over the site. Individual wake shape and intensities associated to buildings D1, D3, B2 and the tanks resemble the experiment, even though the wake extent is generally underestimated (see for example the top left corner of building B2 at $z^* = 0.26$). For the rest of the site, the main source of inaccuracy in the SWIFT simulation is the lack of interaction between obstacles, which misses effects such as wake deviation and flow channelling. The integration of the Hotchkiss and Harlow (1973) scheme describes the flow inside the recirculation zones, however, the presence of a neighbouring building does not fundamentally displace the recirculation zones or deviates the flow. This is particularly visible downwind of the site: the velocity decrease is overestimated inside the narrow recirculation zones produced by the buildings A and B1, while the flow downwind of the group of D buildings is unperturbed and reproduces the incoming boundary layer flow. Additionally, the recirculation zone produced by building A is not impacted by the presence of building B1 in the SWIFT simulation, whereas in the experiment it is displaced towards negative y^* values. This is due to the interpolation of the meteorological wind profile which is then affected by obstacles only inside the perimeter of the geometrically-defined recirculation zones. Outside these regions, the incoming boundary layer flow is reproduced identically and adapted to ensure mass and momentum conservation.

The simplified form of interaction between neighbouring obstacles, which is implemented inside the skimming zones, however breaks the wake of building A at $z^* = 0.26$ (see Fig.7.2c) to reproduce the flow observed experimentally between buildings A and B1 at this height. Nevertheless, it produces an artificial square region of increased velocity inside this same zone at $z^* = 0.78$, which does not correspond to the experimental observations. Since the layer $z^* = 0.78$ cuts buildings B1 and B2 at their last cell in height (hence the absence of visible wakes on Fig.7.2c at $z^* = 0.78$), the interaction between the obstacles A and B1 is not considered in the same way as on the layer $z^* = 0.26$. Experimental evidence of such change of wind direction at this height is visible on Fig.7.2a, but the SWIFT simulation overestimates this effect and its extent.

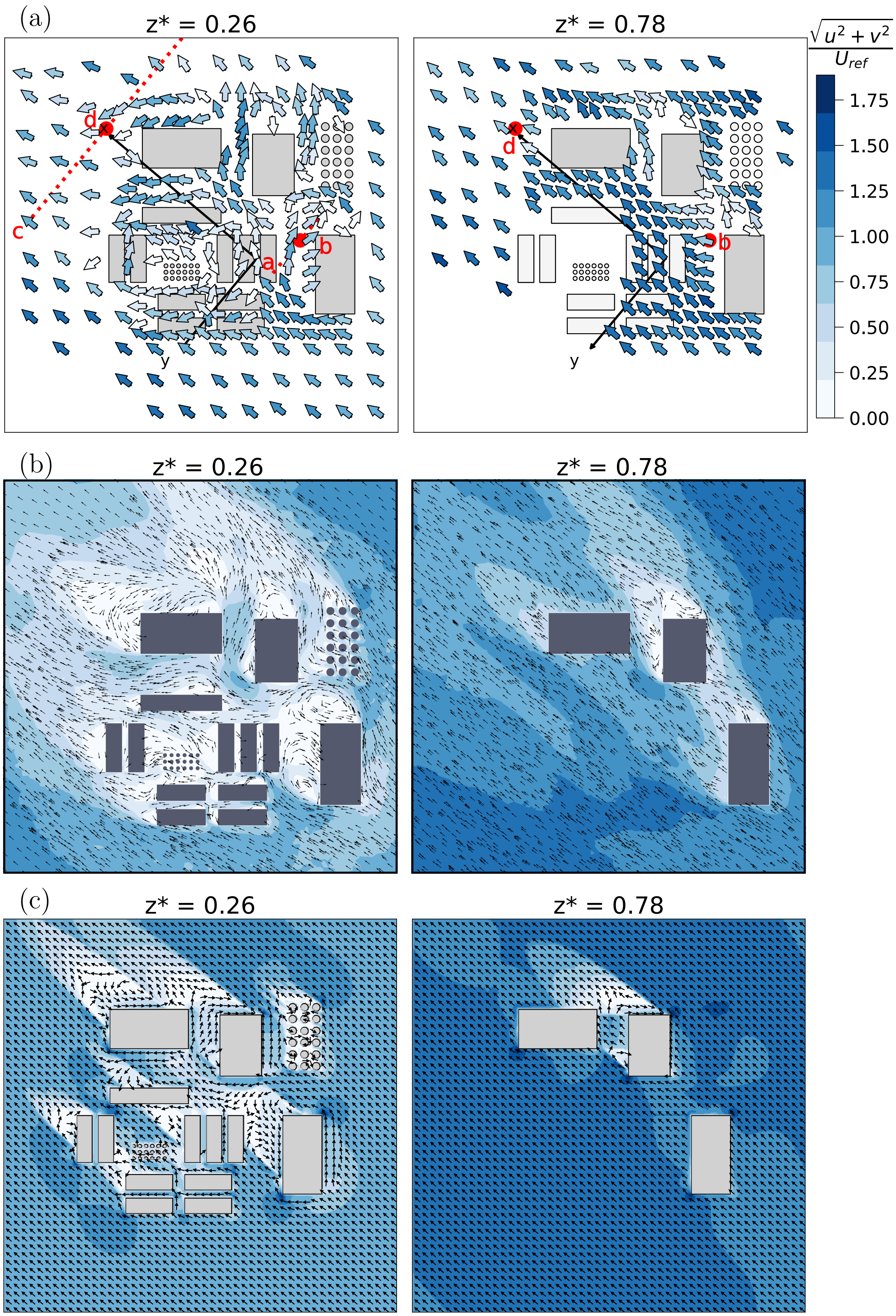

Figure 7.2: Dimensionless velocity field in the 130° incoming wind direction configuration at two heights for **a**: experimental data. **b**: interpolation of the RANS simulations with a 120° and with a 140° incident wind direction. Background colours indicate the norm of velocity while arrows show wind direction. **c**: SWIFT simulations with the same symbology as b. The layer $z^* = 0.78$ coincides with the roof of buildings B1 and B2, which are discretised in the uppermost vertical grid cells of these buildings. This explains the absence of recirculation zones at this height for these two obstacles. Red lines and dots indicate the positions of the horizontal (a and c) and vertical (b and d) profiles of velocity shown on Fig.7.3.

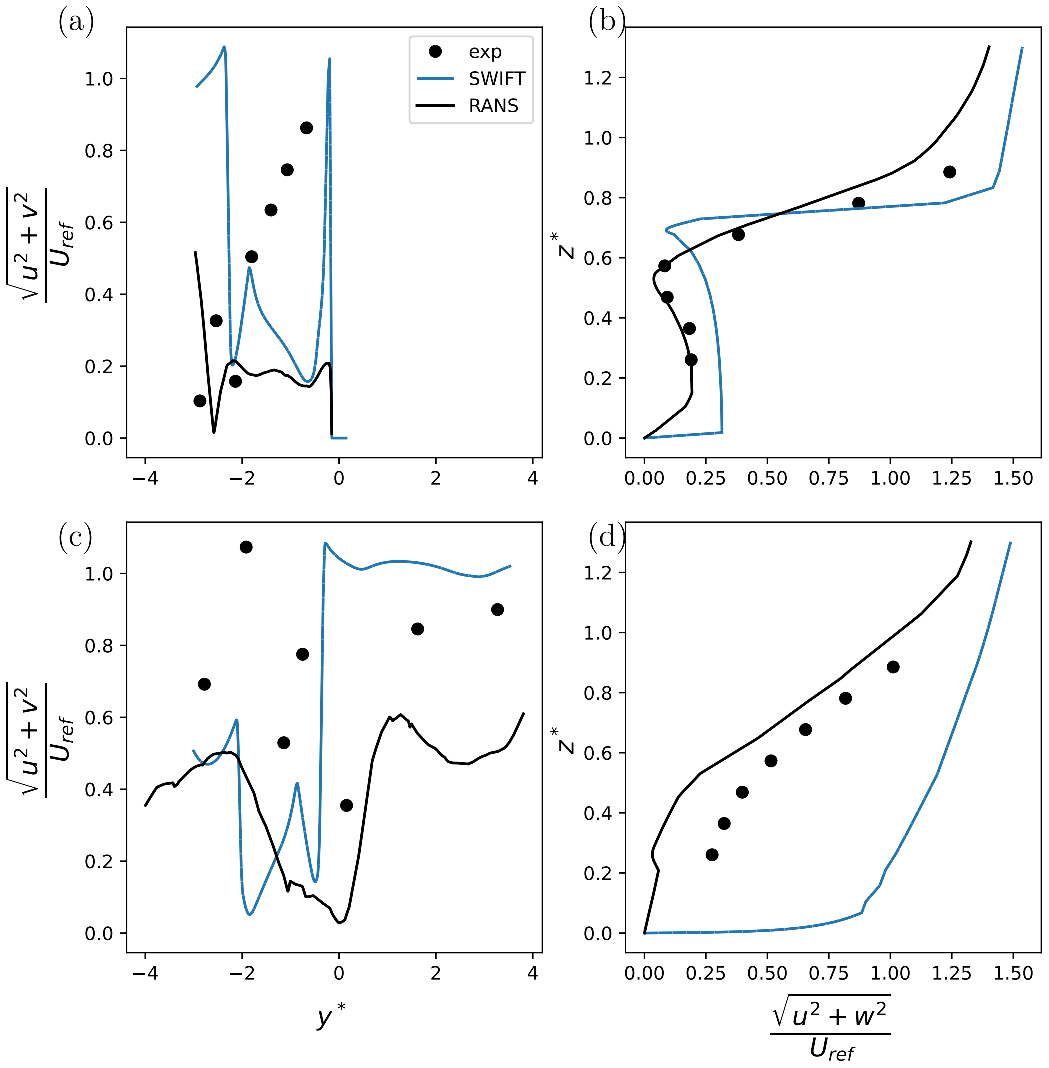

Figure 7.3: Norm of velocity along the profiles shown in Fig.7.2. **a**: horizontal (at $z^* = 0.26$) and **b**: vertical profiles inside the wake of the bottom right building. **c**: horizontal (at $z^* = 0.26$) and **d**: vertical profiles downwind of the site. This corresponds to the viewpoint of someone facing the wind.

Despite these discrepancies, the wind velocity field presented in Fig.7.2c evidences the perturbative effect of obstacles associated to large recirculation zones and strong variations of wind direction.

Profiles inside the wake of building B2, and downwind of the site, are shown in Fig.7.3a and b, and Fig.7.3c and d, respectively. The left panels (a and c) correspond to horizontal profiles, while the right panels (b and d) present vertical profiles whose positions are indicated by red dots on Fig.7.2a. Grid measurement points closest to the lines were taken for horizontal profiles.

Both models underestimate the velocity norm inside the wake of building B2 (see Fig.7.3a), but for different reasons. The RANS simulation globally underestimates the velocity due to the overestimation of the wake width of building B2. On the contrary, in the SWIFT simulation the wake is shifted to the left side of the obstacle due to the absence of the experimentally-observed blocking effect of the D5 building. This is visible in Fig.7.3a as a shift of the SWIFT profile towards positive y^* values. However vertical profiles of velocity inside the wake of this same obstacle (see

Fig.7.3b) are very accurate for both models. Agreement with the experiment is even better for the RANS and the SWIFT results below and over $z^* = 0.6$, respectively.

Downwind of the site (see Fig.7.3c), horizontal profiles of velocity are underestimated by the RANS simulation for the same reason as for Fig.7.3a. However, the profile shape globally resembles that of the experiment. SWIFT locally underestimates the velocity norm due to the shifted wake of building A. The vertical velocity profile downwind of the site (see Fig.7.3d) obtained from RANS reproduces the experimental shape, despite an offset in the velocity values, contrary to the SWIFT result. This is a consequence of the shape of the wake of building B1 being modified by the impact of upwind obstacles forming the site. As a result, the vertical profile reflects decreased velocity in the experiment and the RANS result, while it is located outside the wake of building B1 in the SWIFT simulation, and therefore reproduces the interpolated boundary layer flow.

7.2 ‘Solid’ configuration with a $40°$ incoming wind direction

We now analyse the configuration with a 40° incoming wind direction and the ‘solid’ shape of the upwind obstacle (A), meaning a filled parallelepiped.

Fig.7.4a presents the experimental velocity field, while Fig.7.4b and c show the simulations obtained from RANS and SWIFT, respectively. Since the 40° wind direction was included directly inside the database of RANS simulations, there was no need to interpolate simulations from adjacent incoming wind directions. Comparison of Fig.7.4a and b indicates that the RANS simulation accurately captures the downwind effects of the tallest obstacles (A, B1 and B2) which are placed upwind of the site in this configuration. Notably, the velocity decrease downwind of these obstacles at $z^* = 0.78$ is reproduced until the bottom of the image, despite local underestimations of velocity downwind of the obstacles. However, the predicted flow field on the left edge of the A obstacle does not agree with the experiment, since the RANS simulation predicts a recirculation zone whereas the experiment shows a straight flow following an axis parallel to the building walls. Even though experimental velocity measurements do not reach the edge of the building and may therefore fail to capture a narrow recirculation zone close to the building edge, the analysis of concentration measurements in chapter 8 demonstrate no counter-current pollutant transport in this region. We can thus consider that the few velocity measurements between buildings B1 and A are representative of the global behaviour in this region, which does not correspond to the prediction of RANS simulations.

Several hypotheses could be suggested to explain this discrepancy. First, the RANS methodology models the turbulence instead of resolving all spatio-temporal scales of the flow field, which implies making assumptions that may not correspond to reality, especially inside dense built geometries such as the one investigated in this work. The very complex flow field that develops inside the site includes multiple recirculation zones and intricate interacting behaviours, that represent a challenge for all types of flow modelling methodologies, including the RANS approach. Local inaccuracies are therefore inevitable and inherent to all operational approaches, which seek a compromise between computational efficiency and result accuracy.

Second, the grid size in this region is limited to approximately 20 grid cells between the buildings A and B1. Although this number fulfils the recommendations of Franke and Britter (2011), it should be increased by 50% to effectively resolve the recirculation zone detaching from the top left corner of building A that is observed on Fig.7.4a. Larger grid cells tend to broaden the localised recirculation, which could lead to an extension of the recirculation zone along the entire left wall of the obstacle.

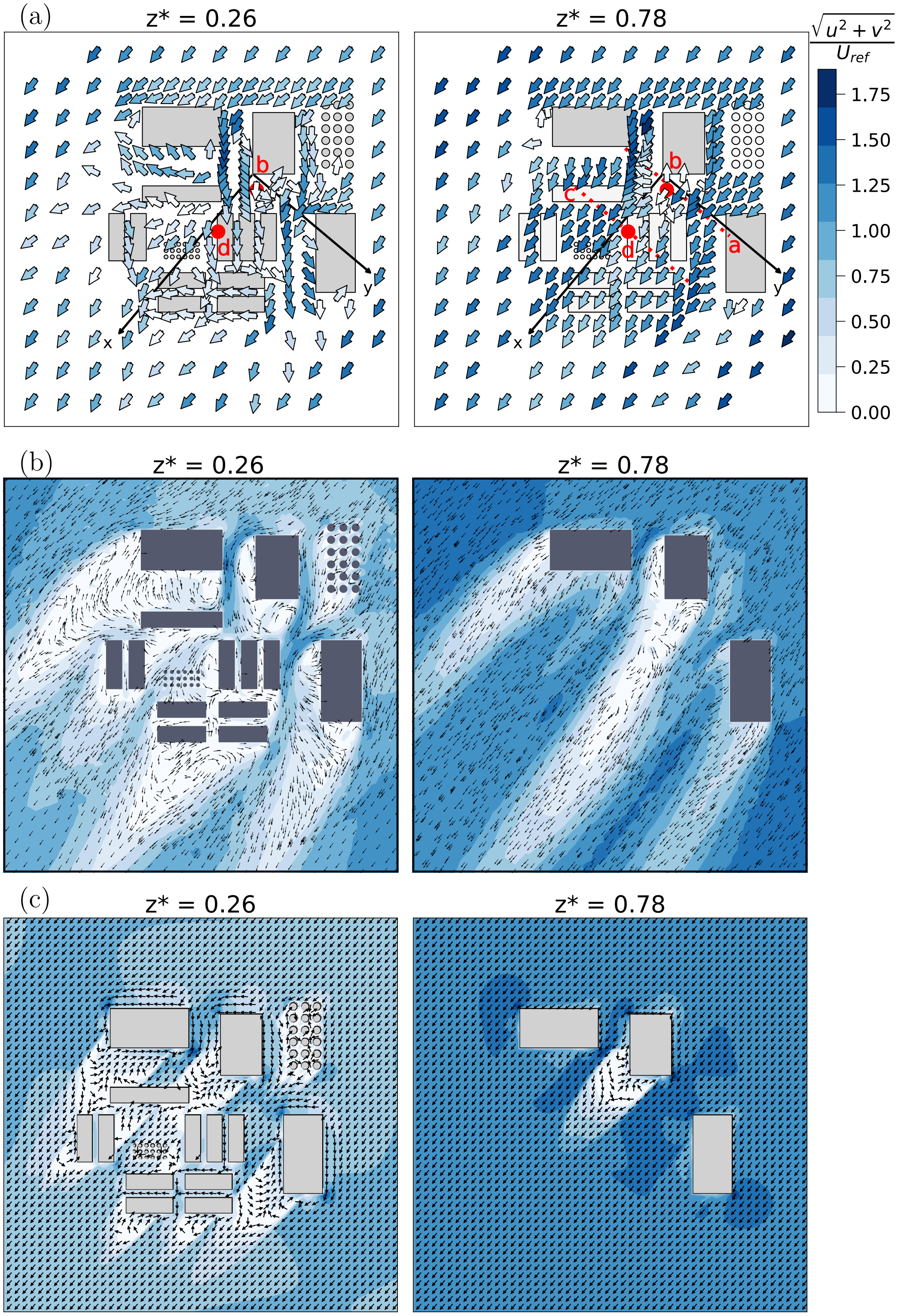

Figure 7.4: Dimensionless velocity field for the 40° 'solid' configuration at two heights for **a**: experimental data, **b**: RANS and **c**: SWIFT simulations. Red lines and dots locate horizontal and vertical profiles of Fig.7.5.

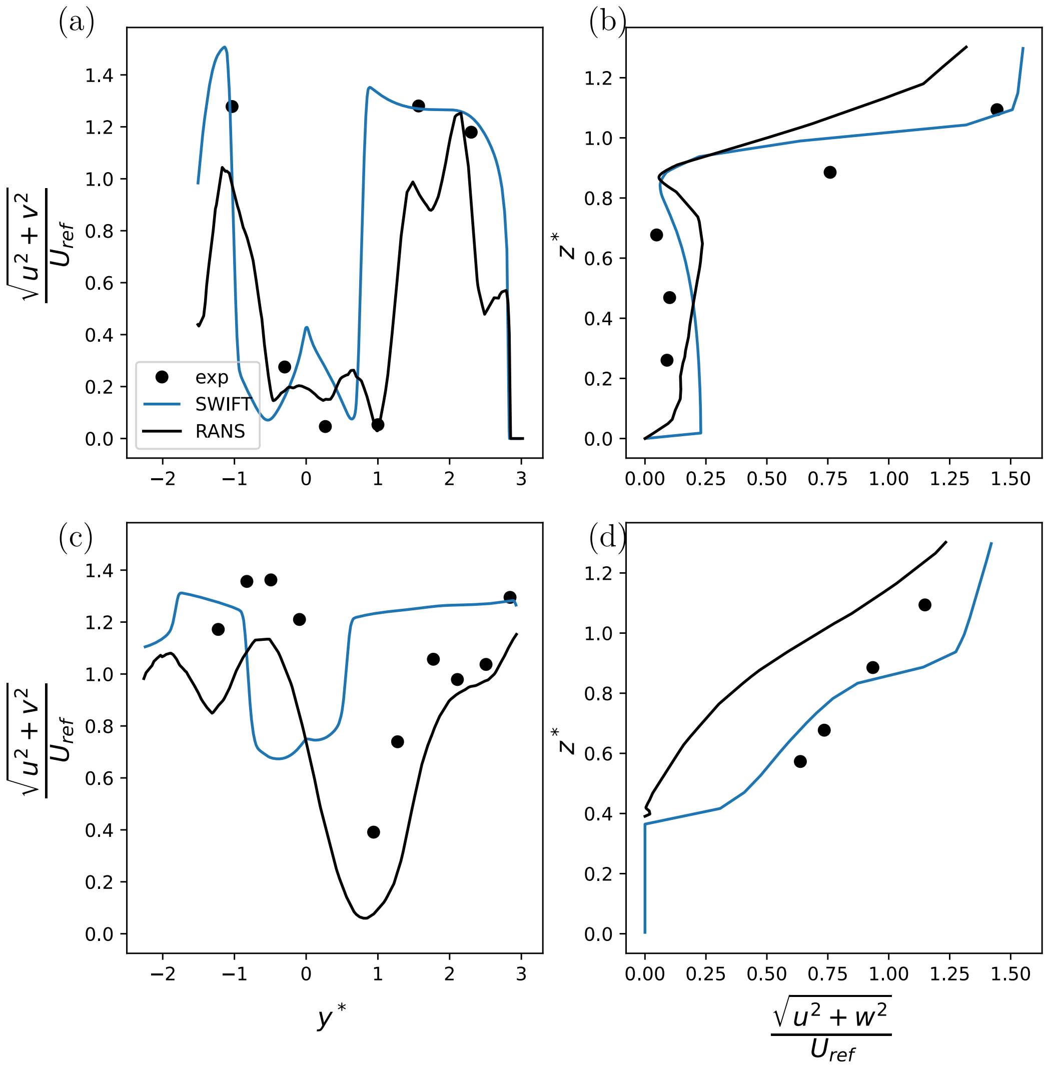

Figure 7.5: Norm of velocity along the profiles shown in Fig.7.4. **a**: Horizontal (at $z^* = 0.78$) and **b**: vertical profiles inside the wake of the upwind building. **c**: Horizontal (at $z^* = 0.78$) and **d**: vertical profiles over the group of small buildings.

Third, the incident wind direction may not be perfectly identical between the simulation and the experiment, as the wind tunnel boundary layer axis tend to slightly deviate from the centre line of the test section (Nironi, 2013). However, we observed no noticeable drift of the incident wind direction between the simulation and the experiment upwind and downwind of the site.

Finally, this discrepancy could be a consequence of the boundary conditions implementation, notably the wall roughness. Its effects on the extent of attached recirculation zones was demonstrated by Michálek et al. (2022) for circular cylinders in wind tunnel. Increased surface roughness decelerates the flow in the immediate vicinity of the wall, eventually leading to a wider and shorter recirculation zone. An inaccurate wall roughness could thus generate the excessively long recirculation zone predicted by the RANS simulation along the left edge of the building.

The SWIFT velocity field, shown in Fig.7.4c, provides less realistic recirculation zones downstream of buildings A, B1 and B2 due to the lack of interaction between each other and with the group of buildings D. However, the wake of building A has a lower extent towards the top of the image, which is closer to the experiment, and a reasonably accurate shape at $z^* = 0.78$. Downwind of the whole site, the SWIFT velocity norm does not decrease as much as in the experiment, due to the spatially restricted effect of each individual obstacle.

The velocity decrease inside the recirculation zone of building A is globally captured by both models as shown on Fig.7.5 on the horizontal (a) and vertical (b) profiles close to the obstacle. Discrepancies observed on Fig.7.5a at the edges of the wake arise from two different processes. The RANS profile slightly underestimates velocity values around $y^* = -1$ because the simulated recirculation zone extends further to the left of building A than that observed experimentally. However, the global shape of the recirculation zone is accurately captured by the simulation over most of the profile. On the other hand, the region around $y^* = 1$, which is inside the experimental wake, lies beyond the geometrically defined limits of the recirculation zone generated by SWIFT, leading to an overestimation of velocity.

Over the horizontal profile in the middle of the site (see Fig.7.5c), the RANS simulation reproduces the wake of the upwind building more accurately than SWIFT. Even though values of the norm of velocity are constantly lower than the experiment, the global profile shape reproduces the experimental data. In contrast, the velocity depletion, that is characteristic of the wake of building A, is shifted along negative y^* values in the SWIFT simulation. Additionally, the velocity decrease is underestimated due to the limited extension of the influence zone downwind of the A building. However, the vertical velocity profiles in this region (see Fig.7.5d) evidence a better fit with the experiment for the SWIFT simulation. In this configuration, the lateral deviation of obstacles wakes due to neighbouring buildings is not captured by SWIFT, contrary to the global vertical behaviour of the flow field. In the far field, downwind of the whole site, the velocity decrease generated by the A building is still visible experimentally (Fig.7.4a) and in the RANS simulation (Fig.7.4b) while it completely disappears from the SWIFT output (Fig.7.4c).

7.3 ‘Dense’ configuration with a 40° incoming wind direction

In the ‘dense’ configuration, the upwind building (A) is replaced by a group of densely packed columns that form a porous obstacle. Since measurements were performed inside the wake of the A building only, we first focus on the simulated wind field over the whole site and compare it to the ‘solid’ case. We then compare simulations to the experiment inside the building wake.

In Fig.7.6a, the shape of the wake of the upwind building is larger than the wake in the ‘solid’ case (see Fig.7.4). The recirculation zone is slightly shifted to the left of the building. Contrary to the RANS simulation, SWIFT (see Fig.7.6b) generates almost no wake for this case. Each column generates an individual recirculation zone, but they do not interact between each other to produce the global effect that is predicted by the RANS simulations.

Further downstream, the two models show completely different behaviours in the open space between the D grouped buildings. The RANS simulation predicts a recirculation zone with low velocities, while SWIFT generates a straight and intense wind. The high intensity flow produced by SWIFT in this open space does not seem realistic, as it is a consequence of the underestimated wake of the upwind building and the lack of interactions between the recirculation zones of the D buildings. As a result, the norm of velocity is globally larger over the whole site in the SWIFT simulation (see Fig.7.6b) than in the RANS prediction (see Fig.7.6a).

We focus on the wake of the A building to compare model outputs with the experiment (see Fig.7.7. The recirculation zone from RANS (see Fig.7.7b) is more realistic even though velocity is underestimated over the whole zone. The SWIFT wind field (see Fig.7.7c) shows small individual wakes, one per single column, that do not interact between each other and thus generate no global recirculation in this region.

The horizontal profile shown in Fig.7.8 evidences this difference: the velocity norm decreases as in the experiment in the SWIFT simulation, but only inside the wake of the closest column. Velocity is overestimated over the rest of the profile. The RANS simulation, on the contrary, provides accurate results over the whole profile. We highlight however that the spatial resolution of the experimental measurements is low in this region, which does not enable a complete description of the velocity profile in this region.

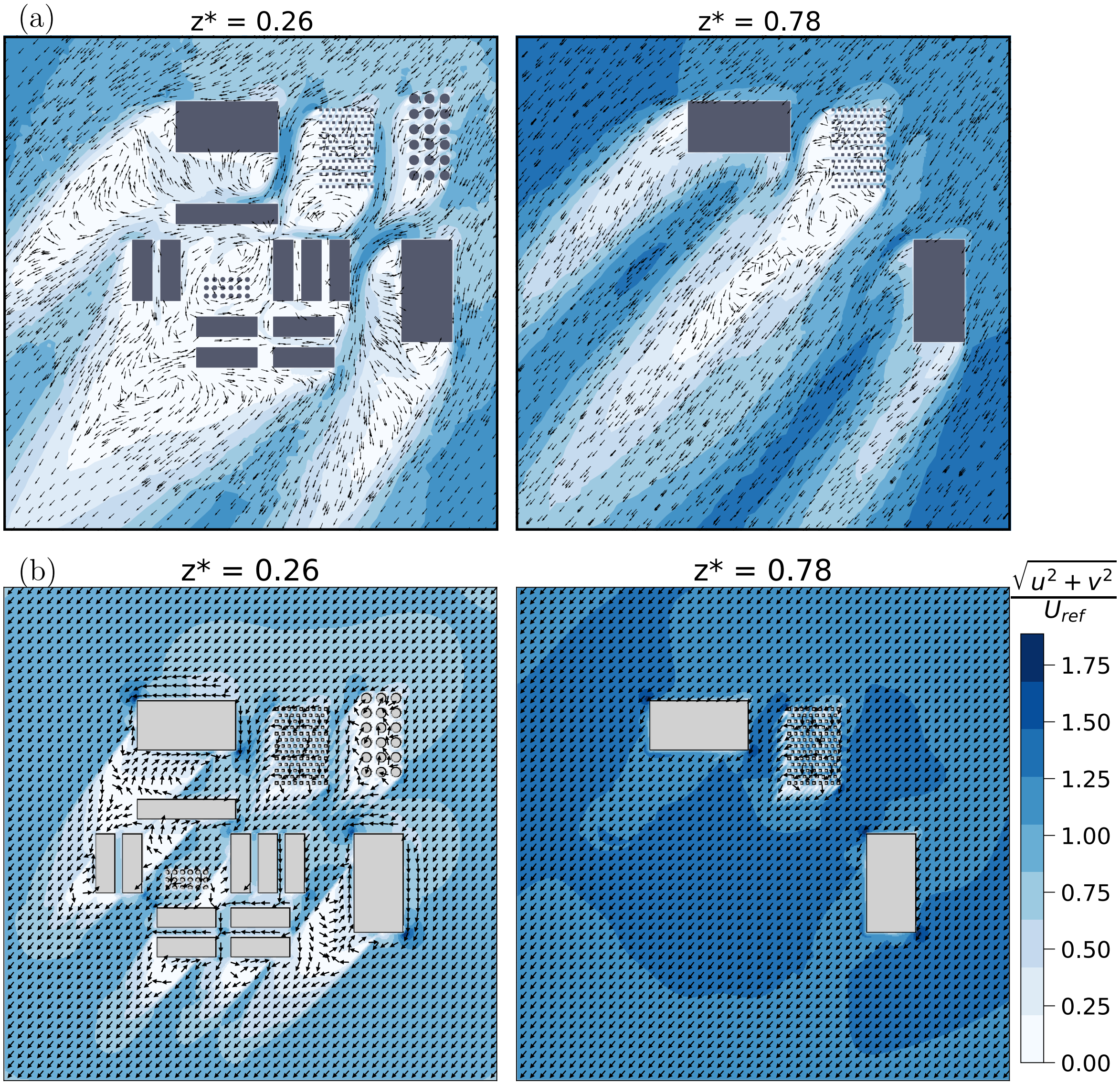

Figure 7.6: Dimensionless velocity field for the 40° ‘dense’ configuration at two heights for **a**: RANS and **b**: SWIFT simulations.

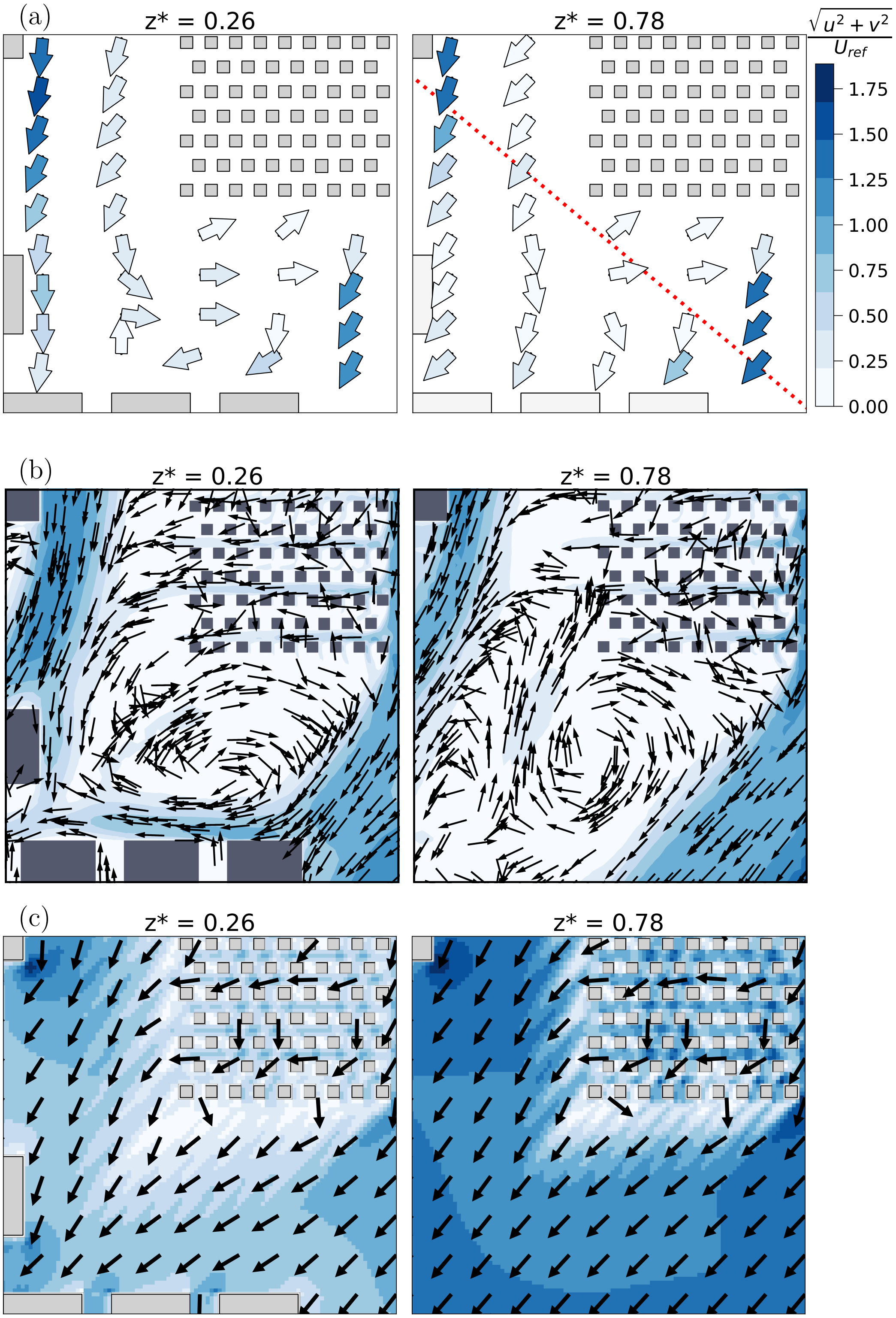

Figure 7.7: Dimensionless velocity fields from **a**: experiment, **b**: RANS and **c**: SWIFT, for the 40° ‘dense’ configuration at two heights, zoomed over the recirculation zone of the porous obstacle.

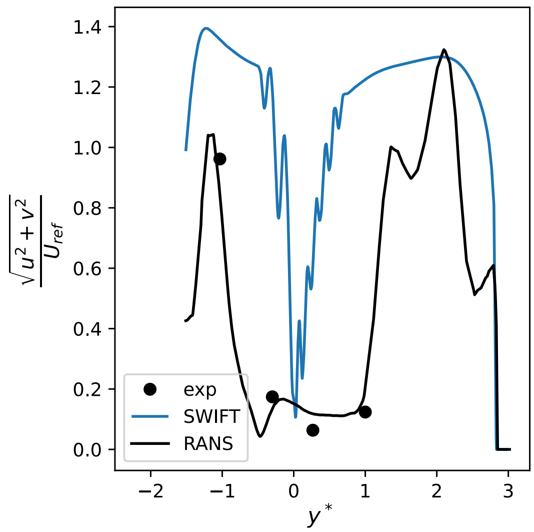

Figure 7.8: Norm of velocity along the profile shown in Fig.7.7 (at $z^* = 0.78$).

As SWIFT is based on a mass-consistent approach, the equations account for wind deviation and acceleration; however, they do not incorporate the drag effects induced by multiple obstacles. As a consequence, the flow deceleration induced by the whole group of columns is not accounted for by the model, which results in the formation of individual wakes for each element of the porous obstacle, as observed in Fig.7.7.

7.4 'Spaced' configuration with a $40°$ incoming wind direction

In the 'spaced' configuration, the upwind building is formed of separated columns that have a much lower impact on the flow field. The RANS simulation, shown in Fig.7.9a, evidences a drastic reduction of the wake of the upwind building, which is however still associated to a strong decrease of the norm of velocity downstream of the obstacle. In contrast, SWIFT generates thin individual wakes that do not interact between each other and that have a very low decreasing effect on velocity. Downstream, Fig.7.9a show the same strong recirculating behaviour that was predicted inside the open space surrounding the small tanks in Fig.7.6a. This recirculating region does not exist in the SWIFT simulation (see Fig.7.9b) as was predicted for the 'dense' case in Fig.7.6b.

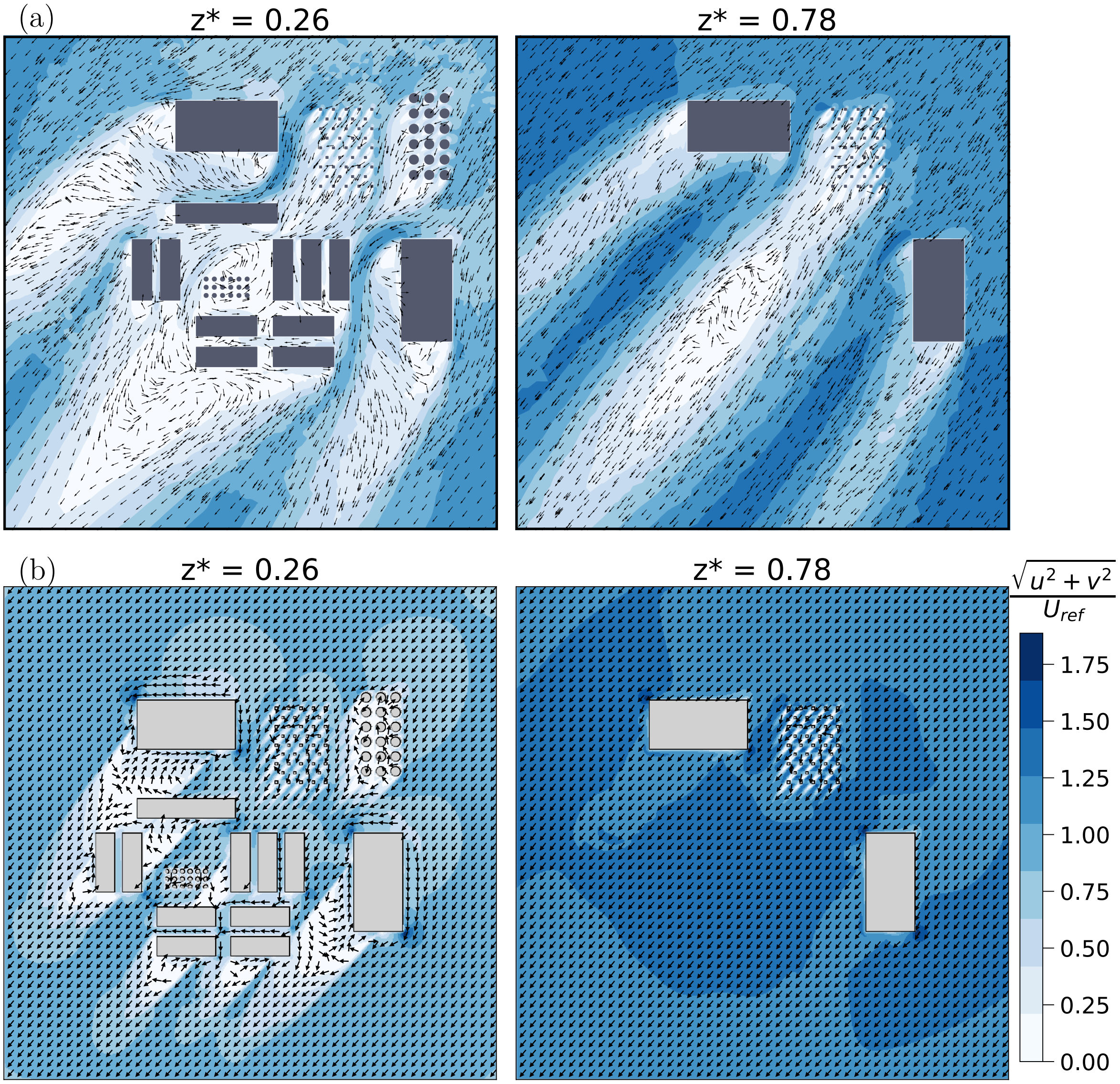

Figure 7.9: Dimensionless velocity field for the 40° ‘spaced’ configuration at two heights for **a**: RANS and **b**: SWIFT simulations.

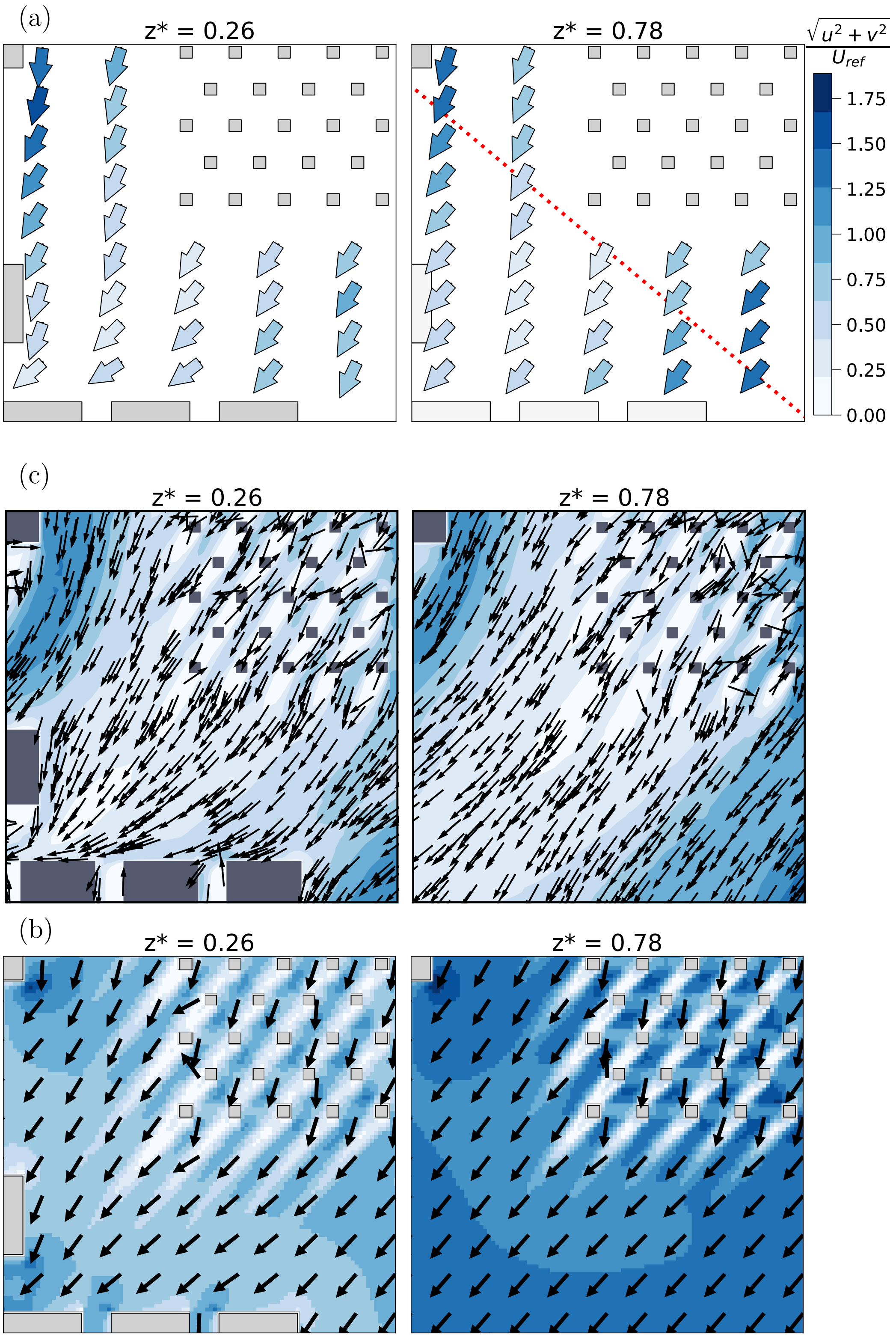

Figure 7.10: Dimensionless velocity fields from **a**: experiment, **b**: RANS and **c**: SWIFT, for the 40° 'spaced' configuration at two heights, zoomed over the recirculation zone of the porous obstacle.

Figure 7.10 enables a more detailed analysis of the region downwind of the A obstacle. Columns have almost no recirculating effect on the flow, but they generate a small decrease in wind velocity that is underestimated by the SWIFT simulation, but slightly overestimated by the RANS velocity field. This observation is confirmed by the horizontal profile on Fig.7.11.

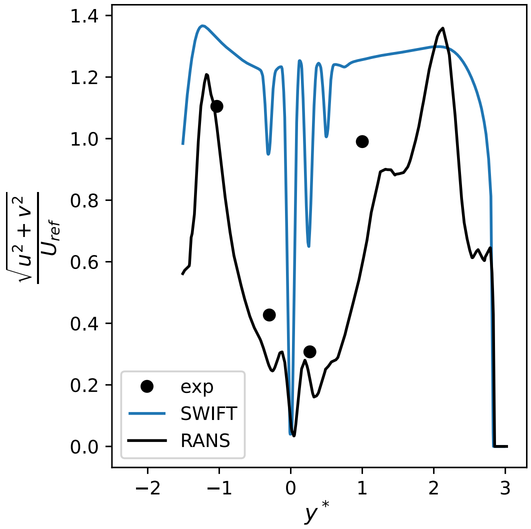

Figure 7.11: Norm of velocity along the profile shown in Fig.7.10 (at $z^* = 0.78$).

7.5 Effect of grid size on PMSS simulations

The accuracy of flow and turbulence simulations is highly dependent on the grid used to discretize the computational domain (Franke and Britter, 2011). The spatial resolution must be sufficiently fine to capture small-scale flow effects, such as secondary recirculating regions, since the grid size affects the prediction of flow separation and reattachment locations around obstacles (Slimani, 2022). However, the refinement of the grid is constrained by computational cost: doubling the resolution in each spatial direction increases the total number of cells by a factor of eight.

To ensure an optimal balance between accuracy and efficiency, a grid convergence analysis is typically performed. This procedure aims to identify the minimum grid resolution beyond which further refinement produces no significant changes in the simulated flow field. Such a preliminary study is essential for determining appropriate grid characteristics for subsequent definitive simulations.

Grid sensitivity studies are commonly conducted in computational fluid dynamics (CFD), and several guidelines have been established based on their outcomes. For instance, Franke and Britter (2011) recommend a minimum obstacle resolution of ten cells per cube root and a minimum spacing of ten cells between adjacent obstacles. Additional recommendations were formulated regarding admissible cell aspect ratios and grid compression factors. These criteria were applied in the computation of the RANS database that provides the input flow field for the SLAM dispersion model. Consequently, the sensitivity analysis of the RANS simulations with respect to mesh resolution is not presented here.

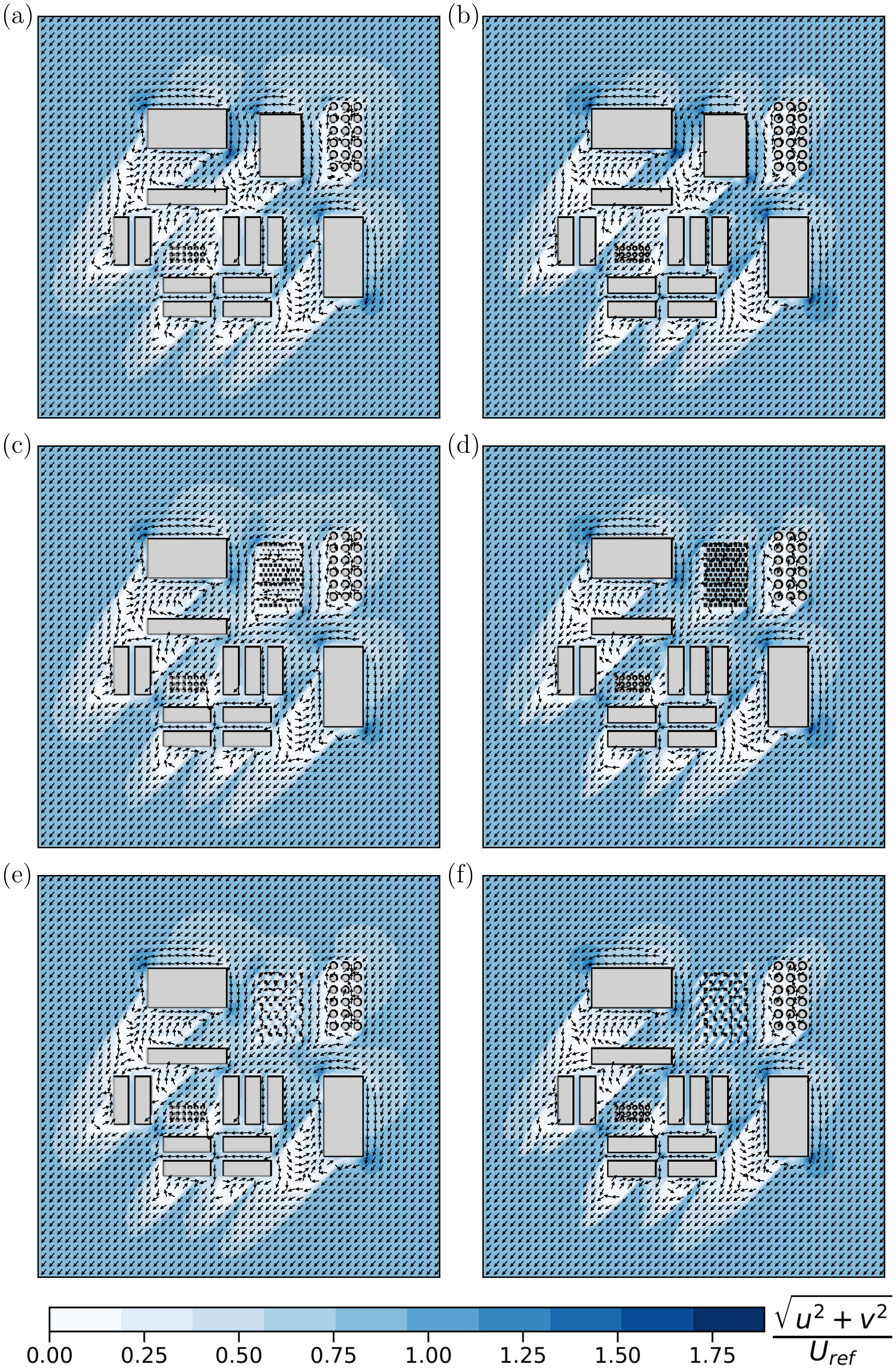

Figure 7.12: SWIFT dimensionless velocity field at $z^* = 0.26$, for a horizontal resolution of **a**, **c**, **e**: 19 cells per length h_A and **b**, **d**, **f**: 38 cells per length h_A and for the **a**, **b**: 'solid', **c**, **d**: 'dense' and **e**, **f**: 'spaced' configurations.

Since the computational approach implemented in PMSS fundamentally differs from that of RANS solvers, no strict meshing criteria of the same kind are defined. Nevertheless, an analysis was conducted to assess the influence of grid resolution on the simulated flow field. We present here two configurations: a coarser grid with cells being $1/19\,h_A$ wide, and a finer grid with cells being $1/38\,h_A$ wide, h_A being the height of the tallest elements of the site. Both grids share the same vertical resolution. The objective was to evaluate how horizontal grid resolution affects the model's ability to represent the influence of obstacles, particularly the thin columns forming the porous building and the group of storage tanks. The results highlight the issues that may arise when the grid is insufficiently refined, as observed with the coarser configuration.

Figure 7.12 shows the simulated velocity field with the two grid resolutions for a 40° incoming wind configuration. The coarse grid case in the ‘solid’ configuration (see Fig.7.12a) presents zones of iso-velocity, evidenced by the colour scale, that are larger upwind and downwind of the obstacles compared to the finer grid (see Fig.7.12b). However, the horizontal grid resolution has negligible effect on the recirculation zones of the largest obstacles. In contrast, we observe larger downstream regions of velocity depletion behind the small tanks in the coarser grid simulation than in the finer grid case. This is a consequence of an insufficient number of grid cells to resolve the flow between the cylinders, and to reproduce their round sections. To avoid the numerical rounding of circular shapes, we defined the porous versions of the A building as a cluster of square-section columns, forming the dense (see Fig.7.12c and d) and spaced (see Fig.7.12e and f) configurations of the A building. In Fig.7.12c, the coarser grid produces slightly larger individual recirculation zones for each column, leading to a slightly enhanced global wake compared to Fig.7.12d. A similar behaviour is observed in the spaced configuration, in Fig.7.12e and f. Overall, the grid resolution primarily affects the representation of small-scale elements, such as the tanks and columns, which are insufficiently resolved with the coarser grid.

The choice was made to keep a resolution of 38 cells per length h_A, which is a compromise between the spatial accuracy and the computational demand. A finer resolution would have required an increased computational cost, to obtain a dispensable improvement of the accuracy of the velocity field. On the opposite, a coarser resolution would not have permitted to accurately reproduce the shapes of thin obstacles, particularly the columns forming the porous building and the groups of tanks. To optimise computing efficiency, the domain was divided into four tiles, on which the flow field was computed in parallel. A similar spatial parallelisation was applied to the concentration field computation.

7.6 Conclusion

This chapter is dedicated to the comparison of the flow field simulated by two different methodologies to the experimental data. On one side, SLAM relies on pre-computed RANS simulations, which are interpolated once the exact wind direction and atmospheric stability are defined. On the other side, PMSS relies on SWIFT, a semi-empirical wind field model (which ensures mass conservation of the flow). As the two approaches are fundamentally different, we compare the simulated flow fields to the wind velocity measurements, in order to assess which effects of the site geometry are captured by the models. Different geometrical configurations of the idealised site are investigated, enabling the variation of the incoming wind direction and the shape of the main building. Both models were used from an operational perspective, following the best practice guidance.

While PMSS produces individual recirculation zones which are attached to each individual obstacles and misses the complex interacting effects generated by the entire group of obstacles, the RANS simulations capture flow features such as channelling effects and distorted recirculation zones. The effect of the upwind building porosity in the 40° incoming flow configurations is particularly strong in PMSS, as individual column wakes are generated instead of a global recirculation zone produced by the whole group of columns. Differences between the results of the two modelling approaches are however smaller in the most porous case, as columns are more spaced and produce a much weaker downwind perturbative effect than the densely packed group of columns.

Local inaccuracies appear in the RANS simulations, notably in the extent of the recirculating region to the side of building A. We assume that this is a consequence of the imposed wall roughness in the RANS simulations, as more rough surfaces tend to decelerate the flow and widen the attached recirculation zones. Additionally, refining the grid in this region could prevent the artificial widening of the recirculating zone by too large grid cells.

The two modelling approaches have advantages and drawbacks which should be known by potential users. While PMSS provides fast simulations suitable to operational approaches, it does not capture the complex flow behaviours produced by neighbouring obstacles. The RANS simulations, which are computed beforehand in the SLAM methodology, reproduce these effects, but inaccuracies in the input parameters, such as the wall roughness, can generate non-negligible errors in the resulting flow field.

Chapter 8

Inter-comparison of the experimental and simulated concentration fields

In this chapter, we focus on the mean concentration field simulated with both approaches. Since both the PMSS and SLAM methodologies are based on Lagrangian dispersion models, the differences in the simulated concentration fields are mainly due to the computation methods for the velocity field. We thus focus on determining the effects of the flow field on the plume shape, the concentration levels reached over the site, and the concentration profiles at several positions on the site.

8.1 Overview of model-data agreement

A first method to quantify the models accuracy is to compare the simulated and experimental mean concentration values at each measurement points, and to compute performance metrics over the model-experiment concentration pairs. The metrics that we consider are the fraction of predictions within a factor of 2 ($FAC2$), the geometric mean bias (MG), the geometric variance (VG), the normalised mean square error ($NMSE$), the absolute factional bias (AFB) and the correlation coefficient (R). They are defined considering C_{mod} and C_{exp} the time-averaged dimensionless concentration from the simulation and the experiment, respectively, N the number of points in the measurement dataset, and $\Big\langle \cdot \Big\rangle$ the average operator over the whole dataset of point concentrations pairs. The metrics write as:

$$FAC2 = \frac{1}{N}\sum_{i=1}^{N} k_i$$

with $k_i = 1$ when $0.5 \leq \frac{C_{mod}}{C_{obs}} \leq 2$ and $k_i = 0$ otherwise,

$$MG = \exp\left(\Big\langle \log(C_{obs}) \Big\rangle - \Big\langle \log(C_{mod}) \Big\rangle\right)$$

$$VG = \exp\left(\Big\langle [\log(C_{obs}) - \log(C_{mod})]^2 \Big\rangle\right)$$

$$NMSE = \frac{\Big\langle (C_{obs} - C_{mod})^2 \Big\rangle}{\Big\langle C_{obs} \Big\rangle \Big\langle C_{mod} \Big\rangle}$$

$$AFB = \frac{2\left\langle |C_{obs} - C_{mod}| \right\rangle}{\left\langle C_{obs} \right\rangle + \left\langle C_{mod} \right\rangle}$$

$$R = \frac{\left\langle \left(C_{obs} - \left\langle C_{obs} \right\rangle\right)\left(C_{mod} - \left\langle C_{mod} \right\rangle\right) \right\rangle}{\sqrt{\left\langle \left(C_{obs} - \left\langle C_{obs} \right\rangle\right)^2 \right\rangle} \cdot \sqrt{\left\langle \left(C_{mod} - \left\langle C_{mod} \right\rangle\right)^2 \right\rangle}}$$

Experimental and model concentration values below $\overline{C^*} = 1$ were replaced by 1 in order to lower the weight of very low concentrations in the computation of the model-data agreement, which is necessary for computation of MG and VG following Chang and Hanna (2004). This limit is above the instrument threshold but corresponds to the experimental concentration encountered at plume borders.

	Target value	Satisfactory value	Possible range
$FAC2$	1	$FAC \geq 0.3$ (Hanna and Chang, 2012)	$[0;1]$
MG	1	$0.7 \leq MG \leq 1.3$ (Marro et al., 2014)	$\mathbb{R}^+$
VG	1	$VG \leq 4$ (Marro et al., 2014)	$\mathbb{R}^+$
$NMSE$	0	$NMSE \leq 6$ (Hanna and Chang, 2012)	$\mathbb{R}^+$
AFB	0	$AFB \leq 0.3$ (Marro et al., 2014)	$[0;2]$
R	1	$R \geq 0.6$ (Nguyen, 2017)	$[-1;1]$

Table 8.1: Metrics characteristics

These performance metrics presented here are not sufficient to reflect a complete overview of the model-data agreement, but all together they provide a quantitative estimate of the systematic and random biases. A perfect model would have values of $FAC2$, MG, VG and R equal to 1, and values of $NMSE$ and AFB equal to 0 as presented in table 8.1. Satisfactory values were taken from Hanna and Chang (2012) for urban terrains when provided, and from Marro et al. (2014) for most other cases, the latter having been determined for model-data comparison with thermal and inertial effects over flat terrains and thus being more strict than needed in our case. No limit value was proposed for R in these articles. We thus took the threshold defined by Nguyen (2017) for model-experiment comparison over urban terrains. Table 8.2 presents the values obtained for both models and for each configuration. $FAC2$ provides information on the model ability to fit to experimental values inside a given acceptance range (here two times above or below the experimental concentration). This measure is not affected by outliers (Papp et al., 2024). A satisfactorily $FAC2$ value would typically be over 0.3 according to Hanna and Chang (2012), which is satisfied by both models in all configurations. However, both models show better $FAC2$ values in the 'S25 spaced' configuration (more than 70% of the points estimated by the models lie within a factor of 2) than in the 'S4' and 'S25 solid' configurations (only 40% to 60% of the points lie within this same range). In particular, the lowest value is attributed to the SLAM simulation of the 'S4' configuration while the highest corresponds to the PMSS simulation of the 'S25 spaced' configuration. $FAC2$ values vary significantly depending the configuration for a same model, and neither SLAM nor PMSS consistently performs better than the other model in all cases.

MG reflects the systematic bias between model and experiment data and it is particularly adapted to datasets with variations reaching several orders of magnitude (Hanna et al., 1991), which is the case of our data. MG values fall into the satisfactory range defined by Marro et al. (2014) in the PMSS simulations of the 'S4', 'S25 solid' and 'S25 spaced' configurations and in

Table 8.2: Performance metrics for both models and all configurations

	Model	**FAC2**	**MG**	**VG**	**NMSE**	**AFB**	**R**
‘S4’ (130° wind)	PMSS	0.518	1.253	3.593	30.349	0.872	0.873
	SLAM	0.406	1.307	40.571	215.196	1.776	-0.007
	Model	**FAC2**	**MG**	**VG**	**NMSE**	**AFB**	**R**
‘S5’ (130° wind)	PMSS	0.554	1.586	2.971	8.976	0.775	0.507
	SLAM	0.753	0.747	2.983	6.25	0.565	0.573
	Model	**FAC2**	**MG**	**VG**	**NMSE**	**AFB**	**R**
‘S25 solid’ (40° wind)	PMSS	0.494	0.775	28.398	8.071	1.134	0.294
	SLAM	0.581	0.384	20.467	5.559	0.853	0.553
	Model	**FAC2**	**MG**	**VG**	**NMSE**	**AFB**	**R**
‘S25 dense’ (40° wind)	PMSS	0.617	2.647	42.976	18.175	1.33	0.409
	SLAM	0.717	0.592	3.241	8.044	0.687	0.722
	Model	**FAC2**	**MG**	**VG**	**NMSE**	**AFB**	**R**
‘S25 spaced’ (40° wind)	PMSS	0.861	1.147	1.536	15.327	0.807	0.578
	SLAM	0.723	0.633	2.854	6.892	0.684	0.88

the SLAM simulation of the ‘S5’ configuration (the SLAM MG value for the ‘S4’ configuration is very close to the limit though). None of the models reach the target interval for this indicator in the ‘S25 dense’ configuration, since $MG_{SLAM} \simeq 0.5$ while $MG_{PMSS} > 2$, corresponding to mean concentrations predicted by SLAM and PMSS that are two times lower and more than two times higher than the experiment, respectively.

Similarly to MG, VG is an adapted indicator for datasets with extreme concentration values, but it provides information on both the systematic and random errors (Chang and Hanna, 2004). Both models meet the target domain in the ‘S5’ and ‘S25 spaced’ configuration, while in the ‘S4’ and the ‘S25 dense’ configurations the condition is satisfied only by PMSS and only by SLAM, respectively.

$NMSE$ is another indicator of the systematic and random error which is however more sensible to outliers (Chang and Hanna, 2004; Hanna et al., 1991). Values of $NMSE$ in the ‘S5’ and ‘S25 solid’ configuration lie close to the upper satisfactory limit of $NMSE$ values defined by Hanna et al. (1991) for urban environments, meaning that the scatter is about 2.4 times the mean. In the ‘S25 dense’ and ‘S25 spaced’ configurations, PMSS values of $NMSE$ are higher than SLAM values, while the highest (meaning worst) $NMSE$ value is reached in the SLAM simulation of the ‘S4’ configuration.

None of the model reaches the target interval for AFB, meaning the systematic error is high in all cases (Marro et al., 2014). Reasonable values ($AFB \leq 1$) of this indicator are reached in the ‘S5’ and ‘S25 spaced’ configurations by both models, by SLAM alone in the ‘S25 solid’ and ‘S25 dense’ configurations, and by PMSS alone in the ‘S4’ configuration.

Finally, the correlation coefficient R provides information on the linear relationship between modelled and measured concentrations, without being affected by additive or multiplicative biases. This indicator is necessary but not sufficient to determine the agreement between the simulated and measured concentration fields (Papp et al., 2024), because it is very sensitive to few good matching pairs and it is affected by the spatial repartition of the points (Chang and Hanna, 2004). Notably, it is more appropriate when measurements points follow a grid rather than transversal profiles (Chang and Hanna, 2004). Satisfactory values are reached by PMSS in the ‘S4’ configuration and by SLAM in the ‘S25 dense’ and ‘S25 spaced’ configurations only. However, the low R values obtained in the ‘S5’ configuration is more representative, since comparison points follow a more resolved regular grid in the open space formed by the D buildings (see Fig.7.1). Correlation is particularly close to zero and even negative in the SLAM simulation of the ‘S4’ configuration, indicating poor model-experiment agreement.

Considering all indicators, both models perform better in the ‘S25 spaced’ configuration, in which the flow is the least affected by the upwind site geometry. The SLAM simulation of the ‘S4’ configuration seems to be problematic, as well as the PMSS simulation of the ‘S25 dense’ configuration. The latter can easily be explained by the inappropriate consideration of the upwind building wake impacting the velocity field over the whole site, that was detailed in section 7.3.

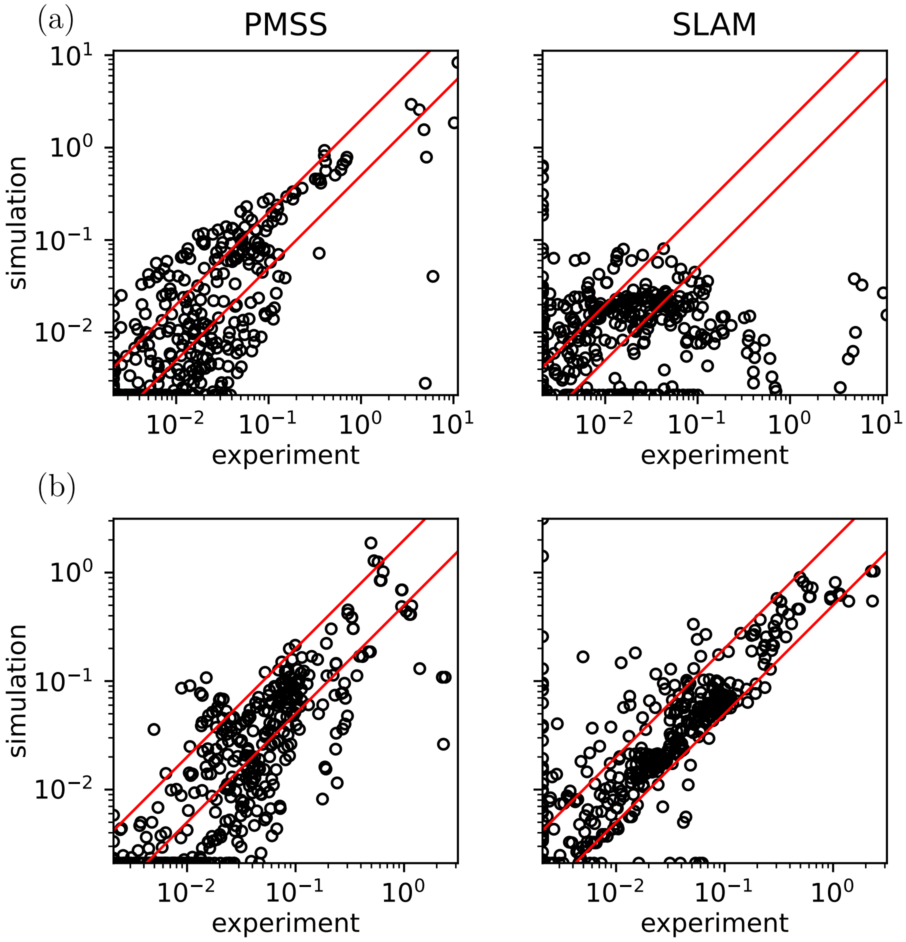

Figure 8.1: Modelled versus experimental mean concentration for configurations: **a**: ‘S4’ and **b**: ‘S5’. Red lines correspond of a factor of 0.5 and 2 of the measurement.

To better understand the extent of the mismatch between simulated and measured mean concentration values, we analyse the scatter plots of these values for the ‘S4’ and ‘S5’ configurations in Fig.8.1, and for the ‘S25 solid’, ‘S25 dense’ and ‘S25 spaced’ configurations in Fig.8.2. Figure 8.1a shows a larger scatter for the SLAM simulation of the ‘S4’ configuration than for the PMSS simulation. Notably, the SLAM panels indicate that many concentration values were predicted low but measured high, or on the contrary measured low but predicted high. Simulations from both models for the ‘S5’ configuration, shown in Fig.8.1b present a lower scatter. Fig.8.2 shows accumulations of points along the x and y axes, that are similar to that observed in Fig.8.1a, suggesting discrepancies in the plume shape and/or alignment. The scatter is high in all configurations. Additionally, SLAM tends to slightly overestimate concentration values in all of the ‘S25’ configurations, while PMSS tends to underestimate concentration mainly in the ‘S25 dense’ and ‘S25 spaced’ cases.

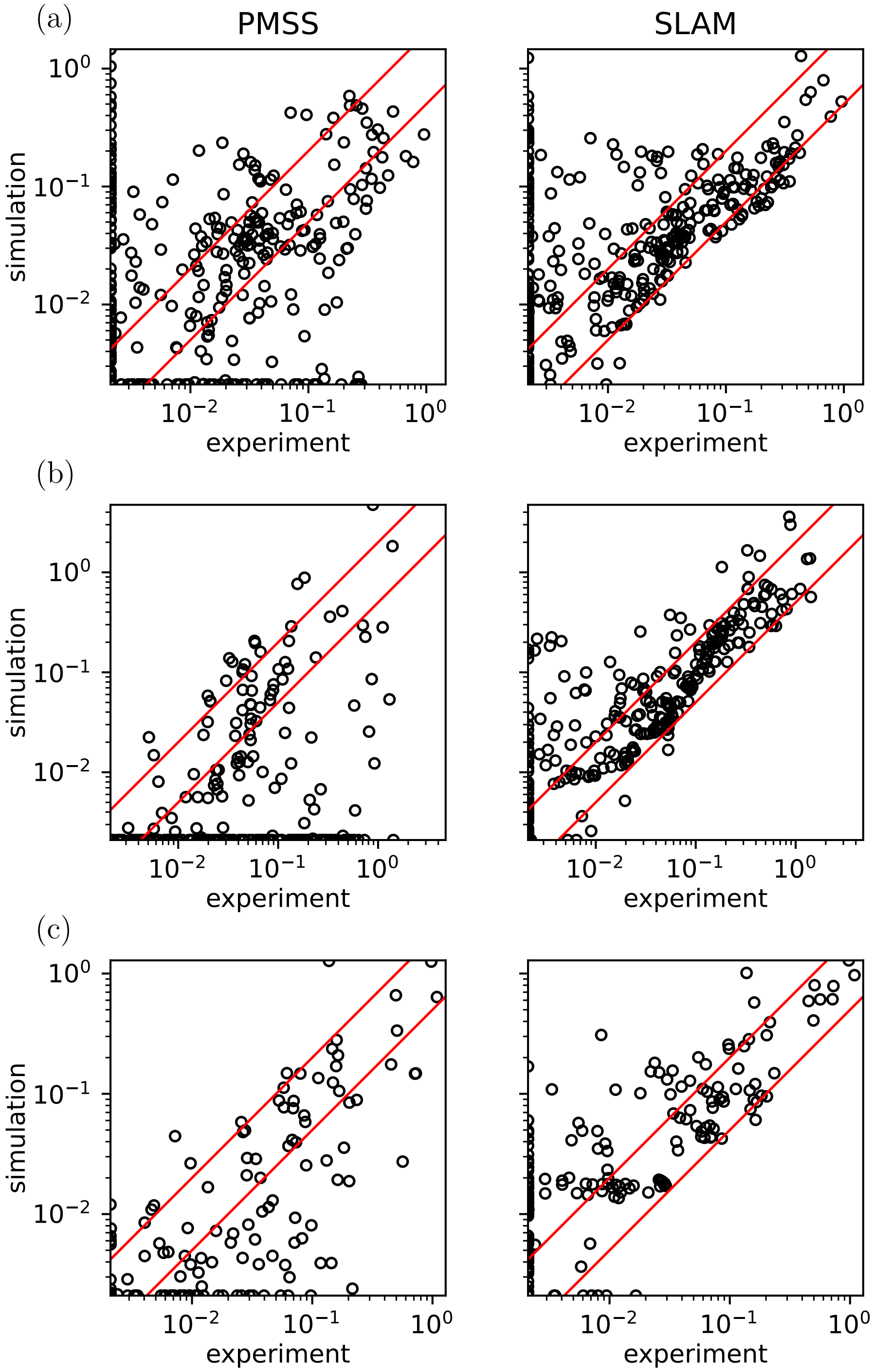

Figure 8.2: Same as Fig.8.1 for the **a**: ‘S5 solid’, **b**: ‘S25 dense’ and **c**: ‘S25 spaced’ configurations. Red lines correspond of a factor of 0.5 and 2 of the measurement.

Performance metrics and scatter plots have the disadvantage to consider only pointwise comparisons of the data, which does not account for the global spatial behaviour of the plume over the whole site. This is particularly problematic when the spatial shift between measured and modelled plumes is so high that the modelled plume does not fall into the volume covered by the measurement points, or only in part, even though the plume width and concentration profiles would correspond to each other, once the shift corrected. All indicators presented in this section are thus not sufficient to understand in details the origin of the mismatch between simulated and measured concentrations, and to determine which features of dispersion were successfully reproduced by the models, and which were inadequately captured. Thence, each configuration is analysed in detail in the following sections, with a focus on the global features of the concentration field: mainly the plume shape, the effects of obstacles, and the transversal and vertical profiles of mean concentration.

8.2 'S4' source in the 130° 'solid' configuration

We now analyse the concentration field simulated by SLAM and PMSS in order to understand why performance metrics reflected a poor accuracy of the SLAM result, and which features of the SLAM and PMSS methodologies improve or worsen the simulation results. Figure 8.3 shows several horizontal slices of the dimensionless mean concentration field generated by the models (background colour) and measured in the wind tunnel (coloured points). The upper and lower lines correspond respectively to the the PMSS and SLAM simulations. For a better readability of the figures, the minimum and the maximum of the colour scale were chosen as the respective minimum and maximum of experimental concentration values, since concentration maxima of both models are higher than the highest concentration value measured in wind tunnel.

Figure 8.3 shows that PMSS reproduces the correct plume shape and centre line position, while SLAM generates a plume that rises over the corridor to then spread along a line parallel to the plume centre line of PMSS and the experiment. This effect then produces a mismatch between the horizontal profiles of concentration in the near field as shown in Fig.8.4a. The profile maxima of the PMSS simulation and the experiment overlap, except for values located at $y^* < -2$, since the model does not capture the whole plume extent in the area between buildings A and B1. However, Fig.8.4a demonstrates that the plume simulated by PMSS is close to reality on both sides of the C building, despite the underestimated plume width. In contrast, the maximum of the SLAM simulation is shifted towards positive y^* values (corresponding to the right-hand side of someone facing the wind). The presence of an artificial line in the PMSS simulations, that is particularly visible between buildings A and B1 at $z^* = 0.62$ in Fig.8.3a, is a consequence of the separation of the domain into four tiles to optimise the parallelisation process. This artefact is however not problematic for the analysis, as it is spatially limited and easily identifiable. This effect would be reduced by adapting the timescale at which tiles exchange particles in the simulation.

The plume rise close to the source in the SLAM simulation is enlightened by the vertical profile shown in Fig.8.4b. The SLAM simulated concentration increases with height and reaches a maximum around $z^* = 0.8$, which is over the height of the D buildings. On the contrary, PMSS and experimental concentration values are larger close to the ground and decrease with increasing height. Nevertheless, in the far field, this effect is attenuated and the SLAM horizontal (see Fig.8.4c) and vertical (see Fig.8.4d) profiles resemble more the experimental data than the PMSS profiles. The incorrect initial plume shape and axis of the SLAM simulation seem to be counterbalanced by the local effects of the obstacles downwind of the source, while the simplified velocity field of the PMSS simulation produces discrepancies that reveal in the far field.

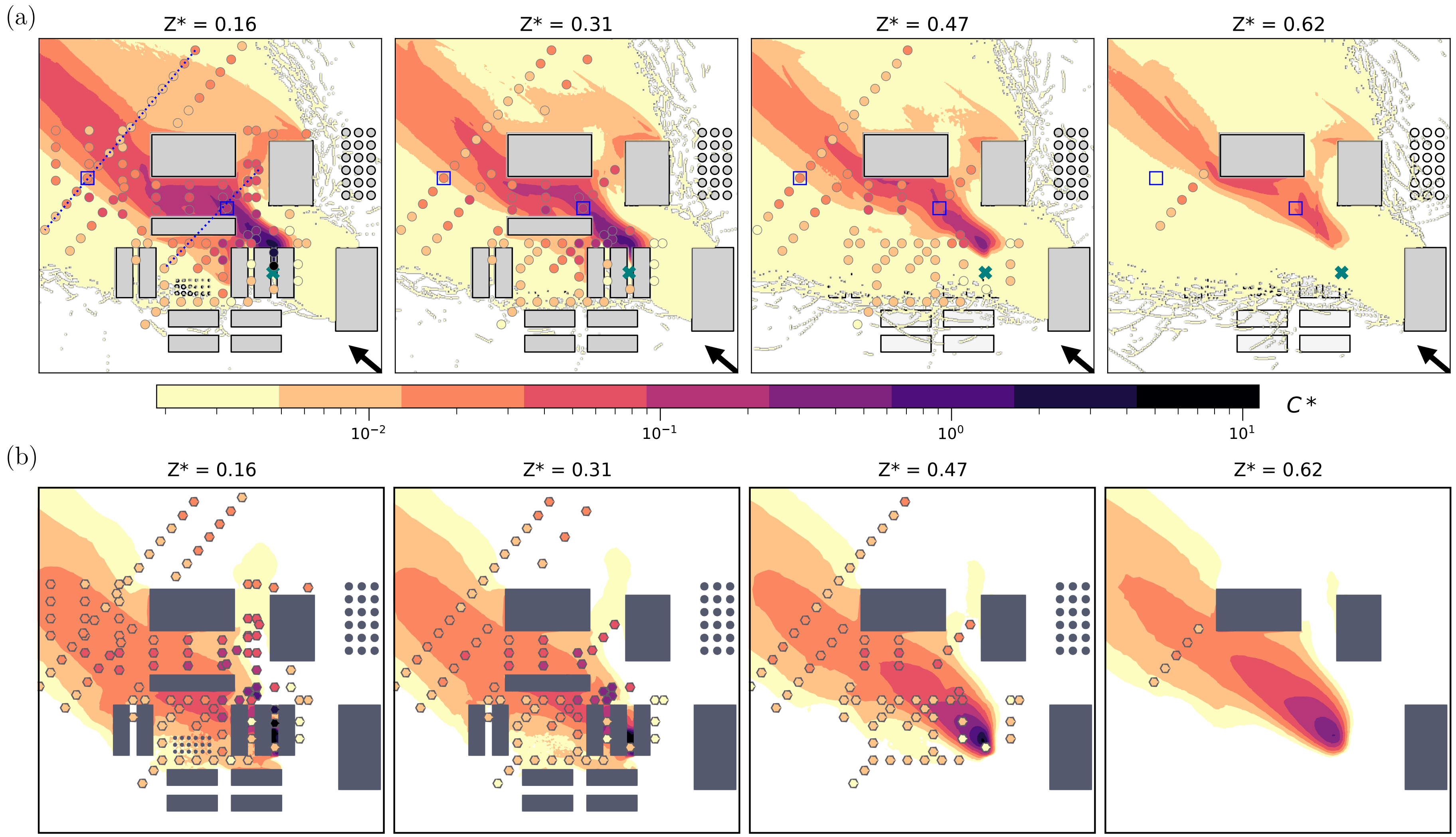

Figure 8.3: Dimensionless concentration field in the 'S4' configuration. The background colours correspond to the **a**: PMSS and **b**: SLAM simulation results while coloured dots represent the experimental concentration.

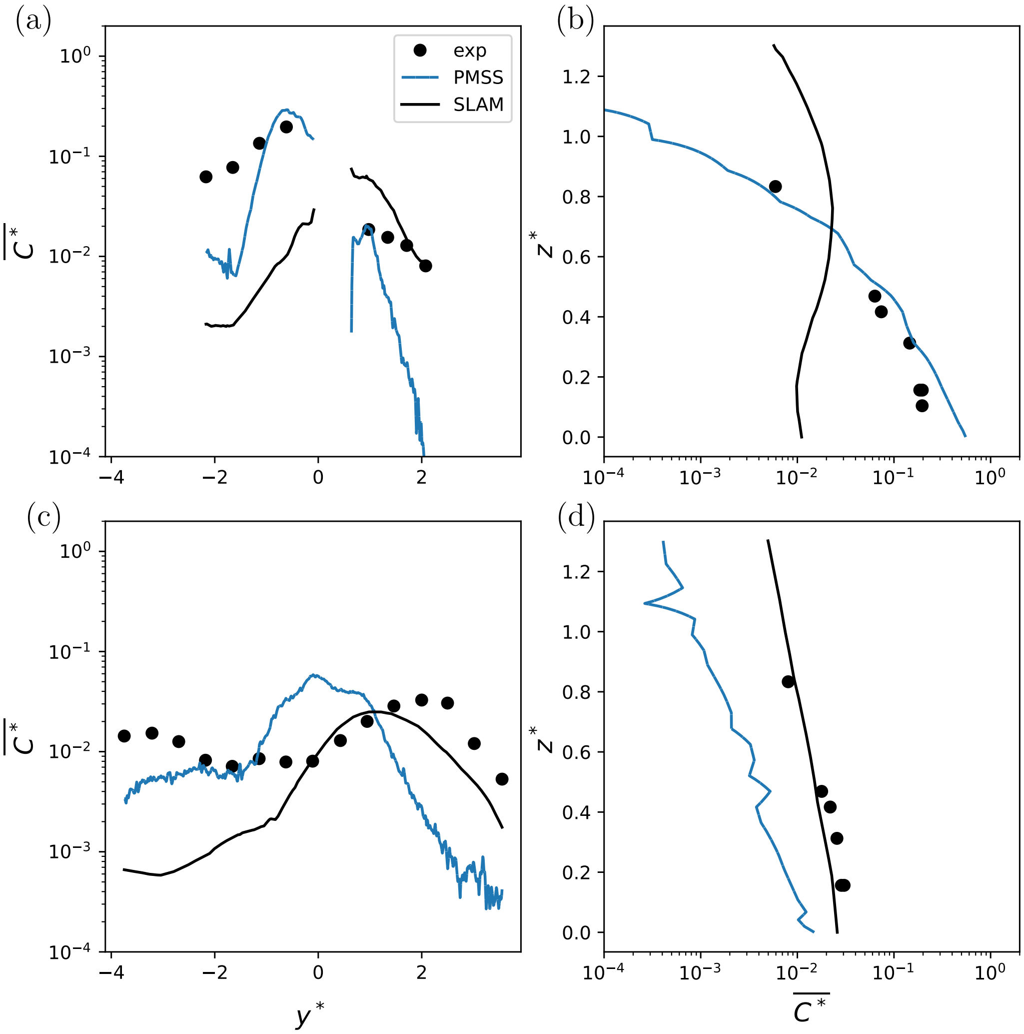

Figure 8.4: Concentration profiles on the locations shown in Fig.8.3. **a**: horizontal profile at $z^* = 0.16$ in the near field, **b**: vertical profile in the near field **c**: horizontal profile at $z^* = 0.16$ in the far field **d**: vertical profile in the far field. The opening in panel **a** is due to the presence of the C building.

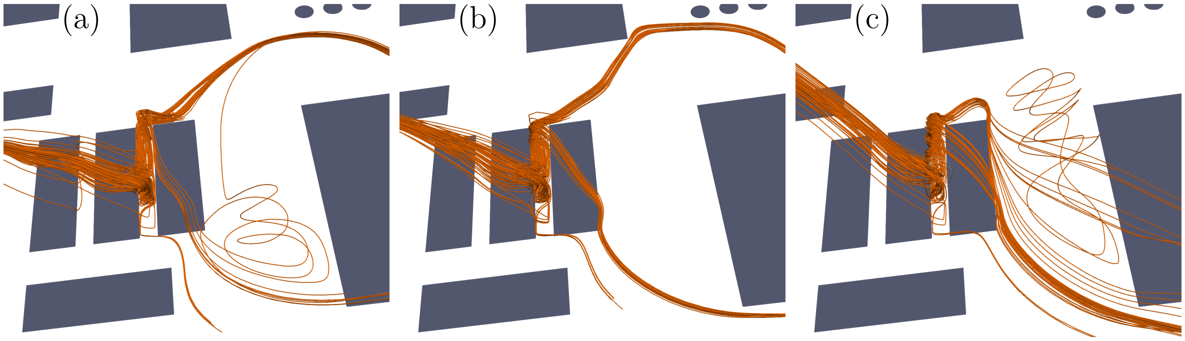

Figure 8.5: Streamlines of the wind field passing by the source position for an incoming wind direction of **a**: 120° (RANS simulation), **b**: 130° (interpolation of the 120° and 140° RANS simulations) and **c**: 140° (RANS simulation).

The origin of the erroneous plume shape close to the source in the SLAM simulation lies in the velocity field inside the corridor in which the source is placed. Instead of generating a wind following the corridor, the RANS interpolated simulation produces a current circumventing the B2 and D5 buildings and entering from the leeward side of the corridor, as evidenced in Fig.8.5b. This countercurrent faces the wind entering from the windward side of the corridor, producing a rising flux around mid-length. This upward flux drives the pollutant emitted by the source, and leads the plume outside of the corridor. Similar behaviours are observed for both RANS simulations with both 120° and 140° incoming wind directions shown in Fig.8.5a and c, respectively. The interpolation of both fields (see Fig.8.5b) thus produces the same behaviour.

In contrast, the flow from the SWIFT simulation follows the corridor and escapes on its end leading to the A building, as was shown previously in Fig.7.2c, carrying the tracer along the corridor. The plume is thus highly concentrated inside the corridor and widens at its end. It then disperses over the open area and it is driven by the flow in this region. The plume thus stays lower than the SLAM plume and is channelled by buildings B1 and C before reaching the far field.

Even though velocity measurements presented in section 7.1 are not sufficiently resolved to determine which of the PMSS and SLAM velocity fields is the closest to reality, the experimental concentration field evidences a plume behaviour much closer to the PMSS simulation in the near field. This implies that the interpolated RANS velocity field is little realistic at this specific position due to the impact of the upwind B2 building and the grouped D obstacles. We suppose that improving the RANS simulations to generate a boundary layer closer to the experiment could positively affect the performance of SLAM in this configuration.

8.3 ‘S5’ source in the $130°$ ‘solid’ configuration

The ‘S5’ case is one of the configurations in which performance metrics and scatter plots presented in section 8.1 show the best agreement between simulated and measured concentration fields, as evidenced by Fig.8.6, that shows the comparison of concentration fields between the experiment and the two models. Notably, simulated and experimental plume shapes show a much better agreement than that observed in the ‘S4’ configuration. The tracer emitted at the source first follows the corridor along D7 to then enter the open space in which the small tanks are placed. In this region, the experimental plume is slightly larger than the simulated plumes, particularly left to buildings D6 and D8. As a consequence, the experimental horizontal concentration profile visible in Fig.8.7a is accurately reproduced by both models below $y^* = 3.5$, but concentration is underestimated for larger y^* values. Both models capture the concentration along the D3–D4 corridor, but SLAM and PMSS, respectively, overestimate and underestimate it. The presence of the tracer at the end of this corridor, right of building C, is predicted by PMSS even though concentration values are lower than measured. It is however not predicted by SLAM due to a flow behaviour in this corridor similar to that observed in the ‘S4’ configuration and depicted in Fig.8.5. The vertical plume shape shown in Fig.8.7b is more accurate in the PMSS simulation, since SLAM overestimates concentration values over the height of the D buildings, as was also observed in the ‘S4’ configuration in section 8.2.

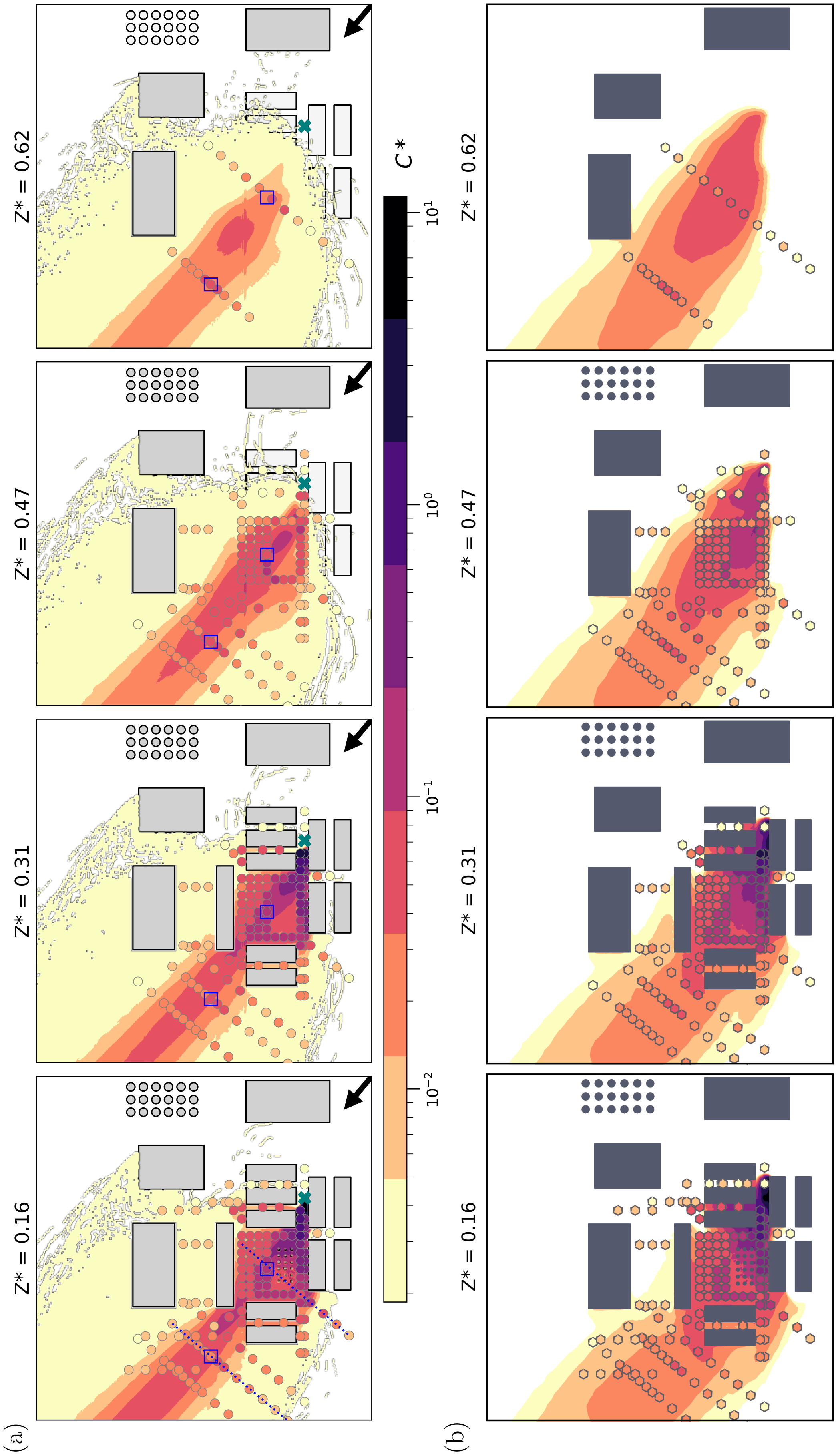

Figure 8.6: Same ad Fig.8.4 for the 'S5' configuration. **a**: PMSS, **b**: SLAM.

In the far field, the PMSS plume centre line is shifted towards negative y^* values, as shown on Fig.8.7c. The level $z^* = 0.16$ of Fig.8.6 enables a visual understanding of this phenomenon: the PMSS plume is narrower and covers the zone left to building B1, while it is closer to buildings D1 and D2 in the experiment and the SLAM simulation. The SLAM horizontal profile fits to experimental data below $y^* = 4$ in Fig.8.7c, but points at plume border to the left of building D1 are not perfectly captured by the simulated concentration field. Vertical plume shapes shown in Fig.8.7d are accurately reproduced by both models.

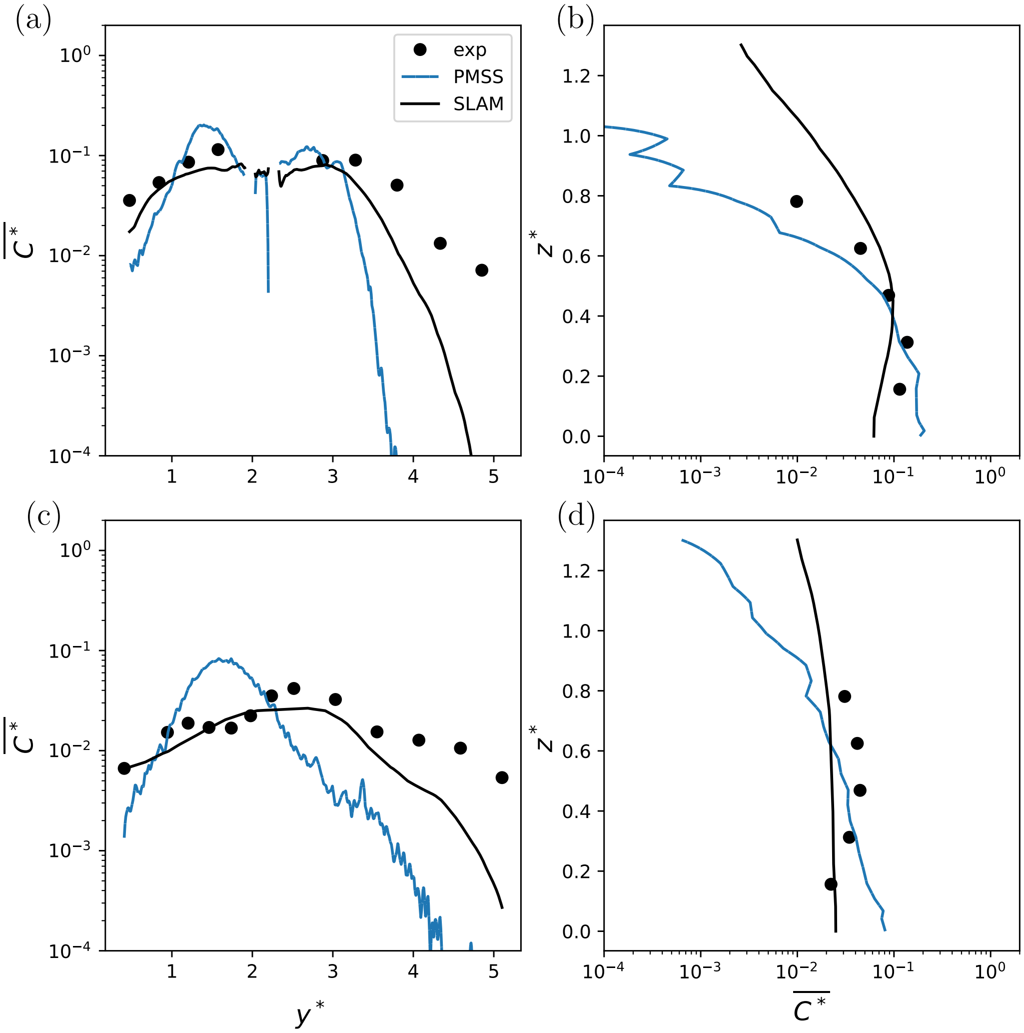

Figure 8.7: Concentration profiles on the locations shown in Fig.8.6. **a**: horizontal profile at $z^* = 0.16$ in the near field, **b**: vertical profile in the near field **c**: horizontal profile at $z^* = 0.16$ in the far field **d**: vertical profile in the far field. The holes in panel **a** is due to the presence of the small tanks.

8.4 ‘S25’ source in the 40° ‘solid’ configuration

In the ‘S25 solid’ configuration, the wake generated by the upwind A building strongly impacts the flow field, as analysed in section 7.2. Performance metrics of table 8.2 demonstrated a low accuracy of both models in this case, and Fig.8.2 enlightened many points aligned along the abscissa or the ordinate, indicating a mismatch regarding the presence of the plume at these points. Figure 8.8 provides information on the positions of these points, for the low z^* levels. Figure 8.9 completes Fig.8.8 by showing concentration maps at higher z^* levels. Local discrepancies in the plume shape appear within the recirculation zone of the upwind obstacle, particularly on its left side, where low concentration measured points cover a high concentration simulated area. This is a consequence of the wind velocity field analysed in Fig.7.2b and c, particularly inside the recirculation zones generated to the bottom and left sides of building A. Experimentally, the wind blows along the left edge of the building and no recirculating behaviour was captured. In contrast the RANS simulation produced a narrow recirculation zone covering this whole side, while in the SWIFT flow field the wake covers the wall until mid-length and develops along the x^* axis.

These recirculation zones transport the pollutant along the left edge of the building, where the experiment captured no concentration at all. However, the pollutant dispersion along the bottom edge of the building is more accurately captured by the models. They both predict high concentration values in this zone and reach concentration maxima close to the maximum measured concentration value as shown on the near field horizontal profile in Fig.8.10a. The zone covered by the simulated plumes between buildings D5 and A globally correspond to the experiment, even though none of the models captures the full extent of the presence of the tracer along the right edge of the D5 building. The shape of the highest concentrated region also vary between models: it is distributed along the wall in Fig.8.8a, while it covers only the building corner in Fig.8.8b, which is why the concentration maxima in Fig.8.10a lie towards more negative and positive y^* values in the SLAM and PMSS simulations, respectively. The wind tunnel measurements do not have a sufficient spatial resolution to determine which of these two behaviours is the closest to reality. Both simulations provide a similar accuracy over the vertical profiles shown in Fig.8.10b.

Model to experiment agreement increases with the distance from the source, since the impact of the upwind building wake is less significant in the mid- and the far-field. Horizontal (see Fig.8.10c) and vertical (see Fig.8.10d) profiles in this region evidence good model-experiment agreement. Some few discrepancies are due to an over- and -under estimation of the plume width by SLAM and PMSS respectively, while in both simulations the plume centre line is slightly shifted towards negative y^* values, compared to the experiment. This mismatch becomes hardly visible in the far field, where both horizontal (see 8.10e) and vertical (see 8.10f) concentration profiles reflect a good accuracy of both models.

While maps (see Fig.8.8 and Fig.8.9) and profiles (see Fig.8.10) present a reasonable agreement between modelled and experimental concentrations over the whole site, the performance metrics of table 8.2 are strongly affected by the mismatch in specific zones, such as the left edge of the A building, the open space between buildings B2 and D, and the space between buildings B1 and C. The detailed analysis of the concentration field is thus necessary to assess the agreement between simulations and the experiment, as well as to understand which dispersion mechanisms are captured by the models and which are not.

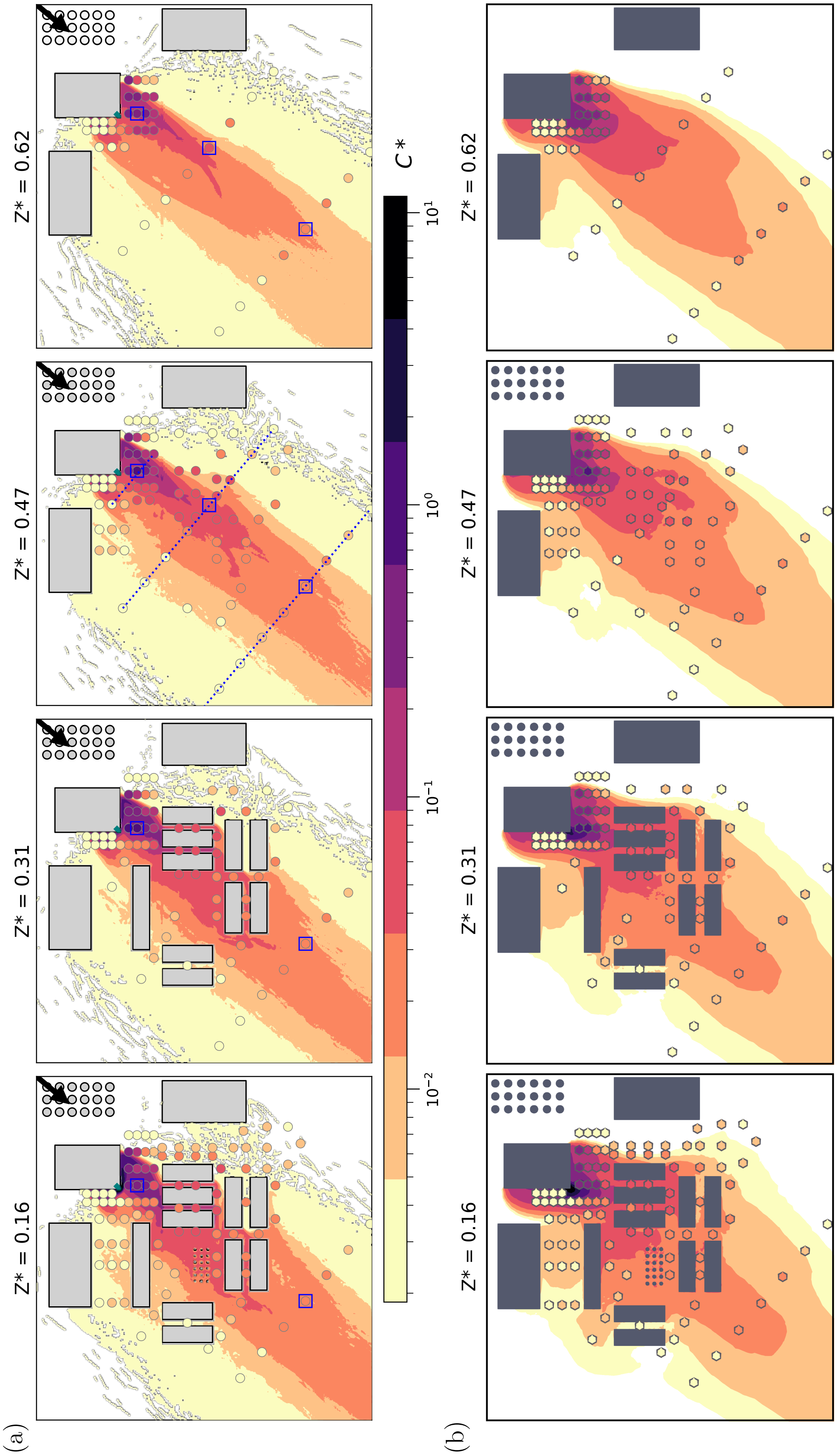

Figure 8.8: Same ad Fig.8.4 for the 'S25 solid' configuration. **a**: PMSS, **b**: SLAM. Higher z^* levels are shown in Fig.8.9.

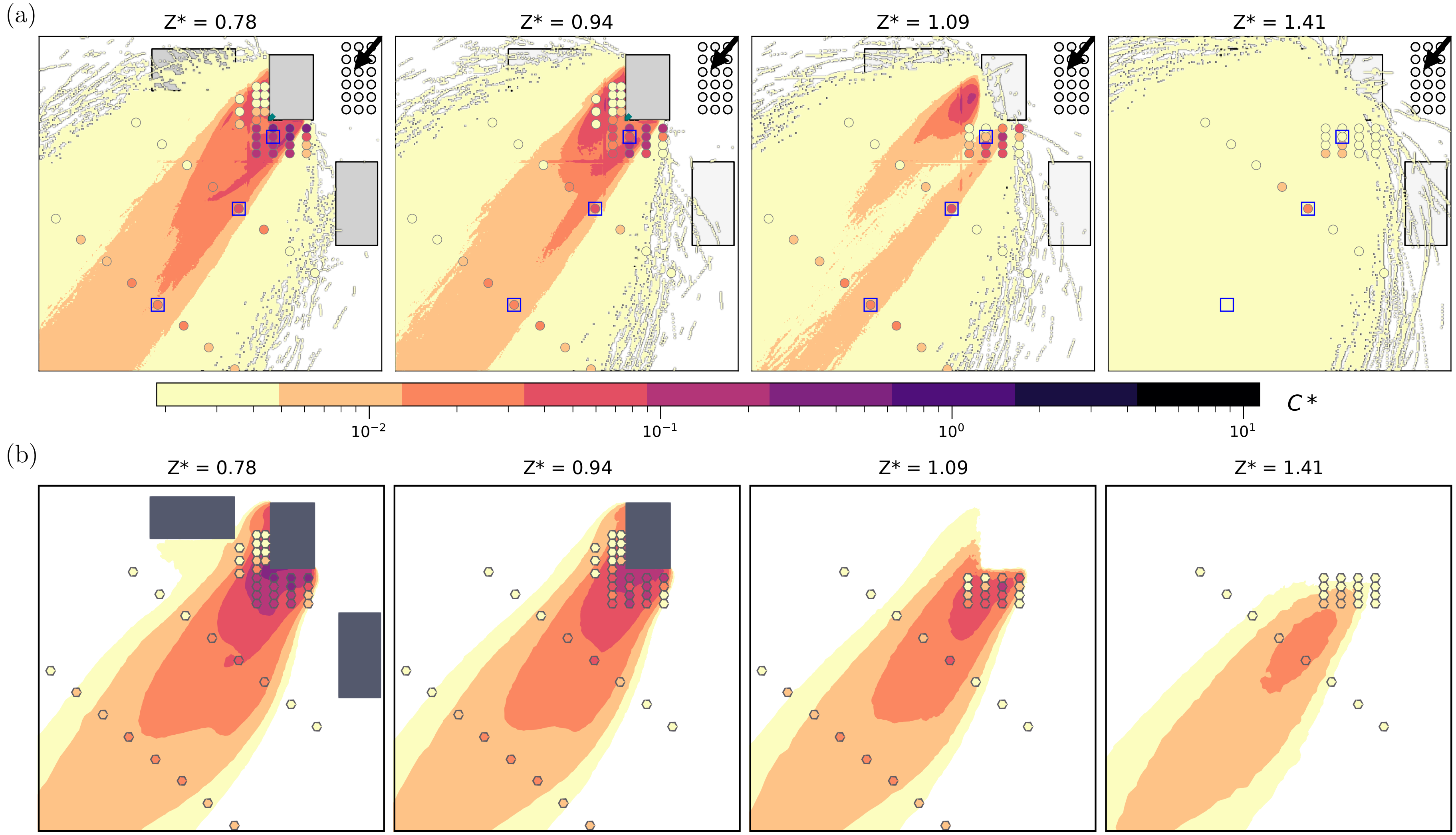

Figure 8.9: Same as Fig.8.8 for higher z^* levels.

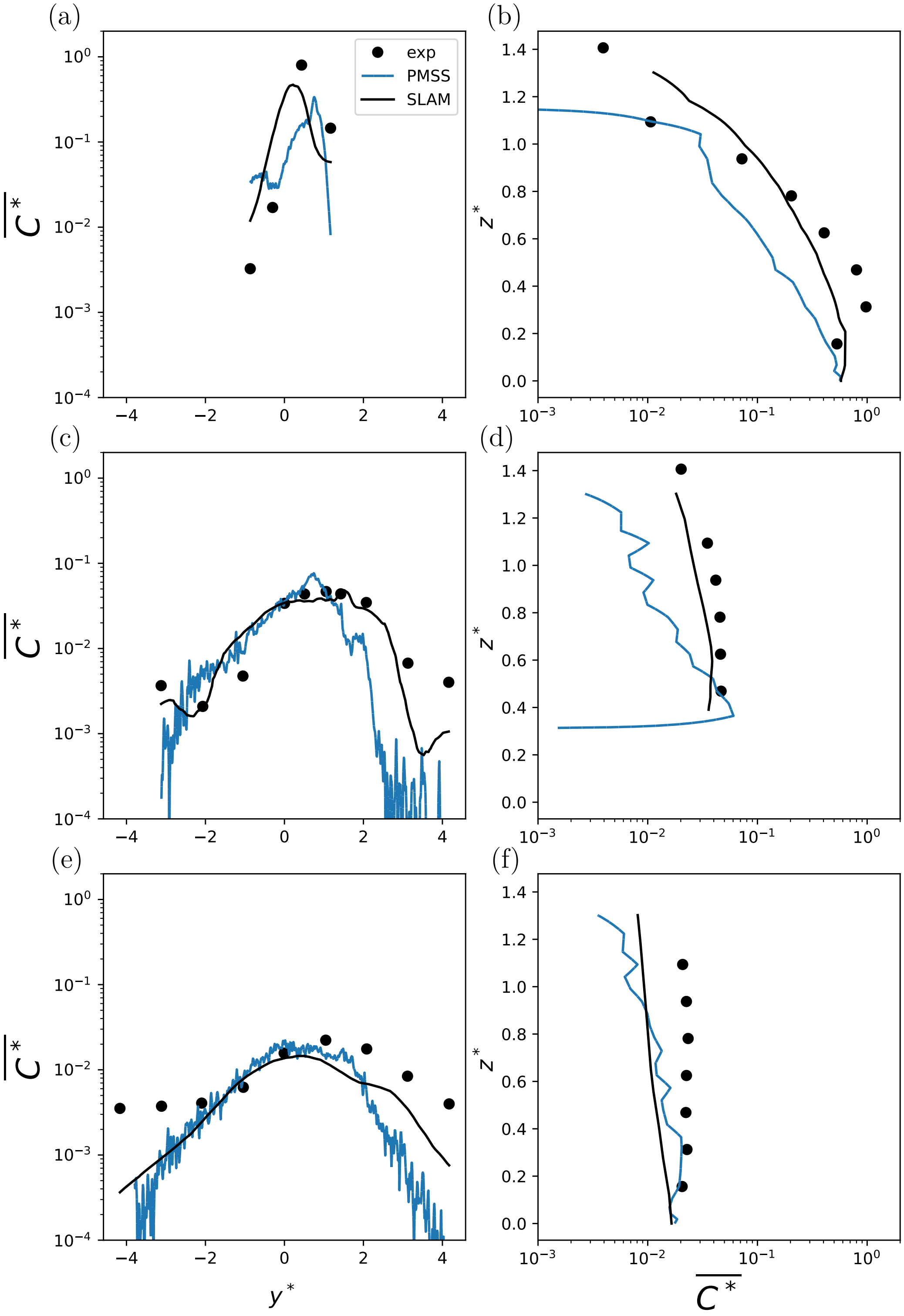

Figure 8.10: Concentration profiles on the locations shown in Fig.8.8. **a**: horizontal profile at $z^* = 0.47$ in the near field, **b**: vertical profile in the near field **c**: horizontal profile at $z^* = 0.47$ in the midfield **d**: vertical profile in the midfield, **e**: horizontal profile at $z^* = 0.47$ in the far field **f**: vertical profile in the far field.

8.5 ‘S25’ source in the 40° ‘dense’ configuration

The PMSS and SLAM simulations of the ‘S25 dense’ configuration produce very different behaviours, as we observed in section 8.1. Notably, performance metrics indicated a low accuracy of the PMSS simulation, which is associated to many points in which the experimental concentration is several orders of magnitude higher than the simulated concentration values, as we observed on Fig.8.2b. In this section, we thus analyse the concentration field and explain the plume behaviour by relating it to the velocity field analysed in section 7.3.

In Fig.8.11 and Fig.8.12, the PMSS simulated plume is narrower than the experimental plume, particularly close to the source. Notably, the model does not well capture the widening of the plume close to the source, due to the shape of the recirculation zone generated by the porous building that was analysed in Fig.7.6. Most measurement points in this region show high concentration values while the model predicts no pollutant at all. On the contrary, the SLAM plume shape close to the source is very accurate, except few discrepancies at plume borders. The simulated plume is as wide as the experimental plume close to the source, over both the left and the bottom edged of the A building. However, concentration values reached close to the source are higher in the simulation compared to the experiment (particularly at $z^* = 0.16$), which could indicate an underestimation of dilution of the pollutant in the recirculation zone of the porous obstacle. The very different behaviours of both models in the near field is evidenced by Fig.8.13a, in which the PMSS profile is much narrower than the SLAM and experimental profiles. Due to its tightness, the PMSS simulated plume overlaps with measurement points only at its borders at this distance from the source, which explains the one order of magnitude underestimation of concentration by PMSS in the vertical profiles shown in Fig.8.13b. In contrast, the SLAM profile fits very accurately to the measurements in this region. The mismatch between PMSS and experimental concentration values in the near field is a direct consequence of the individual column wakes observed in Fig.7.6b, which extent is negligible compared to the recirculation zone produced by the grouped columns in the RANS simulation.

Despite the better agreement between SLAM and experimental concentration fields in the near field, neither model is able to capture the presence of the tracer between buildings B1 and C. We think that this is a consequence inherent to using an averaged velocity field in the simulations, which is not able to reproduce rare intermittent behaviours generated by the obstacles. The contamination of this region by the tracer could be explained by the effect of the corner of building C. Rare passage of the contaminated flow to the side of this corner may carry few highly concentrated puffs in this region, that then fill most of the open space between buildings B1 and C.

The impact of the upwind building weakens with increasing distance from the source, but the underestimation of the PMSS plume width is still visible in the mid- and the far-field, as shown on Fig.8.13c and e. The SLAM horizontal profile globally fits to the experiment. A similar good agreement is observed between the SLAM vertical profile and the experiment in Fig.8.13d. In Fig.8.11 and Fig.8.12, discrepancies appear mainly at ground level and at plume borders, since the experimental plume reaches a larger extent than the simulated plume, even though the extent of the SLAM simulated plume resembles very accurately that of the experimental plume.

The mismatch between the PMSS and experimental concentration fields close to the source produce discrepancies until the far field, since the plume is too narrow and its centre line is shifted towards negative y^* values (see Fig.8.13e). Both models reproduce accurately the vertical plume shape as visible in Fig.8.13f. Hence, in this configuration, the upwind building has a strong impact on the plume in the near field, and capturing this effect is crucial to determine a reliable plume shape over the whole site.

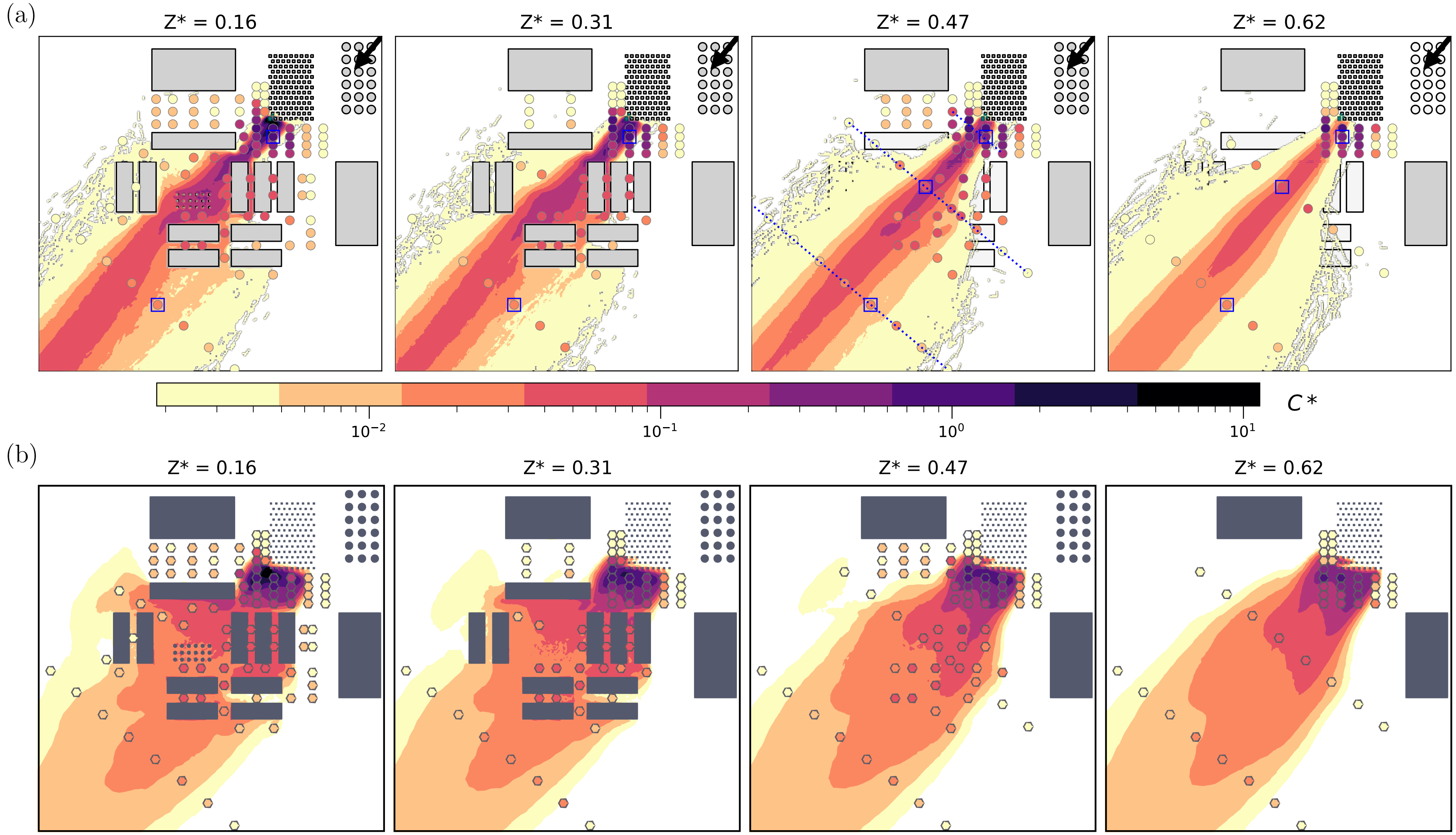

Figure 8.11: Same as Fig.8.8 for the ‘S25 dense’ configuration.

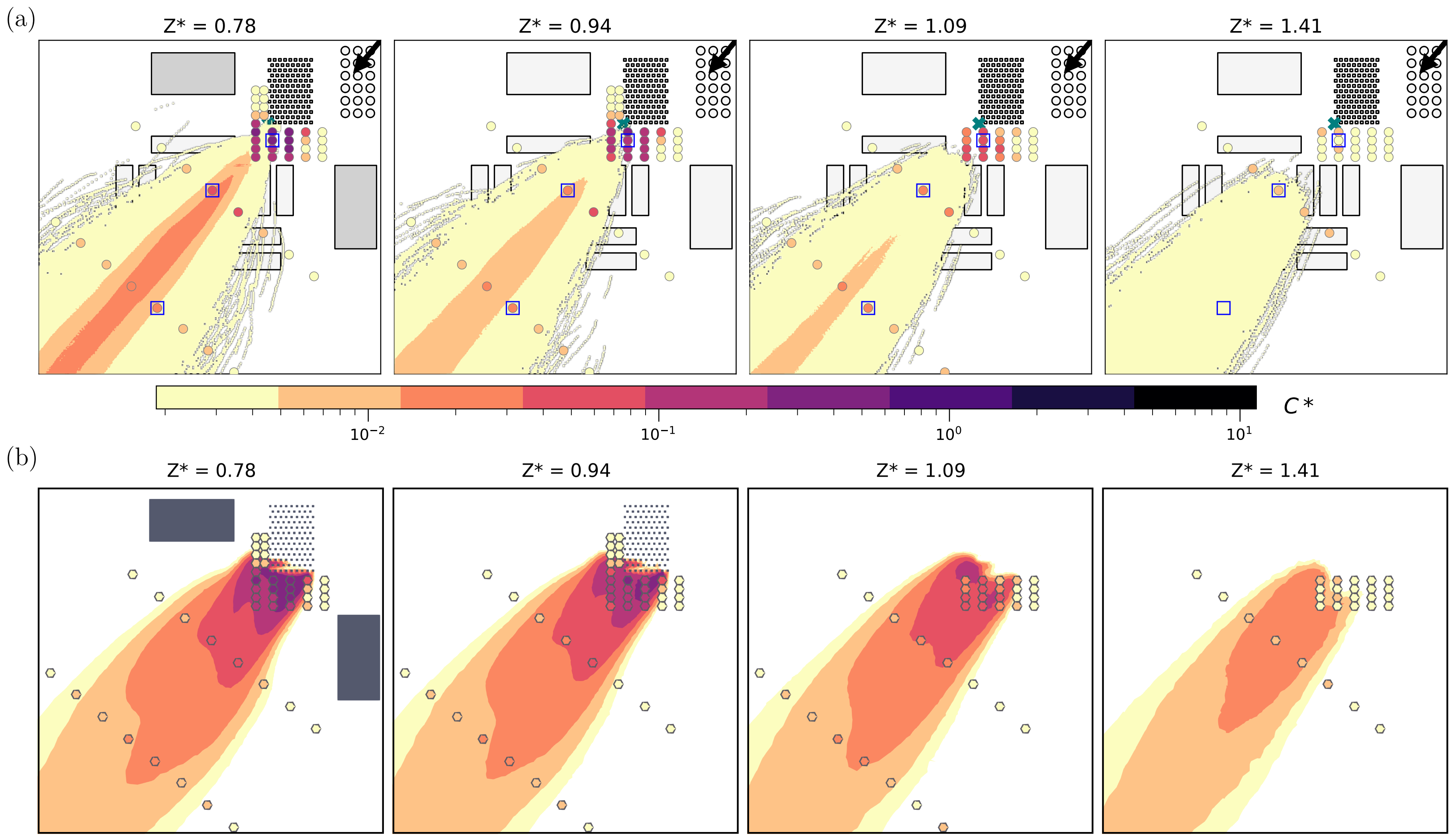

Figure 8.12: Same as Fig.8.11 for higher z^* levels.

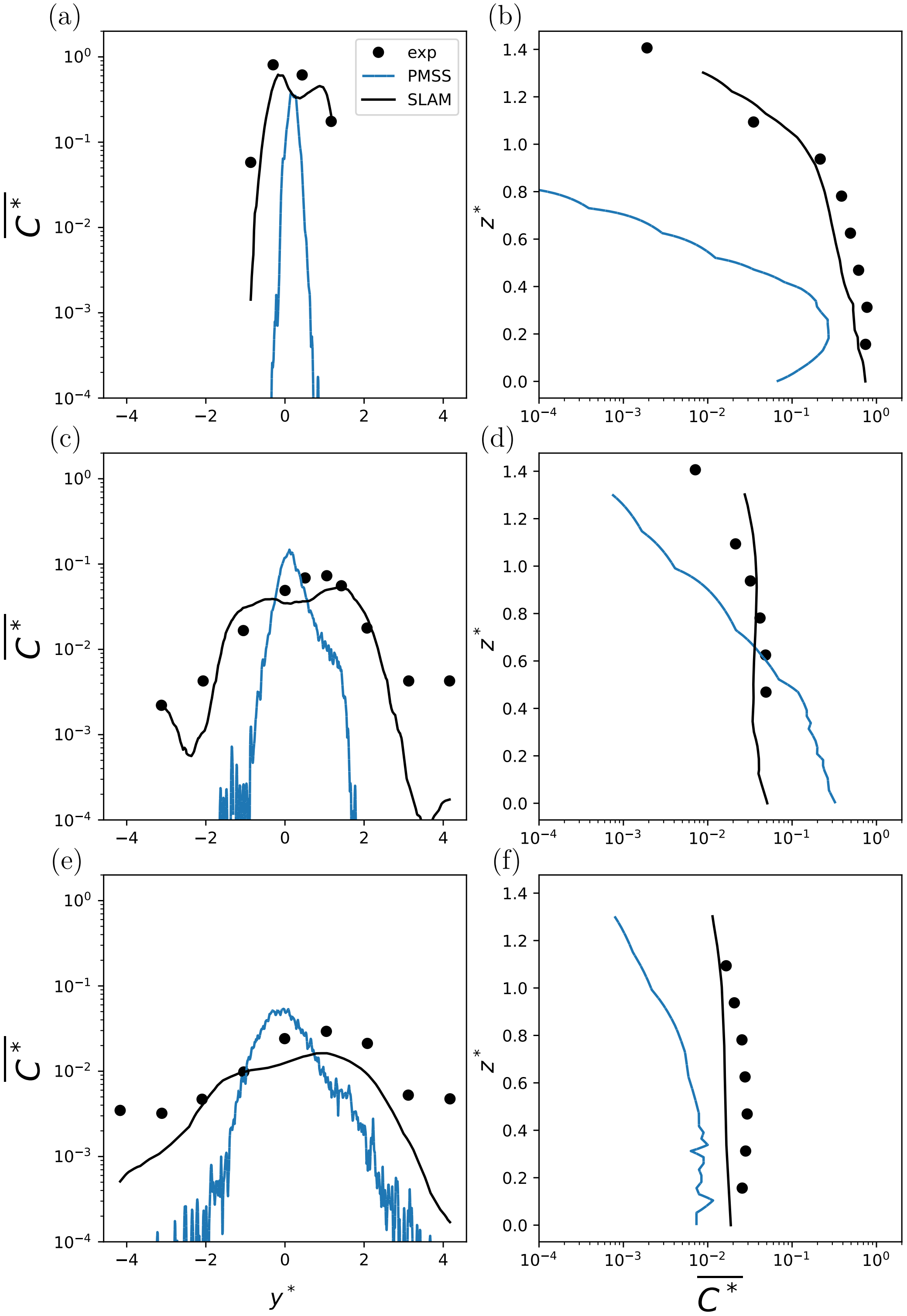

Figure 8.13: Concentration profiles on the locations shown in Fig.8.11. **a**: horizontal profile at $z^* = 0.47$ in the near field, **b**: vertical profile in the near field **c**: horizontal profile at $z^* = 0.47$ in the midfield **d**: vertical profile in the midfield, **e**: horizontal profile at $z^* = 0.47$ in the far field **f**: vertical profile in the far field.

8.6 ‘S25’ source in the 40° ‘spaced’ configuration

The ‘S25 spaced’ configuration is one of the cases in which performance metrics and scatter plots presented in section 8.1 showed best agreement between simulated and measured concentration fields. It is the configuration in which the perturbative effect of the upwind building on the flow field is the lowest, as observed in section 7.4.

Figure 8.14 and figure 8.15 present the concentration field at several heights. Close to the source, the SLAM plume is slightly too large, particularly close to the ground, while the PMSS plume is too narrow. Measurements did not capture the plume centreline at this distance from the source, which explains why both models reach C^* values significantly exceeding the experimental concentration around $y^* = 0$ where there is no measurement point, as visible on Fig. 8.16a. The reduced plume width in this configuration, compared to section 8.4 and section 8.5, is a consequence of the drastic reduction of the upwind building wake. The individual column wakes produced in the SWIFT simulation, which do not interact between each other to produce a global recirculation zone, do not generate strong discrepancies on the concentration field in this case. The contaminated zone in the SLAM simulation also has a reduced extent compared to the ‘S25 solid’ and ‘S25 dense’ configurations, but the plume width is overestimated in the near field compared to experimental values. The vertical plume shape is hardly captured by both models close to the ground, as visible on Fig.8.16b. Neither model predicts the tracer presence inside the open area between buildings B1 and C, which is similar to the phenomenon observed in section 8.5.

In the mid-field, PMSS and SLAM simulations are very accurate, despite few discrepancies due to the slight over- and under-estimation of the plume width in the SLAM and PMSS simulations, respectively (see Fig. 8.16c). Similarly, SLAM and PMSS respectively over- and under-estimate the vertical plume extent, as shown in Fig. 8.16d. The model accuracy increases with the distance from source, the horizontal (see Fig. 8.16e) and vertical (see Fig. 8.16f) concentration profiles being accurately reproduced by both models despite few discrepancies at plume borders.

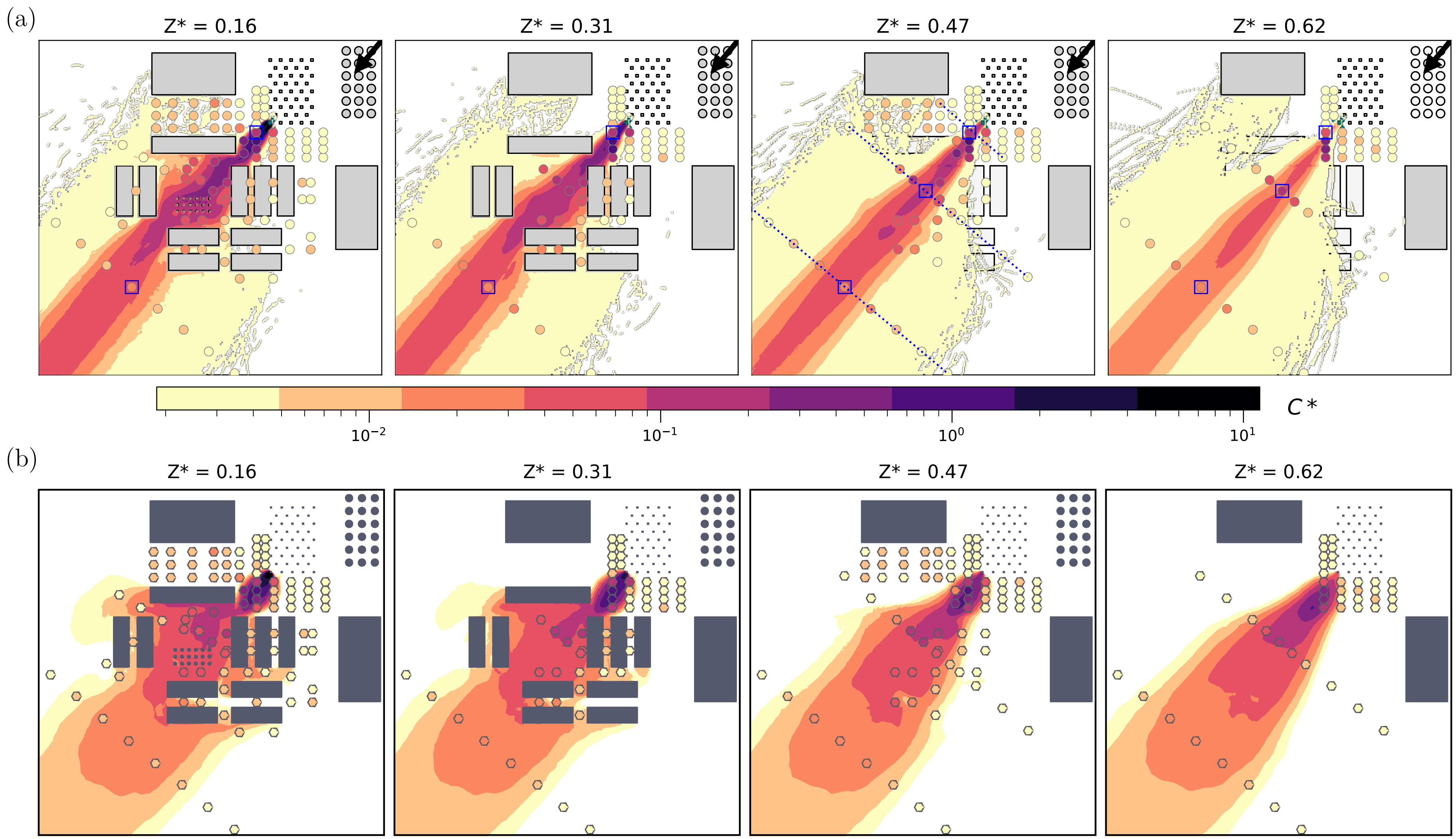

Figure 8.14: Same as Fig.8.8 for the ‘S25 spaced’ configuration.

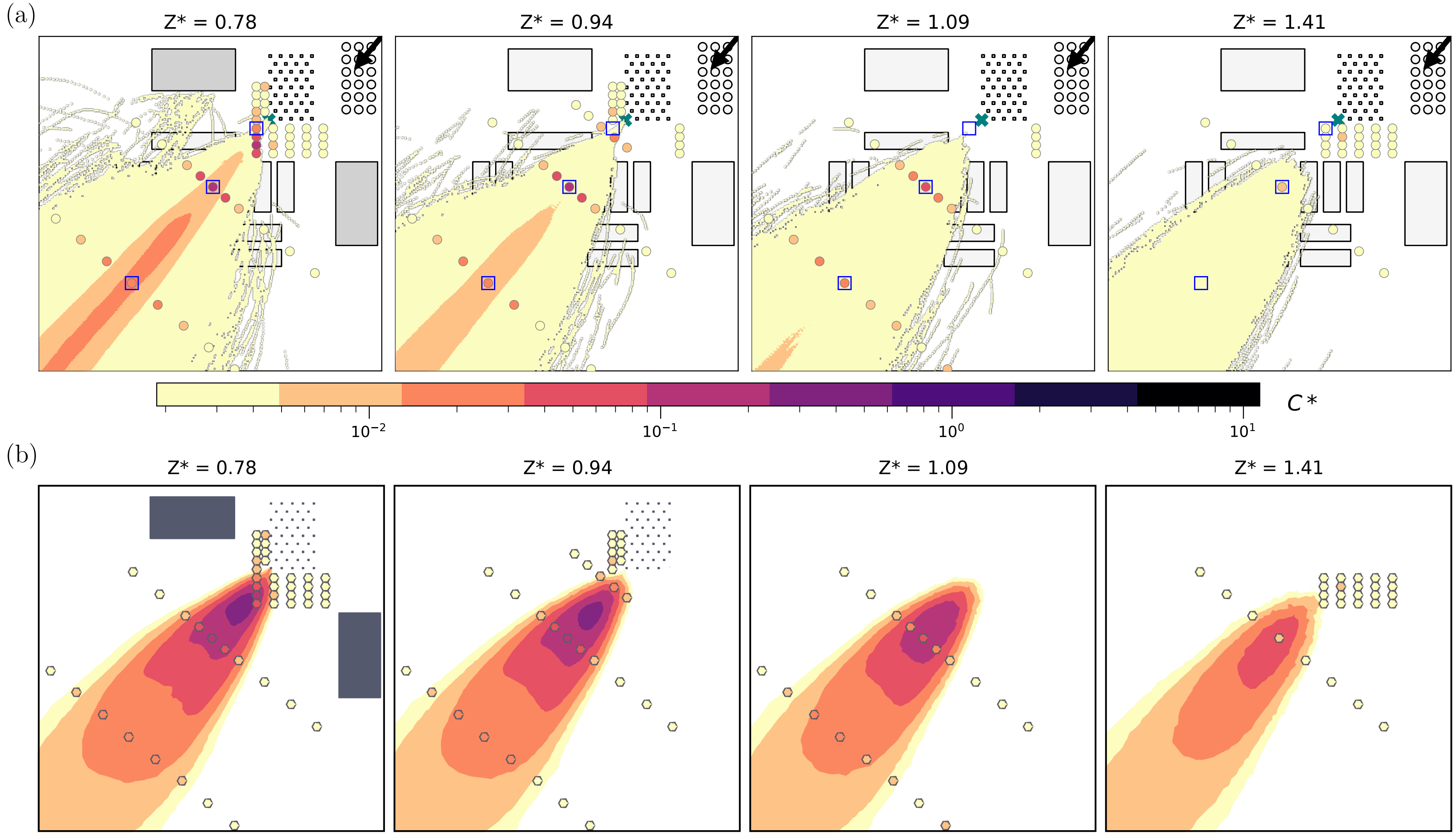

Figure 8.15: Same as Fig.8.14 for higher z^* levels.

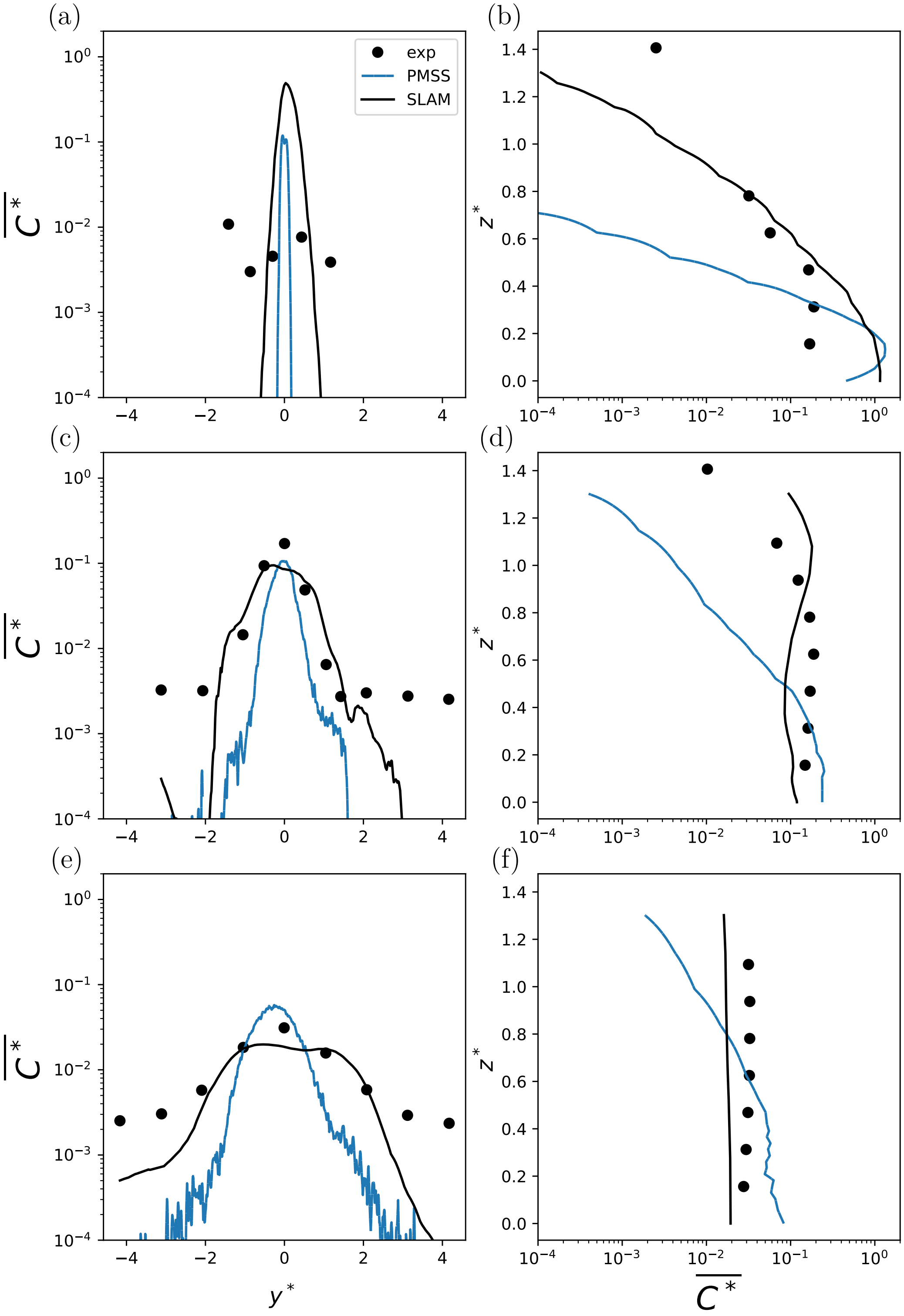

Figure 8.16: Concentration profiles on the locations shown in Fig.8.14. **a**: horizontal profile at $z^* = 0.47$ in the near field, **b**: vertical profile in the near field **c**: horizontal profile at $z^* = 0.47$ in the midfield **d**: vertical profile in the midfield, **e**: horizontal profile at $z^* = 0.47$ in the far field **f**: vertical profile in the far field.

8.7 Conclusion

This chapter presents the comparison of the simulated concentration fields to the experimental data. The performances of each of the two modelling methodologies strongly vary with the site configuration, as advantaging features in one case can become a drawback in another configuration.

The ability of the RANS simulations to reproduce the complex recirculating regions generated by grouped obstacles enables the simulation of very accurate concentration fields with SLAM in the ‘S5’, ‘S25 dense’ and ‘S25 spaced’ configurations. However, the too large recirculation zone to the side of building A in the ‘S25 solid’ configuration produces a mismatch in the plume shape, as this region is covered by the simulated plume while measurements evidence no presence of the tracer. Similarly, the erroneous upwind flow between buildings D4 and D5 in the ‘S4’ configuration lifts the plume and shifts its centreline, leading to a mismatch with the experimental data until the far field.

In contrast to the SLAM methodology, PMSS relies on a semi-empirical representation of the wind field, which does not account for flow interactions induced by neighbouring obstacles. Consequently, its performance is limited in configurations where such interactions play a significant role, as in the ‘S25 dense’ and ‘S25 spaced’ cases. In the ‘S25 solid’ configuration, the wake of the upwind building is too simplified, leading to a mismatch similar to that observed in the SLAM result: tracer presence is predicted where measurements show zero concentrations. The origin of the mismatch however differs between the two methodologies. In contrast, PMSS produces a more accurate result than SLAM in the ‘S4’ configuration, as no upward flux is predicted between the D buildings by this approach. However, PMSS tends to underestimate plume widths, which is consistently observed in the five investigated configurations.

For both modelling methodologies, the inaccurate modelling of dispersion in the near field propagates until the far field, particularly regarding the plume centreline and the plume width.

As none of the numerical models investigated in this work provides the variance of concentration, we did not model concentration fluctuations and peak values from the numerical concentration field, applying the methods presented in part I. Even though Bertagni et al. (2019b) developed a model to analytically estimate the variance of concentration from the transport equation of the PDF, it is however not suitable to complex geometry environments. Concentration variance should thus be provided by dispersion models to enable the computation of concentration fluctuations and peak-to-mean ratios such as developed in part I.

Conclusion of Part II

The systematic comparison of experimental and simulated flow and concentration fields presented in this work has a dual purpose. It first aims at determining the ability of dispersion models to capture the effects of the site geometry on the plume characteristics. Second, it serves to determine the modelling features that most impact the simulated concentration field. We evidence the crucial importance of the accurate modelling of the flow field, particularly for situations in which neighbouring obstacles generate complex interacting wakes. To this end, we designed an idealised industrial site, on which we simulated pollutant dispersion while varying the incoming wind direction, the source position and the building geometry. We notably investigated the effects of a porous structure on the flow and concentration fields. The tallest element of the site, a filled parallelepiped ('solid' configuration), was alternatively replaced by a dense group ('dense' configuration) and a sparse array ('spaced' configuration) of rectangular columns, mimicking complex piping structures often observed on industrial sites.

The two methodologies analysed in this work are very different in their approach of modelling the perturbative effect of obstacles on the flow field. While SWIFT relies on semi-empirical methods to determine leeward and windward recirculation zones attached to each obstacle, SLAM is based on the interpolation of pre-existing RANS simulations included in a pre-computed database. Our analysis evidences that the SWIFT approach produces realistic individual wakes but faces difficulties when complex obstacle arrangements produce interacting perturbative effects on the wind flow field. In particular, large scale channelling effects, and complex shape recirculation zones produced by grouped neighbouring obstacles, are not captured by the model. However, the SWIFT simplified flow field provides a sufficient description of wind velocity in the 'spaced' configuration even though it does not capture the full extent of recirculation zones and the channelling effects of neighbouring buildings on the flow field. The RANS simulations produce more accurate results than SWIFT, as they capture the common effects of grouped obstacles on the flow field. Notably, the RANS capacity to produce a global wake for the grouped columns forming the 'dense' A building proved to be crucial to obtain an accurate velocity field.

The five configurations of the realistic industrial site that were selected for model-experiment comparison were varied, and presented several features that revealed the limits of the two operational dispersion models. In particular, the characteristics of the flow field produced by the RANS simulation of the 130° incident wind direction produced discrepancies when the tracer originated from the 'S4' source. Counter currents generated inside the corridors formed by neighbouring D buildings resulted into the lateral shift of the plume centre line over the whole site. This surprising behaviour could be a consequence of the turbulence parametrisation and the surface roughness estimate, which are thus key parameters that potentially impact the resulting plume. In contrast, when the source was placed inside a less sensitive zone, as in the 'S5' configuration, the mismatch between the RANS and experimental flow fields did not produce strong discrepancies in the concentration field. The source position is thus an impactful parameter that has to be considered with care.

The ‘S25 dense’ configuration also possesses very specific geometrical features which harden the modelling of pollutant dispersion, particularly for PMSS, due to the upwind position of the porous obstacle, which is composed of a group of columns. This induces a strong dependence of the simulated concentration field on the ability of the model to reproduce the global recirculation generated by this obstacle. The global wake is much larger than the sum of individual column wakes, and it can even reach a bigger extent than the wake of a solid obstacle of same dimensions (Taddei et al., 2016). This is why the SLAM methodology, which relies on RANS simulations, produces more accurate plume shapes and concentration mean values than the PMSS method in this particular configuration. SWIFT possesses a feature enabling the consideration of many elements as being linked to form a unique obstacle, which was not tested in this work, since individual columns do not join their neighbours neither by their roof nor by linking elements (such as pipes or corridors at ground level). Further analysis would benefit from exploiting this feature to force a global recirculation zone of the ‘dense’ A building in the SWIFT simulations.

This work demonstrates the importance of considering the effects of obstacles on the wind velocity and pollutant concentration fields, both upwind and downwind of the source. Both methodologies that were tested in this work were able to provide an estimate of the perturbative effect of the site geometry on the simulated flow and concentration fields. PMSS produced reasonably accurate results close to the source, except in the ‘S25 dense’ configuration. Thus, we consider the simplified modelling approach applied in PMSS to be adapted to assess the extent of the contaminated zone in the immediate surrounding of the source, when the latter is far from complex elements having interacting perturbative effects the flow field. However, the PMSS approach reaches its limits in the mid- and the far-fields, due to the lack of consideration of interacting recirculation zones, particularly when they produce wake widening and channelling effects. Plumes produced in the PMSS simulations are globally too narrow at all distances from the source, which was also observed by Trini Castelli (2025).

More accurate results are provided by the SLAM methodology, but this is not systematic and it is highly dependent on the accuracy of the velocity field at small scale. The plume shape was globally captured in all cases except the ‘S4’ configuration, despite slight overestimations of the plume width in the ‘S25 spaced’ configuration, and under-estimations in the ‘S25 solid’ and ‘S5’ configurations. We suppose that most discrepancies originated from the surface roughness estimate, which strongly impacts the shape and number of recirculation zones attached to obstacles.

One of the limits of both of the studied approaches is that an average velocity field is not able to capture some intermittent behaviours notably at building corners, that mainly impact low concentration zones close to plume borders. This was observed particularly in the ‘S25 dense’ and ‘S25 spaced’ configurations, in which the tracer reached zones that are detached to the side of the main plume, in the experiment. Such intermittent behaviours can however be captured only by very time- and resource-consuming flow field simulations, such as LES and DNS. Additionally, the low concentrations generated by these intermittent effects are associated to a lower risk than high concentrations, which are reached around the plume centre line. The accurate consideration of this effect is therefore not a necessary improvement for operational purposes.

The analysis of the PMSS and SLAM operational approaches evidences that dispersion models relying on accurate wind flow simulations are necessary when pollutant dispersion has to be estimated inside complex geometry sites. Simplified approaches such as PMSS are reasonably accurate close to the source, but the plume width has to be corrected further from the source. Methods relying on RANS simulations, such as the SLAM methodology investigated here, are more accurate but they are highly dependent on the input meteorological information that is provided, and they can generate local behaviours that impact dispersion over the whole site. As this numerical study focuses on the mean concentration field, we do not simulate peak concentration values, which can exceed the mean by factors of several tens, nay by several orders of magnitude close to the source. To estimate accurately the risks linked to concentration peaks, it is necessary to access at least to the mean and the variance of concentration (Bertagni et al., 2019a). Simulating the concentration variance is thus a crucial feature that should be implemented in dispersion models for adequate risk estimates of accidental releases inside real built environments.

General conclusion and perspectives

Accidental airborne pollutant releases over industrial sites—resulting from leaks, fires, or explosions—require accurate assessment of health and environmental risks within operational time frames. However, the presence of buildings, tanks, and pipelines generates highly complex flow structures and dispersion phenomena that can only be fully captured using advanced modelling approaches. Consequently, this complexity may limit the applicability of simplified models, which are generally intended for operational use. The key challenge is therefore to identify an appropriate balance in the modelling approach: (i) accurate enough to capture the main flow and dispersion mechanisms, yet (ii) not so detailed that it requires the simulation of small-scale phenomena leading to prohibitive computational costs.

To address this problem, we investigated how the geometrical complexity of an idealised industrial site affects airflow and pollutant dispersion within and downwind of the site. To achieve this, we varied the porosity of one of the buildings within the site, altered the incident wind angles, and examined different pollutant release positions. The research consists of two main parts. The first involves experimental investigations conducted in a wind tunnel, while the second focuses on numerical simulations.

The experimental part of this study focuses on the characterisation of wind and concentration fields in a wind tunnel, with particular attention to concentration fluctuations. The experiments reveal complex recirculation and channelling patterns, with wake dynamics strongly influenced by the porosity of the structures. The statistics of one-point concentration fluctuations are analysed at several distances from the source. Specifically, we investigate the probability distribution function (PDF) of concentration. Near the source, the PDF is reasonably well described by a lognormal distribution, while in the midfield it is more accurately captured by a gamma distribution. This result extends the previously established validity of the gamma model over flat terrains (Cassiani et al., 2020) to built industrial environments. However, neither distribution fully captures the complex shapes of the measured PDFs, which are affected by the presence of obstacles and associated with high fluctuation intensities (i_C). A possible explanation is that the irregular PDF shapes arise from intermittent flow behaviour induced by complex recirculation patterns. Different wind flow regimes can cause tracer puffs to follow varying trajectories and experience different flight times. Consequently, the observed distributions may result from the convolution of PDFs with distinct parameters, leading to the complex shapes measured experimentally.

On the experimental side, future works could focus on deconvoluting the measured concentration PDFs, for instance by assuming a combination of two gamma distributions, to test the validity of this hypothesis. The assumption of a gamma PDF should therefore be applied with caution at locations where obstacles induce intermittent flows, such as near building corners. Nevertheless, high-percentile values are accurately captured by all tested distributions, which is particularly important for risk assessment scenarios involving hazardous peak contaminant exposures, such as evaluating threshold exceedances and peak concentrations. In this context, the model proposed by

Bertagni et al. (2020) provides estimates of threshold-exceedance statistics that could be integrated into operational models as a risk assessment tool. However, the implementation of crossing-time estimators in dispersion models depends on the availability of concentration variance values, which are often not provided by most operational models.

The numerical part of this study presents two operational models for simulating the flow and concentration fields. Both methodologies are based on the Lagrangian formulation of pollutant dispersion, but they differ in how the flow field is computed. PMSS is a semi-empirical model that ensures mass conservation, whereas SLAM relies on a database of pre-computed Reynolds Averaged Navier–Stokes (RANS) simulations. The objective of this comparison is to evaluate how the choice of the modelling approach affects the simulated pollutant concentration field. PMSS generates individual recirculation zones attached to obstacles but fails to capture the global effects of grouped obstacles on the flow. Consequently, concentration predictions are more accurate when the source is located in regions where complex recirculation effects are minimal, such as inside a corridor. Conversely, complex flow patterns produced by a porous structure immediately upwind of the source were not captured, leading to an underestimation of the plume extent across the site. RANS simulations generally provide more accurate results; however, in one of the investigated configurations a surprising counter-current formed inside the corridor containing the source, resulting in a mismatch with experimental data. This discrepancy is suspected to stem from the wall roughness values used as input in the RANS simulations. Therefore, numerical simulations should be interpreted with caution, particularly in operational contexts where input data, such as meteorological conditions and source characteristics, may be approximate due to time or accessibility constraints.

On the modelling side, future improvements could include modifications to the PMSS input to treat the group of columns forming the porous obstacle as a single element, with the aim of capturing the global wake. Additionally, the influence of wall roughness on recirculation zones in RANS simulations should be investigated to quantify its impact on simulation accuracy for the considered configurations. Since concentration variance is essential for modelling concentration fluctuations—a critical tool for risk assessment—implementing a method to compute concentration variance would represent a major advancement for operational models. The statistical characteristics of concentration fluctuations analysed experimentally in this study could be derived from the mean and variance of concentration. This would allow the estimation of high-order percentiles to capture concentration peaks and enable modelling of threshold-exceedance statistics, providing a quantitative assessment of worker exposure to hazardous pollutant levels.

Further studies could also explore negative and buoyant pollutant releases. Industrial sites often contain storage basins with tanks, which can act as area sources when a liquid leaks from the containers, spreads over the surface, and evaporates into the air. Complementary research should investigate how the site geometry affects the dispersion of heavy gases, given that approximately 90% of industrial accidents involve heavy gas leaks (Dou et al., 2022). Additionally, non-neutral atmospheric conditions should be considered, as a stable atmosphere tends to produce narrower, more concentrated pollutant plumes.

Finally, the experimental dataset offers a valuable foundation for future research, particularly in the validation of inverse atmospheric dispersion models. These models aim to estimate the location and mass flow rate of a pollutant source based on measured concentration fields. By providing detailed and well-characterized experimental data, this dataset can help improve model accuracy, test new inversion methodologies, and support the development of more reliable tools for source identification in complex industrial environments.

Bibliography

Abramowitz, M. and Stegun, I. A. (1965). *Handbook of Mathematical Functions, With Formulas, Graphs, and Mathematical Tables*. United States Department of Commerce, National Bureau of Standards. ISBN: 978-0-486-61272-0.

Andronopoulos, S., Grigoriadis, D., Robins, A., Venetsanos, A., Rafailidis, S., and Bartzis, J. (2001). "Three-Dimensional Modelling of Concentration Fluctuations in Complicated Geometry". In: *Environmental Fluid Mechanics* 1.4, pp. 415–440. ISSN: 1573-1510. DOI: `10.1023/A:1015705615846`.

ANSYS (2021). *Ansys Fluent Theory Guide*. ANSYS, Inc.

Ardeshiri, H., Cassiani, M., Park, S. Y., Stohl, A., Pisso, I., and Dinger, A. S. (2020). "On the Convergence and Capability of the Large-Eddy Simulation of Concentration Fluctuations in Passive Plumes for a Neutral Boundary Layer at Infinite Reynolds Number". In: *Boundary-Layer Meteorology* 176.3, pp. 291–327. ISSN: 1573-1472. DOI: `10.1007/s10546-020-00537-6`.

ARIA Technologies (2010). *SWIFT Wind Field Model*.

Arnold, S. J. et al. (2004). "Introduction to the DAPPLE Air Pollution Project". In: *Science of The Total Environment* 332.1, pp. 139–153. ISSN: 0048-9697. DOI: `10.1016/j.scitotenv.2004.04.020`.

Balczó, M. and Lajos, T. (2015). "Flow and Dispersion Phenomena in a Simplified Urban Square". In: *Periodica Polytechnica Civil Engineering* 59.3, pp. 347–360. ISSN: 1587-3773. DOI: `10.3311/PPci.7852`.

Bartzis, J. G., Sfetsos, A., and Andronopoulos, S. (2008). "On the Individual Exposure from Airborne Hazardous Releases: The Effect of Atmospheric Turbulence". In: *Journal of Hazardous Materials* 150.1, pp. 76–82. ISSN: 0304-3894. DOI: `10.1016/j.jhazmat.2007.04.078`.

Bastigkeit, I. (2011). "Als Dissertation angenommen vom Department Geowissenschaften der Universität Hamburg". PhD thesis. Universität Hamburg.

Bertagni, M. B., Camporeale, C., Marro, M., and Salizzoni, P. (2019a). *Crossing Times For A Passive Scalar In a Turbulent Boundary Layer*. EGU General Assembly Presentation. Vienna.

Bertagni, M. B., Marro, M., Salizzoni, P., and Camporeale, C. (2019b). "Solution for the Statistical Moments of Scalar Turbulence". In: *Physical Review Fluids* 4.12, p. 124701. DOI: `10.1103/PhysRevFluids.4.124701`.

Bertagni, M. B., Marro, M., Salizzoni, P., and Camporeale, C. (2020). "Level-Crossing Statistics of a Passive Scalar Dispersed in a Neutral Boundary Layer". In: *Atmospheric Environment* 230, p. 117518. ISSN: 1352-2310. DOI: `10.1016/j.atmosenv.2020.117518`.

Blazek, J. (2015). *Computational Fluid Dynamics: Principles and Applications*. Butterworth-Heinemann. Elsevier. ISBN: 978-0-08-099995-1. DOI: `10.1016/C2013-0-19038-1`.

Bohrer, G., Katul, G. G., Walko, R. L., and Avissar, R. (2009). "Exploring the Effects of Microscale Structural Heterogeneity of Forest Canopies Using Large-Eddy Simulations". In: *Boundary-*

Layer Meteorology 132.3, pp. 351–382. ISSN: 0006-8314, 1573-1472. DOI: `10.1007/s10546-009-9404-4`.

Boppana, V. B. L., Xie, Z.-T., and Castro, I. P. (2010). “Large-Eddy Simulation of Dispersion from Surface Sources in Arrays of Obstacles”. In: *Boundary-Layer Meteorology* 135.3, pp. 433–454. ISSN: 0006-8314, 1573-1472. DOI: `10.1007/s10546-010-9489-9`.

Borgas, M. S. and Sawford, B. L. (1994). “A Family of Stochastic Models for Two-Particle Dispersion in Isotropic Homogeneous Stationary Turbulence”. In: *Journal of Fluid Mechanics* 279, pp. 69–99. ISSN: 1469-7645, 0022-1120. DOI: `10.1017/S0022112094003824`.

Bou-Zeid, E., Overney, J., Rogers, B. D., and Parlange, M. B. (2009). “The Effects of Building Representation and Clustering in Large-Eddy Simulations of Flows in Urban Canopies”. In: *Boundary-Layer Meteorology* 132.3, pp. 415–436. ISSN: 0006-8314, 1573-1472. DOI: `10.1007/s10546-009-9410-6`.

Boussinesq, J. (1897). *Théorie de l’écoulement tourbillonnant et tumultueux des liquides dans les lits rectilignes à grande section*. Paris, France: Gauthier-Villars et fils.

Brancher, M., Hieden, A., Baumann-Stanzer, K., Schauberger, G., and Piringer, M. (2020). “Performance Evaluation of Approaches to Predict Sub-Hourly Peak Odour Concentrations”. In: *Atmospheric Environment: X* 7, p. 100076. ISSN: 2590-1621. DOI: `10.1016/j.aeaoa.2020.100076`.

Briggs, G. A. (1973). *Diffusion Estimation for Small Emissoins*. Tech. rep. Air Resources Atmospheric Turbulence and Diffusion Laboratory.

Carpentieri, M., Hayden, P., and Robins, A. G. (2012). “Wind Tunnel Measurements of Pollutant Turbulent Fluxes in Urban Intersections”. In: *Atmospheric Environment* 46, pp. 669–674. ISSN: 1352-2310. DOI: `10.1016/j.atmosenv.2011.09.083`.

Cassiani, M., Ardeshiri, H., Pisso, I., Salizzoni, P., Marro, M., Stohl, A., Stebel, K., and Park, S. Y. (2024). “The Dynamics of Concentration Fluctuations within Passive Scalar Plumes in a Turbulent Neutral Boundary Layer”. In: *Journal of Fluid Mechanics* 1001, A18. ISSN: 0022-1120, 1469-7645. DOI: `10.1017/jfm.2024.861`.

Cassiani, M., Bertagni, M. B., Marro, M., and Salizzoni, P. (2020). “Concentration Fluctuations from Localized Atmospheric Releases”. In: *Boundary-Layer Meteorology* 177.2, pp. 461–510. ISSN: 1573-1472. DOI: `10.1007/s10546-020-00547-4`.

Chang, J. C. and Hanna, S. R. (2004). “Air Quality Model Performance Evaluation”. In: *Meteorology and Atmospheric Physics* 87.1, pp. 167–196. ISSN: 1436-5065. DOI: `10.1007/s00703-003-0070-7`.

CITEPA (2024). *Rapport Secten, Emission de Gaz à Effets de Serre et de Polluants Atmosphériques En France 1990-2023*. Tech. rep.

Counihan, J., Hunt, J. C. R., and Jackson, P. S. (1974). “Wakes behind Two-Dimensional Surface Obstacles in Turbulent Boundary Layers”. In: *Journal of Fluid Mechanics* 64.3, pp. 529–564. ISSN: 0022-1120, 1469-7645. DOI: `10.1017/S0022112074002539`.

Crank, P. J., Sailor, D. J., Ban-Weiss, G., and Taleghani, M. (2018). “Evaluating the ENVI-met Microscale Model for Suitability in Analysis of Targeted Urban Heat Mitigation Strategies”. In: *Urban Climate* 26, pp. 188–197. ISSN: 2212-0955. DOI: `10.1016/j.uclim.2018.09.002`.

Davidson, M. J., Mylne, K. R., Jones, C. D., Phillips, J. C., Perkins, R. J., Fung, J. C. H., and Hunt, J. C. R. (1995). “Plume Dispersion through Large Groups of Obstacles—A Field Investigation”. In: *Atmospheric Environment* 29.22, pp. 3245–3256. ISSN: 1352-2310. DOI: `10.1016/1352-2310(95)00254-V`.

Del Ponte, A. V., Fellini, S., Marro, M., van Reeuwijk, M., Ridolfi, L., and Salizzoni, P. (2024). “Influence of Street Trees on Turbulent Fluctuations and Transport Processes in an Urban

Canyon: A Wind Tunnel Study". In: *Boundary-Layer Meteorology* 190.2, p. 6. ISSN: 1573-1472. DOI: `10.1007/s10546-023-00843-9`.

Dong, L. X., Zuo, H. C., and Dong, W. C. (2013). "Validation of CALPUFF Applicability within Urban Area". In: *Advanced Materials Research* 726–731, pp. 1813–1816. ISSN: 1662-8985. DOI: `10.4028/www.scientific.net/AMR.726-731.1813`.

Dou, Z. et al. (2022). "Atmospheric Dispersion Prediction of Accidental Release: A Review". In: *Emergency Management Science and Technology* 2.EMST-2022-0009, pp. 1–20. ISSN: 2832-448X. DOI: `10.48130/EMST-2022-0009`.

Duan, R.-R., Hao, K., and Yang, T. (2020). "Air Pollution and Chronic Obstructive Pulmonary Disease". In: *Chronic Diseases and Translational Medicine* 6.4, pp. 260–269. ISSN: 2589-0514. DOI: `10.1016/j.cdtm.2020.05.004`.

Efthimiou, G. C., Andronopoulos, S., Tolias, I., and Venetsanos, A. (2016). "Prediction of the Upper Tail of Concentration Distributions of a Continuous Point Source Release in Urban Environments". In: *Environmental Fluid Mechanics* 16.5, pp. 899–921. ISSN: 1573-1510. DOI: `10.1007/s10652-016-9455-2`.

Elshaer, A., Aboshosha, H., Bitsuamlak, G., El Damatty, A., and Dagnew, A. (2016). "LES Evaluation of Wind-Induced Responses for an Isolated and a Surrounded Tall Building". In: *Engineering Structures* 115, pp. 179–195. ISSN: 0141-0296. DOI: `10.1016/j.engstruct.2016.02.026`.

Fackrell, J. E. (1980). "A Flame Ionisation Detector for Measuring Fluctuating Concentration". In: *Journal of Physics E: Scientific Instruments* 13.8, pp. 888–893. ISSN: 0022-3735. DOI: `10.1088/0022-3735/13/8/021`.

Fackrell, J. E. and Robins, A. G. (1982a). "Concentration Fluctuations and Fluxes in Plumes from Point Sources in a Turbulent Boundary Layer". In: *Journal of Fluid Mechanics* 117, pp. 1–26. ISSN: 1469-7645, 0022-1120. DOI: `10.1017/S0022112082001499`.

Fackrell, J. E. and Robins, A. G. (1982b). "The Effects of Source Size on Concentration Fluctuations in Plumes". In: *Boundary-Layer Meteorology* 22.3, pp. 335–350. ISSN: 1573-1472. DOI: `10.1007/BF00120014`.

Franke, J. and Britter, R. (2011). "Quality Assurance and Improvement of Micro-Scale Meteorological Models". In: *International Journal of Environment and Pollution* 44.1/2/3/4, p. 139. ISSN: 0957-4352, 1741-5101. DOI: `10.1504/IJEP.2011.038412`.

Gadilhe, A, Janvier, L, and Barnaud, G (1993). "Numerical and Experimental Modelling of the Three-Dimensional Turbulent Wind Flow through an Urban Square". In: *Journal of Wind Engineering and Industrial Aerodynamics*. Proceedings of the 1st International on Computational Wind Engineering 46–47, pp. 755–763. ISSN: 0167-6105. DOI: `10.1016/0167-6105(93)90349-S`.

Gailis, R. M. and Hill, A. (2006). "A Wind-Tunnel Simulation of Plume Dispersion Within a Large Array of Obstacles". In: *Boundary-Layer Meteorology* 119.2, pp. 289–338. ISSN: 1573-1472. DOI: `10.1007/s10546-005-9029-1`.

Gailis, R. M., Hill, A., Yee, E., and Hilderman, T. (2007). "Extension of a Fluctuating Plume Model of Tracer Dispersion to a Sheared Boundary Layer and to a Large Array of Obstacles". In: *Boundary-Layer Meteorology* 122.3, pp. 577–607. ISSN: 1573-1472. DOI: `10.1007/s10546-006-9118-9`.

Gardiner, C. W. (1985). *Handbook of Stochastic Methods for Physics, Chemistry and the Natural.* Springer Verlag. ISBN: 3-540-61634-9.

Garratt, J. R. (1994). *The Atmospheric Boundary Layer.* Cambridge University Press. ISBN: 978-0-521-46745-2.

Gifford, F. (1959). “Statistical Properties of A Fluctuating Plume Dispersion Model”. In: *Advances in Geophysics* 6. Ed. by H. E. Landsberg and J. Van Mieghem, pp. 117–137. DOI: `10.1016/S0065-2687(08)60099-0`.

Haan, P. de (1999). “On the Use of Density Kernels for Concentration Estimations within Particle and Puff Dispersion Models”. In: *Atmospheric Environment* 33.13, pp. 2007–2021. ISSN: 1352-2310. DOI: `10.1016/S1352-2310(98)00424-5`.

Hajra, B., Stathopoulos, T., and Bahloul, A. (2013). “A Wind Tunnel Study of the Effects of Adjacent Buildings on Near-Field Pollutant Dispersion from Rooftop Emissions in an Urban Environment”. In: *Journal of Wind Engineering and Industrial Aerodynamics* 119, pp. 133–145. ISSN: 0167-6105. DOI: `10.1016/j.jweia.2013.05.003`.

Hang, J., Li, Y., Sandberg, M., Buccolieri, R., and Di Sabatino, S. (2012). “The Influence of Building Height Variability on Pollutant Dispersion and Pedestrian Ventilation in Idealized High-Rise Urban Areas”. In: *Building and Environment* 56, pp. 346–360. ISSN: 0360-1323. DOI: `10.1016/j.buildenv.2012.03.023`.

Hang, J., Sandberg, M., and Li, Y. (2009). “Effect of Urban Morphology on Wind Condition in Idealized City Models”. In: *Atmospheric Environment* 43.4, pp. 869–878. ISSN: 1352-2310. DOI: `10.1016/j.atmosenv.2008.10.040`.

Hanna, S. R, Strimaitis, D. G., and Chang, J. C. (1991). *Hazard Response Modeling Uncertainty (A Quantitative Method), Vol. I: User’s Guide for Software for Evaluating Hazardous Gas Dispersion Models; Vol. II: Evaluation of Commonly-Used Hazardous Gas Dispersion Models; Vol. III: Components of Uncertainty in Hazardous Gas Dispersion Models.* Tech. rep. A119=A120. Earth Tech, Inc., 196 Baker Avenue, Concord, MA 01742, for Engineering and Services Laboratory, Air Force Engineering and Services Center, Tyndall Air Force Base, FL 32403; and for American Petroleum Institute, 1220 L Street, N.W., Washington, D.C., 20005.

Hanna, S. and Chang, J. (2012). “Acceptance Criteria for Urban Dispersion Model Evaluation”. In: *Meteorology and Atmospheric Physics* 116.3, pp. 133–146. ISSN: 1436-5065. DOI: `10.1007/s00703-011-0177-1`.

Hanna, S. R. (1984). “The Exponential Probability Density Function and Concentration Fluctuations in Smoke Plumes”. In: *Boundary-Layer Meteorology* 29.4, pp. 361–375. ISSN: 1573-1472. DOI: `10.1007/BF00120535`.

Hatcher, R. V., Meroney, R. N., Peterka, J. A., and Kothari, K. (1977). *Dispersion in the Wake of a Model Industrial Complex.* Tech. rep. Fluid Dynamics and Diffusion Laboratory, Department of Civil Engineering, Colorado State University. HDL: `10217/47375`.

Hertwig, D., Gough, H. L., Grimmond, S., Barlow, J. F., Kent, C. W., Lin, W. E., Robins, A. G., and Hayden, P. (2019). “Wake Characteristics of Tall Buildings in a Realistic Urban Canopy”. In: *Boundary-Layer Meteorology* 172.2, pp. 239–270. ISSN: 1573-1472. DOI: `10.1007/s10546-019-00450-7`.

Heus, T. et al. (2010). “Formulation of the Dutch Atmospheric Large-Eddy Simulation (DALES) and Overview of Its Applications”. In: *Geoscientific Model Development* 3.2, pp. 415–444. ISSN: 1991-959X. DOI: `10.5194/gmd-3-415-2010`.

Hinds, W. T. (1969). “Peak-to-Mean Concentration Ratios from Ground-Level Sources in Building Wakes”. In: *Atmospheric Environment (1967)* 3.2, pp. 145–156. ISSN: 0004-6981. DOI: `10.1016/0004-6981(69)90005-5`.

Hirose, C., Nomichi, T., and Ikegaya, N. (2022). “Distributions of Gust and Peak Factors at a Pedestrian Level in a Simplified Urban Canopy Obtained by Particle Image Velocimetry”. In: *Building and Environment* 222, p. 109350. ISSN: 0360-1323. DOI: `10.1016/j.buildenv.2022.109350`.

H'ng, Y. M., Ikegaya, N., Zaki, S. A., Hagishima, A., and Mohammad, A. F. (2022). "Wind-Tunnel Estimation of Mean and Turbulent Wind Speeds within Canopy Layer for Urban Campus". In: *Urban Climate* 41, p. 101064. ISSN: 2212-0955. DOI: `10.1016/j.uclim.2021.101064`.

Hosker, R. P. J. (1981). *Methods for Estimating Wake Flow and Effluent Dispersion near Simple Block-like Buildings.* Tech. rep. NOAA-TM-ERL-ARL-108, 5359876, NOAA–TM–ERL–ARL–108, 5359876. DOI: `10.2172/5359876`.

Hotchkiss, R. S. and Harlow, F. H. (1973). *Air Pollution Transport in Street Canyons.* Tech. rep. EPA-R4-73-029. Washington, D. C.: U.S. Environmental Protection Agency, p. 129.

Hunt, J. C. R. (1971). "A Theory for the Laminar Wake of a Two-Dimensional Body in a Boundary Layer". In: *Journal of Fluid Mechanics* 49.1, pp. 159–178. ISSN: 1469-7645, 0022-1120. DOI: `10.1017/S0022112071001988`.

Irwin, H. P. A. H. (1981). "The Design of Spires for Wind Simulation". In: *Journal of Wind Engineering and Industrial Aerodynamics* 7.3, pp. 361–366. ISSN: 0167-6105. DOI: `10.1016/0167-6105(81)90058-1`.

Janicke, L. and Janicke, U. (2004). *Development of the Dispersion Model AUSTAL2000G.* Berichte Zur Umweltphysik 5. Dunum: Ingenieurbüro Janicke, p. 122.

Janour, Z., Jurcakova, K., Brych, K., Dittrt, F., and Dittrich, F. (2010). "Potential Risks at an Industrial Site: A Wind Tunnel Study". In: *Process Safety and Environmental Protection* 88.3, pp. 185–190. ISSN: 09575820. DOI: `10.1016/j.psep.2010.01.003`.

Jiang, Z., Kobayashi, T., Yamanaka, T., Sandberg, M., Choi, N., Kobayashi, N., Sano, K., and Toyosawa, K. (2023). "Wind Tunnel Experiment of Wind-Induced Single-Sided Ventilation under Generic Sheltered Urban Area". In: *Building and Environment* 242, p. 110615. ISSN: 0360-1323. DOI: `10.1016/j.buildenv.2023.110615`.

Jones, W. P and Launder, B. E (1972). "The Prediction of Laminarization with a Two-Equation Model of Turbulence". In: *International Journal of Heat and Mass Transfer* 15.2, pp. 301–314. ISSN: 0017-9310. DOI: `10.1016/0017-9310(72)90076-2`.

Kampen, N. G. V. (1992). *Stochastic Processes in Physics and Chemistry.* Elsevier. ISBN: 978-0-08-057138-6.

Kanda, M. (2006). "Large-Eddy Simulations on the Effects of Surface Geometry of Building Arrays on Turbulent Organized Structures". In: *Boundary-Layer Meteorology* 118.1, pp. 151–168. ISSN: 1573-1472. DOI: `10.1007/s10546-005-5294-2`.

Kaplan, H. and Dinar, N. (1996). "A Lagrangian Dispersion Model for Calculating Concentration Distribution within a Built-up Domain". In: *Atmospheric Environment* 30.24, pp. 4197–4207. ISSN: 1352-2310. DOI: `10.1016/1352-2310(96)00144-6`.

Kim, Y., Wu, Y., Seigneur, C., and Roustan, Y. (2018). "Multi-Scale Modeling of Urban Air Pollution: Development and Application of a Street-in-Grid Model (v1.0) by Coupling MUNICH (v1.0) and Polair3D (v1.8.1)". In: *Geoscientific Model Development* 11.2, pp. 611–629. ISSN: 1991-959X. DOI: `10.5194/gmd-11-611-2018`.

Klippel, K. (2025). "Flow Variability and Stochastic Dispersion in Street Networks". PhD thesis.

Kolmogorov, A. N. (1941). "Local Structure of Turbulence in Incompressible Fluid under Very High Values of Reynolds Numbers". In: *Dokl. Akad. Nauk SSSR.* 31, pp. 99–101.

Ku, C.-A. and Tsai, H.-K. (2020). "Evaluating the Influence of Urban Morphology on Urban Wind Environment Based on Computational Fluid Dynamics Simulation". In: *ISPRS International Journal of Geo-Information* 9.6, p. 399. ISSN: 2220-9964. DOI: `10.3390/ijgi9060399`.

Kullback, S. and Leibler, R. A. (1951). "On Information and Sufficiency". In: *The Annals of Mathematical Statistics* 22.1, pp. 79–86. ISSN: 0003-4851, 2168-8990. DOI: `10.1214/aoms/1177729694`.

Langevin, P. (1908). "Sur La Théorie Du Mouvement Brownien". In: *Compte Rendu de l'Académie des Sciences (Paris)* 146, pp. 530–533.

Lazaridis, M. (2011). *First Principles of Meteorology and Air Pollution.* Vol. 19. Environmental Pollution. Dordrecht: Springer Netherlands. ISBN: 978-94-007-0161-8 978-94-007-0162-5. DOI: `10.1007/978-94-007-0162-5`.

Lim, H. D. and Vanderwel, C. (2023). "Turbulent Dispersion of a Passive Scalar in a Smooth-Wall Turbulent Boundary Layer". In: *Journal of Fluid Mechanics* 969, A26. ISSN: 0022-1120, 1469-7645. DOI: `10.1017/jfm.2023.562`.

Loomis, D. et al. (2013). "The Carcinogenicity of Outdoor Air Pollution". In: *The Lancet Oncology* 14.13, pp. 1262–1263. ISSN: 1470-2045. DOI: `10.1016/S1470-2045(13)70487-X`.

Luhar, A. K. and Rao, K. S. (1994). "Lagrangian Stochastic Dispersion Model Simulations of Tracer Data in Nocturnal Flows over Complex Terrain". In: *Atmospheric Environment* 28.21, pp. 3417–3431. ISSN: 1352-2310. DOI: `10.1016/1352-2310(94)90002-7`.

Lung, T., Müller, H.-J., Gläser, M., and Möller, B. (2002). "Measurements and Modelling of Full-Scale Concentration Fluctuations". In: *Agratechnische Forschung* 8, pp. 5–15.

Macdonald, R. W. (2000). "Modelling The Mean Velocity Profile In The Urban Canopy Layer". In: *Boundary-Layer Meteorology* 97.1, pp. 25–45. ISSN: 1573-1472. DOI: `10.1023/A:1002785830512`.

Macdonald, R. W., Carter Schofield, S., and Slawson, P. R. (2002). "Physical Modelling of Urban Roughness Using Arrays of Regular Roughness Elements". In: *Water, Air and Soil Pollution: Focus* 2.5, pp. 541–554. ISSN: 1573-2940. DOI: `10.1023/A:1021392914279`.

Macdonald, R. W., Griffiths, R. F., and Hall, D. J. (1998). "A Comparison of Results from Scaled Field and Wind Tunnel Modelling of Dispersion in Arrays of Obstacles". In: *Atmospheric Environment* 32.22, pp. 3845–3862. ISSN: 1352-2310. DOI: `10.1016/S1352-2310(98)80006-X`.

Maronga, B. et al. (2015). "The Parallelized Large-Eddy Simulation Model (PALM) Version 4.0 for Atmospheric and Oceanic Flows: Model Formulation, Recent Developments, and Future Perspectives". In: *Geoscientific Model Development* 8.8, pp. 2515–2551. ISSN: 1991-959X. DOI: `10.5194/gmd-8-2515-2015`.

Marro, M., Gamel, H., Méjean, P., Correia, H., Soulhac, L., and Salizzoni, P. (2020). "High-Frequency Simultaneous Measurements of Velocity and Concentration within Turbulent Flows in Wind-Tunnel Experiments". In: *Experiments in Fluids* 61.12, p. 245. ISSN: 1432-1114. DOI: `10.1007/s00348-020-03074-7`.

Marro, M., Salizzoni, P., Cierco, F. X., Korsakissok, I., Danzi, E., and Soulhac, L. (2014). "Plume Rise and Spread in Buoyant Releases from Elevated Sources in the Lower Atmosphere". In: *Environmental Fluid Mechanics* 14.1, pp. 201–219. ISSN: 1573-1510. DOI: `10.1007/s10652-013-9300-9`.

Marucci, D. and Carpentieri, M. (2020). "Dispersion in an Array of Buildings in Stable and Convective Atmospheric Conditions". In: *Atmospheric Environment* 222, p. 117100. ISSN: 1352-2310. DOI: `10.1016/j.atmosenv.2019.117100`.

Mavroidis, I., Andronopoulos, S., Venetsanos, A., and Bartzis, J. G. (2015). "Numerical Investigation of Concentrations and Concentration Fluctuations around Isolated Obstacles of Different Shapes. Comparison with Wind Tunnel Results". In: *Environmental Fluid Mechanics* 15.5, pp. 999–1034. ISSN: 1567-7419, 1573-1510. DOI: `10.1007/s10652-015-9394-3`.

Michálek, P., Procházka, P., Uruba, V., and Pospíšil, S. (2022). "Influence of Surface Roughness on the Wake Structure of a Circular Cylinder at Reynolds Number 5e3 to 12e3". In: *European Journal of Mechanics - B/Fluids* 96, pp. 15–25. ISSN: 0997-7546. DOI: `10.1016/j.euromechflu.2022.06.003`.

Naden, R. A. and Leeds, J. V. (1972). “The Modification of Plume Models to Account for Long Averaging Times”. In: *Atmospheric Environment (1967)* 6.11, pp. 829–845. ISSN: 0004-6981. DOI: `10.1016/0004-6981(72)90055-8`.

Nguyen, C. V. (2017). “Assimilation de données et couplage d’échelles pour la simulation de la dispersion atmosphérique en milieu urbain”. PhD thesis. Ecole Centrale de Lyon: Université de Lyon.

Nironi, C. (2013). “Concentration Fluctuations of a Passive Scalar in a Turbulent Boundary Layer”. PhD thesis. Ecole Centrale de Lyon: Université de Lyon.

Nironi, C., Salizzoni, P., Marro, M., Mejean, P., Grosjean, N., and Soulhac, L. (2015). “Dispersion of a Passive Scalar Fluctuating Plume in a Turbulent Boundary Layer. Part I: Velocity and Concentration Measurements”. In: *Boundary-Layer Meteorology* 156.3, pp. 415–446. ISSN: 1573-1472. DOI: `10.1007/s10546-015-0040-x`.

Obukhov, A. M. (1971). “Turbulence in an Atmosphere with a Non-Uniform Temperature”. In: *Boundary-Layer Meteorology* 2.1, pp. 7–29. ISSN: 1573-1472. DOI: `10.1007/BF00718085`.

Oettl, D. and Ferrero, E. (2017). “A Simple Model to Assess Odour Hours for Regulatory Purposes”. In: *Atmospheric Environment* 155, pp. 162–173. ISSN: 1352-2310. DOI: `10.1016/j.atmosenv.2017.02.022`.

Oldrini, O., Armand, P., Duchenne, C., Olry, C., Moussafir, J., and Tinarelli, G. (2017). “Description and Preliminary Validation of the PMSS Fast Response Parallel Atmospheric Flow and Dispersion Solver in Complex Built-up Areas”. In: *Environmental Fluid Mechanics* 17.5, pp. 997–1014. ISSN: 1573-1510. DOI: `10.1007/s10652-017-9532-1`.

Ono, A. and Nozu, T. (2024). “Comparison between Wind Tunnel Experiment and Large-Eddy Simulation of Concentration Fluctuations in Pollutant Dispersion in a Realistic Urban Area”. In: *Journal of Wind Engineering and Industrial Aerodynamics* 253, p. 105832. ISSN: 0167-6105. DOI: `10.1016/j.jweia.2024.105832`.

Pandey, G., Venkatram, A., and Arunachalam, S. (2023). “Evaluating AERMOD with Measurements from a Major U.S. Airport Located on a Shoreline”. In: *Atmospheric Environment* 294, p. 119506. ISSN: 1352-2310. DOI: `10.1016/j.atmosenv.2022.119506`.

Pantusheva, M., Mitkov, R., Hristov, P. O., and Petrova-Antonova, D. (2022). “Air Pollution Dispersion Modelling in Urban Environment Using CFD: A Systematic Review”. In: *Atmosphere* 13.10, p. 1640. ISSN: 2073-4433. DOI: `10.3390/atmos13101640`.

Papp, B., Istók, B., Koren, M., Balczó, M., and Kristóf, G. (2024). “Statistical Assessment of the Concentration Fluctuations in Street Canyons via Time-Resolved Wind Tunnel Experiments”. In: *Journal of Wind Engineering and Industrial Aerodynamics* 246, p. 105665. ISSN: 0167-6105. DOI: `10.1016/j.jweia.2024.105665`.

Pasquill, F. (1961). “The Estimation of the Dispersion of Windborne Material”. In: *Meteorology Magazine* 90, pp. 33–40.

Peterka, J. A., Meroney, R. N., and Kothari, K. M. (1985). “Wind Flow Patterns about Buildings”. In: *Journal of Wind Engineering and Industrial Aerodynamics* 21.1, pp. 21–38. ISSN: 0167-6105. DOI: `10.1016/0167-6105(85)90031-5`.

Piomelli, U. and Balaras, E. (2002). “WALL-LAYER MODELS FOR LARGE-EDDY SIMULATIONS”. In: *Annual Review of Fluid Mechanics* 34.Volume 34, 2002, pp. 349–374. ISSN: 0066-4189, 1545-4479. DOI: `10.1146/annurev.fluid.34.082901.144919`.

Piringer, M. and Schauberger, G. (2012). “Dispersion Modelling for Odour Exposure Assessment”. In: *Odour Impact Assessment Handbook*. Ed. by V. Belgiorno, V. Naddeo, and T. Zarra. 1st ed. Wiley, pp. 125–174. ISBN: 978-1-119-96928-0 978-1-118-48126-4. DOI: `10.1002/9781118481264.ch5`.

Piringer, M., Knauder, W., Petz, E., and Schauberger, G. (2015). “A Comparison of Separation Distances against Odour Annoyance Calculated with Two Models”. In: *Atmospheric Environment* 116, pp. 22–35. ISSN: 1352-2310. DOI: `10.1016/j.atmosenv.2015.06.006`.

Pisso, I. et al. (2019). “The Lagrangian Particle Dispersion Model FLEXPART Version 10.4”. In: *Geoscientific Model Development* 12.12, pp. 4955–4997. ISSN: 1991-959X. DOI: `10.5194/gmd-12-4955-2019`.

Pope, S. (2000). *Turbulent Flows*. Cambridge University Press. Cambridge, UK.

Princevac, M., Baik, J.-J., Li, X., Pan, H., and Park, S.-B. (2010). “Lateral Channeling within Rectangular Arrays of Cubical Obstacles”. In: *Journal of Wind Engineering and Industrial Aerodynamics* 98.8, pp. 377–385. ISSN: 0167-6105. DOI: `10.1016/j.jweia.2009.11.001`.

Quaranta, N, De Martini, A, Bellasio, R, Bianconi, R, and Marioni, M (2001). “A Modelling System for the Simulation of Industrial Accidents”. In: *7th International Conference on Harmonisation within Atmospheric Dispersion Modelling for Regulatory Purposes*. Belgirate, Italy.

Ramponi, R., Blocken, B., de Coo, L. B., and Janssen, W. D. (2015). “CFD Simulation of Outdoor Ventilation of Generic Urban Configurations with Different Urban Densities and Equal and Unequal Street Widths”. In: *Building and Environment* 92, pp. 152–166. ISSN: 0360-1323. DOI: `10.1016/j.buildenv.2015.04.018`.

Ratto, C. F., Festa, R., Romeo, C., Frumento, O. A., and Galluzzi, M. (1994). “Mass-Consistent Models for Wind Fields over Complex Terrain: The State of the Art”. In: *Environmental Software* 9.4, pp. 247–268. ISSN: 0266-9838. DOI: `10.1016/0266-9838(94)90023-X`.

Ravina, M., Brignone, M., Urbinati, F., Schiavini, C., Zanetti, M., and Panepinto, D. (2025). “Predicting the Consequences of a NaTech Event: Occupational Short-Term Inhalation Risk Supported by Advanced Pollutant Dispersion Modeling”. In: *Integrated Environmental Assessment and Management*, vjaf073. ISSN: 1551-3777. DOI: `10.1093/inteam/vjaf073`.

Revuz, D. and Yor, M. (1999). *Continuous Martingales and Brownian Motion*. Ed. by S. S. Chern et al. Vol. 293. Grundlehren Der Mathematischen Wissenschaften. Berlin, Heidelberg: Springer. ISBN: 978-3-642-08400-3 978-3-662-06400-9. DOI: `10.1007/978-3-662-06400-9`.

Reynolds, O. (1895). “On the Dynamical Theory of Incompressible Viscous Fluids and the Determination of the Criterion | Philosophical Transactions of the Royal Society of London. (A.)” In: *Phylosophical Transactions of the Royal Society of London* 186, pp. 123–164. DOI: `10.1098/rsta.1895.0004`.

Ridolfi, L., D’Odorico, P., and Laio, F. (2011). *Noise-Induced Phenomena in the Environmental Sciences*. Cambridge University Press. ISBN: 978-1-139-49825-8.

Röckle, R. (1990). “Bestimmung der Strömungsverhältnisse im Bereich komplexer Bebauungsstrukturen”. PhD thesis. Technischen Hochschule Darmstadt.

Ryall, D. B. and Maryon, R. H. (1998). “Validation of the UK Met. Office’s Name Model against the ETEX Dataset”. In: *Atmospheric Environment* 32.24, pp. 4265–4276. ISSN: 1352-2310. DOI: `10.1016/S1352-2310(98)00177-0`.

Salizzoni, P., Fellini, S., Gamel, H., Marro, M., and Soulhac, L. (2025). “Atmospheric Dispersion Downstream a Two-Dimensional Obstacle: Experimental Evaluation of Turbulence Closure Models”. In: *Boundary-Layer Meteorology* 191.3, p. 15. ISSN: 1573-1472. DOI: `10.1007/s10546-025-00905-0`.

Sasaki, Y. (1958). “An ObJective Analysis Based on the Variational Method”. In: *Journal of the Meteorological Society of Japan. Ser. II* 36.3, pp. 77–88. DOI: `10.2151/jmsj1923.36.3_77`.

Schauberger, G. et al. (2012). “Concept to Assess the Human Perception of Odour by Estimating Short-Time Peak Concentrations from One-Hour Mean Values. Reply to a Comment by Janicke et Al." In: *Atmospheric Environment* 54, pp. 624–628. ISSN: 1352-2310. DOI: `10.1016/j.atmosenv.2012.02.017`.

Schiavini, C., Marro, M., Salizzoni, P., Soulhac, L., Ravina, M., Panepinto, D., and Zanetti, M. (2024). "Comparison between Simulation and Wind-Tunnel Experiment for an Idealised Industrial Site". In: *International Workshop on Physical Modelling of Flow and Dispersion Phenomena*. Lyon, France.

Schiavini, C., Marro, M., Salizzoni, P., Soulhac, L., Ravina, M., Panepinto, D., and Zanetti, M. (2025a). "Concentration Fluctuations and Mean Time of Exceeding of Hazard Thresholds on Industrial Sites". In: *EGU 2025*. Copernicus Meetings. DOI: `10.5194/egusphere-egu25-6010`.

Schiavini, C., Ravina, M., Panepinto, D., Zanetti, M., Marro, M., Lamaison, G., Soulhac, L., and Salizzoni, P. (2025b). "Validation of Lagrangian Dispersion Models with Wind Tunnel Experiments for an Idealised Industrial Site". In: *23rd International Conference on Harmonisation within Atmospheric Dispersion Modelling for Regulatory Purposes*. Hamburg, Germany.

Slimani, M. (2022). "Validation numérique et expérimentale d'une approche de modélisation lagrangienne à réponse rapide pour des rejets de substances dangereuses en milieu industriel ou urbain." PhD thesis. Université de Lyon.

Smith, M. (1968). *Recommended Guide for the Prediction of the Dispersion of Airborne Effluents*. American Society for Mechanical Engineers.

Smith, S., Stocker, J., Seaton, M., and Carruthers, D. (2017). "Model Inter-Comparison and Validation of ADMS Plume Chemistry Schemes". In: *International Journal of Environment and Pollution* 62.2-4, pp. 395–406. ISSN: 0957-4352. DOI: `10.1504/IJEP.2017.089427`.

Snoun, H., Krichen, M., and Chérif, H. (2023). "A Comprehensive Review of Gaussian Atmospheric Dispersion Models: Current Usage and Future Perspectives". In: *Euro-Mediterranean Journal for Environmental Integration* 8.1, pp. 219–242. ISSN: 2365-7448. DOI: `10.1007/s41207-023-00354-6`.

Soulhac, L. (2000). "Modélisation de la dispersion atmosphérique à l'intérieur de la canopée urbaine". PhD thesis. Ecole Centrale de Lyon.

Soulhac, L., Lamaison, G., Nguyen, C. V., Charvolin, P., Slimani, M., and Armand, P. (2025). *BUILD: An Operational Lagrangian Model for Atmospheric Dispersion in Built-up Area. Part I: Model Parametrization for Isolated or Wake Interfering Buildings and Validation against RANS, LES and Wind-Tunnel Simulations on a 2D Isolated Obtacle Test-Case.*

Soulhac, L., Salizzoni, P., Cierco, F. X., and Perkins, R. (2011). "The Model SIRANE for Atmospheric Urban Pollutant Dispersion; Part I, Presentation of the Model". In: *Atmospheric Environment* 45.39, pp. 7379–7395. ISSN: 1352-2310. DOI: `10.1016/j.atmosenv.2011.07.008`.

Stull, R. B. (1988). *An Introduction to Boundary Layer Meteorology.*

Sykes, I. (2010). "SCIPUFF Capabilities and Application in Hazard Assessment". In: *13th Conference on Harmonisation within Atmospheric Dispersion Modelling for Regulatory Purposes.* Paris, France.

Taddei, S., Manes, C., and Ganapathisubramani, B. (2016). "Characterisation of Drag and Wake Properties of Canopy Patches Immersed in Turbulent Boundary Layers". In: *Journal of Fluid Mechanics* 798, pp. 27–49. ISSN: 0022-1120, 1469-7645. DOI: `10.1017/jfm.2016.312`.

Talluru, K. M., Hernandez-Silva, C, Philip, J, and Chauhan, K. A. (2017). "Measurements of Scalar Released from Point Sources in a Turbulent Boundary Layer". In: *Measurement Science and Technology* 28.5, p. 055801. ISSN: 0957-0233. DOI: `10.1088/1361-6501/aa614a`.

Tan, W., Li, C., Wang, K., Zhu, G., and Liu, L. (2019). "Geometric Effect of Buildings on the Dispersion of Carbon Dioxide Cloud in Idealized Urban Street Canyons". In: *Process Safety* *and Environmental Protection* 122, pp. 271–280. ISSN: 0957-5820. DOI: `10.1016/j.psep.2018.12.020`.

Taylor, G. I. (1921). "Diffusion by Continuous Movements". In: *Proceedings of the london mathematical society* 2.1, pp. 196–212.

Tennekes, H. (1982). "Similarity Relations, Scaling Laws and Spectral Dynamics". In: *Atmospheric Turbulence and Air Pollution Modelling: A Course Held in The Hague, 21–25 September, 1981.* Ed. by F. T. M. Nieuwstadt and H. van Dop. Atmospheric Sciences Library. Dordrecht: Springer Netherlands, pp. 37–68. ISBN: 978-94-010-9112-1. DOI: `10.1007/978-94-010-9112-1_2`.

Tennekes, H. and Lumley, J. L. (1972). *A First Course in Turbulence.* The MIT Press. ISBN: 978-0-262-20019-6.

Theurer, W., Plate, E. J., and Hoeschele, K. (1996). "Semi-Empirical Models as a Combination of Wind Tunnel and Numerical Dispersion Modelling". In: *Atmospheric Environment* 30.21, pp. 3583–3597. ISSN: 1352-2310. DOI: `10.1016/1352-2310(96)00072-6`.

Thomson, D. J. (1987). "Criteria for the Selection of Stochastic Models of Particle Trajectories in Turbulent Flows". In: *Journal of Fluid Mechanics* 180, pp. 529–556. ISSN: 1469-7645, 0022-1120. DOI: `10.1017/S0022112087001940`.

Thomson, D. J. and Wilson, J. D. (2013). "History of Lagrangian Stochastic Models for Turbulent Dispersion". In: *Geophysical Monograph Series.* Ed. by J. Lin, D. Brunner, C. Gerbig, A. Stohl, A. Luhar, and P. Webley. Washington, D. C.: American Geophysical Union, pp. 19–36. ISBN: 978-1-118-70457-8 978-0-87590-490-0. DOI: `10.1029/2012GM001238`.

Tinarelli, G., Brusasca, G., Oldrini, O., Anfossi, D., Castelli, S. T., and Moussafir, J. (2007). "Micro-Swift-Spray (MSS): A New Modelling System for the Simulation of Dispersion at Microscale. General Description and Validation". In: *Air Pollution Modeling and Its Application XVII.* Ed. by C. Borrego and A.-L. Norman. Boston, MA: Springer US, pp. 449–458. ISBN: 978-0-387-68854-1. DOI: `10.1007/978-0-387-68854-1_49`.

Tinarelli, G. L. and Trini Castelli, S. (2019). "Assessment of the Sensitivity to the Input Conditions with a Lagrangian Particle Dispersion Model in the UDINEE Project". In: *Boundary-Layer Meteorology* 171.3, pp. 491–512. ISSN: 1573-1472. DOI: `10.1007/s10546-018-0413-z`.

Trini Castelli, S. (2025). "Simulations Using the MicroSwiftSpray Modelling System in the Frame of the EXPO-URB Project". In: *23rd International Conference on Harmonisation within Atmospheric Dispersion Modelling for Regulatory Purposes (HARMO23).* Hambourg.

Van Dyke, M. (1982). *An Album of Fluid Motion.* The Parabolic Press. Stanford, California: The Parabolic Press.

Vendel, F., Soulhac, L., Méjean, P., Donnat, L., and Duclaux, O. (2011). "Validation of the Safety Lagrangian Atmospheric Model (SLAM) against a Wind Tunnel Experiment over an Industrial Complex Area". In: *14th Conference on Harmonisation within Atmospheric Dispersion Modelling for Regulatory Purposes.* Kos, Greece, p. 5.

Venkatram, A. (2002). "Accounting for Averaging Time in Air Pollution Modeling". In: *Atmospheric Environment* 36.13, pp. 2165–2170. ISSN: 1352-2310. DOI: `10.1016/S1352-2310(02)00200-5`.

Wang, C. P. (1988). "Laser Doppler Velocimetry". In: *Journal of Quantitative Spectroscopy and Radiative Transfer.* Special Issue on Quantitative Spectroscopy and Laser Diagnostics 40.3, pp. 309–319. ISSN: 0022-4073. DOI: `10.1016/0022-4073(88)90122-7`.

Wieringa, J. (1993). "Representative Roughness Parameters for Homogeneous Terrain". In: *Boundary-Layer Meteorology* 63.4, pp. 323–363. ISSN: 1573-1472. DOI: `10.1007/BF00705357`.

Wilson, J. D. and Sawford, B. L. (1996). “Review of Lagrangian Stochastic Models for Trajectories in the Turbulent Atmosphere”. In: *Boundary-Layer Meteorology* 78.1, pp. 191–210. ISSN: 1573-1472. DOI: `10.1007/BF00122492`.

World Health Organisation (2025). *Air Pollution Data Portal*. `https://www.who.int/data/gho/data/themes/air-pollution`.

Xie, Z.-T. and Castro, I. P. (2009). “Large-Eddy Simulation for Flow and Dispersion in Urban Streets”. In: *Atmospheric Environment* 43.13, pp. 2174–2185. ISSN: 1352-2310. DOI: `10.1016/j.atmosenv.2009.01.016`.

Xie, Z.-T., Hayden, P., Robins, A. G., and Voke, P. R. (2007). “Modelling Extreme Concentrations from a Source in a Turbulent Flow over a Rough Wall”. In: *Atmospheric Environment* 41.16, pp. 3395–3406. ISSN: 1352-2310. DOI: `10.1016/j.atmosenv.2006.12.022`.

Xie, Z. and Castro, I. P. (2006). “LES and RANS for Turbulent Flow over Arrays of Wall-Mounted Obstacles”. In: *Flow, Turbulence and Combustion* 76.3, pp. 291–312. ISSN: 1573-1987. DOI: `10.1007/s10494-006-9018-6`.

Xu, X., Yang, Q., Yoshida, A., and Tamura, Y. (2017). “Characteristics of Pedestrian-Level Wind around Super-Tall Buildings with Various Configurations”. In: *Journal of Wind Engineering and Industrial Aerodynamics* 166, pp. 61–73. ISSN: 0167-6105. DOI: `10.1016/j.jweia.2017.03.013`.

Yee, E. (2001). “An Analytical Model For Threshold Crossing Rates Of Concentration Fluctuations In Dispersing Plumes”. In: *Boundary-Layer Meteorology* 98.3, pp. 517–527. ISSN: 1573-1472. DOI: `10.1023/A:1018751125337`.

Yee, E. and Biltoft, C. A. (2004). “Concentration Fluctuation Measurements in a Plume Dispersing Through a Regular Array of Obstacles”. In: *Boundary-Layer Meteorology* 111.3, pp. 363–415. ISSN: 1573-1472. DOI: `10.1023/B:BOUN.0000016496.83909.ee`.

Yee, E., Chan, R., Kosteniuk, P. R., Chandler, G. M., Biltoft, C. A., and Bowers, J. F. (1994). “Experimental Measurements of Concentration Fluctuations and Scales in a Dispersing Plume in the Atmospheric Surface Layer Obtained Using a Very Fast Response Concentration Detector”. In: *Journal of Applied Meteorology and Climatology* 33.8, pp. 996–1016. ISSN: 1520-0450, 0894-8763. DOI: `10.1175/1520-0450(1994)033<0996:EMOCFA>2.0.CO;2`.

Yee, E., Gailis, R. M., Hill, A., Hilderman, T., and Kiel, D. (2006). “Comparison of Wind-tunnel and Water-channel Simulations of Plume Dispersion through a Large Array of Obstacles with a Scaled Field Experiment”. In: *Boundary-Layer Meteorology* 121.3, pp. 389–432. ISSN: 1573-1472. DOI: `10.1007/s10546-006-9084-2`.

Yee, E., Kosteniuk, P. R., Chandler, G. M., Biltoft, C. A., and Bowers, J. F. (1993a). “Statistical Characteristics of Concentration Fluctuations in Dispersing Plumes in the Atmospheric Surface Layer”. In: *Boundary-Layer Meteorology* 65.1, pp. 69–109. ISSN: 1573-1472. DOI: `10.1007/BF00708819`.

Yee, E., Wilson, D. J., and Zelt, B. W. (1993b). “Probability Distributions of Concentration Fluctuations of a Weakly Diffusive Passive Plume in a Turbulent Boundary Layer”. In: *Boundary-Layer Meteorology* 64.4, pp. 321–354. ISSN: 1573-1472. DOI: `10.1007/BF00711704`.

Zhao, Q., Li, R., Cao, K., Yi, M., and Liu, H. (2024). “Influence of Building Spatial Patterns on Wind Environment and Air Pollution Dispersion inside an Industrial Park Based on CFD Simulation”. In: *Environmental Monitoring and Assessment* 196.5, p. 427. ISSN: 1573-2959. DOI: `10.1007/s10661-024-12593-3`.